

SIMULATION OF VIBRATIONS CAUSED BY FAULTS IN BEARINGS AND GEARS

LAV GURUNATH DESHPANDE

B.E., M.Tech.

A thesis in fulfilment of the requirements for the degree of
Doctor of Philosophy



School of Mechanical and Manufacturing Engineering
The University of New South Wales

July 2014

PLEASE TYPE

THE UNIVERSITY OF NEW SOUTH WALES
Thesis/Dissertation Sheet

Surname or Family name: Deshpande

First name: Lav

Other name/s:

Abbreviation for degree as given in the University calendar: PhD

School: Mechanical and Manufacturing

Faculty: Engineering

Title: Simulation of vibrations caused by faults in bearings and gears

Abstract 350 words maximum: (PLEASE TYPE)

This research presents improved techniques to simulate gearbox vibrations due to faults in gears and bearings.

Lumped parameter models (LPMs) are widely used to study the dynamic behaviour of mechanical systems such as gearboxes. However, LPMs contain limited information about flexible structures such as the casing. This results in poor spectral matching over a wide frequency range, and was found not to properly represent the modulation of gearmesh signals by extended bearing faults, this being affected by interaction with the casing dynamic properties. An alternative approach based on direct finite element analysis (FEA) is not usually viable as the model size and thus computing resource requirements become prohibitive. Hence an improved simulation model was developed by coupling the LPM of the internals (shafts, gears and bearings) with a reduced FE model of the casing based on the Craig-Bampton method of component mode synthesis (CMS) over the frequency range of interest. Prior to model reduction, the FE model of the casing was updated by correlating with the results of experimental modal analysis (EMA). The combined model was equally capable of simulating bearing faults in the UNSW parallel shaft spur gearbox. The responses due to bearing fault entry and exit were investigated, which can be used to predict the fault size – a vital parameter in bearing diagnostics and prognostics. Simulated results compared well with measurements. The combined model was further improved by making a reduced FE model of the internals, to create a full reduced model of the gearbox.

A simplified transverse-torsional LPM was developed to simulate planet gear faults such as tooth cracks and spalls in the UNSW planetary gearbox. The effect of the two simultaneous meshes of the planet gear with the ring and sun gears was investigated since the contact with the two gears is on opposite flanks of each planet gear tooth. The simulated results correlated well with measurements and clearly differentiated the two types of faults with reduction in the stiffness due to a tooth crack visible in both contacts whereas a spall on one flank showed up only in one contact.

Declaration relating to disposition of project thesis/dissertation

I hereby grant to the University of New South Wales or its agents the right to archive and to make available my thesis or dissertation in whole or in part in the University libraries in all forms of media, now or here after known, subject to the provisions of the Copyright Act 1968. I retain all property rights, such as patent rights. I also retain the right to use in future works (such as articles or books) all or part of this thesis or dissertation.

I also authorise University Microfilms to use the 350 word abstract of my thesis in Dissertation Abstracts International (this is applicable to doctoral theses only).

LAV DESHPANDE

KAREL RUBER

24/07/14

Signature

Witness

Date

The University recognises that there may be exceptional circumstances requiring restrictions on copying or conditions on use. Requests for restriction for a period of up to 2 years must be made in writing. Requests for a longer period of restriction may be considered in exceptional circumstances and require the approval of the Dean of Graduate Research.


FOR OFFICE USE ONLY

Date of completion of requirements for Award:

THIS SHEET IS TO BE GLUED TO THE INSIDE FRONT COVER OF THE THESIS

ORIGINALITY STATEMENT

'I hereby declare that this submission is my own work and to the best of my knowledge it contains no materials previously published or written by another person, or substantial proportions of material which have been accepted for the award of any other degree or diploma at UNSW or any other educational institution, except where due acknowledgement is made in the thesis. Any contribution made to the research by others, with whom I have worked at UNSW or elsewhere, is explicitly acknowledged in the thesis. I also declare that the intellectual content of this thesis is the product of my own work, except to the extent that assistance from others in the project's design and conception or in style, presentation and linguistic expression is acknowledged.'

Signed 

Date 24-7-2014

COPYRIGHT STATEMENT

'I hereby grant the University of New South Wales or its agents the right to archive and to make available my thesis or dissertation in whole or part in the University libraries in all forms of media, now or here after known, subject to the provisions of the Copyright Act 1968. I retain all proprietary rights, such as patent rights. I also retain the right to use in future works (such as articles or books) all or part of this thesis or dissertation.

I also authorise University Microfilms to use the 350 word abstract of my thesis in Dissertation Abstract International (this is applicable to doctoral theses only).

I have either used no substantial portions of copyright material in my thesis or I have obtained permission to use copyright material; where permission has not been granted I have applied/will apply for a partial restriction of the digital copy of my thesis or dissertation.'

Signed 

Date 24-7-2014

AUTHENTICITY STATEMENT

'I certify that the Library deposit digital copy is a direct equivalent of the final officially approved version of my thesis. No emendation of content has occurred and if there are any minor variations in formatting, they are the result of the conversion to digital format.'

Signed 

Date 24-7-2014

To my parents

Abstract

This research presents improved techniques to simulate gearbox vibrations due to faults in gears and bearings.

Lumped parameter models (LPMs) are widely used to study the dynamic behaviour of mechanical systems such as gearboxes. However, LPMs contain limited information about flexible structures such as the casing. This results in poor spectral matching over a wide frequency range, and was found not to properly represent the modulation of gearmesh signals by extended bearing faults, this being affected by interaction with the casing dynamic properties. An alternative approach based on direct finite element analysis (FEA) is not usually viable as the model size and thus computing resource requirements become prohibitive. Hence an improved simulation model was developed by coupling the LPM of the internals (shafts, gears and bearings) with a reduced FE model of the casing based on the Craig-Bampton method of component mode synthesis (CMS) over the frequency range of interest. Prior to model reduction, the FE model of the casing was updated by correlating with the results of experimental modal analysis (EMA). The combined model was equally capable of simulating bearing faults in the UNSW parallel shaft spur gearbox. The responses due to bearing fault entry and exit were investigated, which can be used to predict the fault size – a vital parameter in bearing diagnostics and prognostics. Simulated results compared well with measurements. The combined model was further improved by making a reduced FE model of the internals, to create a full reduced model of the gearbox.

A simplified transverse-torsional LPM was developed to simulate planet gear faults such as tooth cracks and spalls in the UNSW planetary gearbox. The effect of the two simultaneous meshes of the planet gear with the ring and sun gears was investigated since the contact with the two gears is on opposite flanks of each planet gear tooth. The simulated results correlated well with measurements and clearly differentiated the two types of faults with reduction in the stiffness due to a tooth crack visible in both contacts whereas a spall on one flank showed up only in one contact.

Acknowledgements

First of all, I would like to express my most sincere gratitude to my supervisor Emeritus Professor Bob Randall for his invaluable guidance, support, patience and unwavering enthusiasm throughout this research project, which has been an extremely rewarding experience for me. Thank you Bob for your trust, effort and for all the opportunities you provided me.

I am deeply grateful to my co-supervisor Dr. Nader Sawalhi for his guidance and support. Thank you Nader for always being approachable and for your willingness to share your knowledge, even while you have been away. I am also deeply thankful to my other co-supervisor Dr. Wade Smith for his interest, advice and guidance especially in the research on the planetary gearbox. Special thanks are also due to Dr. Hiroaki Endo for his time and generosity in sharing the gear dynamic module for adaptation in the planetary simulation models.

I would like to acknowledge with gratitude the financial support provided by the ARC (Australian Research Council) through Discovery project DP0771204, and DSTO (Defence Science and Technology Organisation) through the Centre of Expertise in Helicopter Structures and Diagnostics at UNSW. I would also like to express my sincere thanks to Dr. David Forrester and Dr. Wenyi Wang for their valuable suggestions and feedback.

Special and sincere thanks to Mr. Russell Overall for his assistance in the laboratory testing and to other staff, especially Mr Subash Puthanveetil, Mr. Vince Carnevale, Mr. Radhakrishnan Pullambil, Mr Ian Cassapi, Mr Seetharam Mahadevan and Mr Stephen Kuhle for ensuring the smooth running of the test rig and the instrumentation. Special thanks to the School of Mechanical and Manufacturing Engineering for providing the resources required to complete this research.

I would like to acknowledge the support and encouragement provided by my colleagues and fellow PhD students Jian Chen, Michael Coats and Karel Ruber. I sincerely thank them for sharing their insights through lively discussions and useful feedback.

Special thanks are due to my wife Sunita and my daughter Vinita for all their love and support during the course of this research. Without their help, care and many sacrifices, this thesis would not have been completed. I would also like to thank my brother Kush and his family for their support and encouragement.

And finally, I would like to express my deepest gratitude to my parents who had been a constant source of inspiration, but unfortunately could not see the completion of this thesis. This work is dedicated to the loving memory of my parents.

Table of Contents

Originality Statement	iii
Copyright and Authenticity Statement.....	iv
Abstract	vi
Acknowledgements	vii
List of Figures	xvi
List of Tables	xxiii
List of Abbreviations	xxiv
Chapter 1. Introduction	1
1.1 Background	1
1.2 Research objectives	2
1.3 Methodology	3
1.3.1 Simulation of bearing faults	3
1.3.2 Simulation of planet gear faults	4
1.4 Thesis Structure	5
PART I SIMULATION OF BEARING FAULTS	8
Chapter 2. Review of Rolling Element Bearing Diagnostics and Fault Simulation.....	9
2.1 Introduction	9
2.2 Vibrations generated by rotating machines	10
2.2.1 Vibration induced by Bearings	10
2.2.2 Vibration induced by Gears	12
2.3 Diagnostic techniques	14
2.3.1 Bearing Fault Diagnosis	15
2.3.2 Gear Fault Diagnosis	18
2.3.3 Spectral Kurtosis (SK)	20
2.3.4 SK Enhancement Techniques	21

2.4 Bearing / Gear Vibration Interaction	22
2.4.1 Additive Interaction	22
2.4.2 Multiplicative Interaction	22
2.5 Bearing Simulation Models	22
2.5.1 Dynamic Modelling of the UNSW Gear Test Rig	28
2.6 Model Reduction Techniques	30
2.6.1 Component Mode Synthesis	32
2.7 Gearbox dynamic model developed in this study	36
2.8 References	37
Chapter 3. Experimental Modal Analysis and FE Model Updating of Gearbox Casing ...	46
3.1 Introduction	46
3.2 Overview of finite element model updating	47
3.2.1 Experimental modal analysis	49
3.2.2 Finite element model updating	50
3.2.2.1 Pretest analysis	51
3.2.2.2 Correlation analysis	51
3.2.2.3 Parameter and response selection	52
3.2.2.4 Sensitivity analysis and model updating	52
3.2.3 Sensitivity based model updating	53
3.2.4 Model updating using operational data	53
3.2.5 Model updating applications	54
3.2.5.1 Structural Dynamic Modification (SDM)	54
3.2.5.2 Structural Health Monitoring (SHM)	54
3.3 Experimental Modal Analysis (EMA) of UNSW gearbox casing	55
3.4 Model updating: UNSW gearbox casing	56
3.4.1 FE model of gearbox casing	56
3.4.2 Test-FEA correlation	57
3.5 Summary	60
3.6 References	61

Chapter 4. Gearbox dynamic modeling using model reduction techniques	65
4.1 Introduction	65
4.2 Dynamic modeling of the UNSW gear test rig	66
4.2.1 Rolling element bearing model	67
4.2.2 Modeling of bearing localised fault (inner/outer race)	69
4.2.3 Modeling of bearing extended fault (inner/outer race)	71
4.2.4 Gear Dynamics	72
4.2.5 LPM of gearbox internals	73
4.3 Reduced FE model of the casing	75
4.3.1 Craig-Bampton method of CMS	76
4.3.2 Implementation of Craig-Bampton reduction method	79
4.3.3 Combined model (LPM- reduced FEM).....	82
4.4 Full reduced model of gear test rig (182 DOF model).....	83
4.4.1 Methodology: Full reduced model	84
4.4.2 Reduced dynamic model (full FEM reduction)	85
4.4.3 Modeling of bearing faults	87
4.5 Simulink models	88
4.6 Summary	88
4.7 References	89
Chapter 5. Experimental validation of bearing fault simulation models	92
5.1 Introduction	92
5.2 Experimental set-up	93
5.2.1 Gearbox test rig	93
5.3 Bearing faults	94
5.3.1 Bearings under test	94
5.3.2 Localised outer race fault	95
5.3.3 Localised inner race faults	96
5.3.4 Extended inner race faults	96

5.3.5 Extended outer race faults	97
5.4 Vibration signal measurement	97
5.5 Comparison of experimental and simulation results	98
5.6 Localised faults in the bearing	100
5.6.1 Inner race localised fault	101
5.6.1.1 Comparison of time domain signals	101
5.6.1.2 Comparison of power spectra	103
5.6.1.3 Squared envelope spectra	104
5.6.2 Outer race localised fault	105
5.6.2.1 Comparison of time domain signals	105
5.6.2.2 Comparison of power spectra	106
5.6.2.3 Squared envelope spectra	107
5.7 Extended faults in bearing	108
5.7.1 Inner race extended fault	108
5.7.1.1 Comparison of time domain signals	108
5.7.1.2 Comparison of power spectra	110
5.7.1.3 Comparison of power spectra at selected cyclic frequency	111
5.7.2 Outer race extended fault	115
5.7.2.1 Comparison of time domain signals	115
5.7.2.2 Comparison of power spectra	116
5.7.2.3 Comparison of power spectra at selected cyclic frequency	117
5.8 Fault entry/exit phenomena	119
5.9 Summary	122
5.10 References	124
PART II SIMULATION OF PLANET GEAR FAULTS	127
Chapter 6. Planetary Gear Trains: Vibration Analysis And Simulation Techniques.....	128
6.1 Introduction	128
6.2 Modeling of the planetary system	129

6.2.1 Mesh phasing	131
6.2.2 Deformable gear models	133
6.3 Modeling faults in planetary gear sets	136
6.3.1 Analytical models to predict sideband mechanisms	139
6.3.2 Effect of transfer path on the vibration signal	140
6.4 Signal processing techniques	141
6.5 Planetary simulation model developed in this study	144
6.6 References	145
Chapter 7. Simulation of UNSW Planetary Gearbox	152
7.1 Introduction	152
7.2 UNSW Planetary gearbox: General arrangement	153
7.3 Planetary gearbox – Experimental measurements	155
7.3.1 Test rig	155
7.3.2 Seeded gear faults	156
7.3.3 Instrumentation and data acquisition	156
7.3.4 Test program and conditions	157
7.4 Gear ratios, Expected frequencies and Torque calculations	158
7.5 Contact ratios and mesh stiffness curves	161
7.5.1 Gear tooth stiffness	163
7.6 Kinematic configuration and Mesh phasing	164
7.7 Planetary gearbox – Lumped Parameter Model	167
7.7.1 Assumptions	169
7.7.2 Equations of Motion	169
7.7.2.1 Gear pair (sun-planet, ring-planet).....	170
7.7.2.2 Carrier-planet pair	171
7.7.2.3 The overall assembly	171
7.7.3 Planetary LPM - Rigid body mode	174
7.8 Signal processing methodology	175
7.8.1 Procedure 1: Time synchronous averaging	176

7.8.2 Procedure 2: Autoregressive linear prediction filtering and spectral kurtosis	177
7.8.3 Other signal processing approaches	178
7.9 Results and Discussion	178
7.9.1 Comparison of acceleration spectra	179
7.9.2 Kurtosis with AR linear prediction filtering	181
7.10 Conclusion	188
7.11 References	188
Chapter 8. Summary and Future Work	191
8.1 Summary and conclusions	191
8.1.1 Simulation of bearing faults (Part I Chapters 2-5).....	191
8.1.2 Simulation of planet gear faults (Part II Chapters 6-7).....	194
8.2 Recommendations for future work	195
8.2.1 Simulation of bearing faults (Part I)	195
8.2.2 Simulation of planet gear faults (Part II)	196
8.3 Contribution to Research	197
List of Publications	198
APPENDIX A: Combined LPM-Reduced FE Model (146 DOF)	200
A.1 Introduction	200
A.2 Physical parameters and system matrices - LPM (22 DOF)	201
A.2.1 System matrices	203
A.3 Simulink model - 146 DOF	205
A.4 References	207
APPENDIX B: Full Reduced Model (182 DOF)	208
B.1 Introduction	208
B.2 Gearbox internals	208
B.2.1 Physical parameters	208
B.2.2 Master Degrees of Freedom (MDOFs)	209
B.3 Simulink model - 182 DOF	210
B.4 References	212

APPENDIX C: Planetary Simulation Model	213
C.1 Simulink model: Planetary gear	213
C.2 Planetary gear LPM – Equations of motion	216
C.3 Planetary LPM simulation – Input data	222
C.4 References	223

List of Figures

Figure 1.1 Thesis structure	7
Figure 2.1 Rolling element bearing vibration signal characteristics due to local faults	11
Figure 2.2 Deviations from ideal tooth profile (a) due to deflection under load, (b) due to wear	13
Figure 2.3 Typical vibration spectrum due to wear	13
Figure 2.4 Effect of fault distribution on sideband pattern; (a) local fault (b) distributed fault	14
Figure 2.5 Process showing High Frequency Resonance Technique	16
Figure 2.6 Envelope analysis of bearing fault pulses with and without frequency fluctuation	17
Figure 2.7 Envelope analysis using Hilbert Transform technique	17
Figure 2.8 Load distribution in a rolling element bearing	23
Figure 2.9 Bearing models	24
Figure 2.10 Bearing system model in the principal radial direction	26
Figure 2.11 Bearing fault model using fault elements	26
Figure 2.12 Bearing model proposed by Tadina and Boltežar	27
Figure 2.13 UNSW gearbox test rig & schematic diagram	28
Figure 2.14 Schematic of CMS-MBS interface	35
Figure 3.1 Product development processes	47
Figure 3.2 CAE simulation environment	48
Figure 3.3 General procedure - linking FEA with Test	51
Figure 3.4 The optimal model updating sequence	52
Figure 3.5 EMA - Experimental Setup	55
Figure 3.6 Accelerometer locations	55
Figure 3.7 FE model of UNSW gearbox casing	57

Figure 3.8 MAC before updating	59
Figure 3.9 MAC after updating	59
Figure 3.10 Mode shape comparison [Red - Test model, Blue – FE model]	59
Figure 3.11 Model updating results	60
Figure 4.1 5 DOF bearing-pedestal model	67
Figure 4.2 Two degree of freedom model	68
Figure 4.3 Localised fault on outer race	70
Figure 4.4 Spall geometry – Localised bearing faults	71
Figure 4.5 Rough surface topography representing the extended faults in bearing	72
Figure 4.6 LPM of the pinion and the gear	72
Figure 4.7 34 DOF LPM of the gearbox test rig	74
Figure 4.8 FE model of gearbox casing	75
Figure 4.9 Rearranging the extracted mass and stiffness matrices	81
Figure 4.10 Rearranged mass and stiffness matrices	81
Figure 4.11 FE model of gearbox internals	85
Figure 4.12 CMS reduction of full FE model of gearbox (182 DOFs)	87
Figure 5.1 UNSW gearbox test rig	94
Figure 5.2 Schematic diagram of gearbox test rig	94
Figure 5.3 Bearing under test	95
Figure 5.4 Localised outer race fault	95
Figure 5.5 Localized inner race fault	96
Figure 5.6 Extended inner race fault	96
Figure 5.7 Extended (rough) outer race fault	97
Figure 5.8 Evaluation of total response at the accelerometer position	99
Figure 5.9 Time domain signal – Test	102

Figure 5.10 Time domain signal – LPM 34 DOF	102
Figure 5.11 Time domain signal – 146 DOF	102
Figure 5.12 Time domain signal – 146 DOF	102
Figure 5.13 Time domain signal - 182 DOF	102
Figure 5.14 Time domain signal - 182 DOF	102
Figure 5.15 PSD – Test, Localised inner race fault	103
Figure 5.16: PSD –LPM 34 DOF, Localised inner race fault	103
Figure 5.17 PSD –146 DOF, Localised inner race fault (Approach B)	103
Figure 5.18 PSD –146 DOF, Localised inner race fault (Approach A)	103
Figure 5.19 PSD –182 DOF, Localised inner race fault (Approach B)	103
Figure 5.20: PSD – 182 DOF, Localised inner race fault (Approach A)	103
Figure 5.21 Sq. envelope spectrum – Test, Localised inner race fault	104
Figure 5.22 Sq. envelope spectrum – 34 DOF, Localised inner race fault	104
Figure 5.23 Sq. envelope spectrum –146 DOF, Localised inner race fault (Approach B)	104
Figure 5.24 Sq. envelope spectrum –146 DOF, Localised inner race fault (Approach A)	104
Figure 5.25 Sq. envelope spectrum –182 DOF, Localised inner race fault (Approach B)	104
Figure 5.26 Sq. envelope spectrum –182 DOF, Localised inner race fault (Approach A)	104
Figure 5.27 Time domain signal - Test	105
Figure 5.28 Time domain signal – LPM 34 DOF	105
Figure 5.29 Time domain signal – 146 DOF (Approach B)	105
Figure 5.30 Time domain signal – 146 DOF (Approach A)	105
Figure 5.31 Time domain signal - 182 DOF (Approach B)	105
Figure 5.32 Time domain signal - 182 DOF (Approach A)	105
Figure 5.33 PSD – Test, Localised outer race fault	106
Figure 5.34 PSD –LPM 34 DOF, Localised outer race fault	106
Figure 5.35 PSD – 146 DOF, Localised outer race fault (Approach B)	106
Figure 5.36 PSD – 146 DOF, Localised outer race fault (Approach A)	106

Figure 5.37 PSD – 182 DOF, Localised outer race fault (Approach B)	106
Figure 5.38 PSD – 182 DOF, Localised outer race fault (Approach A)	106
Figure 5.39 Sq. envelope spectrum – Test, Localised outer race fault	107
Figure 5.40 Sq. envelope spectrum – 34 DOF, Localised outer race fault	107
Figure 5.41 Sq. envelope spectrum –146 DOF, Localised outer race fault (Approach B)	107
Figure 5.42 Sq. envelope spectrum –146 DOF, Localised outer race fault (Approach A)	108
Figure 5.43 Sq. envelope spectrum –182 DOF, Localised outer race fault (Approach B)	107
Figure 5.44 Sq. envelope spectrum –182 DOF, Localised outer race fault (Approach A)	108
Figure 5.45 Time domain signal – Test	109
Figure 5.46 Time domain signal – 146 DOF (Approach B)	109
Figure 5.47 Time domain signal – 146 DOF (Approach A)	109
Figure 5.48 Time domain signal - 182 DOF (Approach B)	109
Figure 5.49 Time domain signal - 182 DOF (Approach A)	109
Figure 5.50 PSD – Test, Extended inner race fault	110
Figure 5.51 PSD – LPM 34 DOF, Extended inner race fault	110
Figure 5.52 PSD – 146 DOF, Extended inner race fault (Approach B)	110
Figure 5.53 PSD – 146 DOF, Extended inner race fault (Approach A)	110
Figure 5.54 PSD – 182 DOF, Extended inner race fault (Approach B)	110
Figure 5.55 PSD – 182 DOF, Extended inner race fault (Approach A)	110
Figure 5.56 SCF Test - Extended inner race fault	112
Figure 5.57 SCF 34LPM – Smooth extended inner race fault	113
Figure 5.58 SCF 148 DOF - Extended inner race fault (Approach A)	113
Figure 5.59: SCF 182 DOF - Extended inner race fault (Approach A)	114
Figure 5.60 Time domain signal – Test	115
Figure 5.61 Time domain signal – 146 DOF (Approach B)	115
Figure 5.62 Time domain signal – 146 DOF (Approach A)	115
Figure 5.63 Time domain signal - 182 DOF (Approach B)	115

Figure 5.64 Time domain signal - 182 DOF (Approach A)	115
Figure 5.65 PSD – Test, Extended outer race fault	116
Figure 5.66 PSD – LPM 34 DOF, Extended outer race fault	116
Figure 5.67 PSD – 146 DOF, Extended outer race fault (Approach B)	116
Figure 5.68 PSD – 146 DOF, Extended outer race fault (Approach A)	117
Figure 5.69 PSD – 182 DOF, Extended outer race fault (Approach B)	116
Figure 5.70 PSD – 182 DOF, Extended outer race fault (Approach A)	117
Figure 5.71 SCF Test - Extended outer race fault	118
Figure 5.72 SCF 146 DOF - Extended outer race fault (Approach A)	118
Figure 5.73 SCF 182 DOF - Extended outer race fault (Approach A)	119
Figure 5.74 Test data: Localized inner race fault	121
Figure 5.75 LPM: Localized inner race fault	121
Figure 5.76 146 DOF: Localized inner race fault (Approach A)	121
Figure 5.77 182 DOF: Localized inner race fault (Approach A)	121
Figure 5.78 Test data: Localized outer race fault	122
Figure 5.79 LPM: Localized outer race fault	122
Figure 5.80 146 DOF: Localized outer race fault (Approach A)	122
Figure 5.81 182 DOF: Localized outer race fault (Approach A)	122
Figure 6.1 Planetary gear set dynamic models (n = no of planets)	130
Figure 6.2 Planetary gear lumped-parameter analytical model	131
Figure 6.3 Planetary gear system – Finite element mesh	134
Figure 6.4 Elastic-discrete model of a planetary gear	135
Figure 6.5 Gear mesh stiffness evolution with tooth pitting damage	138
Figure 6.6 Gear mesh stiffness evolution with tooth breakage	138
Figure 6.7 Transfer path with fault on the planet gear	140
Figure 6.8 Signal modulation as seen by an externally mounted accelerometer	142

Figure 6.9 Planet gear vibration separation based on McFadden's method	143
Figure 7.1 Basic layout of planetary gearbox	153
Figure 7.2 Gear details for the UNSW planetary gearbox test rig	154
Figure 7.3 Modified design – Circular sleeve used to locate the ring gear	155
Figure 7.4 UNSW gearbox test rig with planetary gearbox	155
Figure 7.5 Seeded planet gear faults	156
Figure 7.6 Top view of UNSW planetary gearbox showing transducer placement	157
Figure 7.7 Mesh stiffness curves	164
Figure 7.8 Mesh stiffness curve phasing - undamaged gear	165
Figure 7.9 Mesh stiffness curve phasing - damaged gear	166
Figure 7.10 Spall geometry (1 mesh cycle)	167
Figure 7.11 Spall curve (5 carrier cycles)	167
Figure 7.12 Planetary gear sub-systems	168
Figure 7.13 Rigid body mode (Mode 1, Frequency 0 Hz)	175
Figure 7.14 Procedure 1: Time synchronous averaging	176
Figure 7.15 Procedure 2: AR linear prediction filtering and spectral kurtosis	177
Figure 7.16 Simulation: ring gear (Undamaged gear)	180
Figure 7.17 Test: ring gear (Undamaged gear)	180
Figure 7.18 Simulation: ring gear (Tooth crack)	180
Figure 7.19 Test: ring gear Tooth crack opening when meshing with sun	180
Figure 7.20 Test: ring gear Tooth crack opening when meshing with ring	180
Figure 7.21 Simulation: ring gear Tooth spall meshing with ring gear	181
Figure 7.22 Test: ring gear Tooth spall meshing with ring gear	181
Figure 7.23 Simulation: ring gear Tooth spall meshing with sun gear	181
Figure 7.24 Test: ring gear Tooth spall meshing with sun gear	181
Figure 7.25 Simulation: undamaged gear (4 carrier cycles)	183

Figure 7.26 Test: undamaged gear (4 carrier cycles)	183
Figure 7.27 Simulation: Planet tooth crack (4 carrier cycles)	184
Figure 7.28 Test: Planet tooth crack opening when meshing with Sun gear (4 carrier cycles)	184
Figure 7.29 Test: Planet tooth crack opening when meshing with Ring gear (4 carrier cycles)	185
Figure 7.30 Simulation: Planet tooth spall meshing with ring gear (4 carrier cycles)	186
Figure 7.31 Test: Planet tooth spall meshing with ring gear (4 carrier cycles)	186
Figure 7.32 Simulation: Planet tooth spall meshing with sun gear (4 carrier cycles)	187
Figure 7.33 Test: Planet tooth spall meshing with sun gear (4 carrier cycles)	187
Figure A.1 22 DOF LPM - extracted from 34 DOF Model	201
Figure A.2 146 DOF Simulink model	205
Figure A.3 Combining LPM and reduced FE model of casing	206
Figure A.4 Bearing S-function	207
Figure B.1 182 DOF Simulink model	211
Figure B.2 Combining reduced FE models of casing and internals	211
Figure B.3 Bearing S-function	212
Figure C.1 Planetary gear Simulink model	214
Figure C.2 Planetary gear (F/M) module	215

List of Tables

Table 3.1 Comparison of Mode shape pairs	58
Table 4.1 Full reduced FE model - summary of DOFs	86
Table: 5.1 Bearing specifications	94
Table 7.1 Test program	157
Table 7.2 No of teeth on gears in planetary gearbox	158
Table 7.3 Calculation of planetary motion	159
Table 7.4 Gear mesh frequencies of the planetary gearbox	161
Table 7.5 Planetary insert gear data	162
Table 7.6 Rigid body mode	175
Table 7.7 Kurtosis using AR method	182
Table A.1 Physical parameters of gear dynamic model	202
Table A.2 Physical parameters of bearing model	202
Table B.1 FE model properties of gearbox internals	209
Table B.2 FE model of gearbox internals – Summary of MDOFs	209
Table C.1 Mesh frequency force vector	220
Table C.2 Planetary insert gear data	222
Table C.3 Mass and Moment of inertia	222
Table C.4 Bearing support stiffness and damping	222

List of Abbreviations

AM	Amplitude Modulation
ANC	Adaptive Noise Cancellation
ANN	Artificial Neural Networks
AR	Autoregressive
ARMED	Autoregressive Minimum Entropy Deconvolution
BPFI	Ball Pass Frequency Inner race
BPFO	Ball Pass Frequency Outer race
BSF	Ball/Roller Spin Frequency
CAE	Computer Aided Engineering
CB	Craig-Bampton
CMS	Component Mode Synthesis
CR	Contact Ratio
CSAC	Cross Signature Assurance Criteria
CSF	Cross Signature Scale Factor
CWT	Continuous Wavelet Transformation
DFT	Discrete Fourier Transform
DOF	Degrees of Freedom
DRS	Discrete/Random Separation
DSM	Dynamic Substructuring Method
EDM	Electric Discharge Machining
EHD	Elasto-Hydrodynamic
EHL	Elasto-Hydrodynamic Lubrication
EMA	Experimental Modal Analysis
FEM	Finite Element Method
FM	Frequency Modulation
FRF	Frequency Response Functions

FTF	Fundamental Train Frequency
GMF	Gearmesh Frequency
GTE	Geometric Transmission Error
HBM	Harmonic Balance Method
HFRT	High Frequency Resonance Technique
IRS	Improved Reduction System
LoA	Line of Action
LPM	Lumped Parameter Model
MAC	Modal Assurance Criterion
MBS	Multi-Body System
MCM	Machine Condition Monitoring
MCS	Monte Carlo Simulation
MDOF	Master Degrees of Freedom
MED	Minimum Entropy Deconvolution
MNF	Modal Neutral File
ODS	Operational Deflection Shape
OMA	Operational Modal Analysis
PGMF	Planetary Gear Mesh Frequency
PGT	Planetary Gear Train
PM	Phase Modulation
PSD	Power Spectral Density
SCF	Spectral Correlation Function
SGMF	Spur Gear Mesh Frequency
SK	Spectral Kurtosis
SANC	Self Adaptive Noise Cancellation

SDM	Structural Dynamic Modification
SEREP	System Equivalent Reduction Expansion Process
SHM	Structural Health Monitoring
TE	Transmission Error
TPM	Tooth Profile Modification
TSA	Time Synchronous Averaging
UNSW	University of New South Wales
VPD	Virtual Product Development

CHAPTER 1

INTRODUCTION

1.1 Background

It is extremely important that industrial machinery operate without unforeseen breakdowns. The continuous and smooth operation of the machinery must be ensured to prevent catastrophic failures, which can result in the loss of production and compromise human safety. The application of Machine Condition Monitoring (MCM) techniques for the detection, diagnosis and prognosis of incipient faults, has traditionally been an integral part of a maintenance strategy aimed at improving productivity by reducing the downtime and ensuring the safe operation of the equipment.

One such critical equipment is a geared transmission which is found in virtually all industries, namely process industry (petrochemicals, mining), power generation (turbines, engines), transportation (aerospace, automotive) etc. A typical gearbox is characterised by the complex dynamic interaction among the individual components such as gears, shafts, bearings and the casing which adds to the difficulty of accurate diagnosis and prognosis of faults in any of these components.

Current diagnostic techniques for such complex machines can only be applied and interpreted by experts and there is a great need to automate the procedures so that they can be applied more widely, in particular in remote areas where a plant may have to shut down while replacement components are being manufactured and shipped.

Dynamic behaviour of a machine can be predicted with reasonable accuracy using simulation models. These models are capable of generating the characteristic vibration signals in the presence of faults such as in gears and bearings. With the advent of high speed computers it is now possible to simulate the behaviour of the machine structure and predict its performance in the presence of faults in different locations and severity

under various operating conditions, thus eliminating many costly and time consuming experimental tests.

The simulation data can be used to train artificial neural networks (ANNs) to recognise the onset of incipient faults. Moreover simulation can also assist in the development of prognostic algorithms by helping to predict how long a machine can safely be operated ahead of the planned maintenance.

1.2 Research objectives

Failure of gears and bearings is still one of the most common causes and perhaps the major cause of breakdown of industrial machinery. A lot of research has been carried out in the field of machine condition monitoring, especially related to the diagnostics and prognostics of gears and bearings. The development of dynamic simulation models is becoming more popular as it eliminates the need to conduct large numbers of costly and time consuming experiments required to be carried out until failure (some experimentation is required to validate and update simulation models). However, the quest for a more accurate dynamic simulation model still continues, in order to better understand the mechanisms of vibration transmission through machine components, and the influence of various fault types, their locations and severity, to evaluate the remaining useful life of the equipment.

The simulation of bearing faults in a typical gearbox using the traditional lumped parameter modelling (LPM) approach is quite well developed due to the simplicity of the method and the reasonable accuracy of results. However, in the absence of gearbox component (especially the casing) flexibility, the LPM approach fails to properly represent the gear/bearing interaction and is found to be inadequate especially in the simulation of extended faults in the bearing, where the bearing fault frequency modulates the gearmesh in the low frequency region.

Planetary gears (also known as epicyclic gears) are another common form of geared machinery and the preferred mode of power transmission in the automotive, aerospace and wind turbine industries due to their compactness and large torque-to-weight ratio. However, the condition monitoring of the planetary gears is more complex due to the rotating axes of the planet gears and the time-varying transmission path of the vibration signal (depending on the location of the fault). Simulation models of planetary gears

have been widely used to investigate this complex dynamic behaviour. However, a fault on a planet gear, which simultaneously meshes with the ring and the sun gear, adds to further difficulties in the signal processing and presents a unique challenge. One of the objectives of this study is to investigate the effect of these two simultaneous meshes on the vibration signal, and help differentiate between a tooth crack and a spall on a planet gear.

Hence, the development of more realistic simulation models of complex gearboxes, which can provide better predictions of the externally measured vibration responses to faults in gears and bearings, forms the main motivation driving this research project.

The objectives of this research project are:

1. Simulation of bearing faults

- To develop an improved bearing fault simulation model of the UNSW gearbox test rig in the parallel shaft (fixed axis) spur gear configuration
- Obtain simulated vibration signals in the presence of localised and extended faults in the inner and outer races of the bearing
- Experimentally validate simulated vibration signals by comparing with measurements

2. Simulation of gear faults

- To develop a planet gear fault simulation model of the modified version of the UNSW test rig with a planetary gear insert
- Differentiate planet gear tooth cracks from tooth spalls taking into account the effect of the two simultaneous meshes of the planet gear with the sun and ring gears
- Compare simulated vibration signals with experimentally measured signals

1.3 Methodology

1.3.1 Simulation of bearing faults

The dynamic characteristics of the gearbox casing are invariably ignored in the LPM approach, resulting in poor spectral matching over a wide frequency range. It is proposed that this limitation can be overcome by incorporating the casing flexibility and dynamics in the simulation models by the application of model reduction techniques.

Based on these techniques, two different simulation models of the UNSW gearbox with a pair of spur gears were developed, namely,

- Combined LPM of the gearbox internals and the reduced FE model of the casing (146 DOF model)
- Full reduced model – reduced FE models of both the internals and the casing (182 DOF model)

Before implementing the model reduction, the FE model of the gearbox casing was validated and updated, based on the results of Experimental Modal Analysis (EMA).

The simulation models were verified by comparing the vibration signals with the measurements in the presence of localised and extended faults in the bearing inner and outer race.

1.3.2 Simulation of planet gear faults

The gear fault simulation models were developed for the UNSW gear test rig operating in the planetary configuration. A simplified 18 DOF transverse-torsional LPM was developed to simulate planet gear faults such as tooth cracks and spalls. The dissimilar contact ratios at the sun-planet and the ring-planet contacts were taken into account by defining the individual mesh stiffness curves with proper mesh phasing. A signal processing approach based on kurtosis enhancement using autoregressive linear prediction filtering was applied to both the simulated and the measured vibration signals to identify and differentiate between planet gear tooth cracks and spalls.

1.4 Thesis Structure

This thesis is divided into two parts – Part I deals with the simulation of bearing faults (Chapters 2 – 5) whereas simulation of planet gear faults is covered in Part II (Chapters 6 and 7). The outline of thesis structure is illustrated in Figure 1.1.

Chapter 2 of this thesis summarises the progress in the field of machine condition monitoring with specific reference to gears and bearings. The chapter provides an overview of the existing signal processing and diagnostic tools to analyse gear and bearing vibration signals, gear/bearing simulation models and model reduction techniques.

Chapter 3 describes the finite element modelling of the gearbox casing and its validation based on correlation with the results of Experimental Modal Analysis (also known as Modal Testing) and model updating. The updated finite element model of the casing is used in the subsequent development of the dynamic models of the entire gear test rig to simulate the bearing faults.

Chapter 4 illustrates the development of improved dynamic simulation models of the UNSW gearbox test rig using finite element model reduction techniques based on the Craig-Bampton method of component mode synthesis (CMS). The model reduction was carried out on the updated FE model of the gearbox casing. The methodology to simulate vibration signals in the presence of various types of bearing faults is described for the two types of models namely; combined LPM-reduced FEM of casing (146 DOF model) and full reduced model (which includes casing as well as gearbox internal components) of the gear test rig (182 DOF model). The chapter also illustrates the bearing model and gear dynamic model (which form part of the entire gear box test rig) and the modelling of bearing faults.

Chapter 5 summarises the results of the experimental validation of the vibration signals extracted from the bearing fault simulation models. A brief description of the test set-up, instrumentation and bearing fault details are provided. A comparison and discussion of results of the 146 DOF and 182 DOF models are provided. The results are also compared with those of the initial LPM (34 DOF) model. The characteristics of the vibration signals due to the fault entry and exit of the rolling element in the case of the localised bearing faults are investigated and compared with the initial LPM model and the measurements.

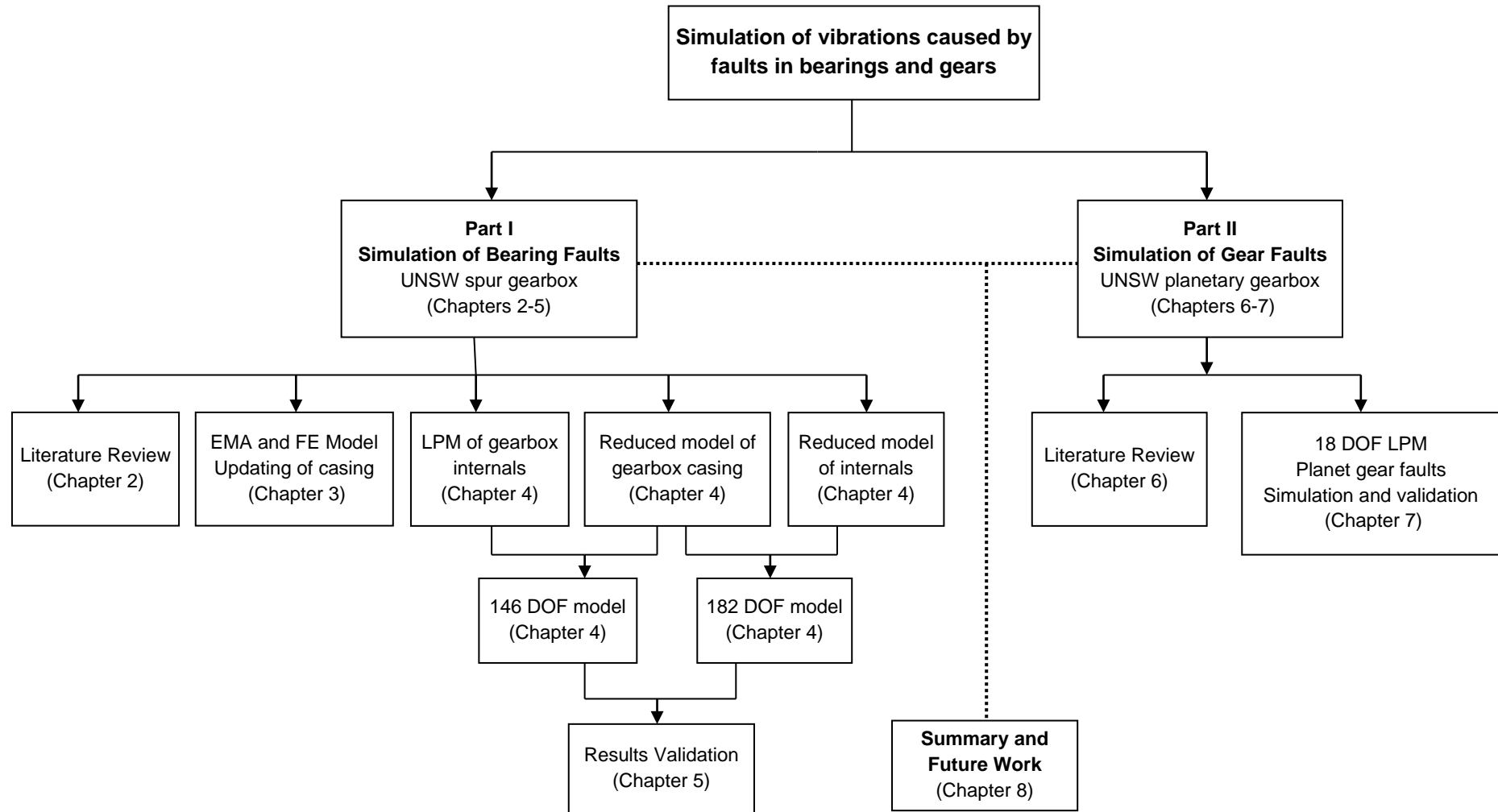
Chapter 6 provides an extensive review of the state of the research pertaining to the simulation of planetary gear systems with specific reference to analytical simulation models, mesh phasing, gear fault simulation and vibration signal processing techniques.

Chapter 7 describes the development of a lumped parameter model (LPM) of the UNSW planetary gearbox along with the details of the experimental set-up, planet gear faults, gear fault simulation methodology and signal processing techniques. A comparison of simulated vibration signals in the presence of planet gear faults such as tooth fillet cracks and spalls with the measured signals is provided. The study also

investigates the effect of the two simultaneous meshes of the planet gear with the sun and the ring gear to differentiate between the two types of gear faults.

Chapter 8 summarises the key findings, provides recommendations for future work and highlights the contributions of the research.

Figure 1.1 Thesis structure



PART I

SIMULATION OF BEARING FAULTS

CHAPTER 2

REVIEW OF ROLLING ELEMENT BEARING DIAGNOSTICS AND FAULT SIMULATION

2.1 Introduction

The main objectives of this research as set out in Chapter 1 are to simulate the vibration signals caused by the faults in bearings and gears. **Part I** of this thesis (Chapters 2-5) describes the simulation of *bearing faults* in the UNSW parallel shaft single stage spur gearbox.

The simulation of *gear faults* is discussed in **Part II** of this thesis (Chapters 6-7) using a lumped parameter model (LPM) of the UNSW planetary gearbox with seeded faults in the planet gears.

The main purpose of this chapter is to summarise the progress in the field of machine condition monitoring (MCM) with specific reference to gears and bearings and to assess the effectiveness of existing diagnostics tools and simulation models.

The information is presented in a logical way, starting with the characteristics of vibrations induced by gears and bearings in the presence of faults, and various signal processing techniques to detect and diagnose these faults. A brief review of various bearing simulation models is given and their ability to simulate bearing-gear interaction in the presence of bearing faults is assessed. Finally, applications of finite element based model reduction techniques are described which can predict the dynamic behaviour of complex systems with reasonable accuracy at an affordable computational cost.

2.2 Vibrations generated by rotating machines

The vibrations measured externally on the operating machines contain valuable information regarding the condition (or health) of the machine. Machines in normal condition exhibit a characteristic ‘vibration signature’ and the presence of faults significantly changes this signature. Vibration signals are also influenced by the speed and load of a machine. However, a typical rotating machinery assumed to be operating under constant load and speed (such as the gearbox investigated in this research), generates vibration signals which can be classified as stationary and/or cyclostationary to which appropriate signal processing techniques can be applied.

Vibration based techniques for monitoring and diagnosis of machine components have been successfully developed over the past thirty years and are now well accepted. Gears and rolling element bearings are critical components in complex machinery to which predictive maintenance is often applied. The characteristics of vibrations induced by the gears and bearings, both in the normal conditions and in the presence of faults are described in the following sections.

2.2.1 Vibration induced by Bearings

A unified approach to analyse all aspects related to the performance of rolling element bearings is given in (Harris, 2001). A comprehensive review of rolling element bearing vibrations and their detection, diagnosis and prognosis can be found in (Howard, 1994). The report addresses the key issues such as the underlying science of bearing vibration, bearing kinematics and dynamics, vibration measurement, signal processing techniques and prognosis of bearing failure.

The vibrations in rolling element bearings occur even if they are geometrically and elastically perfect. The number of rolling elements under load varies with the angular position of the cage, which results in the periodic variation of the assembly stiffness as the cage rotates and generates this so called varying compliance (VC) vibration (Sunnersjö, 1978). This is seen as the harmonics of the roller passage frequency (cage speed times the number of rolling elements) in the spectrum and is not primarily due to geometric deviations (defects in the bearing components).

Vibrations caused by bearing defects are more detrimental and are broadly classified into distributed and localised defects. The distributed faults include surface roughness, waviness, misaligned races and off-size rolling elements whereas cracks, pits and spalls caused by fatigue on the rolling surfaces are termed localised defects (Tandon and Choudhury, 1997).

The most common rolling element bearing faults are damage of the inner race, the outer race and/or rolling elements. During early stages, the faults are localised on the surface and vibrations are generated as a result of repetitive impacts of the moving components on the defect. Hence the overall bearing vibration signal is made up of succession of oscillating pulses (bursts) dominated by the major resonance frequencies of the structure. For a constant rotational speed, these pulses are close to periodic and their frequency is termed the ‘characteristic defect frequency’. Depending on the location of the fault and load distribution on the bearing, the vibration pattern is further modulated (Figure 2.1) either by shaft speed (inner race fault), the cage speed (rolling element fault) or their difference (inner race fault with roller error) (Khan et al., 2000, Randall, 2004).

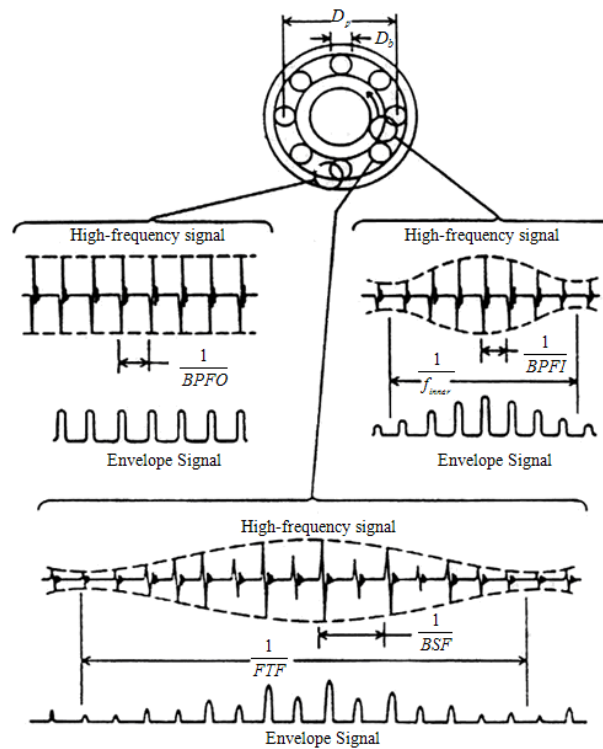


Figure 2.1 Rolling element bearing vibration signal characteristics due to local faults. (Randall, 2004)

The various characteristic defect frequencies for the case of a stationary outer race are given by the following equations (Howard, 1994):

Ball Pass Frequency Inner race (BPFI)

$$f_{BPFI} = \frac{n_b f_{inner}}{2} \left(1 + \frac{D_b}{D_p} \cos \alpha \right) \quad (2.1)$$

Ball Pass Frequency Outer race (BPFO)

$$f_{BPFO} = \frac{n_b f_{inner}}{2} \left(1 - \frac{D_b}{D_p} \cos \alpha \right) \quad (2.2)$$

Fundamental train frequency (FTF)

[Cage rotational frequency relative to outer race]

$$f_{BPFO} = \frac{f_{inner}}{2} \left(1 - \frac{D_b}{D_p} \cos \alpha \right) \quad (2.3)$$

Ball/roller spin frequency (BSF)

[Ball/Roller rotational speed around its axis relative to either race]

$$f_{BSF} = \frac{f_{inner}}{2} \frac{D_p}{D_b} \left(1 - \left(\frac{D_b}{D_p} \cos \alpha \right)^2 \right) \quad (2.4)$$

Where, n_b is the number of rolling elements

D_b and D_p are the rolling element diameter and the pitch diameter of the bearing respectively.

f_{inner} is the rotational speed of the inner race (shaft speed) and α is the contact angle (from the radial).

2.2.2 Vibration induced by Gears

The basics of gears, their vibrations and the mechanisms of noise generation have been extensively dealt with in the book (Smith, 1983). The latest developments in this field that offer an economical solution to the problems of gear design, metrology and prediction of Transmission Error (TE) to tackle the noise and vibration issues are covered in (Smith, 2003).

Gear vibrations are characterised by a periodic signal at the tooth-mesh frequency or one of its multiples and are mainly attributed to the “transmission error” (TE) which is the relative torsional vibration of the two gears, corrected for the gear ratio (Randall, 2004). TE results from a combination of geometric errors of the tooth profiles (resulting either from the initial machining process, or wear) and deflection due to tooth loading (Figure 2.2). Thus even a gear with perfect involute profiles will exhibit some TE under load. Hence it is important to make comparisons of gear vibration spectra under the same load to obtain information about changes in condition.

The tooth deflection under load and uniformly distributed initial machining error or wear is same for each meshing tooth pair. These manifest themselves at the tooth meshing frequency and its harmonics. The effects of wear are often more pronounced at higher harmonics of the tooth meshing frequency (Figure 2.3). Hence it is desirable to include at least the first three harmonics of the highest tooth meshing frequency in the gear vibration monitoring in order to detect wear at the earliest possible stage (Randall, 1982).

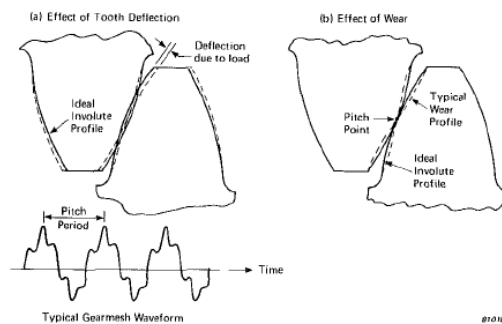


Figure 2.2 Deviations from ideal tooth profile (a) due to deflection under load, (b) due to wear (Randall, 1982)

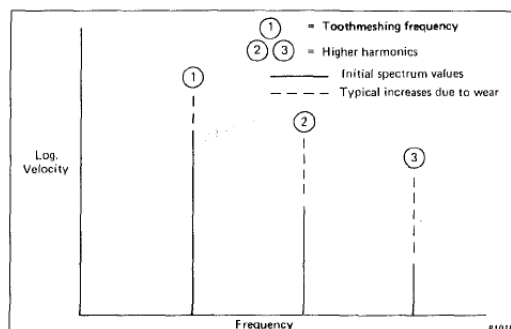


Figure 2.3 Typical vibration spectrum due to wear (Randall, 1982)

The variation in the tooth loading causes vibration amplitude to vary and this results in an amplitude modulation. On the other hand, non-uniform tooth spacing and variations in the rotational speed result in frequency modulation. Frequency modulation can occur even without speed variation because of varying initial time of tooth contact (effectively modulation in space). The same fluctuations in the tooth contact pressure causing amplitude modulation apply a fluctuating torque to the gears and result in angular velocity fluctuations at the same frequency. However, the phase variations of the signal are much greater than the phase variations of the gears themselves. Hence the two modulation effects normally exist simultaneously and the resulting spectrum is a combination of the sidebands produced by both the amplitude and frequency modulation.

Local faults such as cracked teeth, spalls and localised pitting, give rise to components over a very wide frequency range, partly by modulation (for the frequencies around and above the tooth-meshing frequency) and partly as additive impulses (primarily for the frequencies below tooth-mesh). Distributed faults such as misalignment and eccentricity, tend to give higher level sidebands more closely grouped around the tooth-meshing harmonics (Figure 2.4).

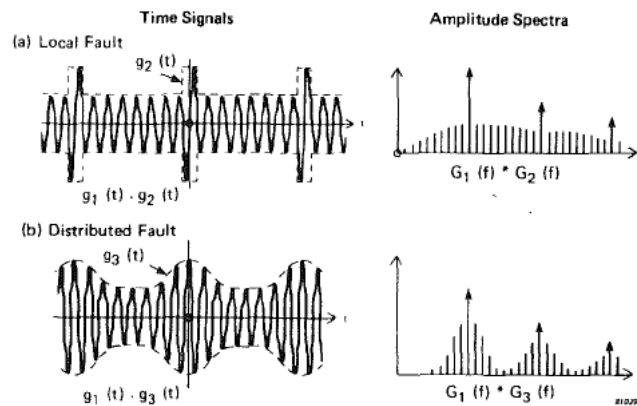


Figure 2.4 Effect of fault distribution on sideband pattern; (a) local fault (b) distributed fault (Randall, 1982)

2.3 Diagnostic techniques

The vibration signal analysis techniques can be subdivided into three main categories namely time domain, frequency domain and time/frequency domain. An overview of

these techniques can be found in (Howard, 1994, Randall, 2011, Aherwar, 2012, Patil et al., 2007).

In a complex system such as a high speed (input is high speed, output is low speed, eg 5 Hz) helicopter gearbox, the gear-related vibrations can extend into the high frequency range where bearing faults also manifest themselves, with a resulting mixture of two types of signal over the whole frequency range . Hence, the diagnostic technique must be able to clearly differentiate between bearing and gear faults through the analysis of their vibration signals.

Typical mixed signals are deterministic (from gears) and random (from measurement noise, fluid flow, bearing etc) signals. Some of the commonly used methods of signal separation are Order Tracking, Time Synchronous Averaging (TSA), Linear Prediction, Adaptive Noise Cancellation (ANC), Self-adaptive Noise Cancellation (SANC) and Discrete/Random Separation (DRS). The residual signal obtained after removing the deterministic part, is further analysed to identify the fault frequencies.

The theoretical background of the vibration signal analysis techniques is explained in (Randall, 2011).

2.3.1 Bearing Fault Diagnosis

An investigation of the characteristic fault frequencies (rate of repetition of bursts) and their modulations to identify and locate the bearing faults forms the basis of bearing diagnostics.

Techniques for the diagnosis of bearings include statistical analysis, spectral analysis, envelope analysis (high frequency resonance analysis), etc. (McFadden and Smith, 1984b).

Vibration monitoring of rolling element bearings by the high-frequency resonance technique (HFRT), also known as demodulated resonance analysis or envelope analysis is presented in (McFadden and Smith, 1984b). In this technique the vibration signal is filtered to isolate a single resonance, and then demodulated to calculate its spectrum. The presence of a defect is indicated by the appearance of a spectral component at the frequency with which the impacts occur (Figure 2.5). McFadden and Smith

demonstrated the use of HFRT technique to detect single and multi-point defects in a rolling element bearing (McFadden and Smith, 1985b, McFadden and Smith, 1984a).

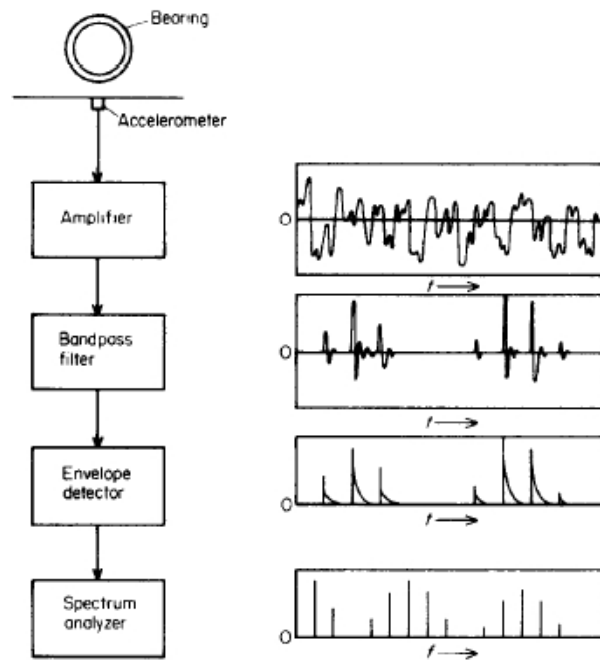


Figure 2.5 Process showing High Frequency Resonance Technique (McFadden and Smith, 1984a)

Although tied to shaft speeds the bearing fault signals are not strictly phase-locked due to variable slip between bearing components. The slippage in the rolling elements and the cage creates small randomness in the frequency and the amplitude of bursts (Ho and Randall, 2000). The resulting signals are not strictly periodic which leads to the smearing of the spectrum components that prevents the ball-pass frequency harmonic spacing from being detected at high frequency. However, the envelope analysis (Figure 2.6) can clearly indicate this frequency spacing of the low harmonics in the envelope spectrum and can be a useful tool for bearing diagnostics.

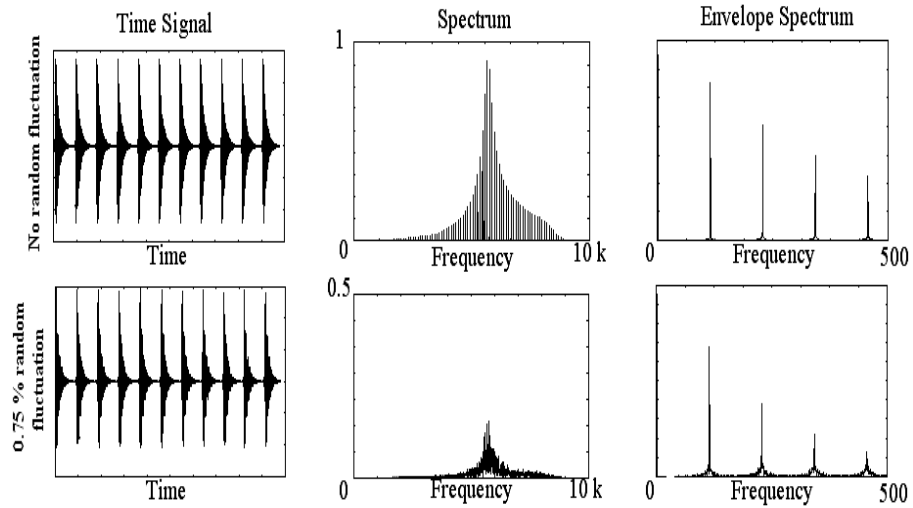


Figure 2.6 Envelope analysis of bearing fault pulses with and without frequency fluctuation (Ho and Randall, 2000)

Figure 2.7 shows the procedure to obtain the envelope spectrum for a typical bearing fault by using Hilbert transform technique (Ho and Randall, 2000). It is generally better to analyse a squared envelope (rather than envelope) since it improves the signal to noise ratio and produces a much clearer spectrum.

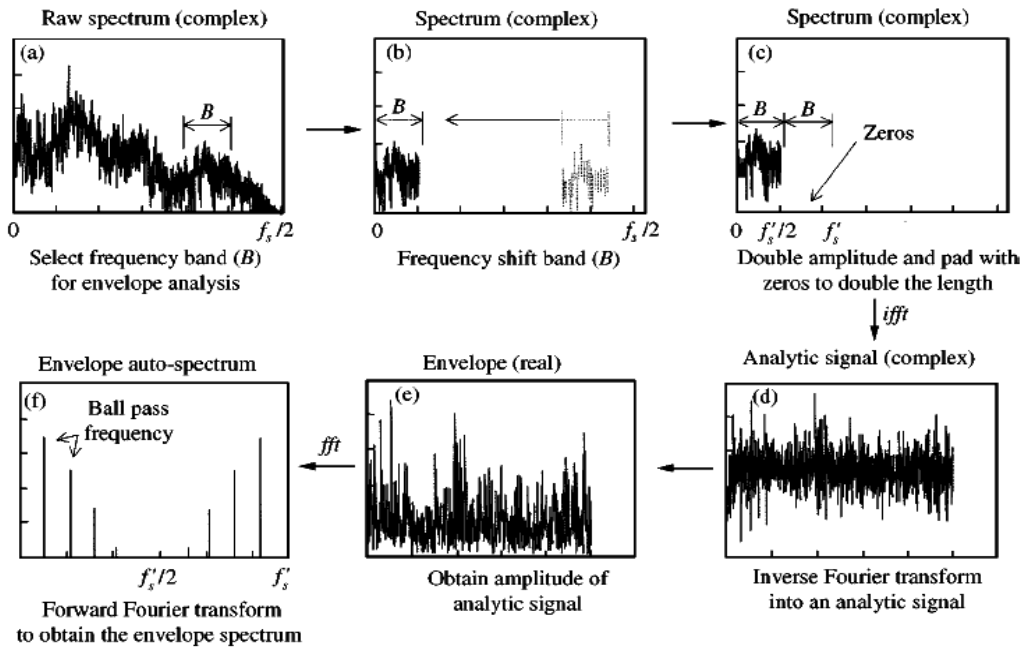


Figure 2.7 Envelope analysis using Hilbert Transform technique (Ho and Randall, 2000)

The envelope spectrum of the bearing fault signal is prone to masking by discrete and random noise which can be removed by the application of the self-adaptive noise cancellation (SANC) technique prior to envelope analysis (Ho and Randall, 2000).

The bearing fault signals which are not periodic, but have a hidden periodicity that can be extracted by demodulation, are known as cyclostationary and are often generated in rotating machines along with deterministic discrete frequency signals. Distributed rather than localised bearing faults give a multiplicative relationship and an approach based on the spectral correlation function (SCF), a characteristic of cyclostationary signals, is needed to differentiate bearing faults from those associated with gears (Antoni and Randall, 2002).

It was demonstrated that the integration of SCF over all frequencies produces the same diagnostic result as the squared envelope spectrum (Randall et al., 2001), thus establishing squared envelope analysis as a valuable tool for the analysis of (pseudo-) cyclostationary signals. The envelope analysis was found to be satisfactory to detect local faults and an added benefit for distributed faults was obtained using the full spectral correlation.

2.3.2 Gear Fault Diagnosis

Some of the conventional established techniques for the diagnosis of gears include synchronous signal averaging, spectral analysis, cepstral analysis, and demodulation analysis (McFadden, 1986, Randall, 1982).

In synchronous signal averaging, the digitised signal is averaged over a large number of cycles, synchronous with the running speed of a particular gear, thereby removing background noise as well as any periodic event not exactly synchronous with the gear in question (Randall, 1982). This method gives direct visualisation of the time signal with localised faults. However, certain faults are not easily seen in the time signal such as distortion of tooth meshing frequency and frequency modulation.

Using the TSA of each gear, Stewart proposed several diagnostic tools by extracting a number of ‘figures of merit’ from the gear spectrum e.g. FM4 which is effectively the

kurtosis of the residual signal obtained by removing the regular gearmeshing pattern (Stewart, 1977).

Cepstrum analysis represents a further spectrum analysis carried out on the logarithmic (amplitude) spectrum and thus detects any periodic structure in the spectrum related to gear faults as given by the families of equally spaced sidebands due to amplitude and frequency modulation (Randall, 1982). Cepstrum analysis, although useful to separate mixtures of sidebands, tends to suppress useful diagnostic information about the global shape of the spectrum. Hence cepstrum analysis can be a valuable tool to supplement spectrum analysis.

It was shown that, similar to an acceleration signal, the TE signal can be successfully used as a diagnostic tool. The TE signal for a pair of gears can be obtained by subtracting the demodulated signals from shaft encoders attached to each gear. The TE signal can then be demodulated (with the tooth mesh frequency as carrier) to highlight the local faults (Sweeney and Randall, 1996).

The above illustration of TE as a diagnostic tool in condition monitoring is in fact referred to as dynamic TE (or TE in operation), which is load dependent and results in the fluctuation of torque transmitted by the gear pair. W. D. Mark (2012) in his latest book stated that the static TE (gears operating at slow speed and transmitting constant load or torque) is the principal source of vibratory excitation. The static TE has two components namely, the load-dependent elastic deformation and the geometric deviation of the tooth working surfaces from equispaced perfect involute surfaces. The latter component is referred to as kinematic transmission-error and is inertia and load independent. Mark used two-dimensional normalised Legendre polynomials to represent tooth working surface deviations. The characteristics of the gear vibration spectra were explained as corresponding to a Discrete Fourier Transform (DFT) by treating the error components for the whole gear, as a set of digital values sampled at the toothmesh frequency.

McFadden (1986) and McFadden and Smith (1985a) examined the modulation of the vibration generated by a gear with a local defect such as a fatigue crack. It was recommended that the complex envelope of the filtered residual be calculated from the

signal average and be used in preference to the unprocessed signal average for the detection of early fatigue crack. The study highlighted the importance of phase modulation in locating gear defects in the early stage which showed little amplitude modulation. However, in the case of an advanced gear tooth crack, it was found that the presence of faults can be predicted using both the amplitude and phase modulation.

Wang (2001) demonstrated the use of a resonance demodulation technique for the early detection of gear tooth cracking, which was based on the fact that a gear tooth fault produces impacts in the meshing vibration that excite structural resonances and the envelope of the structural resonant vibration carries the fault-related information. The kurtosis of the squared envelope signal extracted by resonance demodulation clearly indicated the presence of faults thus providing an effective supplement to the conventional technique based on synchronous signal averaging.

Wang and Wong (2002) demonstrated a successful application of an autoregressive (AR) model-based filter to isolate the impulse-like effect of localised cracks in a gear tooth. Fault indication using AR modelling gives better results than the residual method which is based on removing normal gearmesh signals in the frequency domain. The AR modelling is also carried out on the synchronously averaged signal – AR or linear prediction is simply an alternative way of removing the regular toothmesh signal instead of deleting toothmesh harmonics and low order sidebands from the spectrum. It is shown that the AR modelling method is capable of detecting a gear tooth crack earlier and with a higher level of diagnostic confidence compared with the traditional residual kurtosis method including that used in (Wang, 2001).

2.3.3 Spectral Kurtosis (SK)

Spectral kurtosis (SK) is a statistical tool capable of detecting non-Gaussian components in a signal. These include structural response to an excitation by cracked gear tooth or the transient response due to rolling element bearing fault. The theoretical background of SK is explained in (Antoni, 2006). SK provides additional information about the frequency content of the transients which the traditional power spectral density (PSD) cannot display and provides a robust way of detecting incipient faults in the presence of strong masking noise.

There are two major applications of SK as highlighted by (Antoni and Randall, 2006). The first is in machine surveillance, to detect incipient faults (transient signals) in the presence of strong masking noise. The second application of SK is in machine diagnostics, due to its unique ability to design optimal filters to capture fault signals (mechanical signature). The introduction of the concept of the kurtogram (displaying SK as a function of frequency and spectral resolution) as a prerequisite to envelope analysis clearly shows advantages over other classical techniques. The findings presented in the paper are supported by actual industrial examples pertaining to the monitoring and diagnostics of gear and bearing faults.

Barszcz and Randall (2009) applied the SK technique to detect a tooth crack in the planetary gear section of a wind turbine. The catastrophic gear failure was not detected by conventional methods including synchronous averaging, whereas the proposed method based on SK was able to detect the existence of a tooth crack in the ring gear several weeks before the gear failure.

2.3.4 SK Enhancement Techniques

The use of minimum entropy deconvolution (MED) technique to enhance the ability of the AR-based filtering technique was successfully applied by Endo and Randall (Endo and Randall, 2007) to detect local faults in gears. The combined AR and MED (ARMED) filtering technique showed significant improvement in detecting localised gear faults such as spalls and tooth fillet cracks (TFCs), some of which could not be identified using only the original AR filter.

The successful application of SK requires individual transients to be well separated. This requirement creates difficulties in the implementation of SK for the surveillance and diagnostics of high speed machines such as gas turbines and compressors. Sawalhi et al. proposed an algorithm to enhance the capabilities of SK by combining it with AR based linear prediction filtering and MED technique to analyse signals obtained from a bearing with spalled inner race (Sawalhi et al., 2007). The MED technique deconvolves the effect of the transmission path and clarifies the impulses, even where they are not separated in the original signal. The use of MED technique sharpens the pulses and increases the kurtosis values to a level that reflects the severity of the fault.

2.4 Bearing / Gear Vibration Interaction

In a machine structure, gears and bearings are kinematically coupled and interact with each other as the gearmeshing forces of the gears are affected by the bearing support forces.

2.4.1 Additive Interaction

The interaction is additive in case of localised bearing faults (Antoni and Randall, 2002) and the separation of the bearing signal and gear signal can be achieved by using synchronous averaging, self-adaptive noise cancellation (SANC) or discrete random separation (DRS) (Antoni and Randall, 2004a, Antoni and Randall, 2004b, Ho, 1999). The separation of the two signals is based on the fact that the gear signal is periodic whereas bearing signals contain more randomness due to the slippage of the rolling elements as a result of load angle variation and clearance in the cage. Due to the additive nature of the interaction, bearing signals prevail over certain frequency ranges and can be detected using envelope analysis (high frequency resonance technique) (Ho and Randall, 2000, McFadden and Smith, 1984b). The separation is made possible by the additive nature – once the gear signals are removed, the optimum band for enhancement of the bearing fault is found by SK, MED etc.

2.4.2 Multiplicative Interaction

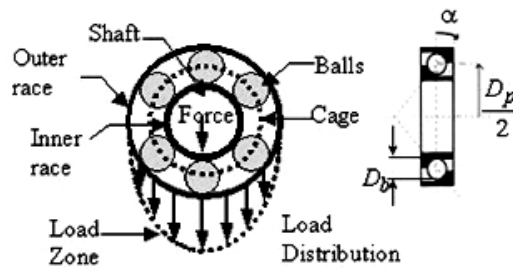
Multiplicative interaction between the gear and bearing vibration signals can cause a modulation of the gear mesh signal and may occur due to the force at the gear mesh being reacted at the bearings and changes in the support given by the bearings. However, the signal can still be decomposed into a periodic component related to gear fault and a 2nd order cyclostationary component containing the information on possible bearing faults (Antoni and Randall, 2002).

2.5 Bearing Simulation Models

The simulation of rolling element bearing vibration is quite complex due to non-linear effects caused by the Hertzian force/deformation relationship, the varying stiffness resulting from load transmission via a changing finite number of rolling elements,

clearance between the rolling elements and the bearing races, and the presence of the lubricant film.

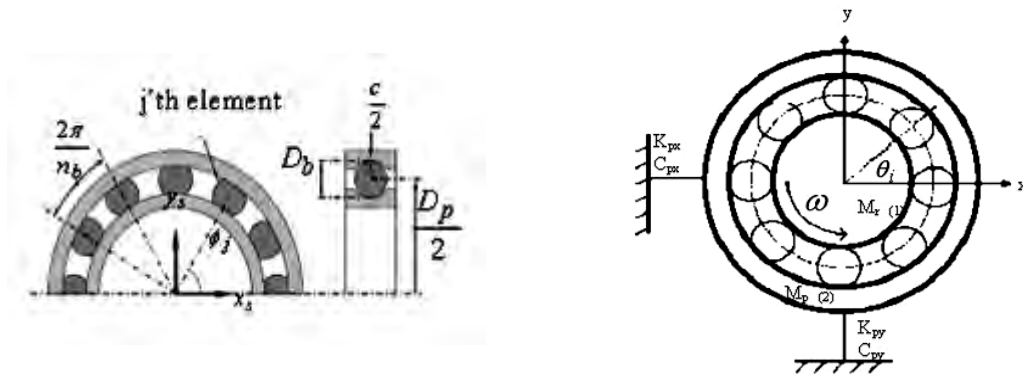
Figure 2.8 shows the basic components of the rolling element bearing along with the load distribution. The initial bearing models which provide the load-deflection relationships, varied from two DOFs representing only the rolling element bearing (Sunnersjö, 1978, Liew et al., 2002, Fukata et al., 1985) to four DOFs which takes into account the additional two DOFs for the pedestal (Feng et al., 2002).



D_b : ball diameter, D_p : pitch diameter, n_b : number of rolling elements
 c : radial clearance, α : load angle

Figure 2.8 Load distribution in a rolling element bearing (Liew et al., 2002)

The main limitation of the original 2 DOF model was the lack of slippage in the rolling elements and the lack of introduced bearing faults, which were incorporated in the 4 DOF model along with mass unbalance in the rotor (Figure 2.9). The four DOF bearing model of Feng et al. was updated by Sawalhi and Randall (2008c) by adding an extra degree of freedom (by attaching a spring mass system to the bearing pedestal) to simulate a typical high frequency resonance response of the bearing. The resulting 5 DOF bearing model was adopted in the improved dynamic models of the UNSW gear test rig developed in this research (described in Chapter 4).



(a) Bearing model (2 DOF)

(Liew et al., 2002)

(b) Bearing model (4 DOF)

(Feng et al., 2002)

Figure 2.9 Bearing models

McFadden and Smith (1984a) developed a mathematical model to describe the vibration produced by a single point defect on the inner race of the bearing under radial load. The model takes into account the effects of bearing geometry, shaft speed, bearing load distribution, transfer function and the exponential decay of vibration, but not slip. The model was extended to describe vibration produced by multiple defects (McFadden and Smith, 1985b). The models were verified by comparing the predicted and measured vibration spectra, in particular envelope spectra.

Lim and Singh [(1990a), (1990b) and (1991)] formulated a new mathematical model of the bearing stiffness matrix (of dimension six) capable of coupling the shaft bending motion and the flexural motion of the casing. The model ignores the elasto-hydrodynamic effects of lubrication and slippage in the rolling elements. The bearing stiffness matrix was inserted in an overall dynamic model of a geared rotor system consisting of spur gear pair, shafts, rolling element bearings and a rigid or flexible casing which was modelled using finite elements. The ability of the model to provide improved predictions of the vibrations transmitted through the bearing components was verified using experimental measurements.

Tandon and Choudhury (1997) presented an analytical model to predict the vibration frequencies of rolling bearings and amplitudes of frequency components due to localised defects on the inner race, outer race and on one of the rolling elements under radial and axial loads. The effect of load, defect locations (angular positions) and pulse

shape (rectangular, triangular and half-sine) on the vibration amplitude was investigated.

Sopanen and Mikkola (2003a) presented a dynamic simulation of a deep-groove ball bearing with six degrees of freedom taking into account non-linear Hertzian contact deformation and elasto-hydrodynamic (EHD) fluid film. The model was capable of simulating distributed defects (waviness) and localised defects in the inner and outer race. The ball bearing model was further implemented as an interface element between the rotor and the housing (of an electric motor application) and the equations of motion were solved using commercial multi-body dynamics software (Sopanen and Mikkola, 2003b).

Choudhury and Tandon (2005) proposed a three DOF lumped-mass rotor-bearing model which includes the effects of shaft and bearing. The excitation was provided by a rectangular pulse to obtain the vibration response due to localised faults in the inner race, outer race and the rolling element. The predicted amplitudes of the spectral components were correlated with measurements whereas the earlier studies were limited to matching only the defect frequencies.

A simple 3 DOF dynamic model (Figure 2.10) was developed by (Sassi et al., 2007) to simulate vibration response of a ball bearing affected by localised faults in the inner and outer race. The elasto-hydrodynamic characteristics of the oil film, sliding friction between the moving parts, and the transfer function between the bearing and the transducer were included in the model. However, the model did not take into account the contributions of the housing and supporting machine elements (which were assumed as rigid).

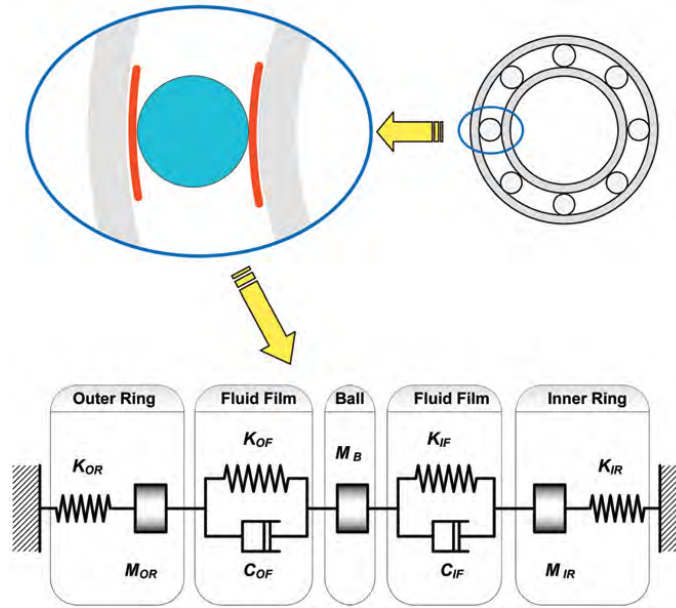


Figure 2.10 Bearing system model in the principal radial direction (Sassi et al., 2007)

Arslan and Aktürk (2008) modelled a rigid shaft supported by a pair of angular contact ball bearings (using a mass-spring system) to investigate bearing vibrations with and without local defects. The equations of motion in radial and axial direction were solved for the shaft and rolling elements.

Doguer et al. (2009) modelled the rolling element bearing as a multi-body system to simulate the bearing behaviour under varying fault parameters (fault width, length and steepness) and operating conditions (angular velocity and load). A local fault was inserted into the bearing inner and outer race using fault elements consisting of spherical shaped bodies (Figure 2.11). In a further study, an extended outer race fault representing the raceway imperfections (modelled as sum of sinusoidal components) was introduced in the model to investigate the combined effect of unbalance, local defect and rough surface (Doguer and Strackeljan, 2011).

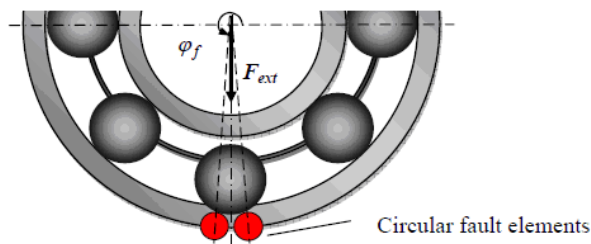


Figure 2.11 Bearing fault model using fault elements (Doguer et al., 2009)

Patel et al. (2010) developed a simplified three DOF dynamic model of a shaft-bearing-housing system. The model was created using springs and lumped masses for the shaft, rolling elements and housing where the mass of the inner and outer race was included in the mass of the shaft and the housing respectively. The vibrations were simulated from a deep groove ball bearing with single and multiple defects (localised faults) on the inner and outer race.

The majority of the above models investigate the vibration response of a bearing due to faults at a constant rotational speed. Tadina and Boltežar (2011) developed an improved bearing model to investigate the vibrations of a ball bearing during run-up (while the shaft's rotational frequency is increasing). The inner race had only 2 DOFs whereas, the deformable outer race was modelled with curved beam finite elements (Figure 2.12). The centrifugal load on the balls and slippage in the bearing components were taken into account while the effect of elasto-hydrodynamic lubrication (EHL) was neglected. The simulated vibration responses with different local faults (in the inner and outer race and the rolling element) were analysed to test the suitability of both the envelope analysis and the continuous wavelet transformation (CWT) techniques.

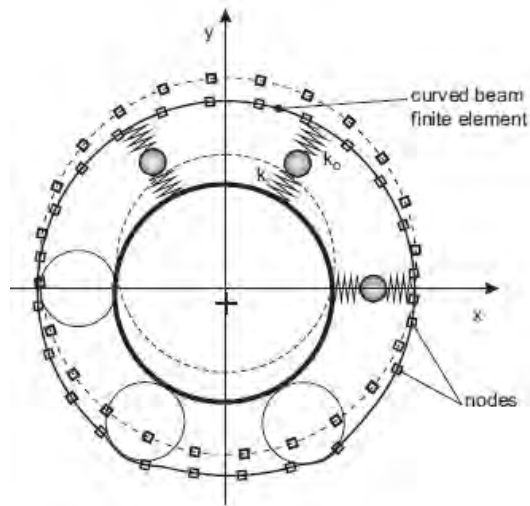


Figure 2.12 Bearing model proposed by Tadina and Boltežar (2011)

Researchers at the University of New South Wales (UNSW) have developed a number of simulation models of a gearbox test rig to diagnose bearing and gear faults. The following section provides a brief summary of the capabilities and limitations of these models.

2.5.1 Dynamic Modelling of the UNSW Gear Test Rig

The gearbox test rig was built by Sweeney (1994) to investigate the effect of gear profile errors on transmission error (TE). The details of the test rig (Figure 2.13) are provided in Chapter 5 as part of the experimental set-up.

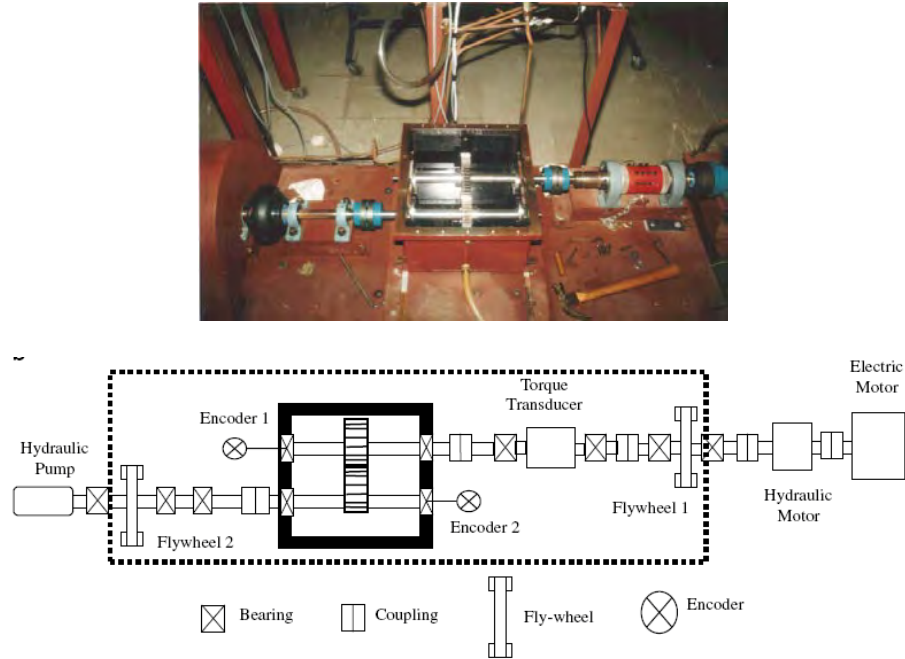


Figure 2.13 UNSW gearbox test rig & schematic diagram (Sawalhi and Randall, 2008c)

The early mathematical models were mainly lumped parameter models (LPM) with the shaft mass and inertia lumped at the bearings or at gears. Sweeney (1994) modelled the rig with 6 DOF which were all for torsional vibration and assuming constant tooth pair meshing stiffness (ie double stiffness with two pairs of teeth in contact).

Du (1997) developed a 12 D OF model of the rig by adding six more DOFs to Sweeney's model to include bending and lateral motion.

Gao and Randall (2000) then developed a 16-DOF model by including the torsional resonance of two encoders. However, the 2-DOF at the motor and the pump were excluded as their effect was isolated by the two flywheels.

Endo (2005) and Endo et al. [(2004), (2009)] simulated spalls and cracks in gear teeth using the 16-DOF model and developed diagnostic techniques to differentiate between the two. The existing diagnostic techniques would indicate the presence of local tooth

faults without being able to differentiate between a spall and a crack. The variation of the mesh stiffness for the two types of faults under varying static load conditions was simulated using a finite element program. The results were used in the lumped parameter dynamic model of the simulated gearbox to obtain the dynamic transmission error (TE) and the acceleration responses under different loads and speeds.

Sawalhi and Randall (2008c) developed a 34 DOF LPM of the UNSW gear test rig to study the interaction between gears and bearings in the presence of faults. The model takes into account time varying nonlinearity of the bearing stiffness (Hertzian contact) and slippage in the bearings and was capable of simulating bearing faults in addition to the spalls and cracks in the gears. The envelope spectra of the simulated vibration signals due to localised faults in the bearing inner and outer race correlated well with the measurements and clearly indicated the bearing fault frequencies - BPFO and BPFI modulated by shaft speed. In the case of an extended fault, due to the cyclostationarity of the vibration signal, a technique based on the spectral correlation function (SCF) was used. SCF was found to be effective in detecting the extended inner race fault, however it failed to indicate the modulation of gearmesh frequency by BPFO as observed in the measurements in case of extended outer race fault (Sawalhi and Randall, 2008d).

The other main limitation of the this LPM (34 DOF) model is that it does not take into account the dynamics of the gearbox casing, which is an important consideration in light weight structures. In the above LPM model, the gearbox casing was modelled as having only 2 D OF to represent a low frequency (rigid body) mode and a high frequency response excited by the bearing faults. Due to this, poor spectral matching between the simulated and measured bearing faults was observed over a wide frequency range, the discrepancy being more pronounced between 2-4 kHz.

The LPM model was further improved by Sawalhi and Randall (2008b) by incorporating more degrees of freedom of the casing (extracted from a finite element model), to give improved matching of the response signals over a wider frequency range (though using the force signals from the LPM model). Frequency Response Functions (FRFs) were extracted from the FE model between the bearing force locations (input points) and accelerometer position (output point). The bearing forces from the LPM model were convolved with the impulse responses corresponding to the FRFs of the

casing. This process of obtaining the response signal is also applied to the improved dynamic models of this thesis and further elaborated in Chapter 5.

The results of the combined LPM and FE model improved the agreement of simulated localised bearing faults with the experimentally measured results when compared to the simple LPM model. In the case of extended outer race fault, the combined LPM and FE model indicated the interaction between gearmesh frequency (GMF) and the BPFO which was apparent in the experimentally measured results but was missing in the pure LPM model (Sawalhi and Randall, 2008a). Even so, the interaction was not properly modelled over the whole frequency range, so it appears the original simulation should be made with a model including the dynamic properties of the casing.

The above limitations of the 34 DOF LPM model clearly justify the need for an improved dynamic simulation model which takes into account the dynamic characteristics of the casing. The application of combined LPM and FEM methods to develop such a model is described in Chapter 4 along with the theoretical background of FE model reduction. The relevant literature review pertaining to the model reduction techniques is presented in the next section.

2.6 Model Reduction Techniques

The capability to analyse complex structures at the design stage (with inherent geometric and/or material nonlinearity), demands sophisticated simulation techniques for the design, control and optimisation of the mechanical systems. The use of traditional methods such as finite element analysis is quite common to solve these complex systems. However, even the simplest form of structural analysis (linear, static) requires a detailed set of grid points or nodes to map internal stresses and strains. This usually results in very large simulation models, perhaps several thousand degrees of freedom (DOFs), which require large computing resources in terms of memory, disk space and computational time. Unlike static analyses, dynamic analyses can be carried out with far fewer DOFs to compute lower order frequencies and their associated mode shapes (Young, 2000). Hence, model reduction techniques have become increasingly popular, with several methods developed in the past decades. The theoretical

background of model order reduction has been extensively covered in the textbook (Qu, 2004).

Another application of model reduction is in establishing correlation between test results and FE models. The experimental results from modal testing are normally used to verify and modify finite element models. However, modal testing has its own limitations since the number of measured DOFs in modal testing is much smaller than the total number of DOFs in the FE model. This incompatibility between the two models can be addressed by applying model reduction techniques to reduce the FE model to the size of the test model or to expand the results of the test model to the size of the FE model (Qu, 2004).

The comparison of various model reduction techniques given below is mainly taken from Koutsovasilis and Beitelschmidt [(2008), (2010)] .

The static reduction method also known as Irons-Guyan method (Guyan, 1965, Irons, 1965) produces smaller size system matrices by eliminating the coordinates at which no external force is applied. The reduction method is exact for static problems; however, for dynamic problems large errors may be introduced due to the fact that the DOFs eliminated may experience inertia forces, which cause their dynamic displacements to differ from the static, the deviation increasing with frequency (Chen and G radin, 1997). High frequency motion is better approximated using dynamic reduction. However, the transformation matrix T_{dyn} depends on the choice of an appropriate initial frequency ω , which is not a trivial task. Guyan reduction is a special case of dynamic reduction, when $\omega = 0$.

Static reduction methods were further improved by O'Callahan (O'Callahan, 1989), with a technique known as the Improved Reduction System (IRS) method. IRS perturbs the static transformation by taking into account the inertia terms as pseudo-static forces. Although the results match the low frequency response resonances of the full system better than static reduction, the IRS reduced stiffness matrix is stiffer than the Guyan reduced matrix and the mass matrix is less suited for orthogonality checks.

The IRS transformation matrix T_{IRS} depends on the reduced mass and stiffness matrices obtained by static reduction. To minimise the error produced by this scheme, IRS could

be extended to the Iterated IRS method (Friswell et al., 1995). Even though the algorithm converges to yield the eigenvalues of the full system, the method results in a too stiff structure (Myklebust and Skallerud, 2002).

The System Equivalent Reduction Expansion Process (SEREP) was originally formulated as a global mapping technique to estimate rotational and unmeasured translational degrees of freedom in experimental data (O'Callahan et al., 1989). Some of the salient features of SEREP are - accuracy of the reduced model is independent of the selection of master DOFs, reduced model frequencies are identical to those of the full system model, expanded reduced mode shapes are identical to those of the full system model. However, the requirement of prior estimation of eigensolutions of the full system limits its usage.

2.6.1 Component Mode Synthesis

Component Mode Synthesis (CMS) also known as substructure coupling is a special class of model-reduction methods based on dynamic condensation. Large complex assemblies of structures commonly found in the automotive and aerospace industry contain several components (substructures), which are invariably designed, analysed and manufactured by different organisations. CMS provides a means of coupling these substructures (component FE models) and enables evaluation of the dynamic response of the significantly reduced overall model of the assembly.

The CMS technique consists in dividing the complex structure in smaller substructures (or superelements) and recovering afterwards the dynamic behaviour of the complex structure by assembling the superelements considering geometric compatibility (equilibrium of nodes) at the interfaces between the various components.

The dynamic analyses of large structures are often carried out using superelements based on the substructuring principle. The structure is divided into a series of components, or superelements, each of which can be processed independently using a reduced set of degrees of freedom. Once all the components have been analysed, the superelements can be assembled to form a reduced model of the complete structure.

The component modes (Ritz vectors) describe the displacement of points within a component. In CMS, a component's physical displacement coordinates are transformed into component generalised coordinates using the Ritz coordinate transformation matrix of selected component modes such as rigid body modes, normal modes, constraint modes and attachment modes. This, in conjunction with the equation of motion in generalised coordinates, forms the *component modal model*.

Several substructure coupling methods have been proposed based on the conditions imposed on the interface nodes between the two adjacent substructures when determining the component mode shapes. These methods are fixed-interface modes (Hurty, 1965, Craig and Bampton, 1968), free-interface modes (Goldman, 1969) and hybrid modes (MacNeal, 1971). A comprehensive review of different types of CMS methods is given in (Craig and Kurdila, 2006).

CMS as an efficient method of model reduction was first proposed by (Hurty, 1965) which was based on the fixed interface modes and constraint modes, the latter being separated into rigid-body modes and redundant constraint modes. However, Craig and Bampton pointed out that it was unnecessary to separate the set of constraint modes, and simplified Hurty's method by treating all interface degrees of freedom together (Craig and Bampton, 1968). This method known as Craig-Bampton (CB) method of CMS is widely adopted due to its superior accuracy, ease of implementation, ease of adding additional modal coordinates and efficient use of computer resources and is available in a number of commercial finite element codes.

Additional benefits of CMS include easier structural dynamic modification which are usually local and can be implemented at the component level to optimize the structure. CMS techniques allow hybrid modelling where one or more complex components can be represented using the experimental data in formulating the global model (Qu, 2004).

Hinke et al. (2009) presented an interesting application of CMS as a framework for uncertainty analysis to predict the variation in the response, caused by product variability introduced by the manufacturing processes. Uncertainties in the properties can be easily introduced at the component level in terms of component physical or modal properties; the latter can even be extracted from the variability in the

experimentally measured data. The CMS reduced models further reduce the cost of multiple reanalysis as might be required in implementing Monte Carlo Simulation (MCS).

The inability to experimentally verify the system submatrices in the case of the fixed-interface CB method limits its usage only to the numerical models. Hence, an alternative approach was proposed by Butland and Avitabile (2010) which utilizes frequency and shape information acquired from modal testing to update reduced order FE models.

The components of a complex structure are normally designed and analysed by different organisations and it is inevitable that some substructures will have non-matching finite element meshes at the interface. The problem is further compounded by the fact that the retention of the entire set of boundary coordinates in the CB-reduced system model results in a large number of interface DOFs, especially in 3D FE models built using solid elements. Hence, an extension of the CB method was presented in (Farhat and Geradin, 1994, Park and Castanier, 2007) that permits coupling of substructures with incompatible interface grids, thereby reducing the number of interface DOFs.

Some of the practical examples of the application of the Craig-Bampton method of CMS are illustrated in the following paragraphs.

Abbes et al. (2005) implemented the Component Mode Synthesis (CMS) or Dynamic Substructuring Method (DSM) based on Craig-Bampton decomposition to analyse a helical gear transmission fitted with an elastic casing. The two shafts connected to each other with a gear pair represented the first substructure, while the elastic casing formed the second substructure. From the recovered eigenvalues of each substructure, the generalised natural frequencies and mode shapes of the assembled gearbox were obtained. A good correlation was obtained between the DSM and FEA results. The observed combined modal deflection confirmed the interaction between the two substructures namely the shafts and the casing. The results of eigensensitivity study due to addition of a stiffener on the casing elastic front plate were presented to highlight the potential of DSM to optimise the vibratory behaviour of complex mechanical structures.

Melani et al. (2008) used a methodology that combines FE modelling and Component Modal Synthesis (CMS) to investigate the dynamic behaviour of a gearbox with a thin walled (flexible) casing. Unlike the LPM, the CMS based model takes into account the flexibility of the gearbox casing but cannot incorporate the nonlinearities related to gear meshing (e.g. oscillating non-linear behaviour of meshing stiffness and backlash); hence these were introduced afterwards in the Simulink dynamic simulation environment. The CMS reduced FE model was used to monitor simulated (virtual) accelerometer signals due to a damaged gear tooth (Carmignani et al., 2009).

Modelling of the dynamic behaviour of a multi-body system (MBS) is approximate due to the assumption of rigid bodies and hence the CMS techniques are widely used to incorporate the component flexibility for realistic simulation. Ulf Sellgren (2003) integrated FE and MBS technology to transfer condensed elastic (flexible) submodels from FE to MBS software (MSC.ADAMS) and to transfer dynamic loads from MBS to FE software to calculate stresses and deflections.

The theory and implementation of CMS to interface nonlinear FEA software with the MBS simulation software was explained in (Bayoumi, 2005). The flexible body was modelled in MSC.Marc and component mode synthesis performed to compute the Craig-Bampton modes. The orthogonalized mode shapes were exported to Modal Neutral File (MNF). The flexible body model from MNF was imported into MSC.ADAMS and attached to the rest of the multibody system model at the interface nodes using a variety of available joint types. The MNF file contains essential data such as finite element model topology, nodal coordinates, the Craig-Bampton mode shapes, generalised mass and stiffness matrices and the list of interface nodes and degrees of freedom. The schematic of the interface is shown in Figure 2.14.

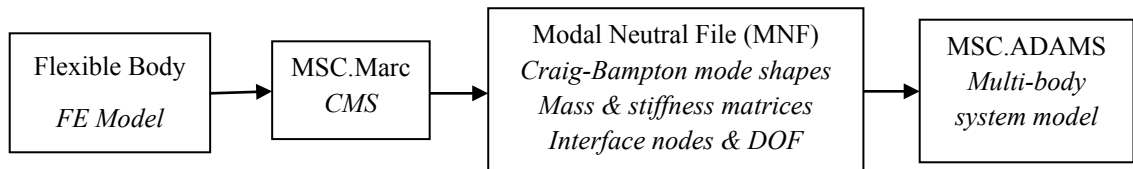


Figure 2.14 Schematic of CMS-MBS interface (Bayoumi, 2005)

The theoretical background and the implementation of Craig-Bampton based CMS is given in Chapter 4 as part of the development of improved dynamic simulation models of the UNSW gearbox.

2.7 Gearbox dynamic model developed in this study

The overview of the bearing simulation models indicates that the majority of the current gear-rotor dynamic models include only the internal rotating components and simple bearing models and typically exclude casing flexibilities. In few instances simplified casing models have been included which were still found to be inadequate in the mid-frequency range where gearmesh forces and the dynamic properties of the casing interact especially in the case of extended faults in the bearing outer race. The main differences between the bearing fault simulation models developed in the current research and the majority of published works are:

- The LPM of gearbox internals was combined with the reduced FE model of the casing to create a combined 146 DOF model which takes into account the dynamic characteristics of the casing. The FE model reduction was carried out based on the Craig-Bampton method of component mode synthesis. Prior to model reduction, the FE model of the casing was updated based on the results of Experimental Modal Analysis. The simulated vibration signals were extracted in the presence of localised and extended faults in the bearing inner and outer race.
- The Craig-Bampton method of CMS was further extended to the gearbox internal components to create a full reduced model (182 DOF) of the entire gear test rig to simulate the bearing faults.

The dynamic modelling of the gearbox test rig using model reduction techniques and the comparison of simulated and measured vibration signals are presented in the following chapters.

2.8 References

- Abbes, MS, Fakhfakh, T & Haddar, M 2005. Gearbox vibratory analysis using carrying, coupling and slave substructures. *International Journal of Simulation Modelling*, 4, 67-75.
- Aherwar, A 2012. An investigation on gearbox fault detection using vibration analysis techniques: A review. *Australian Journal of Mechanical Engineering*, Vol. 10 169-183.
- Antoni, J 2006. The spectral kurtosis: a useful tool for characterising non-stationary signals. *Mechanical Systems and Signal Processing*, 20, 282-307.
- Antoni, J & Randall, RB 2002. Differential Diagnosis of Gear and Bearing Faults. *Journal of Vibration and Acoustics*, 124, 165-171.
- Antoni, J & Randall, RB 2004a. Unsupervised noise cancellation for vibration signals: part I--evaluation of adaptive algorithms. *Mechanical Systems and Signal Processing*, 18, 89-101.
- Antoni, J & Randall, RB 2004b. Unsupervised noise cancellation for vibration signals: part II--a novel frequency-domain algorithm. *Mechanical Systems and Signal Processing*, 18, 103-117.
- Antoni, J & Randall, RB 2006. The spectral kurtosis: application to the vibratory surveillance and diagnostics of rotating machines. *Mechanical Systems and Signal Processing*, 20, 308-331.
- Arslan, H & Aktürk, N 2008. An Investigation of Rolling Element Vibrations Caused by Local Defects. *Journal of Tribology*, 130, 041101-041101.
- Barszcz, T & Randall, RB 2009. Application of spectral kurtosis for detection of a tooth crack in the planetary gear of a wind turbine. *Mechanical Systems and Signal Processing*, 23, 1352-1365.
- Bayoumi, HN 2005. Interfacing FEA and Multibody Simulation Through Component Mode Synthesis. *ASME Conference Proceedings*. ASME.

- Butland, A & Avitabile, P 2010. A reduced order, test verified component mode synthesis approach for system modeling applications. *Mechanical Systems and Signal Processing*, 24, 904-921.
- Carmignani, C, Forte, P & Melani, G 2009. Component modal synthesis modeling of a gearbox for vibration monitoring simulation. *The Sixth International Conference on Condition Monitoring and Machinery Failure Prevention Technologies*. Dublin, Ireland.
- Chen, SL & Géradin, M 1997. An exact model reduction procedure for mechanical systems. *Computer Methods in Applied Mechanics and Engineering*, 143, 69-78.
- Choudhury, A & Tandon, N 2005. Vibration Response of Rolling Element Bearings in a Rotor Bearing System to a Local Defect Under Radial Load. *Journal of Tribology*, 128, 252-261.
- Craig, R & Bampton, M 1968. Coupling of substructures for dynamic analysis *Amer. Inst. Aero. Astro. J.*, 6, 1313–1319.
- Craig, RR & Kurdila, AJ 2006. *Fundamentals of Structural Dynamics*, John Wiley & Sons.
- Doguer, T & Strackeljan, J 2011. Simulation of vibrations due to bearing race imperfections. *8th International Conference on Condition Monitoring and Machinery Failure Prevention Technologies*. Cardiff, United Kingdom.
- Doguer, T, Strackeljan, J & Tkachuk, P 2009. Using a dynamic roller bearing model under varying fault parameters. *6th International Conference on Condition Monitoring and Machinery Failure Prevention Technologies*. Dublin, Ireland.
- Du, S. 1997. *Dynamic modelling and simulation of gear transmission error for gearbox vibration analysis*. Ph.D. Dissertation, University of New South Wales, Sydney, Australia.

- Endo, H. 2005. *Simulation of gear faults and its application to the development of differential diagnostic technique* Ph. D. Dissertation, University of New South Wales, Sydney, Australia.
- Endo, H & Randall, RB 2007. Enhancement of autoregressive model based gear tooth fault detection technique by the use of minimum entropy deconvolution filter. *Mechanical Systems and Signal Processing*, 21, 906-919.
- Endo, H, Randall, RB & Gosselin, C 2004. Differential diagnosis of spall versus cracks in the gear tooth fillet region. *Journal of Failure Analysis and Prevention*, Volume 4(5), 63-71.
- Endo, H, Randall, RB & Gosselin, C 2009. Differential diagnosis of spall vs. cracks in the gear tooth fillet region: Experimental validation. *Mechanical Systems and Signal Processing*, 23, 636-651.
- Farhat, C & Geradin, M 1994. On a component mode synthesis method and its application to incompatible substructures. *Computers & Structures*, 51, 459-473.
- Feng, NS, Hahn, EJ & Randall, RB 2002. Using transient analysis software to simulate vibration signals due to rolling element bearing defects. *3rd Australasian Congress on Applied Mechanics*. Sydney, Australia.
- Friswell, MI, Garvey, SD & Penny, JET 1995. Model reduction using dynamic and iterated IRS techniques. *Journal of Sound and Vibration*, 186, 311-323.
- Fukata, S, Gad, EH, Kondou, T, Ayabe, T & Tamura, H 1985. On the vibration of ball bearings. *Bulletin of JSME*, 28 (239), 899-904.
- Gao, Y & Randall, RB 2000. Simulation of geometric, static and dynamic gear transmission errors, (Report CEVA-2000-01). Centre of Expertise in Vibration Analysis, UNSW, Sydney, .
- Goldman, RL 1969. Vibration analysis by dynamic partitioning. *AIAA Journal*, 7, 1152-1154.
- Guyan, RJ 1965. Reduction of stiffness and mass matrices. *AIAA Journal*, 30, 772-780.

- Harris, TA 2001. *Rolling bearing analysis*, John Wiley & Sons Inc.
- Hinke, L, Dohnal, F, Mace, BR, Waters, TP & Ferguson, NS 2009. Component mode synthesis as a framework for uncertainty analysis. *Journal of Sound and Vibration*, 324, 161-178.
- Ho, D. 1999. *Bearing diagnostics and self-adaptive noise cancellation*. Ph.D. Dissertation, University of New South Wales, Sydney, Australia.
- Ho, D & Randall, RB 2000. Optimisation of bearing diagnostic techniques using simulated and actual bearing fault signals. *Mechanical Systems and Signal Processing*, 14, 763-788.
- Howard, I 1994. A review of rolling element bearing vibration "Detection, Diagnosis and Prognosis", DSTO-RR-0013. DSTO Aeronautical and Maritime Research Laboratory.
- Hurty, WC 1965. Dynamic analysis of structural systems using component modes. *AIAA Journal*, 3, 678-685.
- Irons, BM 1965. Structural eigenvalue problems-elimination of unwanted variables. *AIAA journal*, 3, 961-962.
- Khan, AF, Williams, EJ & Fox, CHJ 2000. Condition Monitoring of rolling element bearings - a comparison of vibration-based techniques for incipient damage detection. *The Seventh International Conference on Vibrations in Rotating Machinery, IMECHE Conference Transactions*. University of Nottingham, UK.
- Koutsovasilis, P & Beitelschmidt, M 2008. Comparison of model reduction techniques for large mechanical systems. *Multibody System Dynamics*, 20, 111-128.
- Koutsovasilis, P & Beitelschmidt, M 2010. Model order reduction of finite element models: improved component mode synthesis. *Mathematical and Computer Modelling of Dynamical Systems*, 16:1, 57 — 73.
- Liew, A, Feng, NS & Hahn, EJ 2002. Transient rolling element bearing systems. *Trans. ASME Turbines and Power*, 124(4), 984-991.

- Lim, TC & Singh, R 1990a. Vibration transmission through rolling element bearings, part I: Bearing stiffness formulation. *Journal of Sound and Vibration*, 139, 179-199.
- Lim, TC & Singh, R 1990b. Vibration transmission through rolling element bearings, part II: System studies. *Journal of Sound and Vibration*, 139, 201-225.
- Lim, TC & Singh, R 1991. Vibration transmission through rolling element bearings. Part III: Geared rotor system studies. *Journal of Sound and Vibration*, 151, 31-54.
- MacNeal, RH 1971. A hybrid method of component mode synthesis. *Computers & Structures*, 1, 581-601.
- Mark, WD 2012. *Performance-Based Gear Metrology: Kinematic - Transmission - Error Computation and Diagnosis*, John Wiley & Sons Inc.
- McFadden, PD 1986. Detecting Fatigue Cracks in Gears by Amplitude and Phase Demodulation of the Meshing Vibration. *Journal of Vibration Acoustics Stress and Reliability in Design*, 108, 165-170.
- McFadden, PD & Smith, JD 1984a. Model for the vibration produced by a single point defect in a rolling element bearing. *Journal of Sound and Vibration*, 96, 69-82.
- McFadden, PD & Smith, JD 1984b. Vibration monitoring of rolling element bearings by the high-frequency resonance technique - a review. *Tribology International*, 17, 3-10.
- McFadden, PD & Smith, JD 1985a. A signal processing technique for detecting local defects in a gear from the signal average of the vibration. *Proc Instn Mech Engrs Vol 199 No C4*.
- McFadden, PD & Smith, JD 1985b. The vibration produced by multiple point defects in a rolling element bearing. *Journal of Sound and Vibration*, 98, 263-273.

- Melani, G, Carmignani, C, Celi, S, Forte, P & Di Carlo, G 2008. Simulation of the transient dynamic behaviour of an aircraft gearbox by C MS. *International Conference on Noise and Vibration Engineering*. Leuven, Belgium.
- Myklebust, LI & Skallerud, B 2002. Model Reduction Methods for Flexible Structures. *15th Nordic Seminar on Computational Mechanics*. Aalborg, Denmark.
- O'Callahan, J, Avitabile, P & Riemer, R 1989. System Equivalent Reduction Expansion Process (SEREP). *Seventh International Modal Analysis Conference*. Las Vegas, Nevada.
- O'Callahan, JC 1989. A procedure for an improved reduced system (IRS) model. *Proc. 7. International Modal Analysis Conference*. Las Vegas.
- Park, K & Castanier, MP 2007. Component Mode Synthesis for Substructures With Non-Matching Interfaces. *SAE Noise and Vibration Conference and Exhibition*. St. Charles, Illinois, USA: SAE International, Warrendale, Pennsylvania, USA.
- Patel, VN, Tandon, N & Pandey, RK 2010. A Dynamic Model for Vibration Studies of Deep Groove Ball Bearings Considering Single and Multiple Defects in Races. *Journal of Tribology*, 132, 041101-1-041101-9.
- Patil, MS, Mathew, J & RajendraKumar, PK 2007. Bearing Signature Analysis as a Medium for Fault Detection: A Review. *Journal of Tribology*, 130, 014001-1-014001-7.
- Qu, Z-Q 2004. *Model Order Reduction Techniques :with Applications in Finite Element Analysis* Springer.
- Randall, RB 1982. A New Method of Modeling Gear Faults. *Journal of Mechanical Design*, 104, 259-267.
- Randall, RB 2004. State of the Art in Monitoring Rotating Machinery - Part 1. *Sound and Vibration*, 38, 14.
- Randall, RB 2011. *Vibration-based Condition Monitoring: Industrial, Aerospace and Automotive Applications* [John Wiley & Sons].

- Randall, RB, Antoni, J & Chobsaard, S 2001. The relationship between spectral correlation and envelope analysis in the diagnostics of bearing faults and other cyclostationary machine signals. *Mechanical Systems and Signal Processing*, 15, 945-962.
- Sassi, S, Badri, B & Thomas, M 2007. A Numerical Model to Predict Damaged Bearing Vibrations. *Journal of Vibration and Control*, 13, 1603-1628.
- Sawalhi, N & Randall, RB 2008a. A Combined Lumped Parameter and Finite Element Model of a Single Stage Gearbox for Bearing Fault Simulation. *COMADEM 2008 (Condition Monitoring and Diagnostic Engineering Management)*. Prague, Czech Republic.
- Sawalhi, N & Randall, RB 2008b. Improved Simulation of Faults in Rolling Element Bearings in Gearboxes. *9th International Conference on Vibrations in Rotating Machinery*. 8-10 September, UK.
- Sawalhi, N & Randall, RB 2008c. Simulating gear and bearing interactions in the presence of faults: Part I. The combined gear bearing dynamic model and the simulation of localised bearing faults. *Mechanical Systems and Signal Processing*, 22, 1924-1951.
- Sawalhi, N & Randall, RB 2008d. Simulating gear and bearing interactions in the presence of faults: Part II: Simulation of the vibrations produced by extended bearing faults. *Mechanical Systems and Signal Processing*, 22, 1952-1966.
- Sawalhi, N, Randall, RB & Endo, H 2007. The enhancement of fault detection and diagnosis in rolling element bearings using minimum entropy deconvolution combined with spectral kurtosis. *Mechanical Systems and Signal Processing*, 21, 2616-2633.
- Sellgren, U 2003. Component mode synthesis - A method for efficient dynamic simulation of complex technical systems. Technical Report, Department of Machine Design, The Royal Institute of Technology (KTH), S-100 44 Stockholm, Sweden.

- Smith, JD 1983. *Gears and their vibration - A basic approach to understanding gear noise*, Marcel Dekker/ Macmillan Press, Ltd.
- Smith, JD 2003. *Gear Noise and Vibration: Second Edition, Revised and Expanded*, CRC Press.
- Sopanen, J & Mikkola, A 2003a. Dynamic model of a deep-groove ball bearing including localized and distributed defects. Part 1: Theory. *Proceedings of the Institution of Mechanical Engineers, Part K: Journal of Multi-body Dynamics*, 217, 201-211.
- Sopanen, J & Mikkola, A 2003b. Dynamic model of a deep-groove ball bearing including localized and distributed defects. Part 2: Implementation and results. *Proceedings of the Institution of Mechanical Engineers, Part K: Journal of Multi-body Dynamics*, 217, 213-223.
- Stewart, RM 1977. Some Useful Data Analysis Techniques for Gearbox Diagnostics. *Proceedings of the Meeting on the Applications of Time Series Analysis, ISVR*. University of Southampton, Southampton, UK.
- Sunnersjö, CS 1978. Varying compliance vibrations of rolling bearings. *Journal of Sound and Vibration*, 58, 363-373.
- Sweeney, P. 1994. *Transmission error measurement and analysis* Ph. D. Dissertation, University of New South Wales, Sydney, Australia.
- Sweeney, PJ & Randall, RB 1996. Gear transmission error measurement using phase demodulation. *Journal of Mechanical Engineering Science*, 210 (C3), 201-213.
- Tadina, M & Boltežar, M 2011. Improved model of a ball bearing for the simulation of vibration signals due to faults during run-up. *Journal of Sound and Vibration*, 330, 4287-4301.
- Tandon, N & Choudhury, A 1997. An analytical model for the prediction of the vibration response of rolling element bearings due to a localized defect. *Journal of Sound and Vibration*, 205, 275-292.

- Wang, W 2001. Early detection of gear tooth cracking using the resonance demodulation technique. *Mechanical Systems and Signal Processing*, 15, 887-903.
- Wang, W & Wong, AK 2002. Autoregressive Model-Based Gear Fault Diagnosis. *Journal of Vibration and Acoustics*, 124, 172-179.
- Young, JT 2000. Primer on the Craig-Bampton Method, (Based on input from William B. Haile).

CHAPTER 3

EXPERIMENTAL MODAL ANALYSIS AND FE MODEL UPDATING OF GEARBOX CASING

3.1 Introduction

The review of literature presented in Chapter 2 highlights the extensive use and potential benefits, as well as the limitations, of simulation models (mainly LPMs), to predict the dynamic behaviour of a machine such as a gearbox.

In order to overcome the limitations of previously developed gearbox simulation models, a new approach was implemented that takes into account the dynamic characteristics of the casing as derived from its finite element model. The resulting model is based on the combination of LPM and FEM, or FEM only, and is used to simulate the dynamics of the UNSW parallel shaft gearbox with bearing faults. LPM is used to model the gearbox internal components such as shafts, gears, and bearings as well as flywheels and encoders, whereas FEM is used to model the gearbox casing to take into account the casing flexibility which could not be properly represented using LPMs. Preliminary investigations indicated the suitability of the combined LPM-FEM approach (Deshpande et al., 2011 , Deshpande et al., 2012, Sawalhi et al., 2011) to identify bearing faults, however the response (PSD spectrum) of the combined model was found to be a poor match in the low frequency region (2–4 kHz) when compared with the measurements.

The simplified FE model of the casing used in earlier simulations was an approximation of the real structure due to the uncertainties in the material properties, geometry and

constraints. The accuracy of simulation depends largely on having a realistic representation of the structure. Hence it was decided to validate the FE model of the casing based on the results of Experimental Modal Analysis (EMA) and rule out inherent assumptions and simplifications in the FE model as a possible source of discrepancy in the simulated results and measured signals. This in particular applies to the low frequency region which can adversely affect the prediction of extended faults in the bearings.

This chapter describes the finite element modelling and validation of the gearbox casing based on the FEA-EMA correlation and model updating.

3.2 Overview of finite element model updating

Computer Aided Engineering (CAE) tools such as finite element method (FEM) of numerical simulations are widely used to analyse large complex structures where the use of classical structural analysis methods become prohibitive.

Figure 3.1 (a) and (b) show schematically the conventional and virtual product development (VPD) processes respectively. The ultimate goal is to significantly reduce the number of physical prototypes required to validate the design.

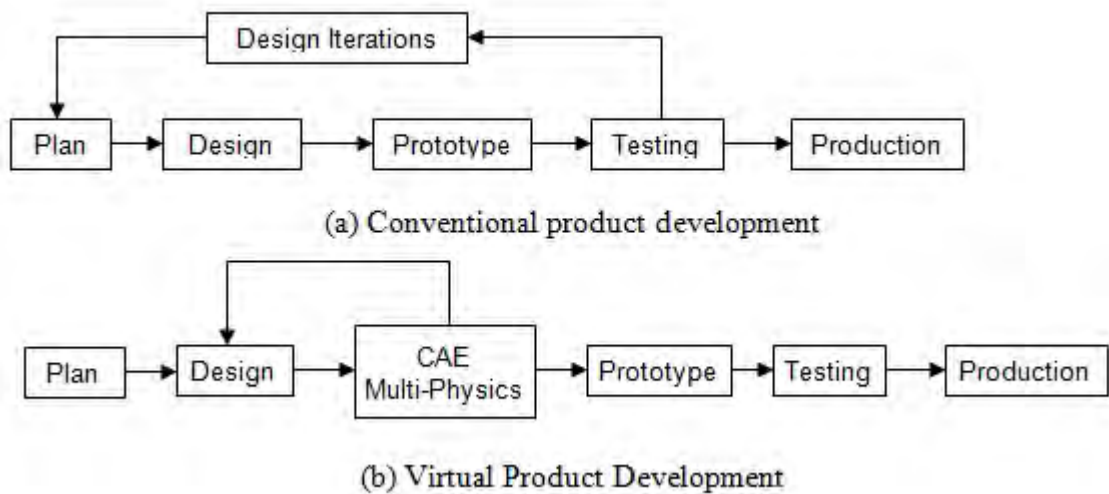


Figure 3.1 Product development processes

Although initially developed specifically for structural analysis, FEM has been evolved to cover diverse engineering disciplines and physical sciences such as heat transfer, fluid flow, electromagnetic, acoustics etc (Figure 3.2).

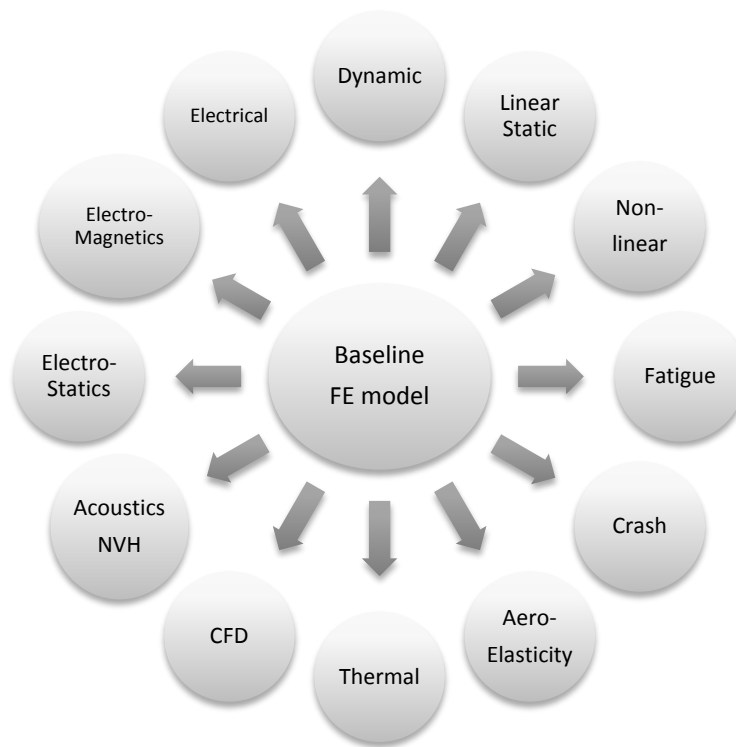


Figure 3.2 CAE simulation environment

Since the structural FE model with the same element library, material data and loading history can be easily extended to include additional physical interactions, the accuracy of simulation depends largely on the realistic representation of the structure and its loading conditions i.e. formulation of the baseline FE model . FEA predictions are often treated with distrust whenever there are discrepancies with the test results. This can be attributed to the possible sources of inaccuracies in the numerical (FEA) model (Dascotte, 2004) such as:

- Physical uncertainty
 - Boundary and initial conditions
 - Material properties, geometry, loads (and their variation with temperature, frequency and load level)

➤ Numerical uncertainty

- Conceptual modelling uncertainty
- Mathematical modelling uncertainty
- Discretisation modelling uncertainty – choice of elements, mesh density, level of geometric detail
- Numerical solution uncertainty – rounding off, convergence tolerance, integration step
- Human mistakes – errors in code etc

Due to above uncertainties in the simulation, it becomes imperative to validate FEA predictions against the test results to gain confidence for further simulations (what-if scenarios). To deal with inaccuracies in analytical models, modelling methods are developed based on Experimental Modal Analysis (EMA) – the area also known as systems identification for the parametric estimation i.e. determination of modal data (natural frequencies, mode shapes and damping) from vibration tests (Mottershead and Friswell, 1993).

3.2.1 Experimental modal analysis

Experimental modal analysis or modal testing as defined by Ewins is ‘a process of testing components and structures with the objective of obtaining a mathematical description of their dynamic or vibration behaviour’ (Ewins, 2000). The field of experimental model analysis has been widely researched and techniques are presented in several books and review papers (Dossing, 1988b, Dossing, 1988a, Snoeys et al., 1987, Maia and e Silva, 1997). Modal analysis aims to define the modal parameters (natural frequencies, mode shapes and damping) assuming structural behaviour is linear and dynamic characteristics are time invariant. The modal parameters obtained from EMA can be used to analyse the current dynamic behaviour of the structure. The results of EMA (modal parameters) can be further used in applications such as structural modifications, assessment of structural integrity and reliability, structural health monitoring and model updating.

3.2.2 Finite element model updating

In order to close the gap between FEA predictions and EMA results, finite element model updating techniques (an iterative procedure based on the sensitivity formulation) are widely adopted. Model updating is a study of the influence of design variable modifications on the system's response and minimising an error function describing deviation between analytical and experimental data (DDS, 2012c). In other words, the purpose of model updating is to modify the mass, stiffness and damping parameters of the numerical model in order to obtain better agreement between numerical results and test data. Once this has been achieved, the final step is to identify dynamic forces using experimental operational responses. A comprehensive review of the model updating history, philosophy and various techniques can be found in (Natke, 1988, Mottershead and Friswell, 1993, Mottershead et al., 2011). The current trends in model updating and the future outlook is described in (Dascotte, 2007).

The conventional FE model updating method based on the measurements from a single test system is considered to be deterministic since it does not take into account the variability in the test structures and uncertainties in the FE model which are already discussed above. The sources of variability in test structures include geometric tolerances and the manufacturing processes. It is common to have scatter in the test data due to the uncertainties related to test setup (component supports, excitation method, transducer location and weight), dynamic loading, instrumentation (calibration, cabling noise) and data acquisition. Techniques like Experimental Modal Analysis are also subject to numerical uncertainty in the mathematical models that are used for modal parameter estimation using curve fitting methods. FE model updating based on probabilistic analysis (or stochastic model updating) using a Monte-Carlo technique with multiple sets of experimental results is illustrated in (Dascotte, 2003, Mares et al., 2006, Mottershead et al., 2006).

The general procedure of linking FEA and Test is shown in Figure 3.3 and can be broadly classified into following stages (Dascotte, 2004):

3.2.2.1 Pretest analysis

A preliminary but sufficiently representative model of the structure can be useful to identify important mode shapes and select optimal sensor locations and locate the directions to measure and excite the structure. In pre-test analysis, the baseline FE model is used to simulate tests by reducing the FE model to test locations and converting it into a test model.

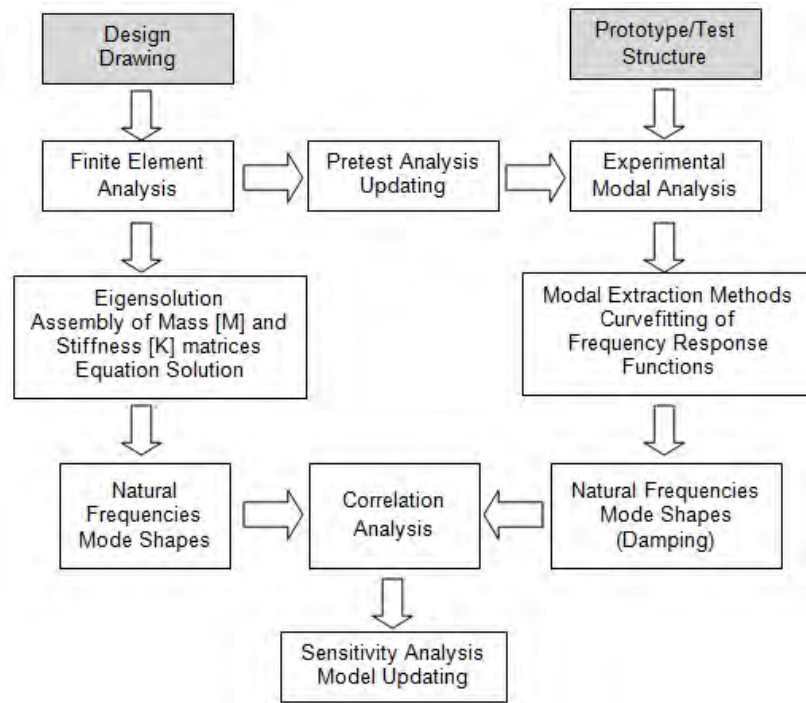


Figure 3.3 General procedure - linking FEA with Test (Dascotte, 2004)

3.2.2.2 Correlation analysis

Correlation between FEA and EMA results can be expressed in terms of resonance frequencies and modal displacements. A commonly used value to compare FEA and experimental mode shapes is the Modal Assurance Criterion (MAC) (Allemang and Brown, 1982). The MAC matrix stores MAC values between all combinations of analytical and test modes. A diagonal value of 1 indicates identical modes or perfect correlation whereas off-diagonal terms indicate the degree of separation or independence between modes (DDS, 2012b). The MAC matrix is used in automatic mode shape pairing during model updating.

3.2.2.3 Parameter and response selection

Updating parameters can be physical properties such as material, geometry, lumped properties (e.g. mass) and damping (modal, viscous, structural). Structural responses such as natural frequencies, mode shapes and FRFs can be selected as updating targets or correlation targets.

3.2.2.4 Sensitivity analysis and model updating

Sensitivity analysis indicates the influence of selected parameters on the target responses and the updated parametric estimations are evaluated based on Bayesian estimator.

The optimal model updating sequence is shown in Figure 3.4.

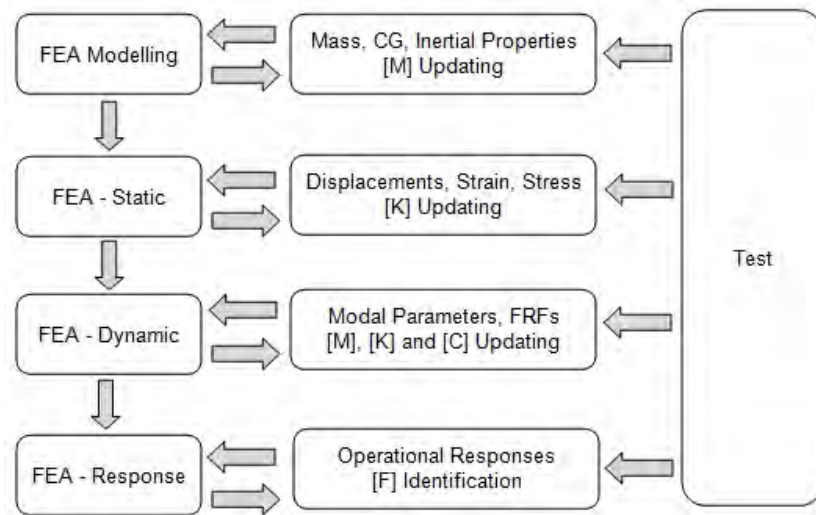


Figure 3.4 The optimal model updating sequence (DDS, 2012c)

Model updating methods can be broadly classified into direct (non-iterative) methods and iterative (sensitivity) methods. In the direct method, the mass and stiffness matrices are updated directly, which although giving an exact match with the EMA modal data, the updated matrices are difficult to interpret and cannot be expressed in terms of the physical parameters of the structure (Modak et al., 2002a). Hence sensitivity based iterative methods are widely used in model updating, these being further classified into modal based updating and FRF based updating.

3.2.3 Sensitivity based model updating

Early model updating techniques used modal based updating (using modal parameters) since the natural frequencies can be measured accurately using EMA. However, later studies used FRF based updating methods due to their advantages over modal based updating (Lin and Ewins, 1990, Imregun et al., 1995b, Imregun et al., 1995a). FRF methods directly employ the measured quantities for updating, thus eliminating modal parameter extraction. FRFs are not subject to averaging and curve-fitting errors and provide information on damping characteristics over the entire measured frequency spectrum. However the main limitation of these early FRF methods was their excessive computational requirements which was overcome by a new efficient method of FE model updating based on FRF correlation functions, namely Cross Signature Assurance Criteria (CSAC) and Cross Signature Scale Factor (CSF) which are a measure of shape and amplitude correlation respectively (Dascotte and Strobbe, 1999, DDS, 2012b).

3.2.4 Model updating using operational data

In the traditional approach of model updating, the results of simulation are compared with the results of EMA i.e. resonance frequencies and mode shapes extracted from the measured FRFs. However, the EMA data which is independent of the applied loads cannot be used for validation purposes where operational loads change the behaviour of the structure. EMA cannot be carried out when the structure is subjected to environmental operational loads such as random excitation due to wind and traffic loads. Hence the Operational Modal Analysis (OMA) technique is widely used as an alternative to Experimental Modal Analysis (EMA). OMA aims at determining the dynamic characteristics of a system in operational conditions, without measuring the natural excitation forces (Heylen et al., 1997). The operational equivalents of experimental FRFs are the operational response spectra which can be transformed into a set of Operational Deflection Shapes (ODS). The FE model can be updated by comparing the numerical ODS with the experimental ODS (Lauwagie et al., 2010).

3.2.5 Model updating applications

Two main applications where model updating techniques can be used effectively are Structural Dynamic Modification (SDM) and Structural Health Monitoring (SHM).

3.2.5.1 Structural Dynamic Modification (SDM)

Structural dynamic design modification techniques have been available as a design tool for several decades. A review of the SDM methodologies and their limitations is presented in (Avitabile, 2003). An updated finite element model which can predict the dynamics of a structure more accurately can be subsequently used to predict the effects of structural modifications with a reasonable accuracy (Modak et al., 2002a, Modak et al., 2002b). Traditional structural modification techniques may not result in the most efficient and feasible solution, however the use of sensitivity based model updating can result in the optimised dynamic behaviour of the structure.

3.2.5.2 Structural Health Monitoring (SHM)

Due to its non-destructive nature, there has been an increasing trend to use model updating techniques as an effective tool in damage detection and Structural Health Monitoring (SHM). An updated FE model exhibits observed dynamic characteristics of a real damaged structure. The structural changes can be detected when the updated model is compared against a reference model of the undamaged structure (DDS, 2012c). Further, the residual life of the structure can be estimated by subjecting the updated (damaged) model to fatigue analysis. The application of finite element model updating to damage detection in beam and stay cable structures is described in (Mordini et al., 2007) and to estimate the crack size and location in a beam is presented in (Sinha and Friswell, 2002).

In the current research, EMA results are used to update the FE model of the UNSW gearbox casing which is incorporated into the dynamic model of the gear test rig. The model updating procedure is described in the following sections.

3.3 Experimental Modal Analysis (EMA) of UNSW gearbox casing

The Experimental Modal Analysis on the gearbox casing was carried out by suspending the casing from a beam using an elastic rope and bungee cords (Figure 3.5). The test mesh or grid points were marked on the casing and the measurements were carried out using the roving hammer (excitation) and fixed accelerometer (reference) method. Three single axis (B&K 4393) accelerometers were fixed to the casing (Figure 3.6) to measure the responses in the X, Y and Z directions. The accelerometers were powered by B&K 2635 Charge Amplifiers. The excitation was provided by using a Hammer with steel tip (B&K 8202). The measurements were carried out using B&K Pulse Front-end and Modal Test Consultant (MTC) software (B&K, 2009).



Figure 3.5 EMA - Experimental Setup

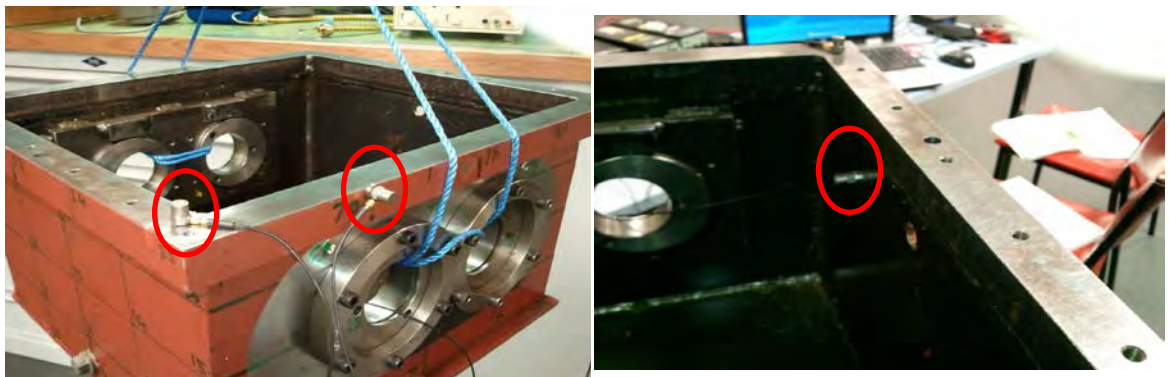


Figure 3.6 Accelerometer locations

A Test model was created using the 3D wireframe geometry of the gearbox indicating the measurement points and associated degrees-of-freedom to facilitate the modal

testing. The Test model had 89 test points where the responses were measured. The test data consisting of the experimentally derived Frequency Response Functions (FRFs) was exported to ME'scope software (ME'scopeVES4.0, 2003). The experimental modal parameters, namely the modal frequency, modal damping and mode shape for each mode were estimated by curve fitting (a process of matching a parametric model of an FRF to experimental data) using the FRF sets. The global curve fit technique (based on the polynomial method) was used to obtain a global modal frequency and damping for each mode, since the modal frequency and damping are the global properties of a structure (meaning the resonance peaks appear at the same frequencies in multiple FRFs). The set of modal frequency and damping values was used to estimate the modal residues known as mode shapes which were used to correlate the Test-FEA models of the gearbox casing [explained in section 3.4]. The modes extracted up to 2 kHz were used in the model updating since the modes tend to overlap at higher frequencies due to increasing absolute damping.

3.4 Model updating: UNSW gearbox casing

3.4.1 FE model of gearbox casing

The gearbox casing is primarily made up of welded steel plates and steel rings. The steel rings when attached to the casing hold the eccentric discs which support the bearings and the shafts. The eccentric arrangement allows the use of different gear ratios by varying the centre distance between the shafts. The finite element model of the casing was created using MSC.Patran software (MSC, 2010). The steel plates in the casing were modelled using shell (4 noded quadrilateral) elements whereas solid (8 noded hexahedral or brick) elements were used for the steel rings (Figure 3.7). The weld fillets were not modelled in the simplified FE model and the nodes in the FE model were assumed to be rigidly connected to represent the welded structure with uniform plate thicknesses. However in reality the casing was made up of thin plates (3 mm vertical plates and 6 mm bottom plate) where there are discontinuities in the welds which will exhibit some flexibility (not fully rigid). Hence, for the realistic simulation, the FE model of the casing needs to be correlated with test (EMA) results. The FE model of the casing had a total of 50694 DOFs.

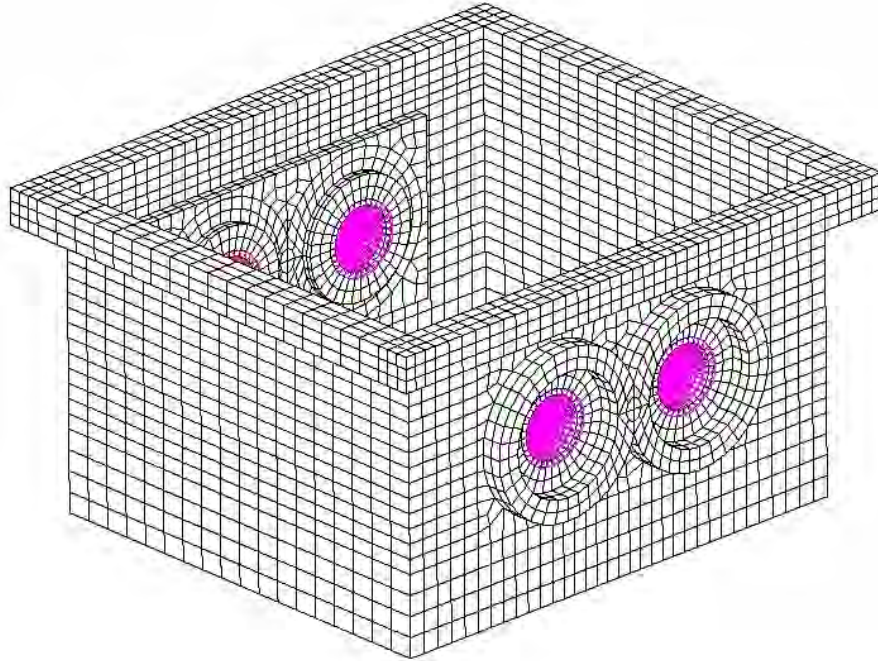


Figure 3.7 FE model of UNSW gearbox casing

3.4.2 Test-FEA correlation

The Test-FEA correlation and Modal-based updating was carried out using FEMTools software (DDS, 2012a). Both the FE model (from MSC.Patran) and the Test model along with the experimental mode shapes (from ME'scope) were imported into a single FEMTools database. Since the Test model is invariably significantly coarser (number of measurement points) than the FE model (total number of nodes), node point pairing was done by transforming and aligning the test model with the FE model. Similarly mode shape pairs were defined (before model updating) based on the MAC (Modal Assurance Criterion) values. MAC is a widely used technique to estimate the degree of correlation between mode shape vectors and is used to pair mode shapes derived from analytical (FE) models with those obtained experimentally.

The gearbox casing was mainly comprised of a welded plate structure with 3 mm thickness for the vertical plates, and 6 mm for the bottom plate. Hence, the plate thickness was considered to be the most appropriate parameter for model updating, to allow for local variations in joint stiffness. The test modal responses (paired natural

frequencies) were used as response parameters. Table 3.1 shows the comparison of FEA and EMA mode shape pairs before and after model updating. The FEA and EMA frequencies correlate well after model updating. There is also small improvement in the MAC values especially at lower frequencies. Figures 3.8 and 3.9 show the graphical display of the MAC values before and after updating in the 3D matrix form. Note that the off-diagonal groups in the MAC diagram were confirmed to be due to spatial under-sampling of the test grid, which was not able to represent the short wavelength of some higher order modes in one direction. Figure 3.10 shows the mode shape comparison for the updated model at paired nodes for a low frequency and for a high frequency.

Table 3.1 Comparison of Mode shape pairs

Mode shape pairs (before updating)						Mode shape pairs (after updating)					
FEA	Hz	EMA	Hz	Diff. (%)	MAC (%)	FEA	Hz	EMA	Hz	Diff. (%)	MAC (%)
1	235.77	1	218.28	8.01	84.4	1	233.02	1	218.28	6.75	84.3
3	372.76	2	345.68	7.83	87.1	3	350.77	2	345.68	1.47	88.7
4	460.21	3	426.89	7.8	71.6	4	433.59	3	426.89	1.57	72.1
5	474.5	4	462.75	2.54	76.3	5	455.37	4	462.75	-1.59	76.3
6	476.51	5	475.93	0.12	77	6	476.28	5	475.93	0.07	77
7	582.59	6	564.88	3.14	88.1	8	560.97	6	564.88	-0.69	88.2
12	794.13	10	706.82	12.35	70.5	12	686.7	9	688.43	-0.25	72.6
13	803.75	12	802.92	0.1	69.8	13	687.97	10	706.82	-2.67	70.8
15	957.23	13	882.92	8.42	83.7	14	802.26	12	802.92	-0.08	77.7
17	1064	15	976.67	8.94	60	15	930.52	13	882.92	5.39	84.4
18	1088.5	16	1006.5	8.14	76.6	18	1009.2	16	1006.5	0.26	76.9
19	1116.9	17	1119	-0.19	77	19	1116.3	17	1119	-0.24	79.2
20	1168.1	18	1145.7	1.96	78.6	20	1142.5	18	1145.7	-0.28	75.3
21	1241.1	19	1239.3	0.15	69.2	21	1231.6	19	1239.3	-0.62	71
22	1297.3	20	1322.1	-1.88	74.6	22	1324.9	20	1322.1	0.21	74.4
33	1767.9	33	1756.6	0.64	67.5	33	1752.3	33	1756.6	-0.24	69.8
35	1860	34	1910.1	-2.62	65.8	37	1971.8	35	1972	-0.01	71.7
37	1985	35	1972	0.66	62.5						

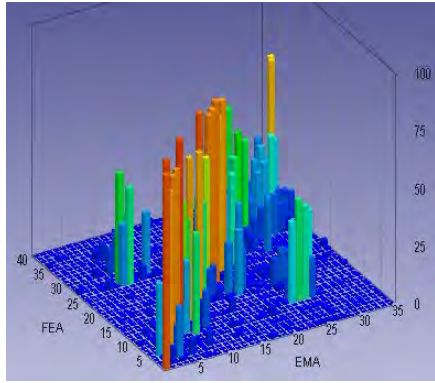


Figure 3.8 MAC before updating

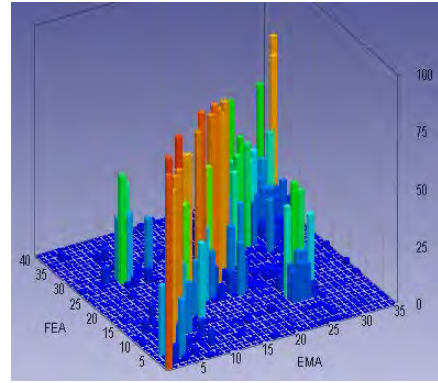
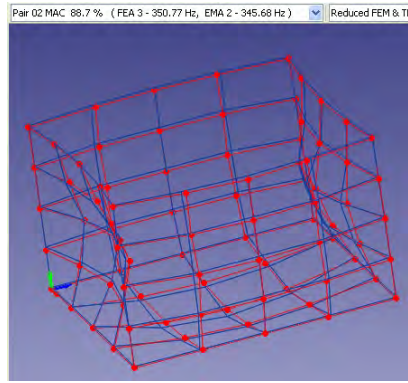
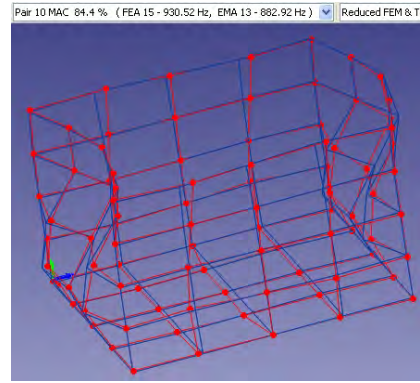


Figure 3.9 MAC after updating



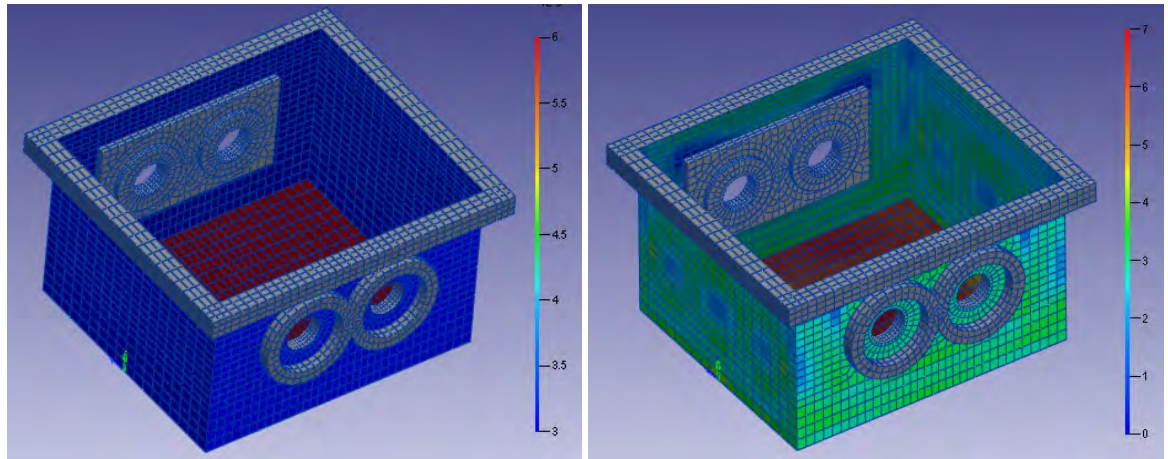
(a) Updated model: mode shape pair 02
(FEA 350.77 Hz, EMA 345.68 Hz,
MAC 88.7%)



(b) Updated model: mode shape pair 10
(FEA 930.52 Hz, EMA 882.92 Hz,
MAC 84.4%)

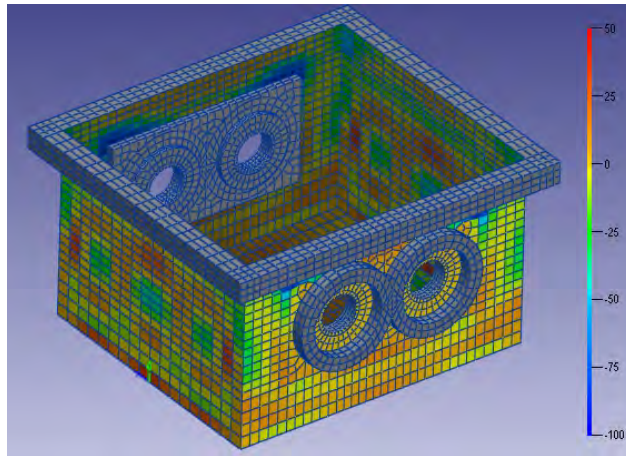
Figure 3.10 Mode shape comparison [Red - Test model, Blue – FE model]

Figure 3.11 shows the results of model updating. The gearbox casing model with original plate thickness contour plot (3 mm vertical and 6 mm bottom plate) is shown in Figure 3.11 (a). Figure 3.11 (b) and 3.11 (c) show the plate thickness contour plots for the updated model and the percentage change in the thickness respectively. It is seen that deviations are concentrated near welded joints.



(a) Thickness (mm) contour plot
(before updating)

(b) Thickness (mm) contour plot
(after updating)



(c) Updated model - Parameter thickness (% change)

Figure 3.11 Model updating results

3.5 Summary

Model updating techniques show great potential to bridge the gap between FEA models and EMA results. The improved correlation allows the use of simulation models with greater confidence. Due to its non-destructive nature, model updating techniques are increasingly used in applications such as SDM and SHM where the primary objective is to reduce the maintenance costs and increase safety of the structure.

The EMA-FEA correlation and model updating described in this chapter clearly establish the validity of the FE model of the casing. The model reduction technique was

applied to the **updated FE model of the casing** and the reduced casing model was used to develop the dynamic model of the UNSW gearbox test rig in the presence of bearing faults (as described in Chapter 4).

3.6 References

- Allemang, RJ & Brown, DL 1982. A correlation coefficient for modal vector analysis. *Proceedings, International Modal Analysis Conference (IMAC I)*. Orlando, Florida.
- Avitabile, P 2003. Twenty years of structural dynamic modification - a review. *Sound and Vibration*, 37, 14.
- B&K 2009. PULSE Analyzer & PULSE LabShop Version 14. Brüel & Kjær Sound & Vibration Measurement A/S <http://bksv.com/>.
- Dascotte, E 2003. The use of FE model updating and probabilistic analysis for dealing with uncertainty in structural dynamics simulation. *Japan Modal Analysis Conference (JMAC)*. Tokyo, Japan.
- Dascotte, E 2004. Linking FEA with Test. *Sound and Vibration, ProQuest Science Journals*, 38, 12-17.
- Dascotte, E 2007. Model Updating for Structural Dynamics: Past, Present and Future Outlook. *International Conference on Engineering Dynamics (ICED)*. Carvoeiro, Algarve, Portugal.
- Dascotte, E & Strobbe, J 1999. Updating finite element models using FRF correlation functions *Proceedings of the 17th International Modal Analysis Conference (IMAC)*, Kissimmee, Florida.
- DDS 2012a. (Dynamic Design Solutions N.V.), FEMtools Version 3.6.
- DDS 2012b. (Dynamic Design Solutions NV), *FEMtools Model Updating - Theoretical Manual, Version 3.6*.

- DDS 2012c. *(Dynamic Design Solutions NV), FEMtools Model Updating User's Guide, Version 3.6.*
- Deshpande, L, Sawalhi, N & Randall, R 2011 Improved gearbox simulations for diagnostic and prognostics purposes using finite element model reduction techniques *Australian Journal of Mechanical Engineering* 8 91-101
- Deshpande, L, Sawalhi, N & Randall, RB 2012. Gearbox bearing fault simulation using a finite element model reduction technique. *25th International Congress on Condition Monitoring and Diagnostic Engineering Management*. Huddersfield, UK.
- Dossing, O 1988a. *Structural Testing Part 2: Modal Analysis and Simulation*, Brüel & Kjær.
- Dossing, O 1988b. *Structural Testing Part I: Mechanical Mobility Measurements*, Brüel & Kjær.
- Ewins, DJ 2000. *Modal Testing, Theory, Practice, and Application*, Research Studies Pre; 2 edition (September 26, 2000).
- Heylen, W, Lammens, S & Sas, P 1997. *Modal Analysis Theory and Testing*, Katholieke Universiteit Leuven, Departement Werktuigkunde, Leuven, Belgium.
- Imregun, M, Sanliturk, KY & Ewins, DJ 1995a. Finite element model updating using frequency response function data: II. Case study on a medium-size finite element model. *Mechanical Systems and Signal Processing*, 9, 203-213.
- Imregun, M, Visser, WJ & Ewins, DJ 1995b. Finite element model updating using frequency response function data: I. Theory and initial investigation. *Mechanical Systems and Signal Processing*, 9, 187-202.

- Lauwagie, T, Guggenberger, J, Strobbe, J & Dascotte, E 2010. Model updating using operational data. *International Seminar on Modal Analysis (ISMA)*. Leuven, Belgium.
- Lin, RM & Ewins, DJ 1990. Model updating using FRF data. *Proceedings of the 15th international seminar on modal analysis*. Leuven, Belgium.
- Maia, NM & e Silva, JMM 1997. *Theoretical and Experimental Modal Analysis*, Baldock, England: Research Studies Press.
- Mares, C, Mottershead, JE & Friswell, MI 2006. Stochastic model updating: Part 1— theory and simulated example. *Mechanical Systems and Signal Processing*, 20, 1674-1695.
- ME'scopeVES4.0 2003. Vibrant Technology <http://www.vibetech.com/>.
- Modak, SV, Kundra, TK & Nakra, BC 2002a. Prediction of dynamic characteristics using updated finite element models. *Journal of Sound and Vibration*, 254, 447-467.
- Modak, SV, Kundra, TK & Nakra, BC 2002b. Use of an updated finite element model for dynamic design. *Mechanical Systems and Signal Processing*, 16, 303-322.
- Mordini, A, Savov, K & Wenzel, H 2007. The finite element model updating: A powerful tool for structural health monitoring. *Structural Engineering International*, 4, 352-358.
- Mottershead, JE & Friswell, MI 1993. Model updating in structural dynamics: a survey. *Journal of Sound and Vibration*, 167, 347-375.
- Mottershead, JE, Link, M & Friswell, MI 2011. The sensitivity method in finite element model updating: A tutorial. *Mechanical Systems and Signal Processing*, 25, 2275-2296.

- Mottershead, JE, Mares, C, James, S & Friswell, MI 2006. Stochastic model updating: Part 2—application to a set of physical structures. *Mechanical Systems and Signal Processing*, 20, 2171-2185.
- MSC 2010. MSC.Patran v2010 (finite element modelling software).
- Natke, HG 1988. Updating computational models in the frequency domain based on measured data: a survey. *Probabilistic Engineering Mechanics*, 3, 28-35.
- Sawalhi, N, Deshpande, L & Randall, RB 2011. Improved simulations of faults in gearboxes for diagnostic and prognostic purposes using a reduced finite element model of the casing. *7th DSTO International Conference on Health & Usage Monitoring (HUMS2011)*. Melbourne, Australia.
- Sinha, JK & Friswell, MI 2002. Model updating: A tool for reliable modelling, design modification and diagnosis. *The Shock and Vibration Digest*, 34, 27-35.
- Snoeys, R, Sas, P, Heylen, W & Van der Auweraer, H 1987. Trends in experimental modal analysis. *Mechanical Systems and Signal Processing*, 1, 5-27.

CHAPTER 4

GEARBOX DYNAMIC MODELLING USING MODEL REDUCTION TECHNIQUES

4.1 Introduction

In the past, researchers have widely used Lumped Parameter Models (LPMs) to simulate the dynamics of mechanical systems such as shafts and gears in a gearbox. In addition to simulating the complex behaviour between the various components, LPMs were also implemented to simulate vibration signals in the presence of gear and bearing faults.

In the LPM model, the gearbox inertias are lumped at certain locations such as gears, shafts, bearings etc. The resulting simulation model has a limited number of degrees-of-freedom (DOFs), which facilitates studying the behaviour of gears and bearings in the presence of nonlinearities and geometrical faults (Endo, 2005, Sawalhi and Randall, 2008a, Sawalhi and Randall, 2008b). The main limitation of LPMs is their inability to include the casing dynamics (due to the limited representation of the modes of the gearbox casing and the internals), which is an important consideration in light weight structures such as in aircraft applications and cannot be ignored in the simulation models. Additionally, LPMs are found to exhibit poor spectral matching over a wide frequency range.

Finite element (FE) analysis provides an alternative approach to simulate the dynamic behaviour of the structure. FE modelling is well suited to predicting the dynamic behaviour of continuous elastic systems such as a gearbox casing, where the mass is distributed over the structure. FE models in general have a large number of DOFs; and

require large computing resources which make the simulation of the whole system's response in the presence of nonlinearities and to gear and bearing faults much more complicated. This in turn limits the usefulness of the simulated results and restricts their later usage in the diagnostics and prognostics of gears and bearings.

Hence in order to address the limitations of both the LPM and FEM models, a new methodology using finite element model reduction techniques has been proposed. Unlike stress analyses, which require large number of DOFs in the FE model, the dynamic behaviour can be predicted with reasonable accuracy using a reduced or much smaller number of DOFs. Hence there is a growing trend to use FE model reduction methods to create accurate low order dynamic models before calculating eigenfrequencies and eigenmodes.

This chapter illustrates the dynamic modelling of the UNSW gearbox test rig using a finite element model reduction technique based on the Craig-Bampton (CB) method of component mode synthesis (CMS). The methodology to simulate vibration signals in the presence of various types of bearing faults is described in Section 4.2.2 and 4.2.3 for the two types of models namely - combined LPM-reduced FEM of casing (146 DOF model) and full reduced model of the gear test rig (182 DOF model). Both the models utilize the mass and stiffness matrices of the updated FE model of the casing obtained through modal testing (described in Chapter 3). Prior to describing the model reduction technique, the lumped parameter model of the gearbox internal components (required to create a combined LPM-FEM model) is discussed in the following sections with reference to the bearing model (with and without fault) and the gear model.

4.2 Dynamic modelling of the UNSW gear test rig

A brief history of the dynamic simulation models of the UNSW gearbox test rig was presented in Chapter 2 (Sweeney, 1994, Du, 1997, Ho, 1999, Endo, 2005, Sawalhi, 2007), the majority of which were based on the LPM approach. From the modelling point of view, the dynamic model of the entire test rig can be considered to be comprised of two substructures namely the gearbox casing and the internals and

includes a bearing model and a gear dynamic model to simulate the gear/bearing interaction in a gearbox.

4.2.1 Rolling element bearing model

The LPM of the gearbox internals used in this research was based on the 34 DOF LPM of the gearbox test rig developed earlier (Sawalhi, 2007).

Figure 4.1 shows a schematic of a 5 DOF bearing pedestal model incorporated into the 34 DOF LPM (Sawalhi, 2007) of the gearbox test rig wherein an extra degree of freedom was added to represent a typical high frequency resonance response of the bearing housing. The main improvements in the 34 DOF LPM were the incorporation of non-linearity in a rolling bearing due to non-linear Hertzian contact forces, time varying stiffness resulting from the variable load transmission caused by the positioning of the rolling elements and the clearance between the rolling elements and bearing races.

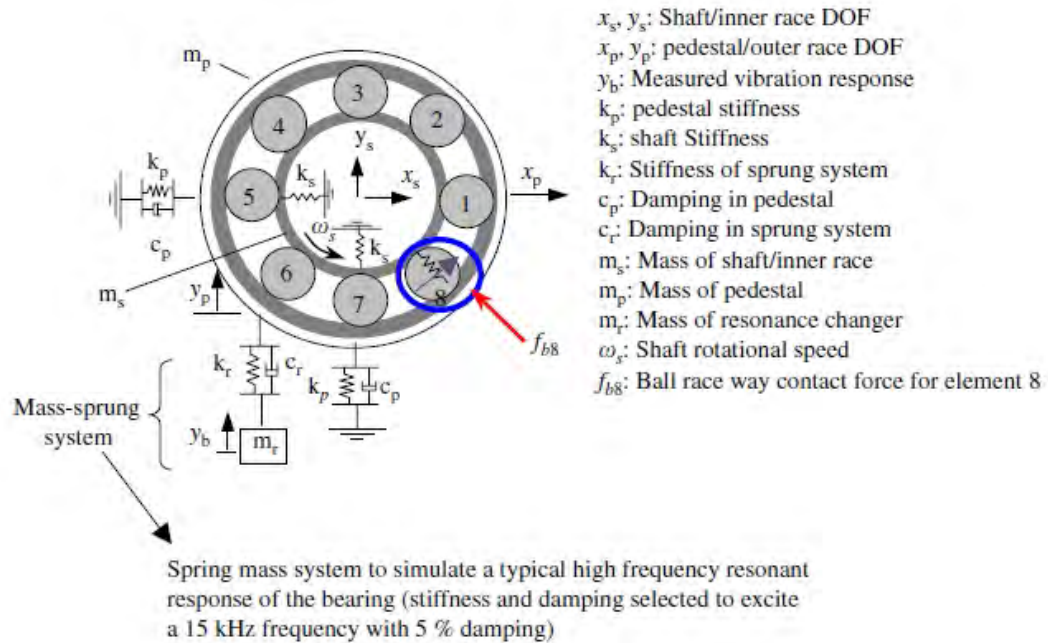


Figure 4.1 5 DOF bearing-pedestal model (Sawalhi and Randall, 2008a)

The above 5 DOF bearing-pedestal model was adapted in the current research by removing the extra degree of freedom (spring mass system in Figure 4.1) to create the combined LPM-reduced FEM (146 DOF) and the full reduced FEM (182 DOF) models.

Note that the pedestal DOFs now relate to the corresponding DOFs on the reduced model of the casing (where the bearing centre points are attached). For the sake of simplicity, the slippage in the rolling element bearing (with fault) was not included in the proposed 146 and 182 DOF models (even though slippage was modelled in the 34 DOF LPM, it was not properly represented and needs correction).

The general equations of motion for this rotor-bearing system are:

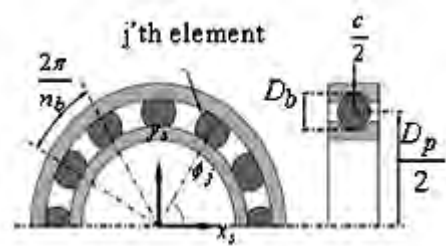
$$m_s \ddot{x}_s + k_s(x_s) + f_x((x_s - x_p), \omega_s, dt) = 0 \quad (4.1)$$

$$m_s \ddot{y}_s + k_s(y_s) + f_y((y_s - y_p), \omega_s, dt) = 0 \quad (4.2)$$

$$m_p \ddot{x}_p + c_p \dot{x}_p + k_p(x_p) - f_x((x_s - x_p), \omega_s, dt) = 0 \quad (4.3)$$

$$m_p \ddot{y}_p + c_p \dot{y}_p + k_p(y_p) - f_y((y_s - y_p), \omega_s, dt) = 0 \quad (4.4)$$

The overall forces (f_x, f_y) on the shaft in the two orthogonal directions (x, y) can be obtained by summing the contact forces on each of the rolling elements (Figure 4.2)



D_b : ball diameter, D_p : pitch diameter, n_b : number of rolling elements

c : radial clearance, α : load angle

Figure 4.2 Two degree of freedom model (Liew et al., 2002)

The overall contact deformation (compression) δ_j for the j^{th} rolling element can be expressed in terms of inner race displacement relative to the outer race (in both the x and y directions), the time varying element position ϕ_j , clearance c , fault switch β_j , and defect depth C_d .

$$\delta_j = (x_s - x_p) \cos \phi_j + (y_s - y_p) \sin \phi_j - c - \beta_j C_d \quad (4.5)$$

Since the compression occurs only when δ_j is positive, a contact state γ_j (of δ_j rolling element) is introduced as:

$$\gamma_j = \begin{cases} 1, & \text{if } \delta_j > 0 \\ 0, & \text{otherwise} \end{cases} \quad (4.6)$$

The angular positions of the rolling elements ϕ_j , are functions of previous cage position ϕ_0 , cage speed ω_c (calculated from geometry and shaft speed ω_s assuming no slippage) and time increment dt .

$$\phi_j = \frac{2\pi(j-1)}{n_b} + \omega_c dt + \phi_0 \quad (4.7)$$

$$\omega_c = \left(1 - \frac{D_b}{D_p}\right) \frac{\omega_s}{2} \quad (4.8)$$

Using Hertzian theory for non-linear stiffness, the ball raceway contact force is given by

$$f = k_b \delta^n \quad (4.9)$$

where, k_b = load deflection factor, depends on the contact geometry and the elastic contacts of the material, and exponent $n = 1.5$ for ball bearings and 1.1 for roller bearings. The units of k_b depend on the units used e.g. N/mⁿ.

The total force for a ball bearing with n_b balls can be calculated by summing the contact forces in the x and y directions and is given by:

$$f_x = k_b \sum_{j=1}^{n_b} \gamma_j \delta_j^{1.5} \cos \phi_j \quad (4.10)$$

$$f_y = k_b \sum_{j=1}^{n_b} \gamma_j \delta_j^{1.5} \sin \phi_j \quad (4.11)$$

4.2.2 Modelling of bearing localised fault (inner/outer race)

The localised faults in the bearing inner and outer race are defined using a fault switch β_j . The switch indicates the loss of contact when a rolling element passes over a spall of

depth (C_d) at a defined angular position (ϕ_d) over an angular distance of $\Delta\phi_d$ (Figure 4.3).

$$\beta_j = \begin{cases} 1, & \text{if } \phi_d < \phi_j < \phi_d + \Delta\phi_d \\ 0, & \text{otherwise} \end{cases} \quad (4.12)$$

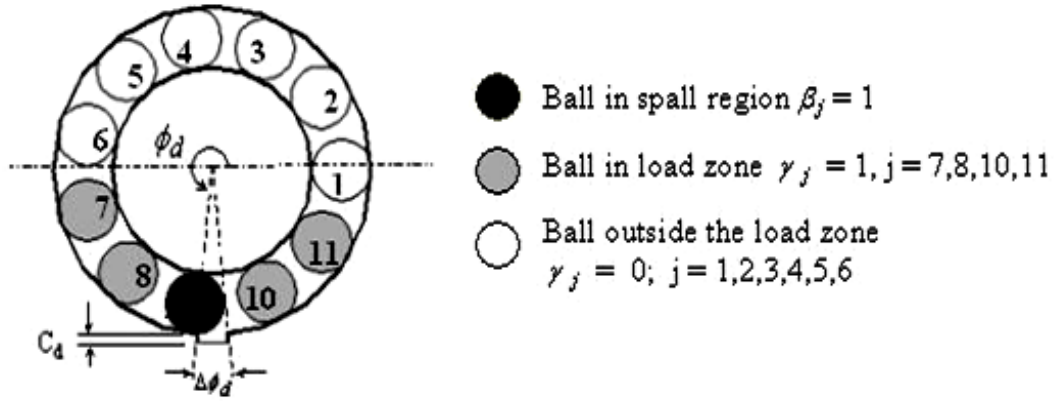


Figure 4.3 Localised fault on outer race (Sawalhi, 2007)

The location of outer race fault is fixed in the load zone (between ϕ_d and $\phi_d + \Delta\phi_d$), whereas the inner race fault rotates at the shaft speed ω_s and is given by:

$$\phi_d = \omega_s t + \phi_{d0} \quad (4.13)$$

where ϕ_{d0} is the initial starting location of the spall.

The validity of vibration signals obtained from the seeded bearing faults depends on the realistic representation of the fault geometry in the simulation. The earlier models (Figure 4.4 (a)) assumed sudden loss of contact as the rolling element entered the spall region and instant regaining of the contact when exiting the fault resulting in a large impulsive force (Feng et al., 2002). In an attempt to model arbitrary fault geometries, in particular for extended faults, the geometry was specified as a function of roll angle by defining the depth of the spall as a function of rolling element position, and this was attempted for local faults (Sawalhi and Randall, 2010) but modelling errors were later discovered. In fact, these models resulted in two impulses which were incorrectly believed to be the fault entry and exit, and it was subsequently found that the spacing

between the two impulses was not related to the fault width (Sawalhi and Randall, 2011). The dynamic model analysed in this paper includes a further update of the fault geometry where the curvature at both the entry and exit corresponds to the radius of the rolling element as shown in Figure 4.4 (b). The depth of the spall (localised inner and outer race) was scaled to allow for the local deformation of the sharp edge or wear of the fault. The sudden change in direction occurs at the fault exit when the ball is halfway through the spall.



(a) Fault geometry – earlier simulations. (b) Updated fault geometry.

Figure 4.4 Spall geometry – Localised bearing faults

4.2.3 Modelling of bearing extended fault (inner/outer race)

During operation of a bearing the localised faults become extended by progressive fatigue and then they smoothen by the successive passage of the rolling elements so that the faults extend beyond the spacing between two rolling elements. These ‘smooth extended faults’ do not necessarily generate sharp impulses and hence the envelope analysis technique may fail to detect the fault frequencies (Antoni and Randall, 2002).

An extended fault geometry as defined by Sawalhi was adapted in this research to describe a rough surface topography (Sawalhi, 2007). The procedure consists of generating Gaussian noise scaled to the required surface roughness, low pass filtering to fit the radius of the rolling element to the profile of the surface waviness and superimposing it on a bucket shaped surface to provide smooth entry and exit. The resulting topography of the rough surface, shown in Figure 4.5, still does not allow for smooth entry and exit of the rolling elements. The depth of the spall was scaled so as to achieve the smooth topography for both the extended inner and outer race faults.

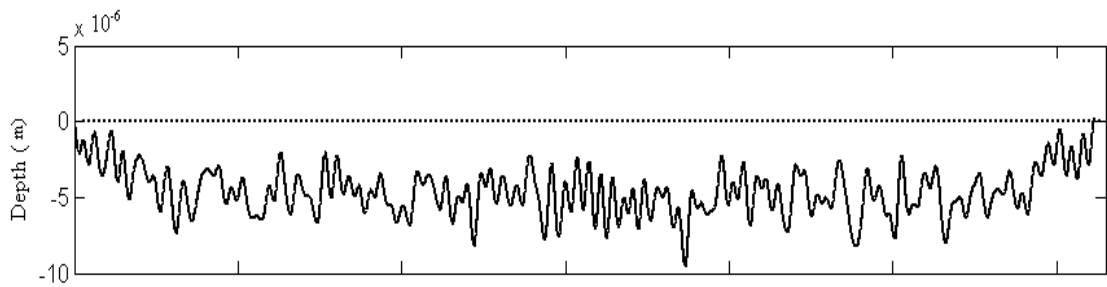


Figure 4.5 Rough surface topography representing the extended faults in bearing
(Sawalhi, 2007)

4.2.4 Gear Dynamics

The gear dynamic model incorporated into the LPM of the internals is based on the model developed by Endo to simulate the gear faults (Endo, 2005). The LPM of the pinion and gear pair can be modelled as cylindrical inertias connected by the position dependent stiffness variable $k_m(\theta)$, the damping coefficient C_m , and the geometric transmission error (GTE) of the gear pair $e_t(\theta)$ and is shown in Figure 4.6.

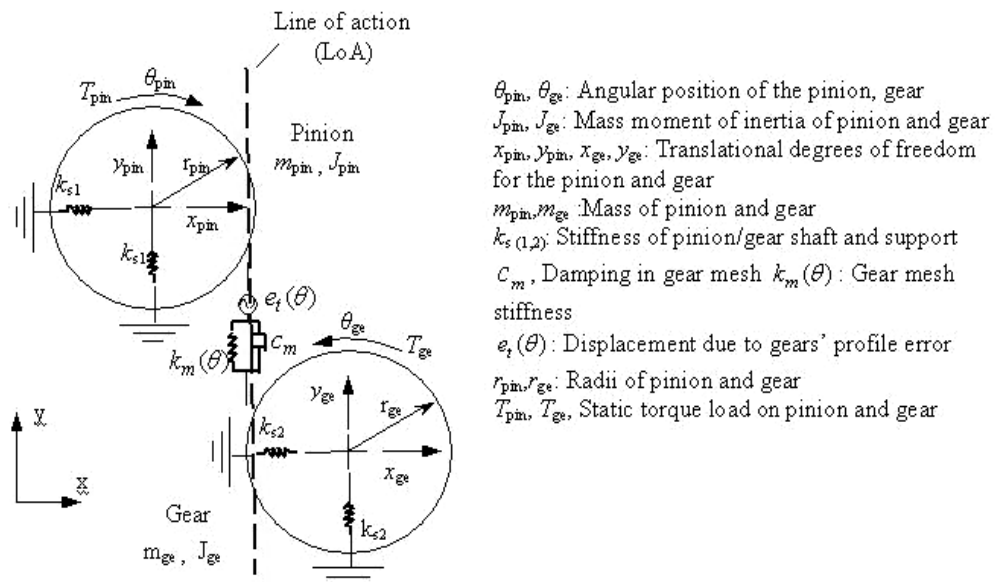


Figure 4.6 LPM of the pinion and the gear (Endo, 2005)

In the current simulation, $e_t(\theta)$ represents the combined effect of runout error, tooth profile error and an error term (or noise). The error term accounts for the variation of torque on the transmission error (TE) and higher TE harmonics in the model.

$$e_t(\theta) = e_{runout} + e_{toothprofile} + error\ term \quad (4.14)$$

$$Runout\ error \quad e_{runout} = 30 \times 10^{-6} \sin\left(\frac{2\pi t}{T} + \phi_k\right) \quad (4.15)$$

$$Tooth\ profile\ error \quad e_{toothprofile} = 15 \times 10^{-6} \sin\left(\frac{2\pi tN}{T} + \phi_k\right) \quad (4.16)$$

$$error\ term = 0.2 \times 10^{-6} randn \quad (4.17)$$

where: N : number of teeth on a gear

T : shaft rotational speed

ϕ_k : phase difference

The gearmesh stiffness $k_m(\theta)$ which represents the load and position dependent nonlinearity (due to the effect of Hertzian contact between the meshing gear teeth) was obtained by static simulation (Endo, 2005). Both $e_t(\theta)$ and $k_m(\theta)$ were included in the dynamic model in the form of a look-up table. Friction forces at the gearmesh were neglected and the gearmesh was considered to be free from contact loss as the gears were assumed to operate under sufficient load.

The gear model has six degrees of freedom – two rotational (θ_{pin} , θ_{ge}) and four translational (x_{pin} , y_{pin} , x_{ge} , y_{ge}). The dynamic equations of motion for the rotational and translational DOFs along the line of action (LoA) are given by:

$$m_i \ddot{y}_i + k_{si} y_i - c_m (r_2 \dot{\theta}_2 - r_1 \dot{\theta}_1 - \dot{x}_2 + \dot{x}_1 + \dot{e}_t) - k_m r_i (r_2 \theta_2 - r_1 \theta_1 - x_2 + x_1 + e_t) = 0 \quad (4.18)$$

$$J_i \ddot{\theta} + c_m r_i (r_2 \dot{\theta}_2 - r_1 \dot{\theta}_1 - \dot{x}_2 + \dot{x}_1 + \dot{e}_t) + k_m r_i (r_2 \theta_2 - r_1 \theta_1 - x_2 + x_1 + e_t) = T_i \quad (4.19)$$

where $i = 1, 2$ (1 for gear, 2 for pinion)

4.2.5 LPM of gearbox internals

Figure 4.7 shows the 34 DOF LPM of the gearbox test rig (Sawalhi and Randall, 2008a). Based on this model, a dynamic model of the gearbox internals with 22 DOFs

was created by removing three DOFs at each of the four bearings (corresponding to two pedestal DOFs in the x and y direction and a mass/spring system in the y direction). The model is based on the following assumptions (Sawalhi and Randall, 2008a):

- Shaft mass and inertia are lumped at the bearings or at the gears
- Translational degrees of freedom are considered along the line of action (LoA) and perpendicular to it, with the LoA aligned vertically.
- Static transmission error of the gears (geometric and elastic) is included.
- Friction between the gear teeth is neglected.
- The gearmesh is assumed free of contact loss.
- The bearing stiffness is non-linear and time varying.
- Rolling element inertia is ignored.
- There are no contact surface imperfections apart from the inner race and outer race localised and extended defects.
- Linear damping is applicable.

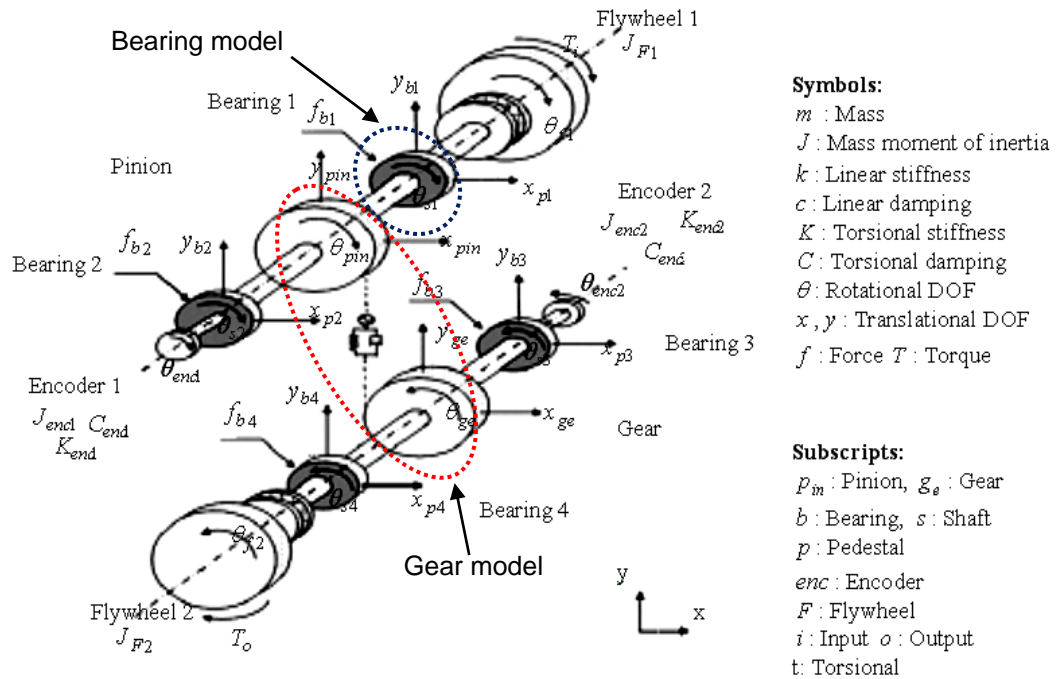


Figure 4.7 34 DOF LPM of the gearbox test rig (Sawalhi, 2007)

The translational and rotational equations of motion can be written as:

$$M\ddot{x} + c\dot{x} + kx = F_x \quad (4.20)$$

$$M\ddot{y} + c\dot{y} + ky = F_y \quad (4.21)$$

$$J\ddot{\theta} + C\dot{\theta} + K\theta = T \quad (4.22)$$

There are 22 DOFs in the LPM of the internals with 10 rotational DOFs and 12 translational DOFs. These internal DOFs are combined with casing DOFs (after reduction) to create a combined LPM-reduced FEM model as described in the following sections. The details of input parameters, system matrices and the Simulink block diagrams are given in Appendix A.

4.3 Reduced FE model of the casing

A detailed FE model of the gearbox casing was described in Chapter 3 and is reproduced again in Figure 4.8. This FE model of the casing is deployed in the dynamic simulation models of the UNSW gearbox test rig and is an updated version created by correlating the FE model with the results of Experimental Modal Analysis (EMA) described in Chapter 3.

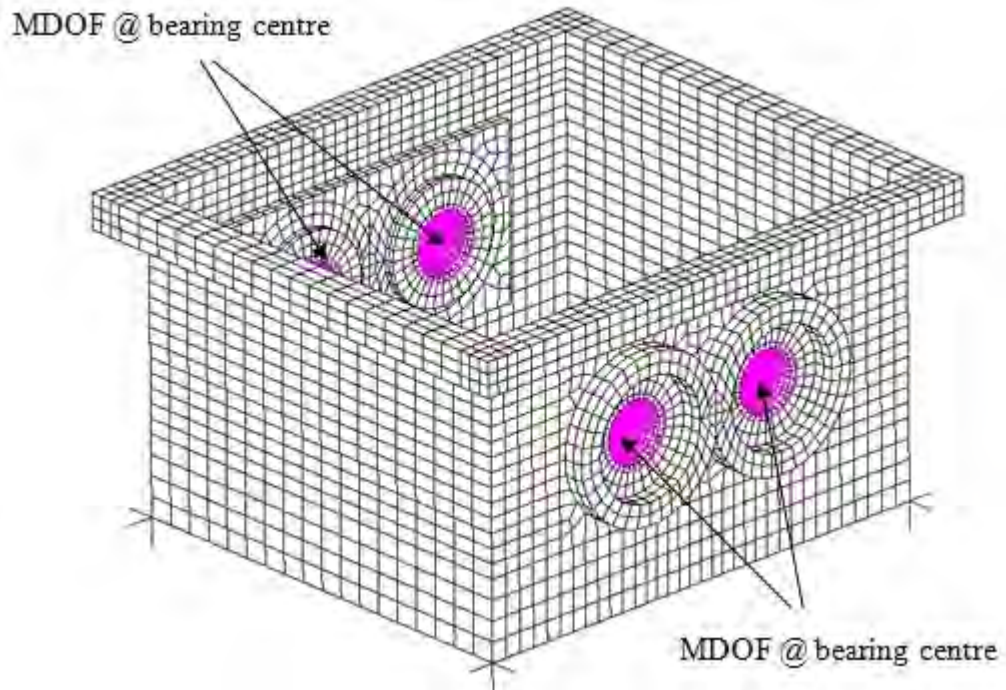


Figure 4.8 FE model of gearbox casing

4.3.1 Craig-Bampton method of CMS

An overview of model reduction techniques was provided in the literature review (Chapter 2). The Craig-Bampton method of component mode synthesis provides a relatively simple way of coupling the components and the ease of adding the additional modal coordinates depending on the frequency range of interest. The method produces highly accurate models with relatively few component modes and hence is widely used in a number of commercial finite element codes (Qu, 2004). Hence, the Craig-Bampton method is implemented in the current research to create the reduced models of the gearbox casing and its internal components.

The Craig-Bampton method (Craig and Bampton, 1968) is a dynamic reduction method used to reduce the size of the finite element models. In this method, the motion of the whole structure is represented as a combination of boundary points (so called master degrees of freedom) and modes of the structure assuming the master degrees of freedom are held fixed. Unlike Guyan reduction (Guyan, 1965), which only accounts for the stiffness matrix, Craig-Bampton accounts for both the mass and stiffness. Furthermore, it enables defining the frequency range of interest by identifying the modes of interest and including these as a part of the transform matrix. The decomposition of the model into both physical DOFs (master DOFs) and modal coordinates allows the flexibility of connecting the finite elements to other substructures, while maintaining a reasonably good result within a required frequency range. In the current application it is very convenient, as the excitation is not from forces, but from geometric mismatch at the connection points (gear transmission error and bearing geometric error). (Note that the Craig-Bampton “modes” are not the same as the final modes of the whole combined structure, but the differences in frequency are primarily at the low order modes, whereas the frequencies of high order modes are much less affected by the boundary conditions, and the *upper* C-B mode frequencies can be used as a good indication of frequency range.)

Earlier simulations (Sawalhi et al., 2011, Deshpande et al., 2012b, Deshpande et al., 2012a, Deshpande et al., 2013) also found the Craig-Bampton method of model reduction most suitable due to its ability to generate a combined (hybrid) model valid up

to a specific maximum frequency of interest. Physical (spatial) coordinates are used to define the non-linear and time varying interactions between the internals and the casing. These are combined with the modal coordinates of the remaining slave DOFs, resulting in a greatly reduced dynamic model which can be easily expanded to a higher frequency range by increasing the number of modes.

The Craig-Bampton methodology as described in (Gordan, 2008) and (Carmignani et al., 2009) is summarised below.

In the Craig-Bampton reduction method, the equation of motion (dynamic equilibrium) of each superelement (substructure), without considering the effect of damping, can be expressed as in Eqn. (4.22):

$$[M]\{\ddot{u}\} + [k]\{u\} = \{F\} \quad (4.23)$$

where $[M]$ is the mass matrix, $[k]$ is the stiffness matrix, $\{F\}$ is the nodal forces,

$\{u\}$ and $\{\ddot{u}\}$ are the nodal displacements and accelerations respectively.

The key to reducing the substructure is to split the degrees of freedom into master $\{u_m\}$ (at the connecting nodes) and slaves $\{u_s\}$ (at the internal nodes). The mass, the stiffness and the force matrices are re-arranged accordingly as follows:

$$\overbrace{\begin{bmatrix} M_{mm} & M_{ms} \\ M_{sm} & M_{ss} \end{bmatrix}}^M \begin{Bmatrix} \ddot{u}_m \\ \ddot{u}_s \end{Bmatrix} + \overbrace{\begin{bmatrix} k_{mm} & k_{ms} \\ k_{sm} & k_{ss} \end{bmatrix}}^k \begin{Bmatrix} u_m \\ u_s \end{Bmatrix} = \begin{Bmatrix} F_m \\ 0 \end{Bmatrix} \quad (4.24)$$

The subscript m denotes master, s denotes slave. Furthermore, the slave degrees of freedom (internals) can be written using generalized coordinates - modal coordinates (q) using the fixed interface method, i.e. using the mode shapes of the superelement by fixing the master degrees of freedom nodes (connecting/boundary nodes). The transformation matrix (T) is the one that achieves the following:

$$\begin{Bmatrix} u_m \\ u_s \end{Bmatrix} = T \begin{Bmatrix} u_m \\ q \end{Bmatrix} \quad (4.25)$$

For the fixed interface method, the transformation matrix (T) can be expressed as shown in Eqn. (4.26):

$$T = \begin{bmatrix} I & 0 \\ G_{sm} & \phi_s \end{bmatrix} \quad (4.26)$$

where,

$$G_{sm} = -k_{ss}^{-1} k_{sm} \quad (4.27)$$

and ϕ_s is the modal matrix of the internal DOF with the interfaces fixed.

Applying this transformation, the number of DOF of the component will be reduced. The new reduced mass and stiffness matrices can be extracted using Eqns (4.28) and (4.29) respectively:

$$M_{reduced} = T^t M T \quad (4.28)$$

and

$$k_{reduced} = T^t k T \quad (4.29)$$

Thus Eqn (4.24) can be re-written in the new reduced form using the reduced mass and stiffness matrices as well as the modal coordinates as follows:

$$\overbrace{\begin{bmatrix} M_{bb} & M_{bq} \\ M_{qb} & M_{qq} \end{bmatrix}}^{M_{reduced}} \begin{Bmatrix} \ddot{u}_m \\ \ddot{q} \end{Bmatrix} + \overbrace{\begin{bmatrix} k_{bb} & 0 \\ 0 & k_{qq} \end{bmatrix}}^{k_{reduced}} \begin{Bmatrix} u_m \\ q \end{Bmatrix} = \overbrace{\begin{Bmatrix} F_m \\ 0 \end{Bmatrix}}^{F_{reduced}} \quad (4.30)$$

where M_{bb} is the boundary mass matrix i.e. total mass properties translated to the boundary points.

k_{bb} is the interface stiffness matrix i.e. stiffness associated with displacing one boundary DOF while the others are held fixed.

M_{bq} is the component matrix (M_{qb} is the transpose of M_{bq})

If the mode shapes have been mass normalized (typically they are) then:

$$k_{qq} = \begin{bmatrix} \backslash & & 0 \\ & \lambda_i & \\ 0 & & \backslash \end{bmatrix} \quad (4.31)$$

where λ_i is the eigenvalues; $\lambda_i = k_i / m_i = \omega_i^2$

and,

$$M_{qq} = \begin{bmatrix} \backslash & & 0 \\ & I & \\ 0 & & \backslash \end{bmatrix} \quad (4.32)$$

Finally the dynamic equation of motion (including damping) using the Craig-Bampton transform can be written as:

$$\begin{bmatrix} M_{bb} & M_{bq} \\ M_{qb} & I \end{bmatrix} \begin{Bmatrix} \ddot{u}_m \\ \ddot{q} \end{Bmatrix} + \begin{bmatrix} 0 & 0 \\ 0 & 2\zeta\omega \end{bmatrix} \begin{Bmatrix} \dot{u}_m \\ \dot{q} \end{Bmatrix} + \begin{bmatrix} k_{bb} & 0 \\ 0 & \omega^2 \end{bmatrix} \begin{Bmatrix} u_m \\ q \end{Bmatrix} = \begin{Bmatrix} F_m \\ 0 \end{Bmatrix} \quad (4.33)$$

where $2\zeta\omega$ = modal damping (ζ = fraction of critical damping).

4.3.2 Implementation of Craig-Bampton reduction method

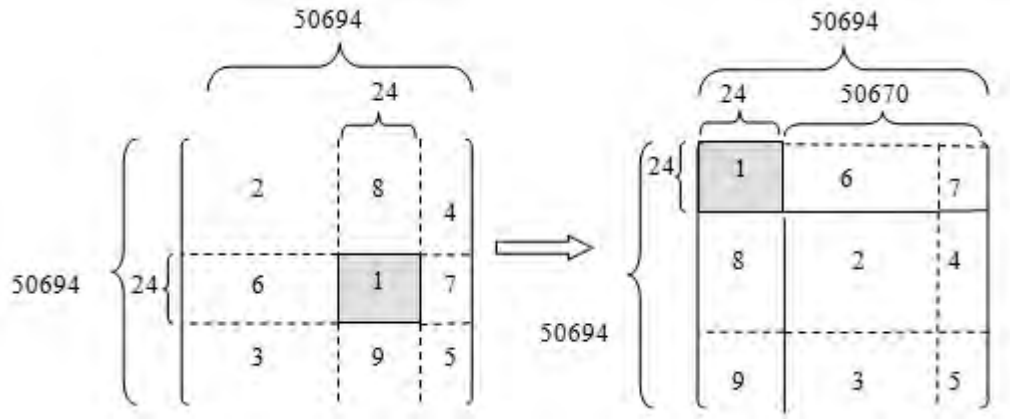
The finite element model of the UNSW gearbox shown in Figure 4.8 has 50694 DOFs. Thus the mass matrix $[M]$ and the stiffness matrix $[k]$ are square matrices of size 50694×50694 . The centre nodes of the four bearings in the casing FE model were selected as master degrees of freedom which allow the connection between the reduced casing model and the LPM using time varying nonlinear springs representing the bearings. The

system is excited by the time-varying parameters and geometric mismatch (in particular from faults) in these bearings.

With 6 DOFs at each bearing centre node, there are 24 master degrees of freedom (boundary DOFs). By selecting the first 100 modes (modes up to 4.4 kHz), the reduced model will have mass and stiffness matrices $[M_{reduced}]$ and $[k_{reduced}]$ of size 124×124 i.e. 24 boundary coordinates and 100 modes (or generalised coordinates). Although the simulation model is only fully valid up to 4 kHz based on the number of modal coordinates included in the model, the selected frequency range is found to be adequate to study the gear/bearing interaction in the frequency range below 5 kHz.

The process of obtaining the reduced mass and stiffness matrices has been done on a step-by-step basis using FEMtools® - a general purpose FEA, dynamic and model updating software (DDS, 2012) and Matlab® as follows:

1. The mass matrix $[M]$ and stiffness matrix $[K]$ (both in binary format) were extracted from the FEMtools® finite element package and imported into Matlab® as *sparse* matrices. Since the size of the individual matrix is 50694×50694 , it is practically impossible to work with such a size of matrix in Matlab®, without using the sparse matrix formulation.
2. $[M]$ and $[K]$ were rearranged to have the master degrees of freedom (24×24) in the upper left hand corner of the matrix, and the slaves (50670×50670) in the lower right hand corner. Figure 4.9 illustrates the re-arrangement applied to both the mass and the stiffness matrices.



Matrix 1: Master degrees of freedom [M_{mm} for mass and k_{mm} for stiffness]

Matrices 6, 7: component matrix [M_{ms} for mass and k_{ms} for stiffness]

Matrices 8, 9 : inverse [M_{ms} for mass and k_{ms} for stiffness]

Matrices 2, 4, 3, 5: Slave degrees of freedom [M_{ss} for mass and k_{ss} for stiffness]

Figure 4.9 Rearranging the extracted mass and stiffness matrices

This rearrangement (Figure 4.10) gives an order equivalent to the one shown in Eqn. 4.24.

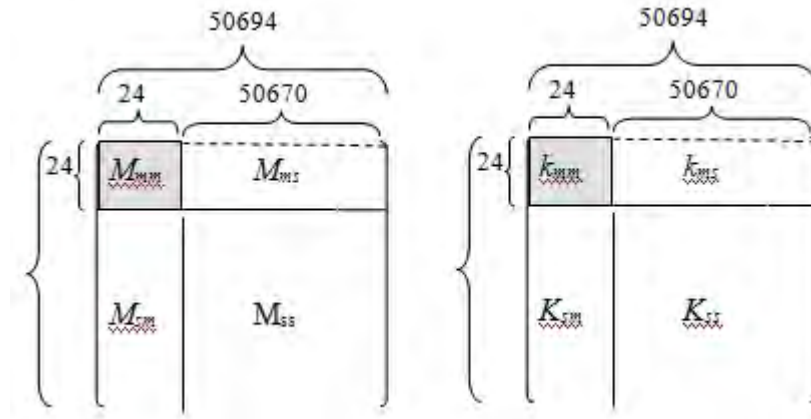


Figure 4.10 Rearranged mass and stiffness matrices

- After rearranging the mass and stiffness matrices as shown in Figure 4.10, the G_{sm} matrix (Eqn. 4.27) was calculated. The size of G_{sm} is 50670×24 .

4. The ϕ_s matrix (mode shapes of the gearbox with fixed master degrees of freedom) was extracted from FEMtools®. Each mode shape was placed in a vector, thus the size of ϕ_s is 50670×100 (Slave degrees of freedom \times the number of retained modes)
5. The T matrix was formed using Eqn. 4.26.
6. The reduced mass and stiffness matrices (124×124) were found using Eqns. 4.28 and 4.29 respectively. However, the off-diagonal zeros as observed in Eqns. 4.31, 4.32 and 4.33 have to be enforced as the direct calculations resulted in values of order 10^{-8} to 10^{-16} (practically zeros). Keeping these values affects the stability of the solution and in particular gives a near singular inverse mass matrix.

4.3.3 Combined model (LPM- reduced FEM)

The LPM consisted of 22 DOFs corresponding to the gearbox internals (such as shafts, gears and bearings) and flywheels and encoders which were attached to the input and output shafts. The greatly reduced mass and stiffness matrices of the casing (obtained using the Craig-Bampton method of component mode synthesis as described in the previous section) were combined with the LPM model in the Matlab/Simulink® environment to create a combined LPM-reduced updated FE model. The full casing model had 50694 DOFs whereas the reduced casing model had only 124 DOFs which were made up of 24 master DOFs corresponding to 4 bearing centre nodes (each with 6 DOFs) plus 100 modes with master DOFs fixed. The resulting combined model had a total of 146 DOFs (46 physical DOFs and 100 modal or generalised coordinates extending to 4 kHz). The modal damping ($\zeta = 4\%$) was introduced in the model (Eqn. 4.33). The equations of motion were redefined at the bearing/casing connection points and the combined 146 DOF model (LPM + reduced FEA) was solved to obtain the vibration signals in the presence of bearing faults.

The model was then solved and the forces and acceleration responses were obtained. Eqn. 4.25 was used to expand both the physical and the modal responses back to the slave degrees of freedom. This gives a combination of both the physical response from

the master degrees of freedom and the modal coordinates, which can be achieved by combining Eqns. 4.25 and 4.26 as follows:

$$\begin{Bmatrix} u_m \\ u_s \end{Bmatrix} = \begin{bmatrix} I & 0 \\ G_{sm} & \phi_s \end{bmatrix} \begin{Bmatrix} u_m \\ q \end{Bmatrix} \quad (4.34)$$

The responses at the slave degrees of freedom (such as at the accelerometer position) can be obtained using equation 4.35 as follows:

$$u_s = G_{sm} u_m + \phi_s q \quad (4.35)$$

4.4 Full reduced model of gear test rig (182 DOF model)

The modelling approach using the combined LPM and the reduced FE model of the casing (146 DOF model) was described in Section 4.3.3. The combined model was found to be capable of simulating the localised (inner and outer race) faults as well as the extended (inner and outer race) faults in the bearing. Although the combined 146 DOF model does take into account the flexibility of the casing however, the use of the LPM approach to characterize the gearbox internals (shafts, gears, bearings etc) results in a significantly lower number of DOFs to fully describe the dynamic behaviour of the internals. This limited representation of the modes of the internals seemed to contribute to the poor spectral matching over a wide frequency range. Hence it was decided to further improve the 146 DOF model by using a full reduced model of the gearbox which would properly represent the interaction of the bearing fault frequency with the gearmesh especially in the case of the extended faults.

This section describes an updated simulation model where a finite element model reduction technique based on the Craig-Bampton method of component mode synthesis (CMS), described earlier in this chapter, was used to extract the greatly reduced mass and stiffness matrices of not only the gearbox casing but also of the gearbox internal components based on the frequency range of interest. The extracted mass and stiffness matrices were imported into Matlab/Simulink® to develop the dynamic model of the UNSW gearbox test rig. The resulting model has a total of 182 degrees-of-freedom and also has the capability of simulating time varying stiffness nonlinearities and geometric

faults in gears and bearings. The simulation model contains more degrees of freedom (DOFs) for the gearbox internals as compared with the 34 DOF LPM and the 146 DOF combined model in addition to large number of casing modes. The methodology to develop the full reduced model (182 DOF) is described in the following sections.

4.4.1 Methodology: Full reduced model

The dynamic simulation model presented in this section is created by replacing the LPM part of the combined model with the reduced FE model of the gearbox internals which in turn is assembled with the previously generated reduced FE model of the casing Figure 4.8.

A finite element model of the gearbox internals comprising input and output shafts, gears, bearings as well as flywheels and encoders was created using MSC/Patran and Nastran version 2010 (MSC, 2010). The shafts were modelled with beam elements and gears with shell elements. Rigid body elements were used to connect the gears to the shafts and the bearings to the casing. Flywheels and encoders were modelled using inertial elements with appropriate inertial properties and connected to the shafts with torsional springs (their lateral motions were not modelled). The gearbox casing was mounted on rubber pads which were modelled as spring elements. The shaft diameter (where the coupling is located) was adjusted so as to provide an equivalent rotational inertia of the coupling. Before reduction, the FE model of the casing had 50694 DOFs whereas the gearbox internals (input and output shaft gear assembly with flywheels and encoders) had 1680 DOFs. The FE model of the gearbox internals is shown in Figure 4.11. The details of the corresponding mass, inertia and stiffness properties are given in Appendix B.

Master degrees of freedom (MDOFs) must be specified in order to create reduced FE models of the gearbox internals. Twenty four MDOFs were selected for the casing (at the bearing centre nodes similar to the 146 DOF model) and sixteen for the gearbox internals. The MDOF set mainly included the degrees-of-freedom associated with the nodes corresponding to the bearing centre points, shaft gear connection points, flywheels, and gearmesh locations. The MDOFs were selected so as to enable

connection of the reduced model of the internals with the reduced model of the casing and to capture the flexibility of both the internal components and the casing. The locations of the selected master DOFs in case of gearbox internals is shown in Figure 4.11 and the corresponding degrees of freedom are tabulated in Appendix B.

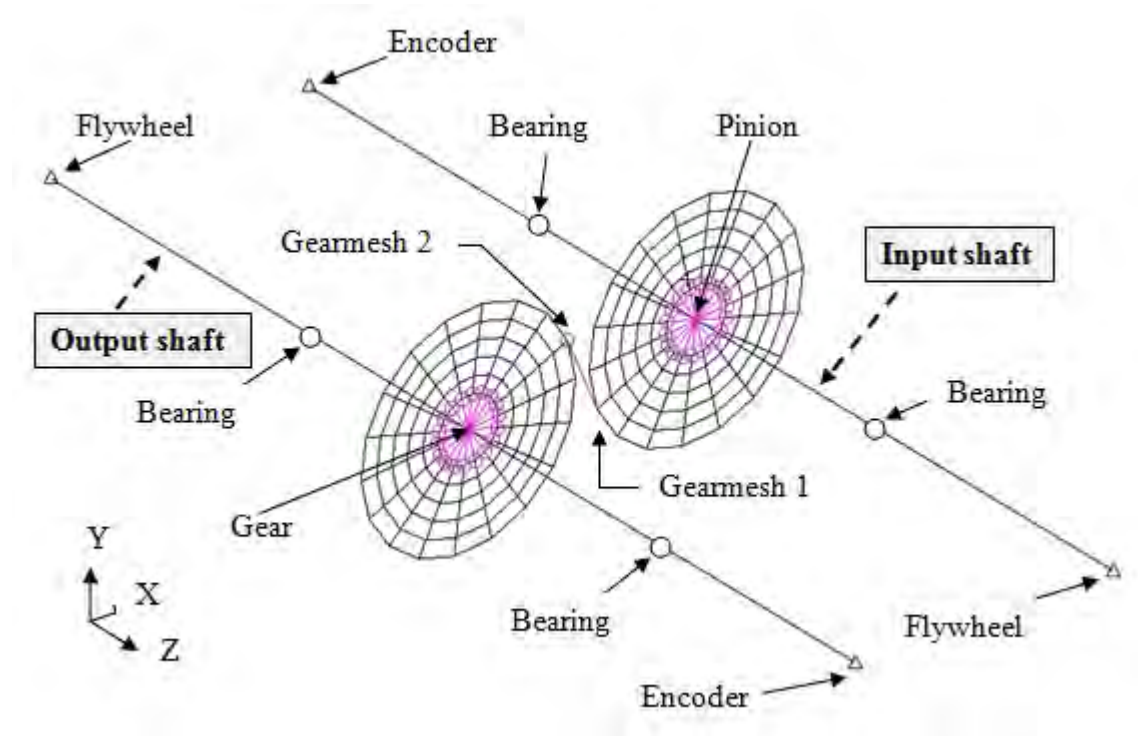


Figure 4.11 FE model of gearbox internals

4.4.2 Reduced dynamic model (full FEM reduction)

The theoretical background of the finite element model reduction technique based on the Craig-Bampton (CB) method of Component Mode Synthesis (CMS) and its implementation to develop a reduced FE model of the gearbox casing was described in Section 4.3.1 and 4.3.2. The Craig-Bampton method of CMS was further implemented to generate the reduced FE model of the entire gearbox test rig which was created by assembling the two subsystems namely:

- Reduced FE model of the gearbox internals
- Reduced FE model of the gearbox casing

The summary of DOFs of the full reduced model (182 DOFs) is shown in Table 4.1. The generalised coordinates based on the selected number of modes correspond to a frequency range of 8.7 kHz for the internals and 4.4 kHz for the casing, which is found to be adequate to study the gear/bearing interaction in the frequency range below 5 kHz.

Table 4.1 Full reduced FE model - summary of DOFs

Reduced FE model	Physical coordinates (MDOFs)	Generalised (modal) coordinates	Total DOFs
Gearbox internals	16	42	58
Casing	24	100	124
Entire gear box	40	142	182

The reduced FE model of the entire gear box had a total of 182 DOFs with 40 physical (masters) and 142 modal coordinates. The mass and stiffness matrices of the internals and the casing were assembled in Matlab/Simulink® environment as shown in Figure 4.12.

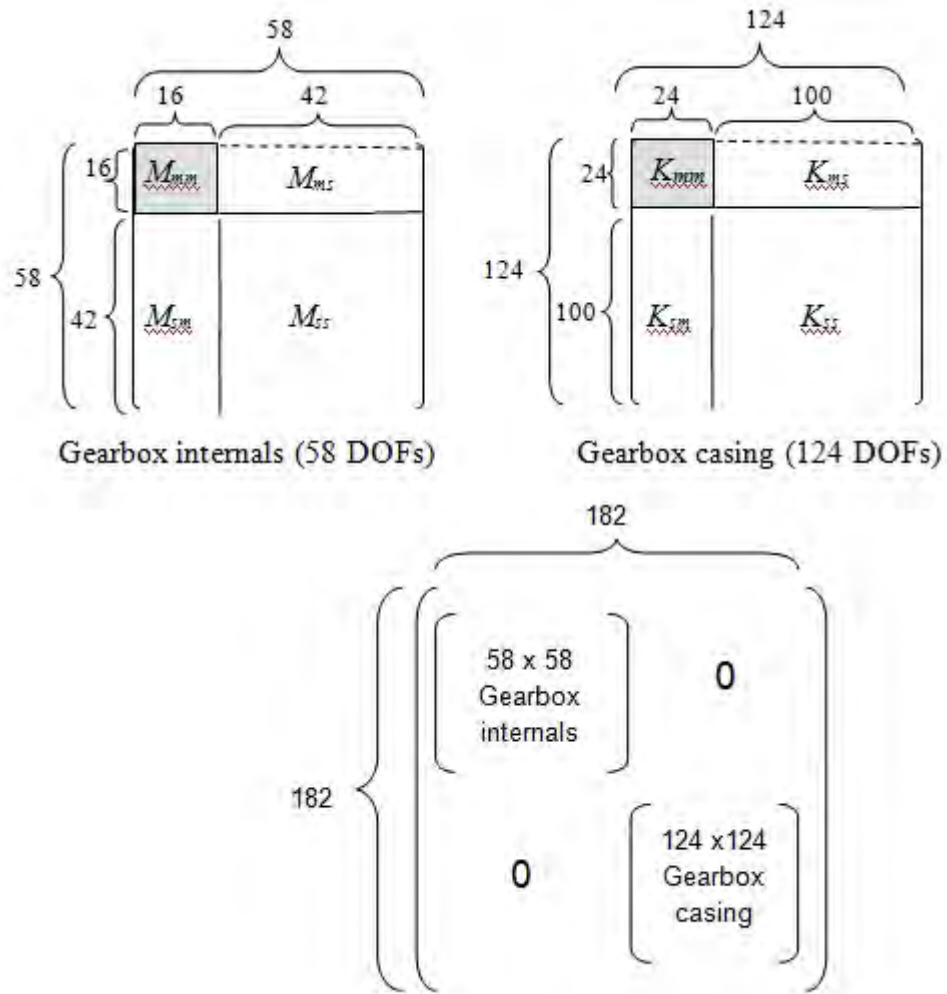


Figure 4.12 CMS reduction of full FE model of gearbox (182 DOFs)

The total response of the 182 DOF model now includes contributions due to the flexibility and dynamics of both the internals and the casing. The simulation model contains more DOFs for the internals as compared with the LPM model, in addition to a large number of casing modes. The full reduced model of the entire gear test rig was used to simulate the localised and extended faults in the bearing inner and outer race.

4.4.3 Modelling of bearing faults

The fault geometries inserted in the 182 DOF (full reduced) model are identical to those used in the 146 DOF (combined LPM-reduced FEM) model. The details of the fault

geometries for the localised and extended bearing faults (in the inner and outer race) are described in Sections 4.2.2 and 4.2.3.

4.5 Simulink models

The dynamic models (146 and 182 D OF) were simulated in the Matlab/Simulink environment and the equations of motion were solved using the ordinary differential equation solver ODE45 which is based on the 4th order Runge-Kutta method. The simulations were carried out under 50 Nm load at 10 Hz constant shaft frequency. A special Matlab S-function was used to represent the bearing model (with and without fault) whereas a look-up table was used to include the load dependent non-linearity of the gearmesh stiffness (Endo, 2005).

The details of both the Simulink models along with the block diagrams are given in Appendices A and B.

4.6 Summary

In the past, researchers have been able to simulate gear/bearing faults using the dynamic models of a machine structure such as a gearbox. Most of these models were based on the lumped parameter modelling approach and either completely ignored the effects of the gearbox casing or included a simplified version of it built into the model. However, these models were found to be inadequate in the mid-frequency region where gearmesh forces and the dynamic properties of the casing interact. In the case of light weight structures such as a helicopter gearbox, the low flexural frequencies of some components, especially those of the casing, cannot be ignored in the system dynamic model.

The development of an improved dynamic simulation method is presented in this chapter, wherein a finite element model reduction technique based on the Craig-Bampton method of component mode synthesis (CMS) is implemented. Two different models were developed, namely, the 146 D OF (combined LPM-reduced FEM of casing) and 182 D OF (full reduced FEM of gearbox) are presented. The proposed methodology enables the inclusion of more accurate casing characteristics in the

dynamic model up to a specified frequency of interest, thereby improving the predictions over a wide frequency range.

The dynamic model was solved interactively to obtain simulated vibration signals in the presence of localised and extended faults in the bearing inner and outer race. The results of the simulation and the comparison with the experimental measurements are discussed in Chapter 5.

4.7 References

- Antoni, J & Randall, RB 2002. Differential Diagnosis of Gear and Bearing Faults. *Journal of Vibration and Acoustics*, 124, 165-171.
- Carmignani, C, Forte, P & Melani, G 2009. Component modal synthesis modeling of a gearbox for vibration monitoring simulation. *The Sixth International Conference on Condition Monitoring and Machinery Failure Prevention Technologies*. Dublin, Ireland.
- Craig, R & Bampton, M 1968. Coupling of substructures for dynamic analysis *Amer. Inst. Aero. Astro. J.*, 6, 1313–1319.
- DDS 2012. (Dynamic Design Solutions N.V.), FEMtools Version 3.6.
- Deshpande, L, Sawalhi, N & Randall, RB 2012a. Gearbox bearing fault simulation using a finite element model reduction technique. *25th International Congress on Condition Monitoring and Diagnostic Engineering Management*. Huddersfield, UK.
- Deshpande, L, Sawalhi, N & Randall, RB 2012b. Improved simulation of bearing faults using a finite element model reduction technique. *The Ninth International Conference on Condition Monitoring and Machinery Failure Prevention Technologies*. London, UK.

- Deshpande, LG, Sawalhi, NM & Randall, RB 2013. Application of finite element model updating and reduction techniques to simulate gearbox bearing faults. *Australian Journal of Multi-Disciplinary Engineering*, Vol 10 No 2, 1-12.
- Du, S. 1997. *Dynamic modelling and simulation of gear transmission error for gearbox vibration analysis*. Ph.D. Dissertation, University of New South Wales, Sydney, Australia.
- Endo, H. 2005. *Simulation of gear faults and its application to the development of differential diagnostic technique* Ph. D. Dissertation, University of New South Wales, Sydney, Australia.
- Feng, NS, Hahn, EJ & Randall, RB 2002. Using transient analysis software to simulate vibration signals due to rolling element bearing defects. *3rd Australasian Congress on Applied Mechanics*. Sydney, Australia.
- Gordan, S 2008. *FEMCI the book*: http://femci.gsfc.nasa.gov/craig_bampton/index.html
- Guyan, RJ 1965. Reduction of stiffness and mass matrices. *AIAA Journal*, 30, 772-780.
- Ho, D. 1999. *Bearing diagnostics and self-adaptive noise cancellation*. Ph.D. Dissertation, University of New South Wales, Sydney, Australia.
- Liew, A, Feng, NS & Hahn, EJ 2002. Transient rolling element bearing systems. *Trans. ASME Turbines and Power*, 124(4), 984-991.
- MSC 2010. MSC.Patran v2010 (finite element modelling software).
- Qu, Z-Q 2004. *Model Order Reduction Techniques :with Applications in Finite Element Analysis* Springer.
- Sawalhi, N. 2007. *Diagnostics, prognostics and fault simulation for rolling element bearings*. Ph. D. Dissertation, University of New South Wales, Sydney, Australia.

- Sawalhi, N, Deshpande, L & Randall, RB 2011. Improved simulations of faults in gearboxes for diagnostic and prognostic purposes using a reduced finite element model of the casing. *7th DSTO International Conference on Health & Usage Monitoring (HUMS2011)*. Melbourne, Australia.
- Sawalhi, N & Randall, RB 2008a. Simulating gear and bearing interactions in the presence of faults: Part I. The combined gear bearing dynamic model and the simulation of localised bearing faults. *Mechanical Systems and Signal Processing*, 22, 1924-1951.
- Sawalhi, N & Randall, RB 2008b. Simulating gear and bearing interactions in the presence of faults: Part II: Simulation of the vibrations produced by extended bearing faults. *Mechanical Systems and Signal Processing*, 22, 1952-1966.
- Sawalhi, N & Randall, RB 2010. Improved simulations for fault size estimation in rolling element bearings. *The Seventh International Conference on Condition Monitoring and Machinery Failure Prevention Technologies*. UK.
- Sawalhi, N & Randall, RB 2011. Vibration response of spalled rolling element bearings: Observations, simulations and signal processing techniques to track the spall size. *Mechanical Systems and Signal Processing*, 25, 846-870.
- Sweeney, P. 1994. *Transmission error measurement and analysis* Ph. D. Dissertation, University of New South Wales, Sydney, Australia.

CHAPTER 5

EXPERIMENTAL VALIDATION OF BEARING FAULT SIMULATION MODELS

5.1 Introduction

The early dynamic simulation models of the UNSW gearbox test rig were discussed in Chapter 2 (Section 2.5.1). The methodology to create the improved dynamic models namely, the combined LPM-reduced FEM (146 DOF) and the full reduced FEM (182 DOF) using the Craig-Bampton (CB) method of CMS was illustrated in Chapter 4. In order to gain the confidence in the simulation models, it was necessary to compare the results of simulated vibration signals (with and without bearing fault) with those obtained experimentally.

This chapter summarises the results of the experimental validation of the vibration signals extracted from the improved bearing fault simulation models. A brief description of the test set-up, instrumentation and bearing fault details is provided. This is followed by the comparison and discussion of results of the 146 DOF and 182 DOF models. The results are also compared with those of the initial 34 DOF LPM (Sawalhi, 2007) model. The characteristics of the vibration signals due to fault entry and exit of the rolling element in the case of localised bearing faults are investigated and compared with the LPM model and measurements.

5.2 Experimental set-up

5.2.1 Gearbox test rig

The dynamic models described in Chapter 4 simulate the UNSW gearbox test rig (Figures 5.1 and 5.2), which was built initially to study the effect of gear faults on transmission error (Sweeney, 1994). The test rig consists of a single stage gearbox (in this case using spur gears with 1:1 ratio and 32 teeth on each gear) and is driven primarily by a 3-phase electric motor, but with circulating power via a hydraulic pump/motor set. The input and output shafts are arranged in parallel and each shaft is supported by two double row self aligning ball bearings. The flywheels are used to reduce the fluctuations of the input and output shaft speeds with couplings used to attenuate the shaft torsional vibration. A torque transducer connected to the input shaft is capable of linear measurement to over 200 Nm.

The speed of the input shaft is controlled by adjusting the frequency of the voltage applied to the motor using a frequency controller. The hydraulic pump connected to the output shaft provides the loading on the gears which is controlled by adjusting the pressure relief valve that regulates the fluid flow out of the pump. The hydraulic motor is connected in series with the electric motor and re-circulates the pressurised fluid from the pump. The re-circulating power system enables the economical operation of the test rig as it provides power for the normal running of the test rig, whereas the electrical motor supplies only the small amount of power to compensate the losses.

Based on the electric motor rating (5.5 kW, 8 pole, AC induction motor), the maximum speed of the test rig is 725 rpm. The maximum torque is 130 Nm which is limited by pump volume and the maximum pressure. The details of the test rig along with the operating instructions are given in (Stokes, 2000, Du, 1997, Endo, 2005).

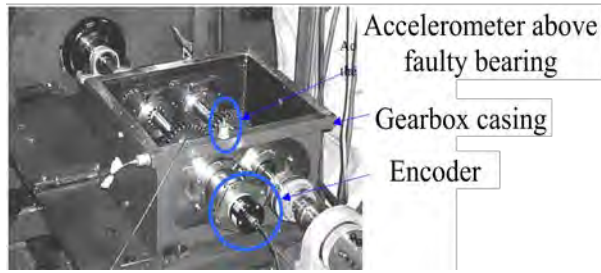


Figure 5.1 UNSW gearbox test rig. (Sawalhi, 2007)

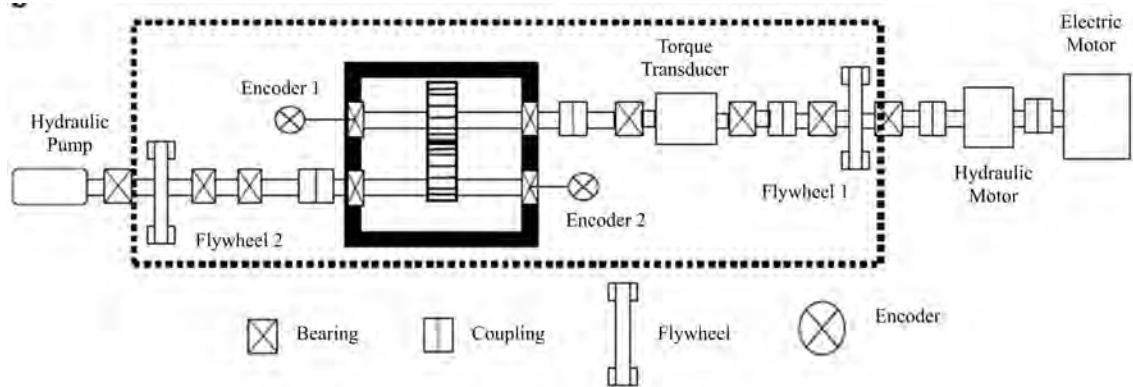


Figure 5.2 Schematic diagram of gearbox test rig (Sawalhi, 2007)

5.3 Bearing faults

5.3.1 Bearings under test

The bearings under test were double row self-aligning type (Koyo 1205), and can be easily disassembled, and assembled back after incorporating seeded faults in the bearing inner race, outer race or rolling elements (Figure 5.3). Table 5.1 shows the specifications of the bearing.

Table: 5.1 Bearing specifications

Bearing	Inner race diameter	Outer race diameter	Pitch diameter	Ball diameter	No. of balls	Contact angle
Koyo 1205	25 mm	52 mm	38.5 mm	7.12 mm	12	0°

The bearings with the seeded faults used in the earlier investigations (Ho, 1999) were used in the current research to capture the vibration signals in the presence of localised and extended faults in the inner and outer race. The fault dimensions/geometry was inserted into the bearing's S-function (in Matlab/Simulink) to simulate the vibration

generated from the test rig as a result of these faults (described in Chapter 4). The details of the seeded faults are described in the following sections.



Figure 5.3 Bearing under test (Koyo 1205)

5.3.2 Localised outer race fault

The localised fault in the bearing outer race was produced using spark erosion or Electric Discharge Machining (EDM) process. This created a notch in the outer race with a rectangular cross section (Figure 5.4) with 0.8 mm width and 0.3 mm depth. The fault spanned over half of the race width so that only one set of balls was impacting with the fault.

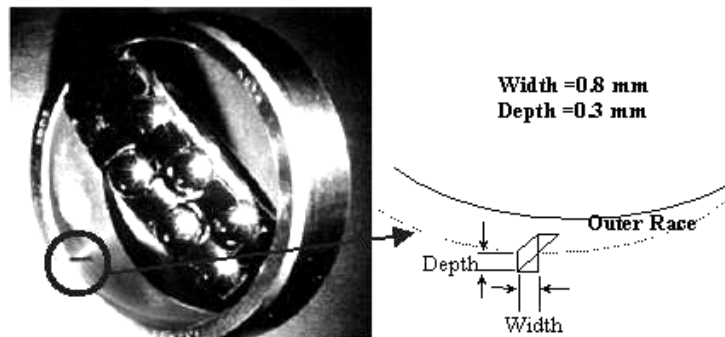


Figure 5.4 Localised outer race fault (Ho, 1999)

Since the outer race is stationary (fixed in the gearbox housing), the bearing was positioned such that the outer race fault always remained in the loaded zone, where the fault is most likely to occur.

Although the actual depth of the fault is 0.3 mm, theoretically the maximum depth the ball would be able to reach is $19.1\text{ }\mu\text{m}$ (outer race fault) which was set in the simulation model. The fault width was set to 0.8 mm, same as the actual physical dimension.

5.3.3 Localised inner race faults

The EDM process was also used to create a localised fault in the bearing inner race with 0.8 mm width and 0.3 mm depth, which spanned over half of the race width (Figure 5.5).



Figure 5.5 Localized inner race fault

Although the actual depth of the fault is 0.3 mm, theoretically the maximum depth the ball would be able to reach is 27.6 μm (inner race fault). In the simulation model, the fault depth was set to 40 μm (to make the simulated results of the same order as the measurements) whereas the fault width was set to 0.8 mm (same as the actual physical dimension).

5.3.4 Extended inner race faults

The bearing faults extending beyond the spacing between two rolling elements are considered as extended faults. Figure 5.6 shows an extended fault inserted in the inner race of the bearing which was created by grinding one eighth of the circumference (12 mm).



Figure 5.6 Extended inner race fault

The topography of the simulated extended fault described in Chapter 4 (Section 4.2.3) was inserted in the revised bearing simulation models (146 DOF and 182 DOF).

5.3.5 Extended outer race faults

A bearing with a rough fault created on the outer race using an electric etching pencil (Figure 5.7), was used to extract the measured vibration signals.(Ho, 1999).



Figure 5.7 Extended (rough) outer race fault (Ho, 1999)

The topography of the extended outer race fault used in the simulation models (146 and 182 DOF) was based on the methodology described in Section 4.2.3.

The elasto-hydrodynamic effect of the oil film was not taken into account in the simulations, and the dry bearing model results in a more impulsive vibration signal. This makes creating a smooth (non-impulsive) extended fault more difficult. The localised faults are not greatly affected by the lack of oil film.

5.4 Vibration signal measurement

A baseline measurement was carried out initially, by operating the test rig with all four good bearings which form the reference signal (or spectrum) for subsequent comparisons with the signals from the faulty bearings. The measurements were repeated by replacing one of the good bearings by a bearing with a seeded fault (described in Section 5.3). The faulty bearings were installed in the same location in all the measurements i.e. at the free end of the driven shaft which provided an easy access to replace the bearings. (This corresponds to the bearing #3 in the simulation models.)

The vibration signals were recorded by positioning an accelerometer (B&K 4393) on top of the gearbox casing above the defective bearing. The signals were sampled at 65536 Hz. The output of the torque transducer was verified through calibration and was used to measure the torque at the input shaft. An optical encoder (type Heidenhain ROD 426) was connected to the free end of the driving shaft using a special diaphragm

coupling (Heidenhain type K03). The encoder provided 900 pulses per revolution as well as once per rev tacho signal (which could be used in identifying the number of shaft rotations and synchronous averaging of the signal). All the measurements were carried out under a 50 Nm load and at a constant shaft frequency of 10 Hz.

The existing gearbox test rig was first commissioned in 1994 at UNSW. The most recent measurements carried out as part of this research (described above) were found to be of poor quality as compared with the previous measurements which were taken when the test rig was relatively new and in good condition. Although the realignment of the rig was carried out before collecting the latest set of measurements, the deterioration in the working of the rig components and the hydraulic control system could not be completely rectified. Hence it was decided to use the earlier measurements (Sawalhi, 2007) of the localised and the extended faults to validate the simulated vibration signals.

5.5 Comparison of experimental and simulation results

The comparison of the simulated vibration signals (in the presence of bearing faults) from the 146 and 182 DOF models with the experimental measurements is presented in this section. The effect of the model reduction technique and the inclusion of more DOFs for the casing and the internals are assessed by comparing the simulated results with the 34 DOF full lumped parameter model developed earlier. The vibration signal processing was carried out using MATLAB software R2009a. The harmonic and sideband cursor programs (Liew and Ho, 2000) were used to identify the fault frequencies, sidebands and their harmonics.

Based on the bearing specifications (Table 5.1), the defect frequencies (frequencies at which the ball passes the defect on the outer race (BPFO) or the inner race (BPFI) can be estimated for the outer race as 48.8 Hz and for the inner race as 71.1 Hz. The fundamental train frequency (FTF) is estimated at 4.1 Hz, while the speed at which the balls spin (BSF) is 26.5 Hz.

In the case of the 34 DOF LPM model, only the acceleration signal in the vertical direction from the defective bearing was available, which was used to create the power spectral density (PSD) plots. The signal was further processed to identify the bearing faults by generating the squared envelope and/or spectral correlation plots depending on

the type of the fault. In contrast to the LPM model, the improved simulation models (146 DOF and 182 DOF), developed in this research, enable the extraction of vibration signal at the top of the gearbox casing (above the defective bearing), the location of which corresponds to the actual position of the accelerometer in the measurements. Two different approaches were used to obtain this simulated vibration signal at the accelerometer position as shown in Figure 5.8.

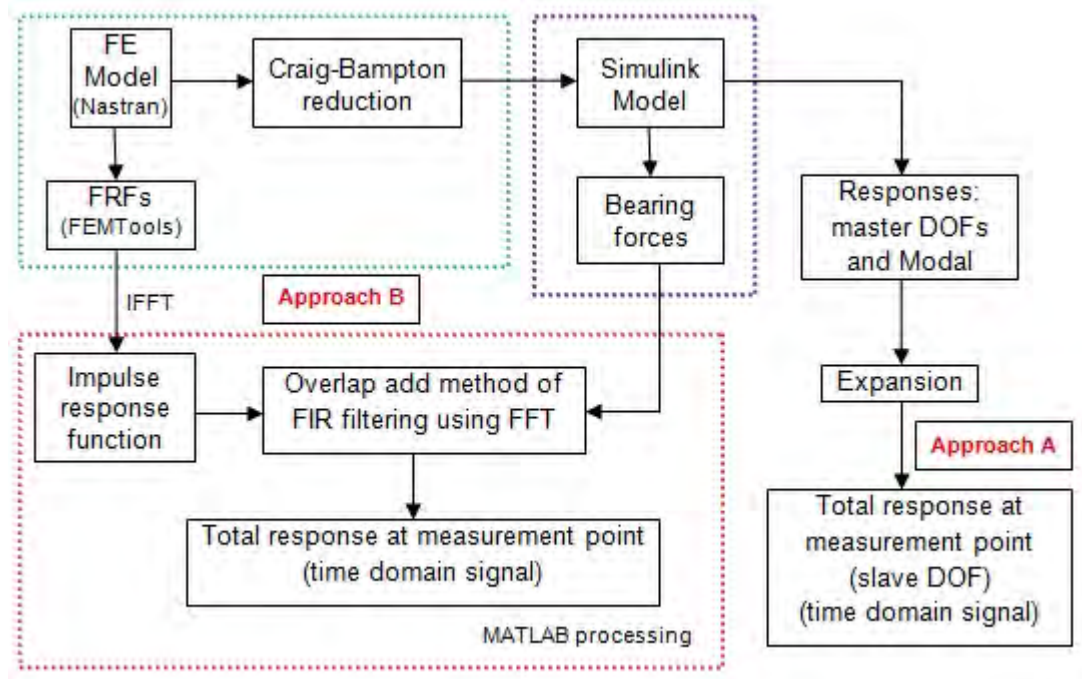


Figure 5.8 Evaluation of total response at the accelerometer position

Figure 5.8 shows the flowchart to obtain the total response at the measurement point from the simulation models (146 and 182 DOFs). In Approach A, the total response is evaluated by expanding both the physical and modal responses back to the slave DOFs of interest (based on Equation 4.35 in Chapter 4), which also represented a virtual sensor corresponding to a physical accelerometer location used in the experimental testing (Sawalhi et al., 2011). Using this approach, the results were valid only up to 4 kHz (which corresponds to the selected set of 100 modes). In order to improve the accuracy of the simulation models and extend this to a higher frequency range, the bearing forces from the LPM-reduced casing model (146 DOF) and the full reduced model (182 DOF) were extracted and convolved with the impulse responses corresponding to the frequency response functions (FRFs) of the gearbox casing (Approach B, Figure 5.8). The FRFs were extracted from the FE model by synthesizing

them from the natural frequencies and mode shapes using FEMTools (DDS, 2012) software which computes the FRFs based on the modal superposition of the selected mode set. The FRFs were calculated between the bearing force locations (input points) and accelerometer position (output point) located on the casing directly above the faulty bearing.

This approach of extracting the forces and convolving them with the impulse response was earlier proposed in (Sawalhi and Randall, 2008a). However, when this was done for the LPM model, the dynamic interaction was not fully accounted for in the low frequency region. By reducing the FE model of the casing and then convolving the LPM-reduced forces with the impulse responses, results in a more interactive approach which has a higher valid frequency range. This is also viable at higher frequency, where the results mainly depend on the modal density rather than the individual modes, and also where the response is more to local rather than extended faults, already shown to be well modelled by the simpler models.

The simulated bearing forces were applied to the full size FE model of the casing to estimate responses over a wider frequency range than the valid range of the forces. For example, the LPM only had a limited number of resonances of the internals, plus the two of the casing, while the reduced FE model only included casing resonances up to 4 kHz (for generating the forces) but the casing resonances up to 20 kHz were used for estimating responses.

The assessment of the simulated (146 and 182 DOF model) and the measured vibration signals are based on the comparison of the following plots:

- Time domain signals (all types of bearing faults)
- Power Spectral Density (PSD) plots (all types of bearing faults)
- Squared envelope spectra (bearing localised faults)
- Spectral Correlation Function (SCF) (bearing extended faults)

5.6 Localised faults in the bearing

The interaction between the gears and bearings in the case of localised bearing faults is additive as the bearing fault excites high frequency bands away from the gear mesh

frequencies. This enables filtering and separating the fault signal from the gear signal due to the fact that the gear signal is periodic whereas the bearing signal is random due to the slippage of the rolling elements as a result of load angle variation (known as a pseudo-cyclostationary signal as described by Antoni and Randall [(2002),(2003)]). The bearing faults can be identified using envelope analysis by de modulating a high frequency band which can be identified by spectral kurtosis (SK) (Antoni and Randall, 2006). A cepstrum prewhitening technique (Sawalhi and Randall, 2011a) was also used in some cases which effectively removes the harmonics of shaft and gearmesh. The resulting residual contains the cyclostationary bearing fault signal and was used to generate the envelope spectra.

5.6.1 Inner race localised fault

5.6.1.1 Comparison of time domain signals

The vibration signals in the time domain (acceleration vs. time) are shown in Figures 5:9 to 5.14. The comparison is made for one complete revolution of the gear/pinion set (32 teeth, 1:1 ratio). This corresponds to 4800 samples in the case of the 34 DOF LPM model against 6554 samples in the case of measurements and simulation (146 and 182 DOF) models. The measured and the simulated signals correlate well in terms of gearmesh pattern. The signals indicate the prevailing effects of the gearmesh which mask the bearing fault.

Time domain signals – Localised inner race fault

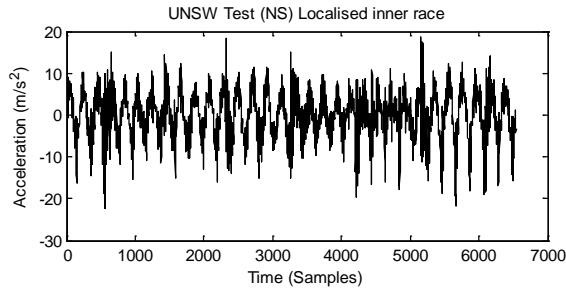


Figure 5.9 Time domain signal – Test

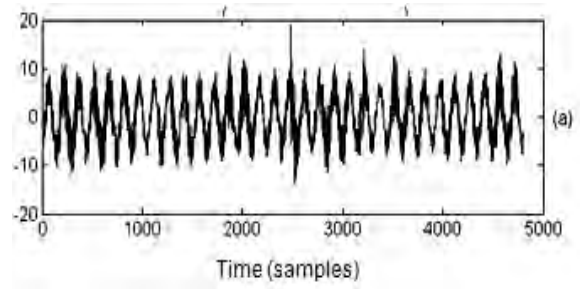


Figure 5.10 Time domain signal – LPM 34 DOF (Sawalhi, 2007)

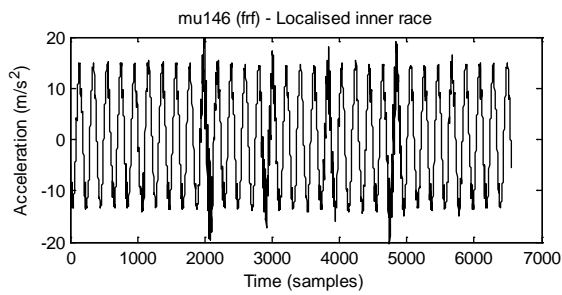


Figure 5.11 Time domain signal – 146 DOF (Approach B)

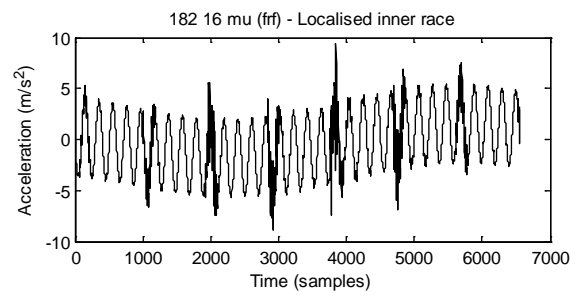


Figure 5.13 Time domain signal - 182 DOF (Approach B)

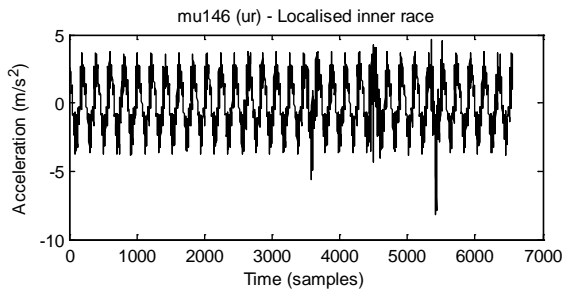


Figure 5.12 Time domain signal – 146 DOF (Approach A)

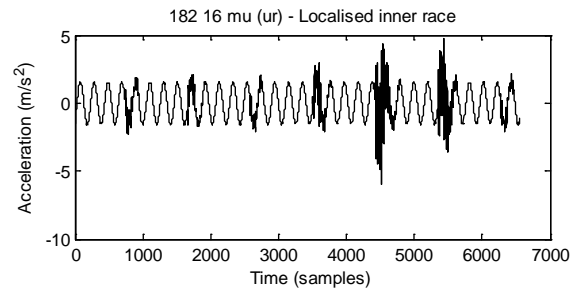


Figure 5.14 Time domain signal - 182 DOF (Approach A)

5.6.1.2 Comparison of power spectra

The comparison of the power spectral density (PSD) is shown in Figures 5.15 to 5.20 for the experimental measurements and the 34 DOF LPM, 146 and 182 DOF simulation models. An increase in the dB level can be observed between the good and the faulty bearing in the high frequency region as a result of the bearing fault. The shape of the spectra in the case of the improved simulation models (146 and 182 DOF) show better match with the measurements as compared to the LPM model. The improved correlation can be seen especially in the low frequency range of 2-4 kHz which was lacking in the case of the LPM.

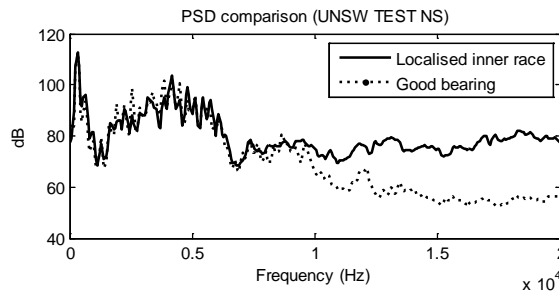


Figure 5.15 PSD – Test
Localised inner race fault

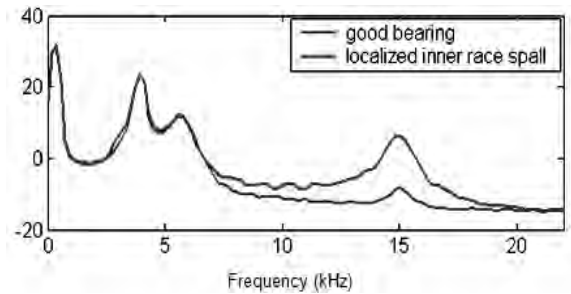


Figure 5.16 PSD –LPM 34 DOF (Sawalhi, 2007)
Localised inner race fault

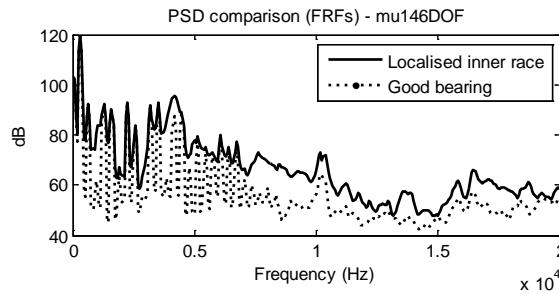


Figure 5.17 PSD –146 DOF
Localised inner race fault (Approach B)

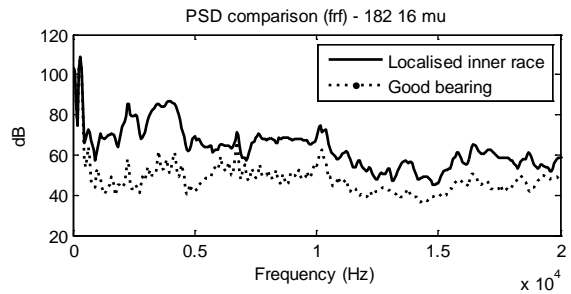


Figure 5.19 PSD –182 DOF
Localised inner race fault (Approach B)

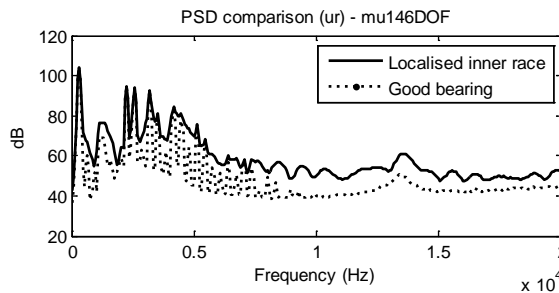


Figure 5.18 PSD –146 DOF
Localised inner race fault (Approach A)

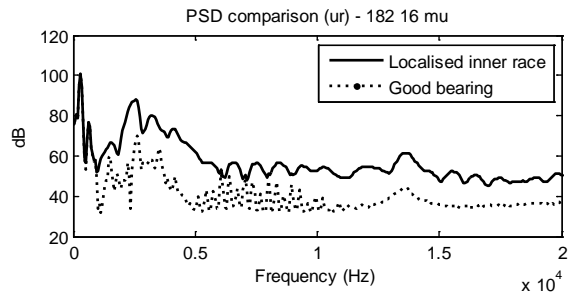


Figure 5.20 PSD – 182 DOF
Localised inner race fault (Approach A)

5.6.1.3 Squared envelope spectra

The squared envelope spectra of the simulation models and measurements are shown in Figures 5.21 to 5.26. The simulated results correlate well with the measurements which clearly identify BPFI harmonics of 71 Hz (Ball Pass Frequency Inner Race). Further, in the case of localised inner race fault, the modulating sidebands spaced at 10 Hz shaft frequency are seen in all the plots.

The 34 DOF LPM model is equally capable of identifying the fault frequencies (BPFI) due to the localised fault in the bearing inner race. It appears that there is no substantial gain in using the reduced model approach apart from improvements in spectra in the 2-4 kHz region.

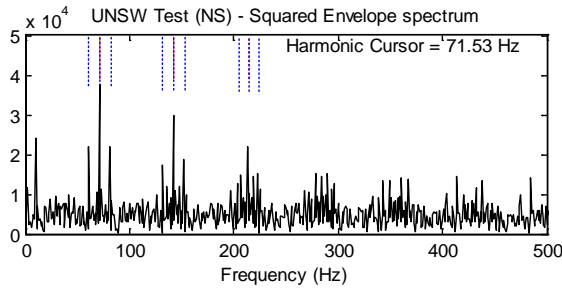


Figure 5.21 Sq. envelope spectrum – Test
Localised inner race fault

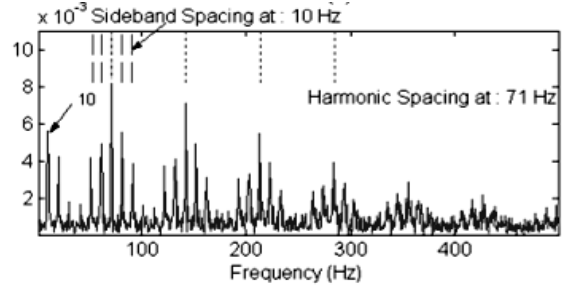


Figure 5.22 Sq. envelope spectrum – 34 DOF
Localised inner race fault (Sawalhi, 2007)

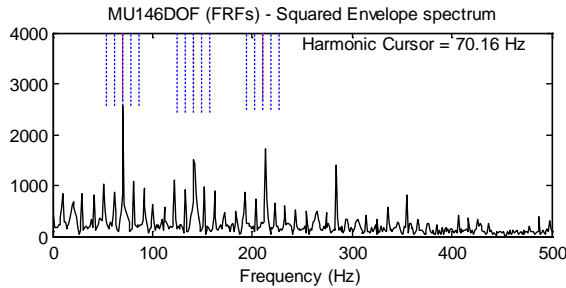


Figure 5.23 Sq. envelope spectrum –146 DOF
Localised inner race fault (Approach B)

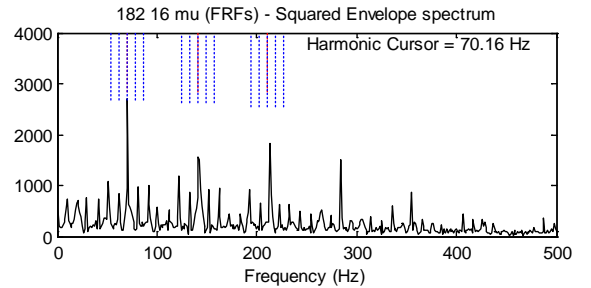


Figure 5.25 Sq. envelope spectrum –182 DOF
Localised inner race fault (Approach B)

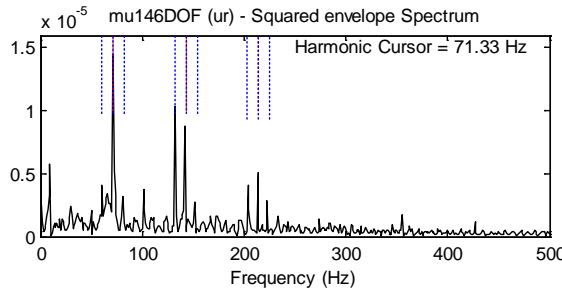


Figure 5.24 Sq. envelope spectrum –146 DOF
Localised inner race fault (Approach A)

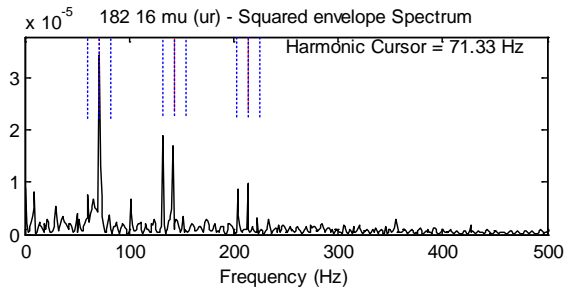


Figure 5.26 Sq. envelope spectrum –182 DOF
Localised inner race fault (Approach A)

5.6.2 Outer race localised fault

5.6.2.1 Comparison of time domain signals

The vibration signals in the time domain (acceleration vs. time) are shown in Figures 5.27 to 5.32. The comparison is made for one complete revolution of the gear/pinion set (32 teeth, 1:1 ratio). This corresponds to 4800 samples in the case 34 DOF LPM model against 6554 samples in the case of measurements and simulation (146 and 182 DOF) models. The measured and the simulated signals correlate well in terms of gearmesh pattern. Similar to the localised inner race fault, the dominating effect of the gearmesh signal that masks the bearing faults is also observed in the case of localised outer race fault.

Time domain signals – Localised outer race fault

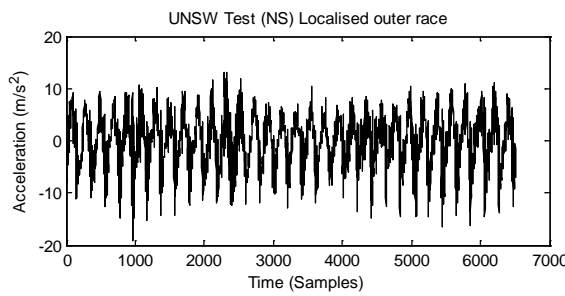


Figure 5.27 Time domain signal - Test

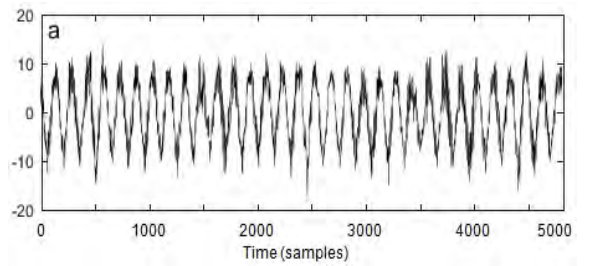


Figure 5.28 Time domain signal – LPM 34 DOF (Sawalhi, 2007)

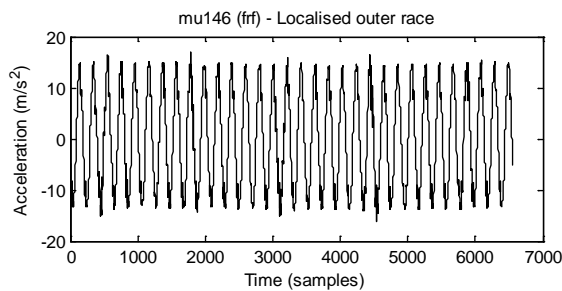


Figure 5.29 Time domain signal – 146 DOF (Approach B)

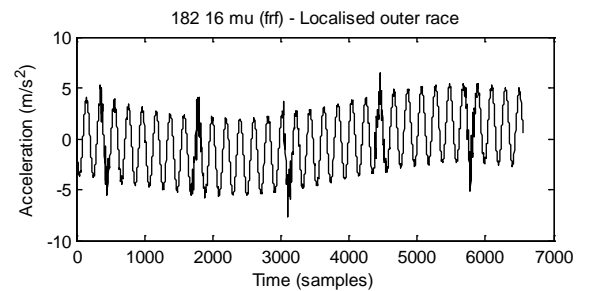


Figure 5.31 Time domain signal - 182 DOF (Approach B)

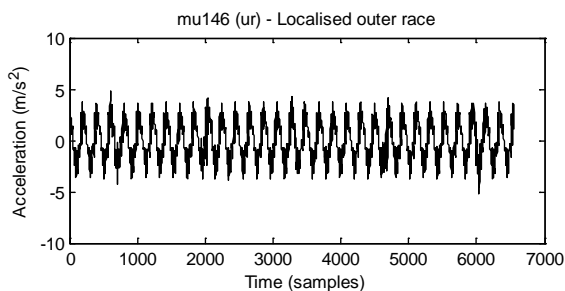


Figure 5.30 Time domain signal – 146 DOF (Approach A)

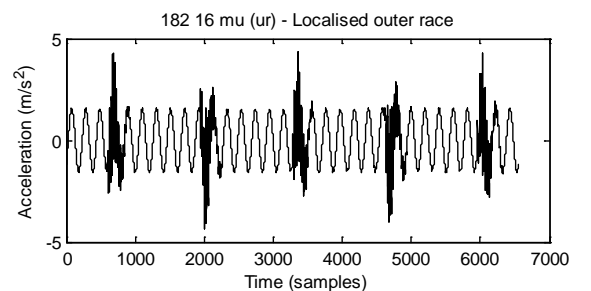


Figure 5.32 Time domain signal - 182 DOF (Approach A)

5.6.2.2 Comparison of power spectra

The comparison of the power spectral density (PSD) is shown in Figures 5.33 to 5.38 for the experimental measurements and the 34 DOF LPM, 146 and 182 DOF simulation models. An increase in the dB level can be observed between the good and the faulty bearing in the high frequency region as a result of the bearing fault, though not as much as for the inner race fault. Here also the shape of the spectra in the case of the improved simulation models (146 and 182 DOF) shows better match with the measurements. This is evident from the improved correlation in the low frequency region of 2-4 kHz, which is clearly missing in the case of 34 DOF LPM model (Figure 5.34).

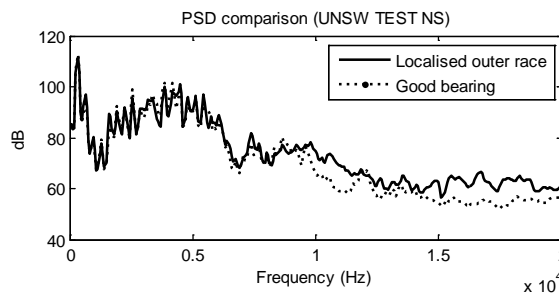


Figure 5.33 PSD – Test
Localised outer race fault

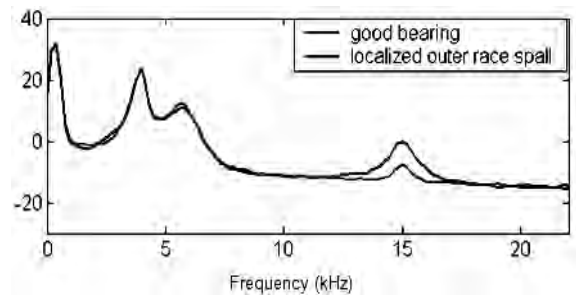


Figure 5.34 PSD –LPM 34 DOF (Sawalhi, 2007)
Localised outer race fault

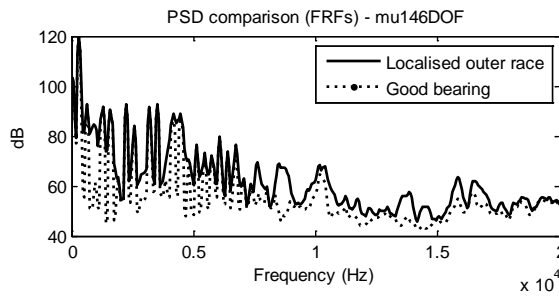


Figure 5.35 PSD – 146 DOF
Localised outer race fault (Approach B)

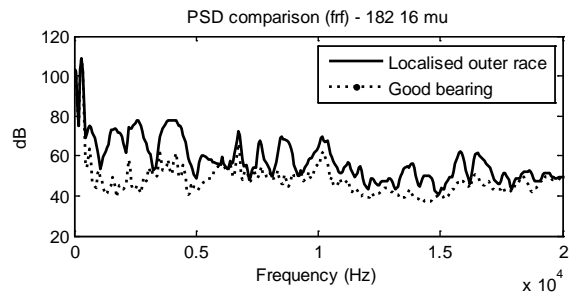


Figure 5.37 PSD – 182 DOF
Localised outer race fault (Approach B)

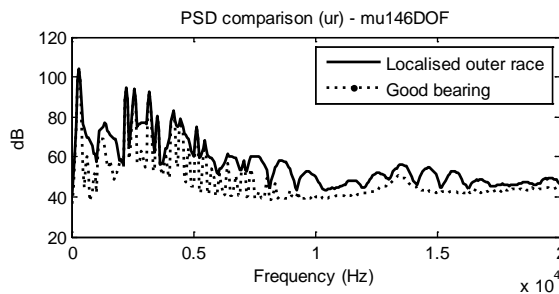


Figure 5.36 PSD – 146 DOF
Localised outer race fault (Approach A)

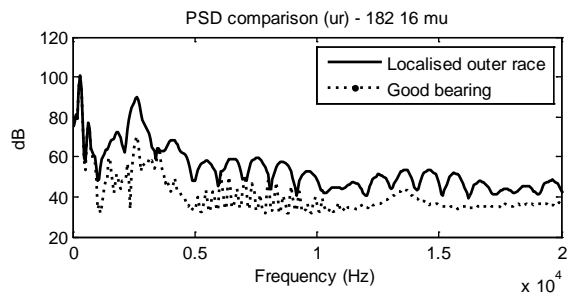


Figure 5.38 PSD – 182 DOF
Localised outer race fault (Approach A)

5.6.2.3 Squared envelope spectra

The squared envelope spectra of the simulation models and measurements are shown in Figures 5.39 to 5.44. The simulated results correlate well with the measurements which clearly identify BPFO harmonics of 48.8 Hz (Ball Pass Frequency outer Race). In the case of fixed outer race, the fault always remains in the loading zone, and this leads to the absence of any modulating sidebands (seen in the case of a localised fault in the rotating inner race).

The 34 D OF LPM model is seen to be equally capable of identifying the fault frequencies (harmonics of BPFO) due to the localised faults in the bearing outer race. It appears that the benefits of using the model reduction techniques (to include the casing dynamics) are mainly in the better spectral correlation in the low frequency region.

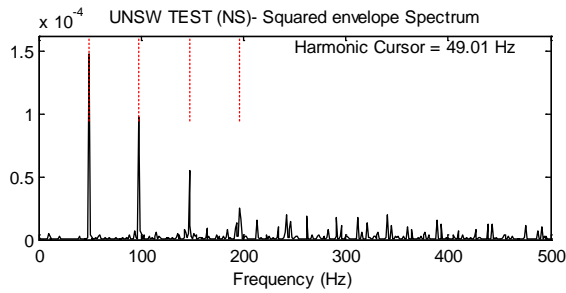


Figure 5.39 Sq. envelope spectrum – Test
Localised outer race fault

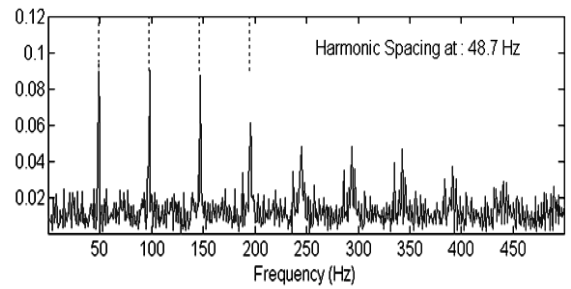


Figure 5.40 Sq. envelope spectrum – 34 DOF
Localised outer race fault (Sawalhi, 2007)

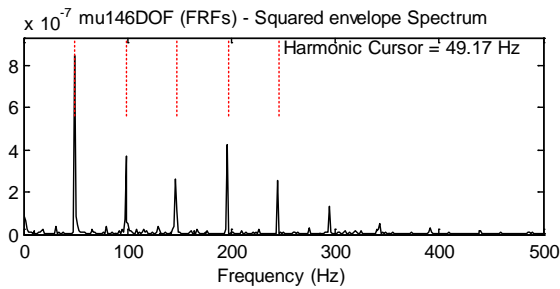


Figure 5.41 Sq. envelope spectrum –146 DOF
Localised outer race fault (Approach B)

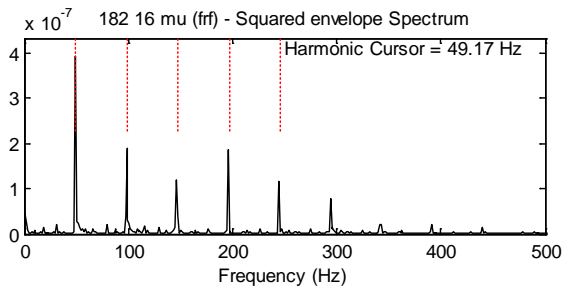


Figure 5.43 Sq. envelope spectrum –182 DOF
Localised outer race fault (Approach B)

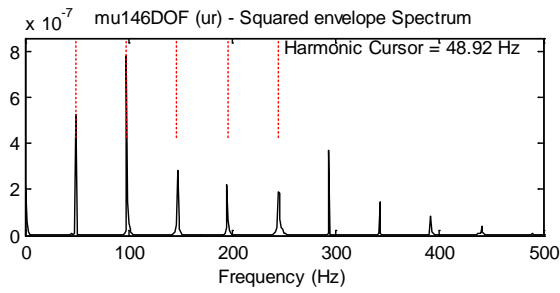


Figure 5.42 Sq. envelope spectrum –146 DOF
Localised outer race fault (Approach A)

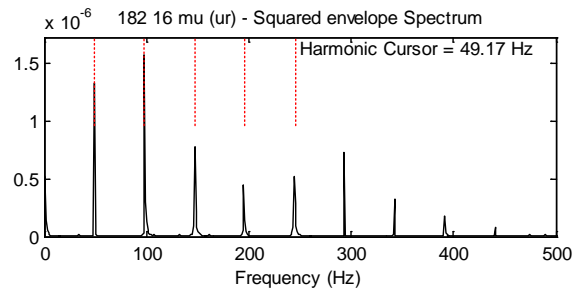


Figure 5.44 Sq. envelope spectrum –182 DOF
Localised outer race fault (Approach A)

5.7 Extended faults in bearing

The vibration signal due to a smoothened extended fault is shown to be purely cyclostationary due to its non-impulsive characteristics with randomly distributed phases (Antoni and Randall, 2002). This is in contrast with the pseudo-cyclostationarity observed in the case of localised bearing faults. This may render the traditional techniques of envelope analyses ineffective in analysing smoothed extended bearing faults since in most cases, the spectrum will be dominated by the shaft speed and its harmonics. Hence, an entirely different signal processing technique based on the cyclostationary properties of the signal is required to identify the fault (Antoni and Randall, 2002). This is further discussed in Section 5.7.1.3.

5.7.1 Inner race extended fault

5.7.1.1 Comparison of time domain signals

The vibration signals in the time domain (acceleration vs. time) are shown in Figures 5:45 to 5.49. The comparison is made for one complete revolution of the gear/pinion set (32 teeth, 1:1 ratio). This corresponds to 6554 samples in the case of measurements and simulation (146 and 182 DOF) models. The measured and the simulated signals correlate well in terms of gearmesh pattern.

Time domain signals – Extended inner race fault (rough)

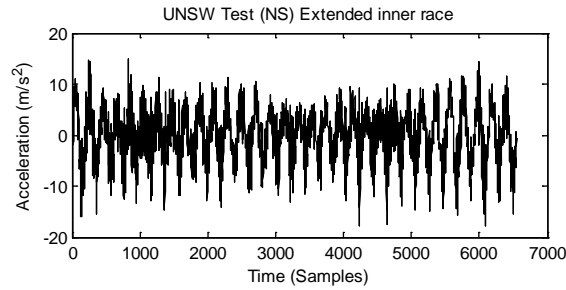
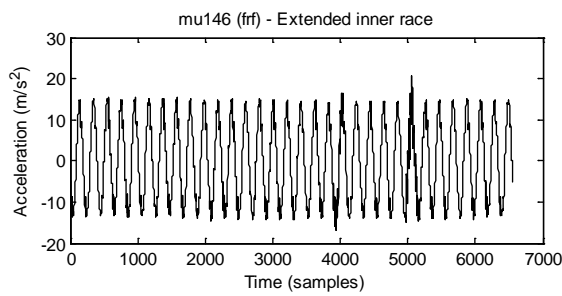
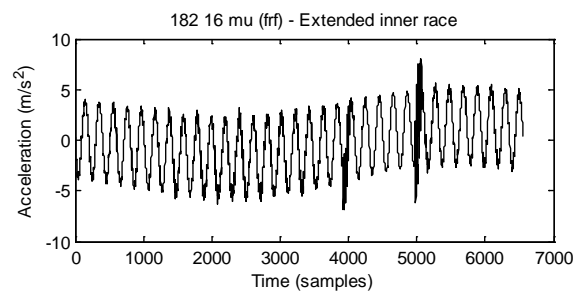
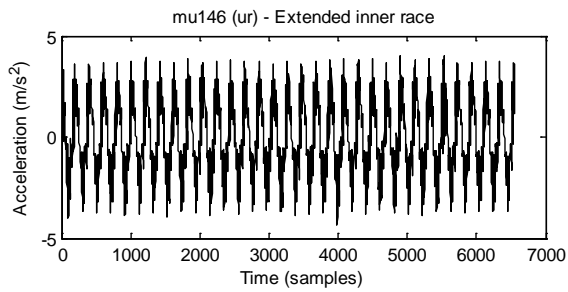
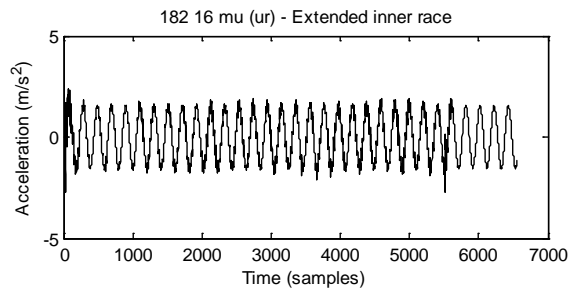


Figure 5.45 Time domain signal – Test

Figure 5.46 Time domain signal – 146 DOF
(Approach B)Figure 5.48 Time domain signal - 182 DOF
(Approach B)Figure 5.47 Time domain signal – 146 DOF
(Approach A)Figure 5.49 Time domain signal - 182 DOF
(Approach A)

5.7.1.2 Comparison of power spectra

The comparison of the power spectral density (PSD) is shown in Figures 5.50 to 5.55 for the experimental measurements and the simulation models in the presence of rough extended inner race fault. The simulated spectra correlate well with the measured spectra except in the case of the 34 DOF LPM model. A smoother fault with lower roughness was used at that time to simulate the 34 DOF LPM, which shows a much smaller dB difference between the good and the faulty bearing as compared with those for the 146 and 182 DOF models. This indicates that the fault geometry used in these models is still impulsive. However, there is better match of the spectra in the low frequency region of 2-4 kHz where the LPM was found to be deficient.

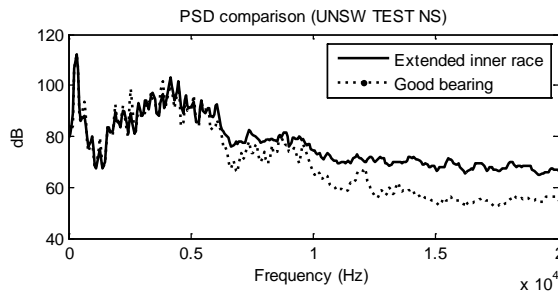


Figure 5.50 PSD – Test
Extended inner race fault

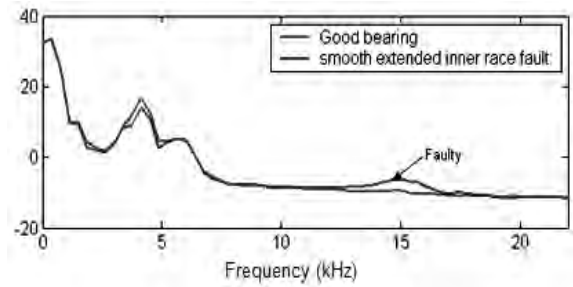


Figure 5.51 PSD – LPM 34 DOF (Sawalhi, 2007)
Extended inner race fault

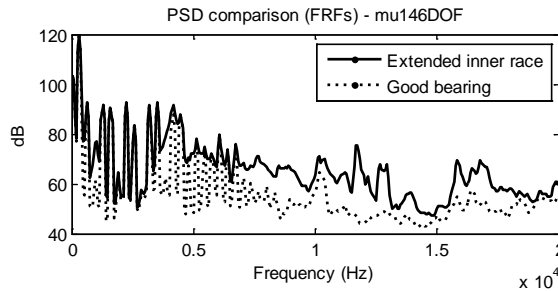


Figure 5.52 PSD – 146 DOF
Extended inner race fault (Approach B)

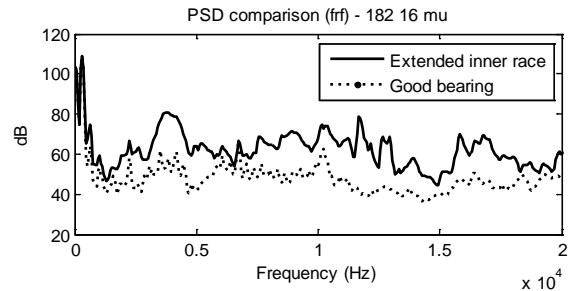


Figure 5.54 PSD – 182 DOF
Extended inner race fault (Approach B)

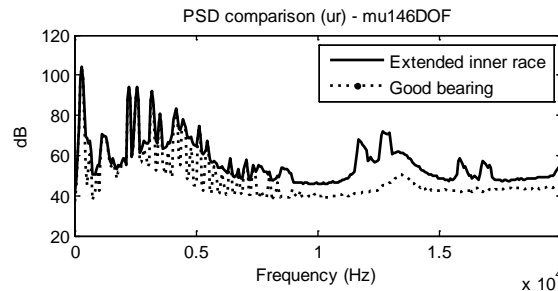


Figure 5.53 PSD – 146 DOF
Extended inner race fault (Approach A)

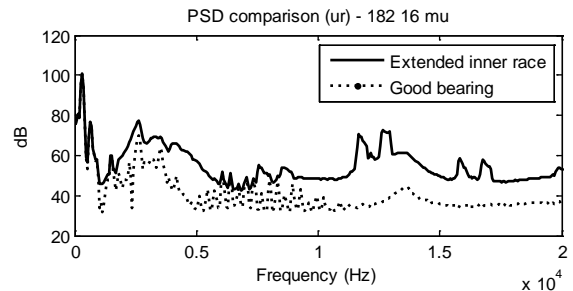


Figure 5.55 PSD – 182 DOF
Extended inner race fault (Approach A)

5.7.1.3 Comparison of power spectra at selected cyclic frequency

As mentioned earlier, a bearing fault is considered as an extended or distributed fault when the fault extends beyond the spacing between two rolling elements and is often less impulsive due to smoothing by the continuous passage of the rolling elements. Unlike localised faults in the bearing, the extended faults cannot always be separated using a demodulation technique such as envelope analysis. In the case of extended faults the interaction between the gears and bearings is multiplicative as the bearing fault modulates the gear signal and the resulting vibration signal is purely cyclostationary (for an inner race fault).

The presence of extended bearing faults can be confirmed by using Spectral Correlation Functions (SCF) which isolate the spectral content for each cyclic or modulating frequency (Antoni and Randall, 2002) and excluding stationary noise (which is only at zero cyclic frequency). Spectral correlation analysis is normally applied after removing the deterministic gear components, leaving only the random second order cyclostationary components which can be attributed to the presence of extended bearing faults.

Figures 5.56 to 5.59 show SCF plots of the measurements and the simulation models (LPM, 146 and 182 DOF) for the case of the rough extended fault in the inner race. The results are presented up to 10 kHz, although in the simulation model, they are only fully valid up to 4 kHz (Approach A) due to the number of modal coordinates included in the model. The selected frequency range is found to be adequate for studying gear/bearing interactions below 5 kHz. In the case of the 146 and 182 DOF simulation models, the SCF comparisons are shown using Approach A, since it is valid for the frequency range of interest below 5 kHz.

In each case, the results are presented in four sub-plots. For example, in the case of extended inner race fault (Figure 5.56), subplots (a) and (b) in the top row indicate the SCF at zero and 10 Hz cyclic frequency, respectively, where the SCF at zero frequency is in fact the normal power spectrum. Subplots (c) and (d) show SCF plots of the residual signal (after removing the deterministic gear components using the DRS technique) at the cyclic frequencies $\alpha = 0$ and Ω (10 Hz shaft speed) respectively. At

zero cyclic frequency in (c), the increase in the dB difference is because of the removal of the masking by the gears, whereas the increased dB difference for $\alpha = 10$ Hz (shaft speed) in (d) implies the existence of an extended inner race fault once masking by the gears is removed.

In the case of the rough extended inner race fault (Figure 5.56 (d)), the expected dB difference in the frequency region below 5 kHz is not clearly seen. This is in contrast with the measurements carried out on the same test rig (when the rig was in good condition) at different speeds and non 1:1 gear ratio, which showed significant dB difference in the low frequency region (Antoni and Randall, 2002). However, the SCF results of the improved simulation models (142 and 182 DOF) correlate much better with these original measurements. Thus it appears that including the casing dynamic properties in the time domain simulation increases the interaction of the extended fault with the gear meshing, as expected.

The squared envelope spectrum of the vibration signal (in the presence of the rough extended inner race fault) was found to be dominated by the harmonics of shaft frequency (10 Hz) with the absence of BPFI fault frequencies.

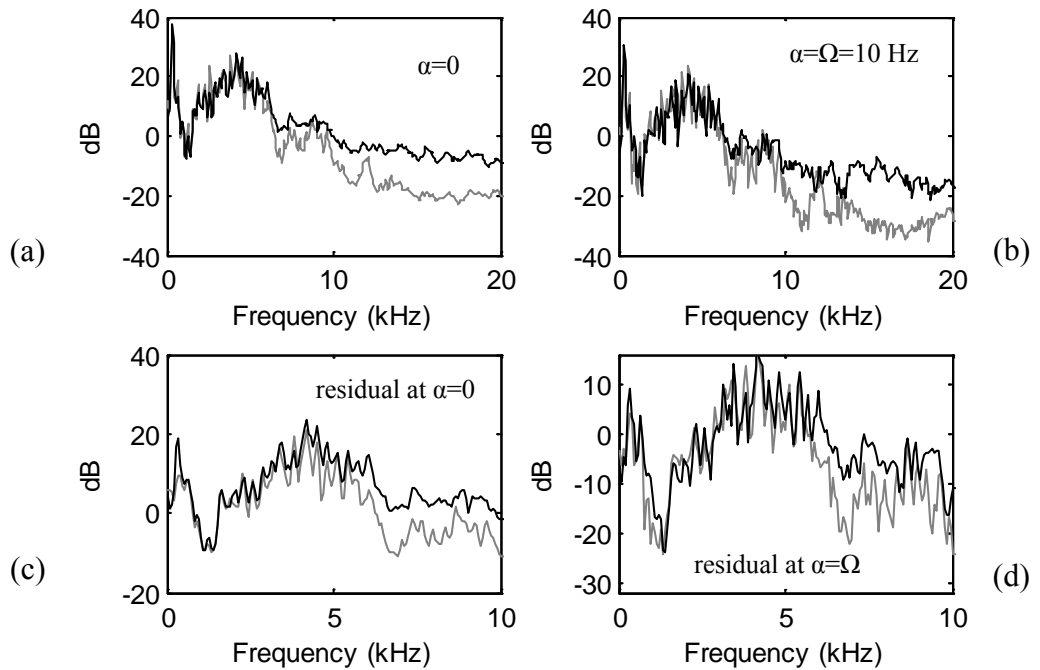


Figure 5.56 SCF Test - Extended inner race fault

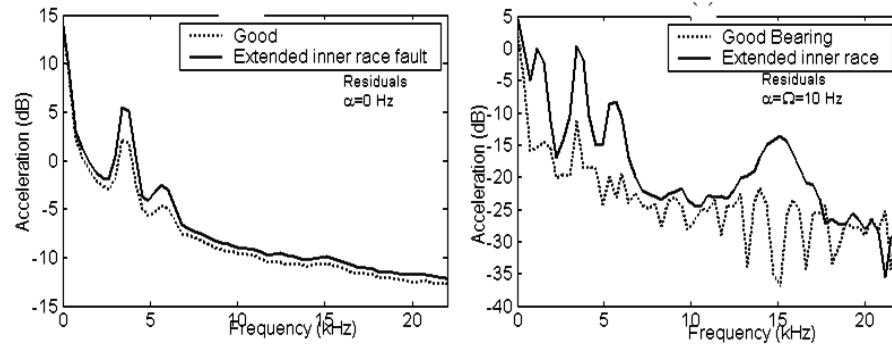


Figure 5.57 SCF 34LPM – Smooth extended inner race fault (Sawalhi, 2007)

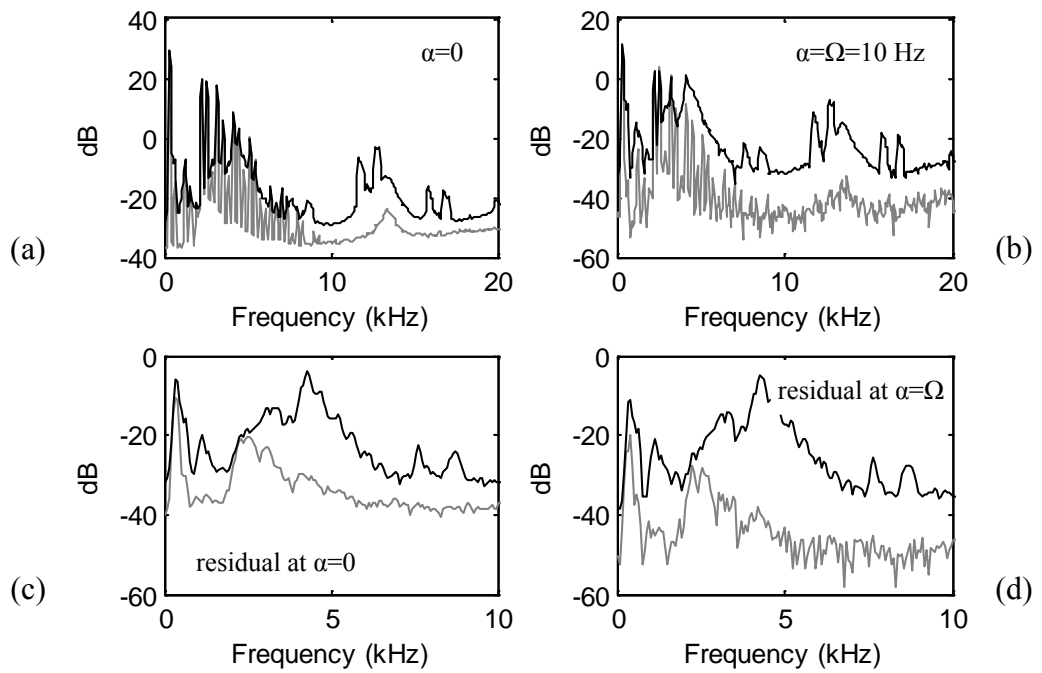


Figure 5.58 SCF 148 DOF - Extended inner race fault (Approach A)

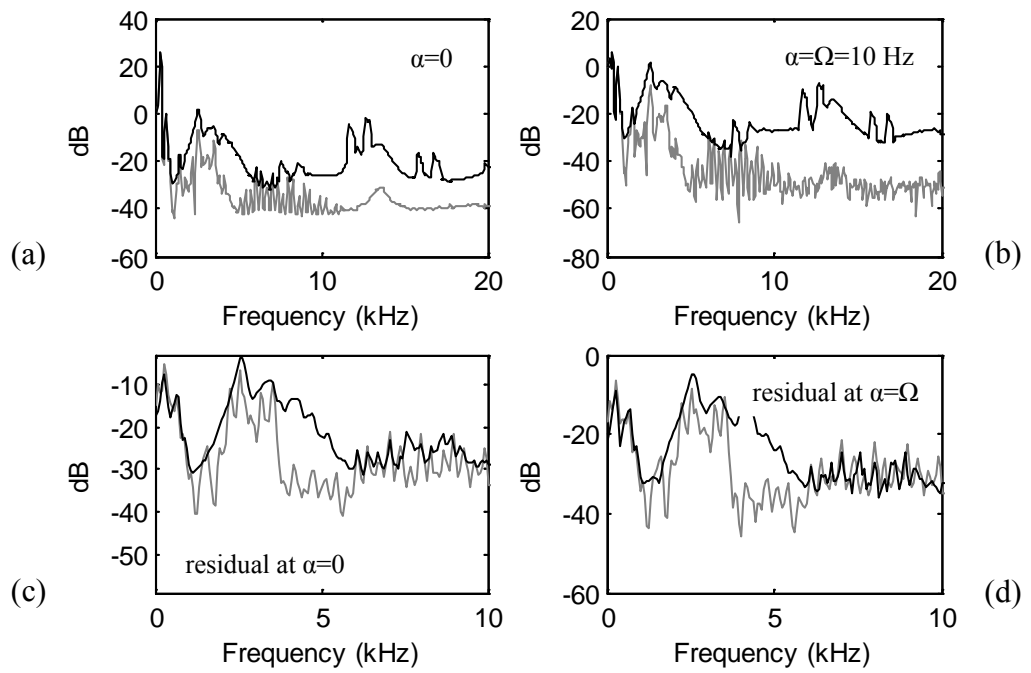


Figure 5.59 SCF 182 DOF - Extended inner race fault (Approach A)

5.7.2 Outer race extended fault

5.7.2.1 Comparison of time domain signals

The vibration signals in the time domain (acceleration vs. time) due to an extended fault in the bearing outer race are shown in Figures 5.60 to 5.64. The comparison is made for one complete revolution of the gear/pinion set (32 teeth, 1:1 ratio). This corresponds to 6554 samples in the case of measurements and simulation (146 and 182 DOF) models. The measured and the simulated signals correlate well in terms of gearmesh pattern.

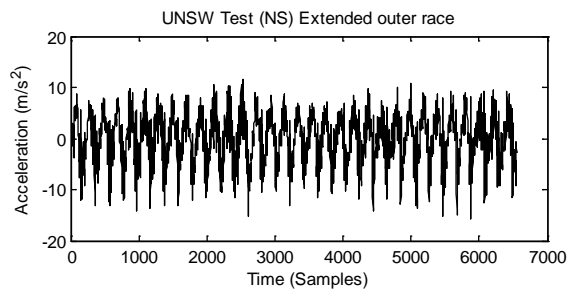


Figure 5.60 Time domain signal – Test

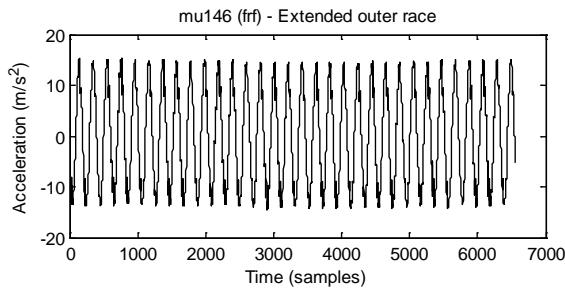


Figure 5.61 Time domain signal – 146 DOF
(Approach B)

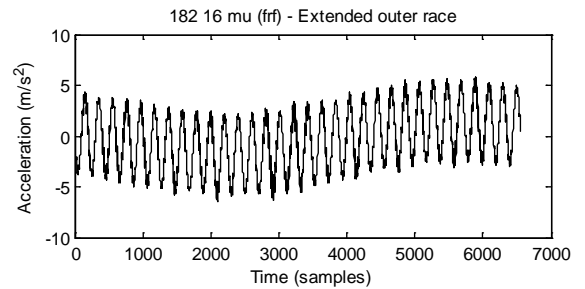


Figure 5.63 Time domain signal - 182 DOF
(Approach B)

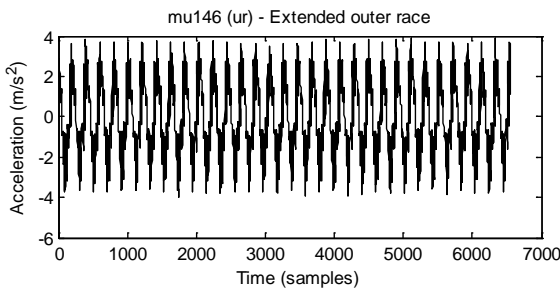


Figure 5.62 Time domain signal – 146 DOF
(Approach A)

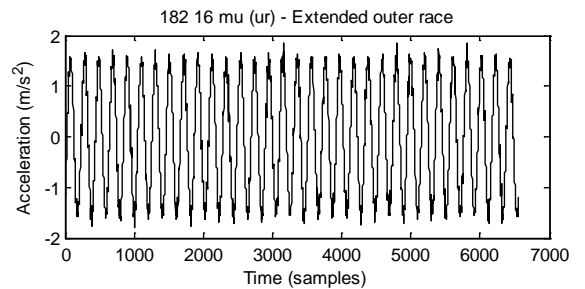


Figure 5.64 Time domain signal - 182 DOF
(Approach A)

5.7.2.2 Comparison of power spectra

The comparison of the power spectral density (PSD) is shown in Figures 5.65 to 5.70 for the experimental measurements and the simulation models in the presence of a rough extended outer race fault. The simulated spectra correlate well with the measured spectra except in the case of the 34 DOF LPM model. The PSD plot for the LPM model is based on the smooth extended outer race fault (rough geometry was not simulated at that time), which shows much smaller dB difference between the good and the faulty bearing as compared with those for the 146 and 182 DOF models. This indicates that the fault geometry used in these revised models is still impulsive. However, there is better match of the spectra in the low frequency region of 2-4 kHz which is poorly represented in the LPM.

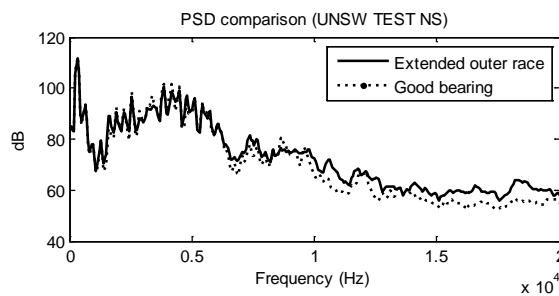


Figure 5.65 PSD – Test
Extended outer race fault

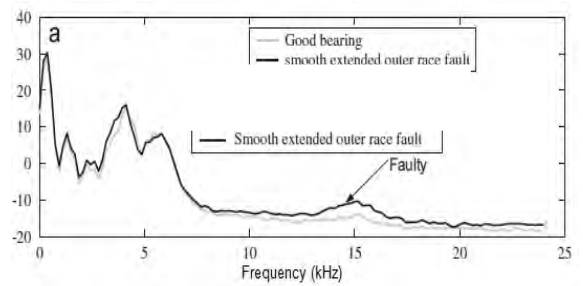


Figure 5.66 PSD – LPM 34 DOF
Extended outer race fault (Sawalhi and Randall,
2008b)

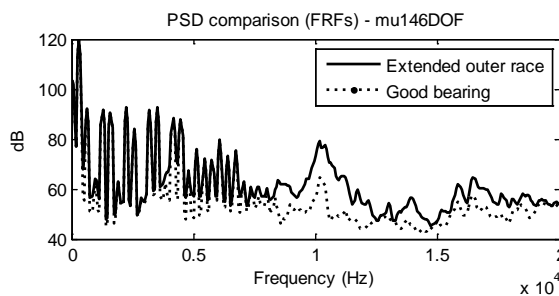


Figure 5.67 PSD – 146 DOF
Extended outer race fault (Approach B)

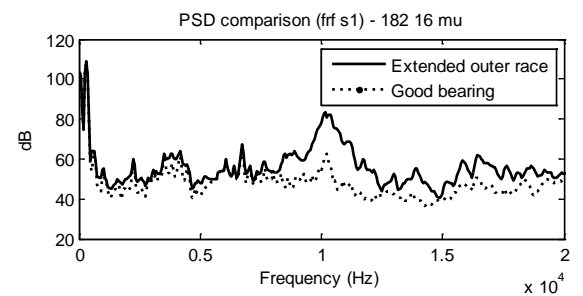


Figure 5.69 PSD – 182 DOF
Extended outer race fault (Approach B)

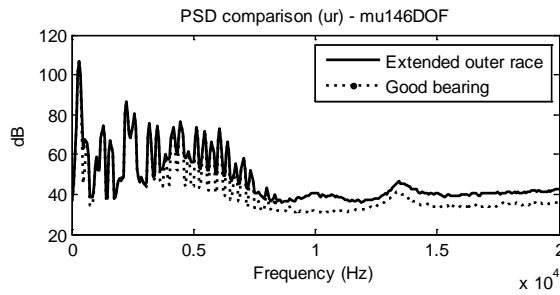


Figure 5.68 PSD – 146 DOF
Extended outer race fault (Approach A)

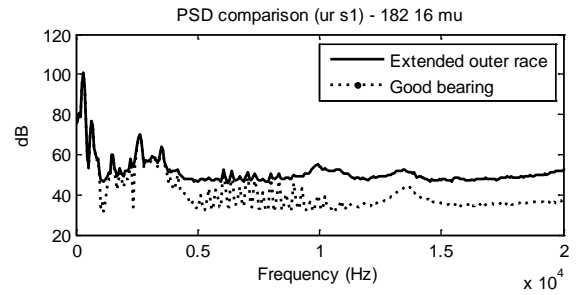


Figure 5.70 PSD – 182 DOF
Extended outer race fault (Approach A)

5.7.2.3 Comparison of power spectra at selected cyclic frequency

The SCF plots for the extended faults in the bearing outer race were created using the procedure described in Section 5.7.1.3. The only difference was that the cyclic frequency (Ω) was set to 48.8 Hz (BPFO) since the outer race was fixed and the fault remains stationary in the load zone (Figure 5.71 to 5.73). The presence of the extended outer race fault is evident by the dB difference in the low frequency region in the residual signal (after removing the deterministic gear signal) and comparing the cyclic spectra at BPFO. The expected dB difference in the residual signal is not evident in Figure 5.71 (d). However, the 146 and 182 DOF simulation models showed much larger dB difference in the low frequency region for the extended faults (Figures 5.72 (d) and 5.73 (d)), which are in agreement with the original measurements (Antoni and Randall, 2002).

The squared envelope spectra of the vibration signals (in the presence of the rough extended outer race fault) were found to be dominated by the harmonics of the BPFO fault frequency. This probably indicates that the fault geometry is still impulsive and requires further development to accurately predict the extended roughness part of extended outer race fault.

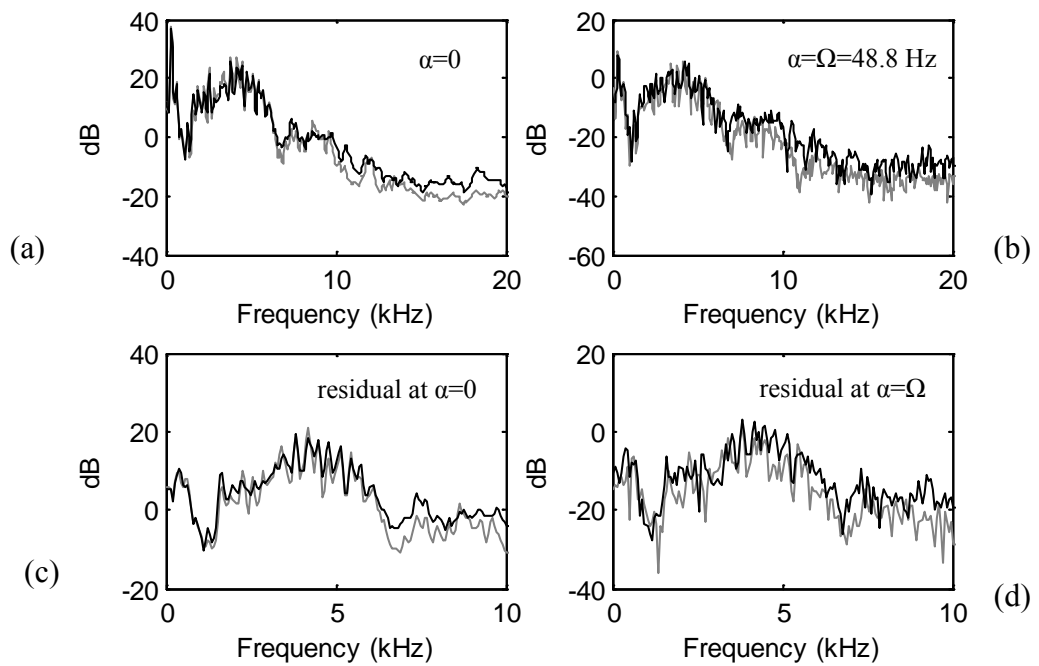


Figure 5.71 SCF Test - Extended outer race fault

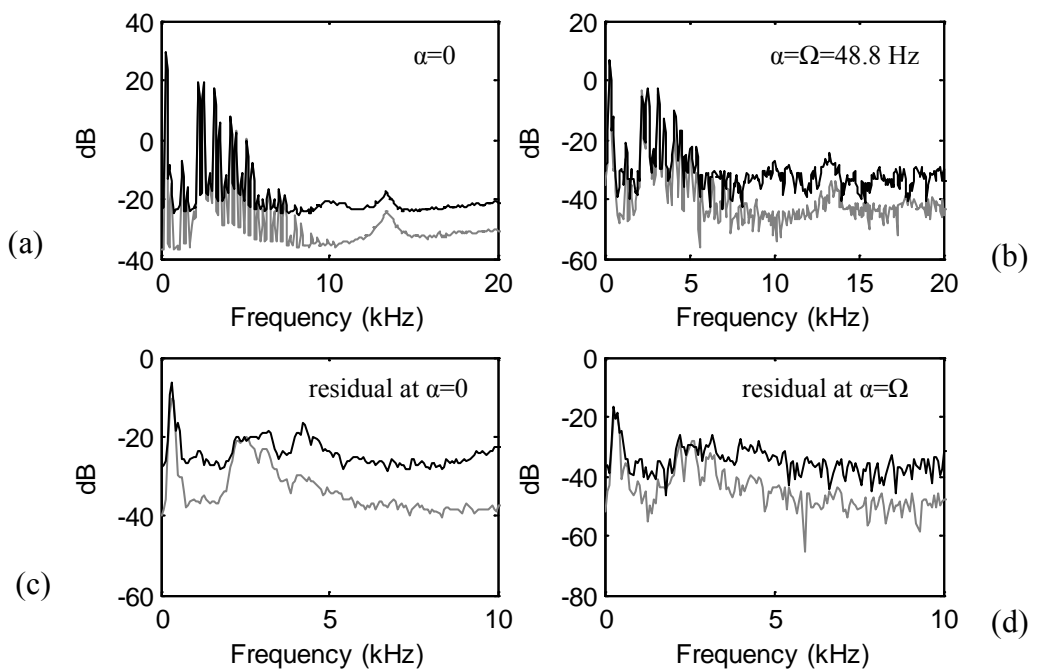


Figure 5.72 SCF 146 DOF - Extended outer race fault (Approach A)

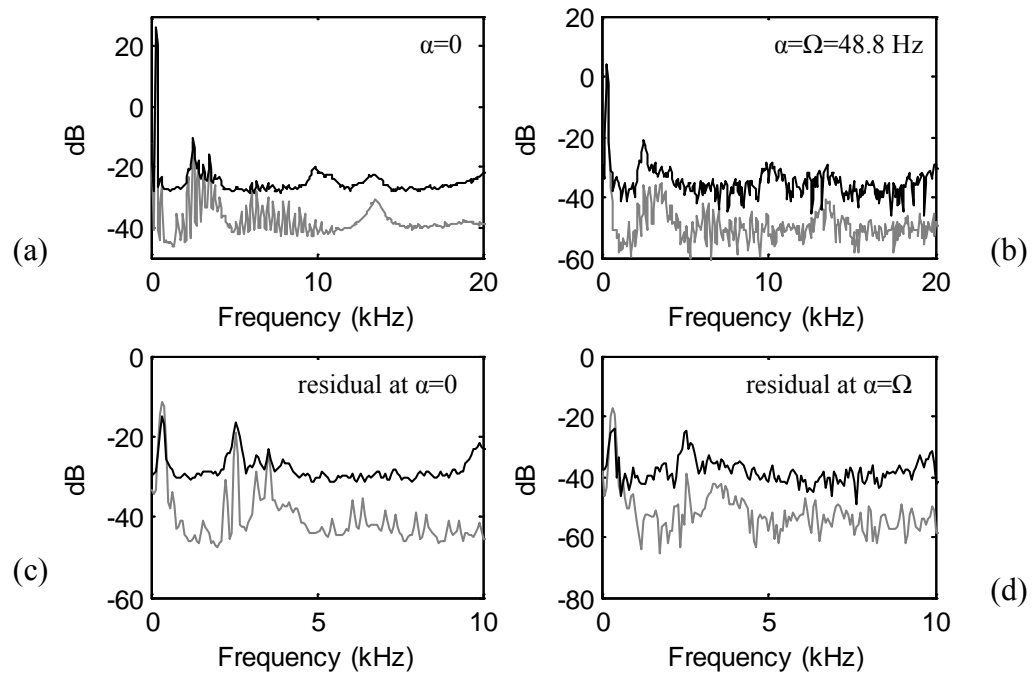


Figure 5.73 SCF 182 DOF - Extended outer race fault (Approach A)

5.8 Fault entry/exit phenomena

There are two parts to the vibration signal from a local spall in a bearing, the first originating from the entry of the rolling element into the fault (de-stress) and the second due to exit from the fault (re-stress). The resulting acceleration can normally be described as a low frequency step response at the entry, since the sudden change in curvature at the entry represents a step in acceleration. At the spall exit, the centre of the rolling element would have to change direction suddenly, resulting in a step in velocity or an impulse in acceleration (Sawalhi and Randall, 2011b).

The study of fault entry and exit was earlier described in (Deshpande et al., 2012). The revised results based on the updated FE model of the casing are presented in this section along with the additional results for the 182 DOF model.

Based on the PSD comparisons, Approach A appears to give reasonable results in terms of spectral matching and hence the subsequent results are shown using this approach.

The vibration signals obtained from the measurements and simulations were further processed to enhance the step and impulse responses at the entry and exit of the spall

using signal prewhitening. The entry into the fault in principle gives a low frequency step response, while the impact on exit excites a much broader band impulse response. Prewhitening the signals using the cepstrum (Sawalhi and Randall, 2011a) or autoregressive (AR) method (Sawalhi and Randall, 2011b) increases the relative strength of the entry event, although the two events still tend to be different in frequency content. The cepstrum prewhitening method is used in the current investigation.

Figures 5.74 to 5.81 indicate the rolling element fault entry and exit events for a single pulse for the measured and the simulated vibration signals. The fault entry and exit events are marked with arrows in the figures. The step response at the entry and the impulse response at exit are clearly seen in the simulated results and correlate well with the test results in the case of localised inner race fault. However, there is a better match of the step response of the LPM model with a localised outer race fault with that observed in the test results than for the 146 DOF and 182 DOF models. This indicates that further signal processing is required on the simulation models and test data (with outer race fault) and this will form part of future work.

The results also confirm that the impact event takes place when the centre of the rolling element is located at half the spall width. The average time to impact is found to be approximately 0.6 ms for a 0.8 mm fault width, which is independent of the location of the fault i.e. whether on the inner or outer race. This observation is in agreement with the theoretical explanation given in (Sawalhi and Randall, 2011b).

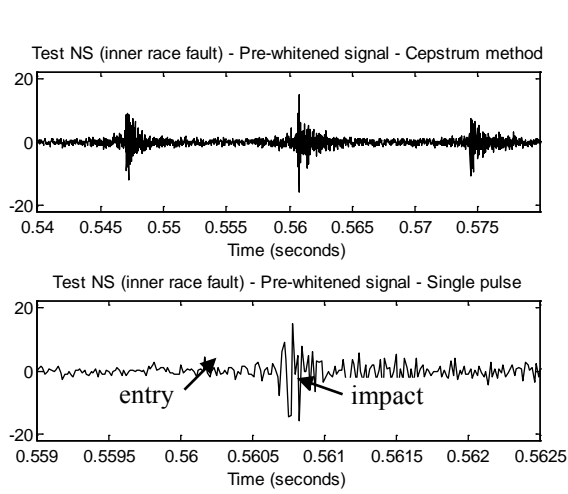


Figure 5.74 Test data: Localized inner race fault

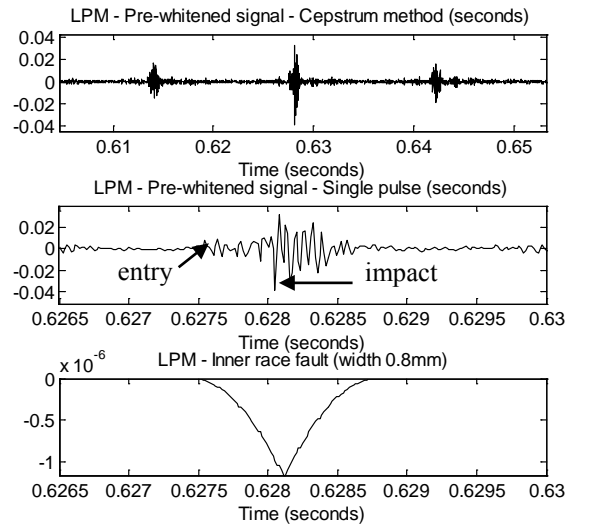
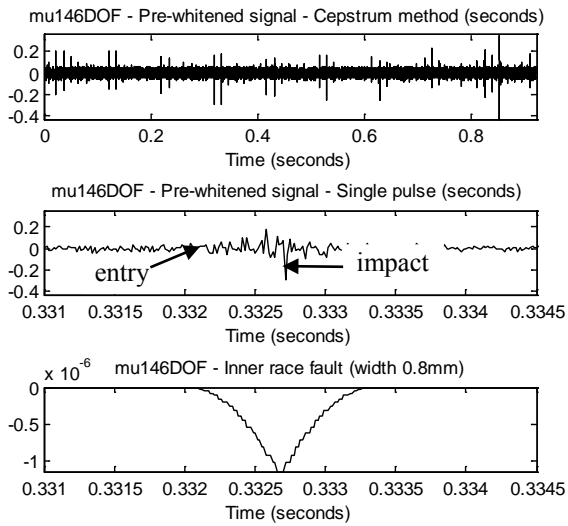
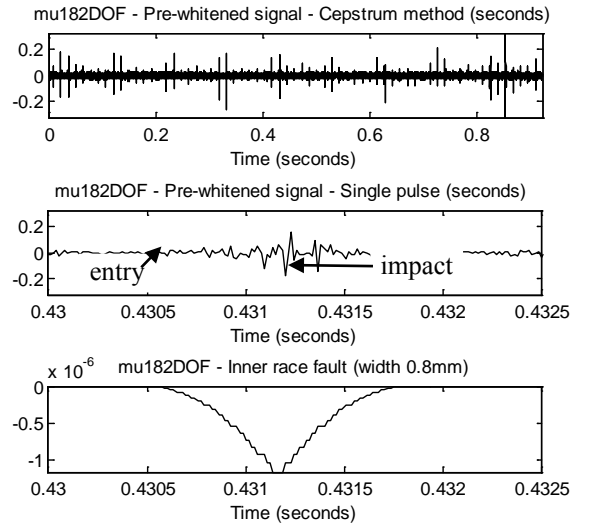


Figure 5.75 LPM: Localized inner race fault

Figure 5.76 146 DOF: Localized inner race fault
(Approach A)Figure 5.77 182 DOF: Localized inner race fault
(Approach A)

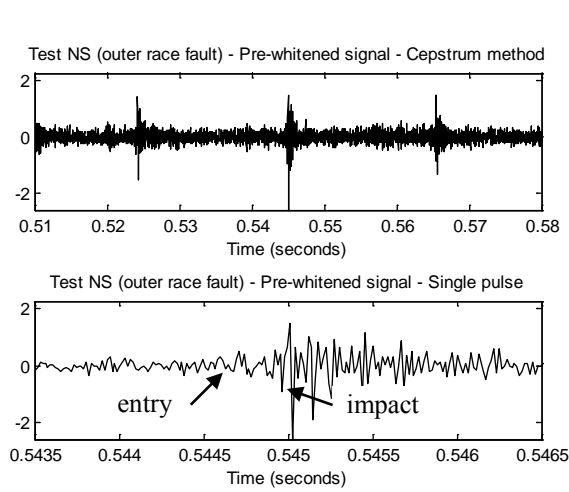


Figure 5.78 Test data: Localized outer race fault

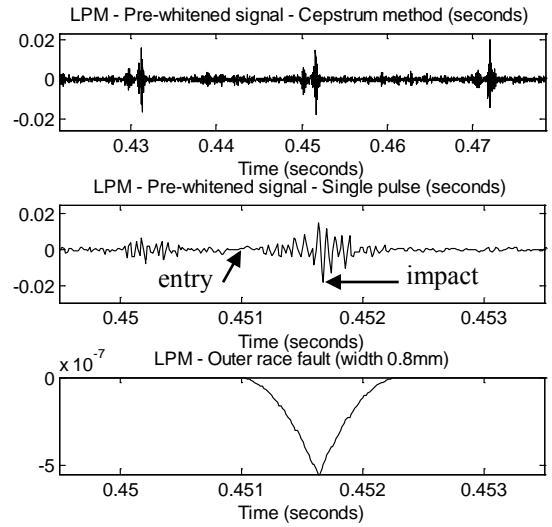
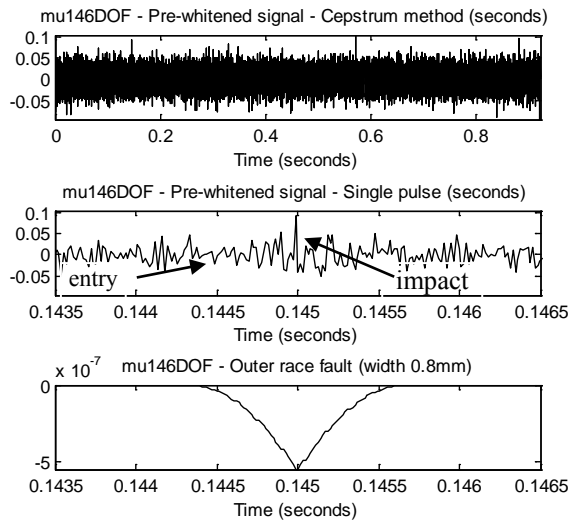
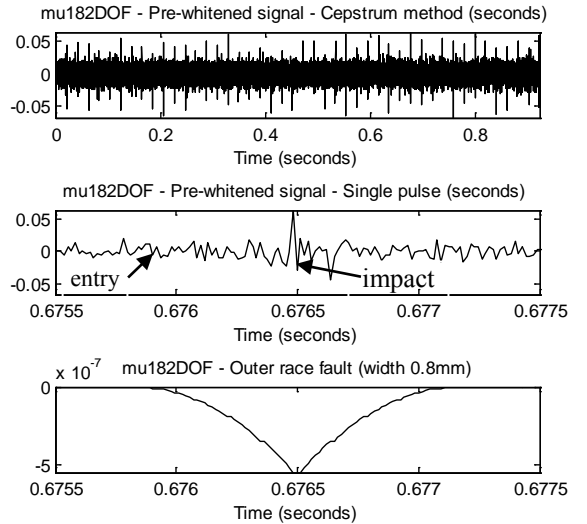


Figure 5.79 LPM: Localized outer race fault

Figure 5.80 146 DOF: Localized outer race fault
(Approach A)Figure 5.81 182 DOF: Localized outer race fault
(Approach A)

5.9 Summary

This chapter describes the experimental validation of the improved bearing fault simulation models namely the 146 and 182 DOF models. The models were developed using model reduction techniques, which enable the inclusion of the dynamic properties of the gearbox casing and better representation of the gear/bearing interaction. The vibration signals were extracted using two different approaches namely the force convolution method and the response at a slave DOF using the Craig-Bampton method. The measurements and the simulations were carried out in the presence of localised and extended faults in the inner and outer race of the bearing.

The characteristics of the simulated vibration signals correlate well with the measurements especially in the low frequency region of 2-4 kHz which was the main limitation of the LPM model. The diagnostic techniques such as cepstrum prewhitening and envelope analysis were applied to the vibration signals to identify the fault frequencies. The improved simulation models clearly identify the localised fault frequencies (BPFI and BPFO). However, two aspects of the simulated vibration signal characteristics need to be investigated further namely, the aliasing in the spectra observed in the case of both the 146 and 182 DOF models and the reduced clarity of the gearmesh frequencies in 182 DOF model.

The techniques of envelope analysis and SCF were employed to identify the extended faults in the bearing inner and outer race. The simulated results (146 and 182 DOF models) in the presence of rough extended inner race fault were in good agreement with the measurements and indicate the modulation of the gearmesh frequency by the shaft speed.

In the case of the rough extended outer race fault, the modulation of the gearmesh frequencies by BPFO is seen in both the simulation models and measurements. However, the simulated envelope spectra indicate harmonics of BPFO (over a wide frequency range) meaning that the fault geometry is still impulsive and needs to be modified to attain the smooth extended fault. This is proposed as part of future work.

Cepstrum prewhitening was carried out on the measured and simulated vibration signals to enhance the step and impulse responses at the fault entry and exit. There was a better agreement of the simulated results (146 and 182 DOF) with the measurements in the case of localised inner race faults than in the case of localised outer race faults, but the measurements also showed more noise in this case. However, the LPM model provided a clear indication of these two events for both types of faults. The results confirm that the average time to impact corresponds to half the spall width. The methodology can be used to estimate the spall size which is an important monitoring parameter in the bearing prognostics.

The analysis times for the 146 DOF and 182 DOF models were approximately 2 hours and 3 hours respectively on a standard desktop PC (Intel i5, 8 GB RAM). Both the

simulation models were found to be effective in generating the characteristic vibrations similar to those produced by the gearbox test rig with and without bearing fault. The full reduced model (182 DOF) with the additional DOFs for the internals (in addition to the large number casing DOFs) does not appear to provide further benefits. However, the use of FE modelling to characterise the gearbox internals in the case of 182 DOF model, eliminates the need to manually generate the stiffness matrices from the equations of motion, and increases the ease of incorporating additional DOFs or modal coordinates for the internals. This significantly reduces the modelling time for the 182 DOF model when compared to the 146 DOF model and more than compensates for the increased simulation time.

The good correlation obtained between the measured and the simulated results establish the validity of the bearing fault simulation models which adequately represent the gear/bearing interaction in the mid-frequency region. The matching with experimental results is still far from perfect however, and requires further development. The improved simulation models can be used to simulate faults of different sizes and locations and to develop more efficient diagnostic and prognostic algorithms.

5.10 References

- Antoni, J & Randall, RB 2002. Differential Diagnosis of Gear and Bearing Faults. *Journal of Vibration and Acoustics*, 124, 165-171.
- Antoni, J & Randall, RB 2003. A stochastic model for simulation and diagnostics of rolling element bearings with localized faults. *Journal of Vibration and Acoustics*, 125, 282-289.
- Antoni, J & Randall, RB 2006. The spectral kurtosis: application to the vibratory surveillance and diagnostics of rotating machines. *Mechanical Systems and Signal Processing*, 20, 308-331.
- DDS 2012. (Dynamic Design Solutions N.V.), FEMtools Version 3.6.
- Deshpande, L, Sawalhi, N & Randall, RB 2012. Gearbox bearing fault simulation using a finite element model reduction technique. *25th International Congress on*

Condition Monitoring and Diagnostic Engineering Management. Huddersfield, UK.

Du, S. 1997. *Dynamic modelling and simulation of gear transmission error for gearbox vibration analysis*. Ph.D. Dissertation, University of New South Wales, Sydney, Australia.

Endo, H. 2005. *Simulation of gear faults and its application to the development of differential diagnostic technique* Ph. D. Dissertation, University of New South Wales, Sydney, Australia.

Ho, D. 1999. *Bearing diagnostics and self-adaptive noise cancellation*. Ph.D. Dissertation, University of New South Wales, Sydney, Australia.

Liew, A & Ho, D 2000. "Harmonic Cursor" and "Sideband Cursor", Matlab programs to enhance the information presented in the Frequency Spectrum, School of Mechanical and Manufacturing Engineering, University of New South Wales.

Sawalhi, N. 2007. *Diagnostics, prognostics and fault simulation for rolling element bearings*. Ph. D. Dissertation, University of New South Wales, Sydney, Australia.

Sawalhi, N, Deshpande, L & Randall, RB 2011. Improved simulations of faults in gearboxes for diagnostic and prognostic purposes using a reduced finite element model of the casing. *7th DSTO International Conference on Health & Usage Monitoring (HUMS2011)*. Melbourne, Australia.

Sawalhi, N & Randall, RB 2008a. A Combined Lumped Parameter and Finite Element Model of a Single Stage Gearbox for Bearing Fault Simulation. *COMADEM 2008 (Condition Monitoring and Diagnostic Engineering Management)*. Prague, Czech Republic.

Sawalhi, N & Randall, RB 2008b. Simulating gear and bearing interactions in the presence of faults: Part II: Simulation of the vibrations produced by extended bearing faults. *Mechanical Systems and Signal Processing*, 22, 1952-1966.

- Sawalhi, N & Randall, RB 2011a. Signal pre-whitening using cepstrum editing (liftering) to enhance fault detection in rolling element bearings. *24th International Congress on Condition Monitoring and Diagnostics Engineering Management (COMADEM2011)*. Stavanger, Norway.
- Sawalhi, N & Randall, RB 2011b. Vibration response of spalled rolling element bearings: Observations, simulations and signal processing techniques to track the spall size. *Mechanical Systems and Signal Processing*, 25, 846-870.
- Stokes, J. 2000. *Gearbox diagnostics*. B.E. Thesis, The University of New South Wales, Sydney, Australia.
- Sweeney, P. 1994. *Transmission error measurement and analysis* Ph. D. Dissertation, University of New South Wales, Sydney, Australia.

PART II

SIMULATION OF PLANET GEAR FAULTS

CHAPTER 6

PLANETARY GEAR TRAINS: VIBRATION ANALYSIS AND SIMULATION TECHNIQUES

6.1 Introduction

Modelling of the UNSW single stage parallel shaft spur gearbox and the simulation of *bearing faults* was described in Part I of this research thesis (Chapters 3-5). The relevant literature pertaining to the simulation and extraction of bearing faults was covered in Chapter 2. The Part II of the thesis describes the modelling of the UNSW planetary gearbox and simulation of *gear faults*. The UNSW planetary gearbox was built by inserting the planetary gear set (comprising the sun gear, ring gear and the planets mounted on the planet carrier) into the existing gearbox casing. The details of the UNSW planetary gearbox are given in chapter 7. This chapter provides an extensive literature review of the planetary gear fault simulation techniques.

Planetary gears are widely used to transmit power in many applications such as automotive, aircraft, marine and wind turbines. Some of the advantages of planetary transmissions are compactness due to co-axial shaft arrangement, large torque-to-weight ratio due to load sharing by multiple sun and ring gear meshes and high power efficiency. However, similar to the parallel shaft spur gear transmissions, the planetary systems are also not immune to the problems arising from the gear vibrations. The prediction of noise and vibration and detection of faults by machine condition monitoring are vital for the smooth operation of the planetary gearboxes in industrial applications. Dynamic simulation models offer a viable alternative to investigate the vibration characteristics of the components without the need for costly and time consuming experiments until failure. This chapter provides a review of the state of the

research pertaining to the simulation of planetary gear systems and is divided into three main sub-sections namely,

- Modelling of the planetary system
- Simulation of faults (with specific emphasis on gear faults which are investigated in this research work)
- Signal processing techniques

6.2 Modelling of the planetary system

The dynamics of planetary transmissions has been extensively studied by researchers. Early researchers developed lumped parameter models with varying complexity to conduct static and dynamic analysis and to estimate natural frequencies, vibration modes, and dynamic forces and responses through the application of mesh phasing.

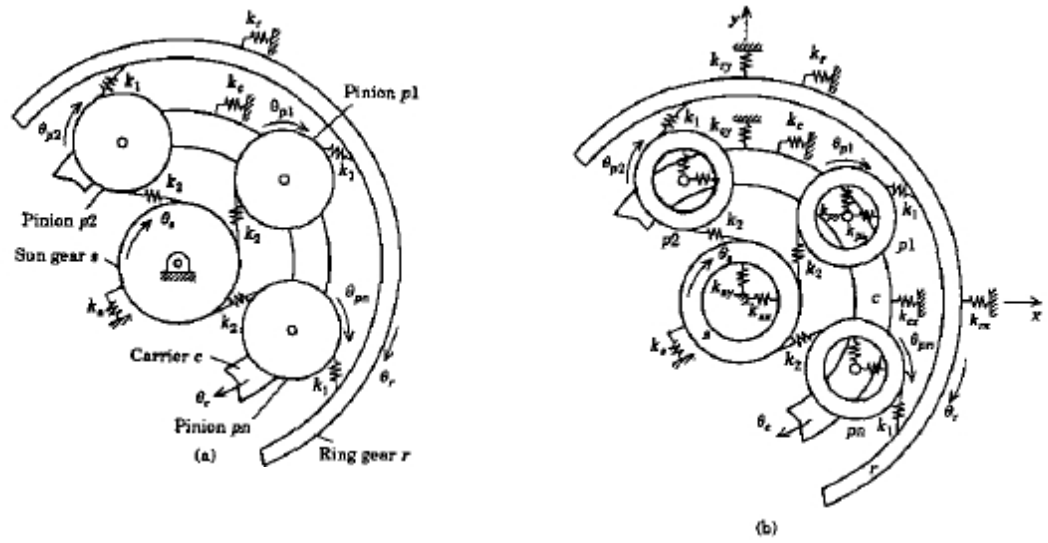
Cunliffe et al. (1974) developed a two dimensional mathematical model with 13 degrees of freedom (DOFs) and six nonlinear tooth meshes to predict natural frequencies, mode shapes and tooth mesh forces. The damping was applied only at the supports and the damping across the mesh in dynamic tooth contacts was ignored.

Ma and Botman (1985) used a mathematical model of a five planet planetary system to determine dynamic tooth loads and load sharing among planets by taking into account the effects of nonlinear tooth stiffnesses, ring gear flexibility, gear errors and misalignment. However, the simplified model included the effect of transmission error (which contributes to dynamic excitation) in only one of the planet gears and the other planets, ring and sun gears were assumed ideal.

The dynamic response of a lumped model (Saada and Velez, 1995) induced by mesh parametric excitations was examined by Velez and Flamand (1996) using the computationally efficient Ritz method. The procedure was validated by comparing with the results given by direct integration.

A simplified pure torsional model of a single stage planetary gear set was proposed by Kahraman (1994b) to obtain closed form expressions for natural modes of a planetary gear train. The pure torsional model (Figure 6.1a) was found to be reasonably accurate

within the large range of bearing stiffnesses however, the transverse-torsional model developed by Kahraman (1994a), provides a more general and accurate means of modelling planetary gear sets. The transverse-torsional model (Figure 6.1b) which takes into account the nonlinear time varying effects of mesh stiffness fluctuations and tooth separations was used to simulate the dynamic load sharing characteristics of a general planetary transmission with an arbitrary number of planets. The model was also used to study the sensitivity of dynamic load sharing characteristics to design parameters and manufacturing and assembly related variations of the planetary transmissions.



(a) Torsional model: $(n+3)$ dofs

(b) Transverse-Torsional model: $3(n+3)$ dofs

Figure 6.1 Planetary gear set dynamic models (n = no of planets) (Kahraman, 1994b)

Lin and Parker (1999a) developed an analytical model to investigate the unique properties of planetary gear free vibration of equally spaced planets using a 2D torsional-translational model as shown in Figure 6.2. It was shown that these special unique properties result from the cyclic symmetry of the planets and all vibration modes can be classified into one of three types, namely, rotational, translational and planet modes.

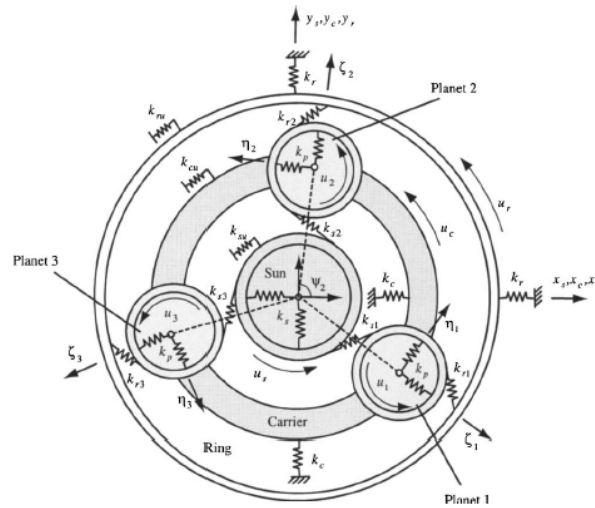


Figure 6.2 Planetary gear lumped-parameter analytical model
(Ambarisha and Parker, 2006)

However, in certain applications, assembly limitations may cause the planets to be unequally spaced resulting in the loss of cyclic symmetry. The analytical model was further developed to evaluate structured vibration characteristics of planetary gears with unequally spaced or diametrically opposite planets (Lin and Parker, 2000) and it was shown that the unique modal properties of the equally spaced planet systems are preserved in the unequally spaced planet systems. The same analytical model was also used to investigate sensitivities to key planetary design parameters such as mesh and support stiffnesses, component masses, moment of inertia, and operating speed (Lin and Parker, 1999b).

In the case of high speed planetary gears used in turbo-fan and turbo-prop engine applications, the gyroscopic effect becomes significant and needs to be included in the equations of motion for the 2D torsional-translational model. The high speed planetary gears were also found to have structured vibration properties with three distinct mode types, namely, rotational, translational and planet modes (Cooley and Parker, 2012).

6.2.1 Mesh phasing

The 2D dynamic models were also used to examine relative phase relationships among multiple planetary gear meshes and it was shown that by selecting the number of planet gears, certain planet position angles and tooth number combinations, it is possible to neutralise or cancel the individual gear mesh forces that get transmitted to the housing

(Seager, 1975, Toda and Botman, 1979, Palmer and Fuehler, 1977). The self-equilibrium of the mesh forces reduces the net forces and torques on the sun, ring and carrier. Hence planet phasing offers an economically viable means of reducing planetary gear vibration since no elaborate design changes or stringent manufacturing tolerances are required (Parker and Wu, 2012b).

During the operation of planetary gears, resonant response is produced if the mesh frequency or its harmonics are close to a natural frequency. The increased vibration and noise due to large dynamic tooth loads increases the risk of fatigue failure and hence mesh phasing can be used to selectively eliminate resonant conditions. Parker and Ambarisha (2006) analytically derived design rules using a 2D lumped parameter analytical model to suppress certain harmonics of planet mode response in planetary gear dynamics through mesh phasing using symmetry of planetary gear systems and gear tooth mesh periodicity.

Mesh stiffness variation due to changing number of teeth in contact causes parametric excitation of the system which can lead to instability such as tooth separation, increased dynamic loads and damage to gears and bearings. Lin and Parker (2002) used a torsional vibration model with different contact ratios and planet phasing to identify operating conditions leading to parametric instability. It was shown that under certain phasing conditions (through proper selection of design parameters); particular parametric instabilities can be eliminated.

Most of the 2D Planetary Gear Train (PGT) models considered mainly spur gears. However, helical gears are especially preferred in automotive transmissions due to their quieter nature. Kahraman (1994c) developed a generic dynamic model of a planetary gear train with helical gears to perform a parametric study on the effect of planet mesh phasing and cancellation of gear mesh forces on the dynamic behaviour. The linear time-invariant equations of motion were solved to obtain the natural modes and the forced vibration response due to static transmission errors.

A purely torsional non-linear time-varying dynamic model was proposed by Al-shyyab and Kahraman (2007) which takes into account periodically time-varying gear mesh stiffnesses, gear backlash clearances and phasing relationships as a function of planet

position angles, number of planets and number of teeth on the gears. The non-linear equations of motion were solved using a harmonic balance method (HBM) and the solution was compared with numerical simulation results.

The majority of the earlier planetary models used constant pressure angle and contact ratios. However, Kim et al. (2012) showed that the translational motions of component gears due to bearing deformation can result in time-varying pressure angles and contact ratios. The resulting coupled non-linear equations of motion were derived using Lagrange's equation. It was found that the dynamic response exhibits more frequency components and greater dynamic radial displacement of planetary gears when compared with the model with constant pressure angle and contact ratios.

6.2.2 Deformable gear models

All the above lumped parameter models assume gears as rigid bodies with the tooth meshes and support bearings represented using springs and dampers. In certain applications e.g. aerospace, a thin ring gear is used to maximise the power density, minimise the mass and improve load sharing among planets. Hence recently, dynamic simulation models with deformable gear bodies have been developed by researchers and some of these use a commercial finite element software 'Calyx' (Vijayakar). Parker et al. (2000) examined the dynamic response of a helicopter planetary gear system using a unique semi-analytical finite element/tooth contact mechanics model. The contact model employed uses FEM (Figure 6.3) and surface integral methods in conjunction, which significantly reduces the computational and memory requirements (Vijayakar, 1991). The main advantage of this approach is that the dynamic excitation comprising time-varying mesh stiffnesses and transmission errors is evaluated internally (within the FE model) at each time step, thus eliminating the need to provide these externally as in the case of conventional LPMs where they are often difficult to measure or estimate, especially in the case of planetary gears.

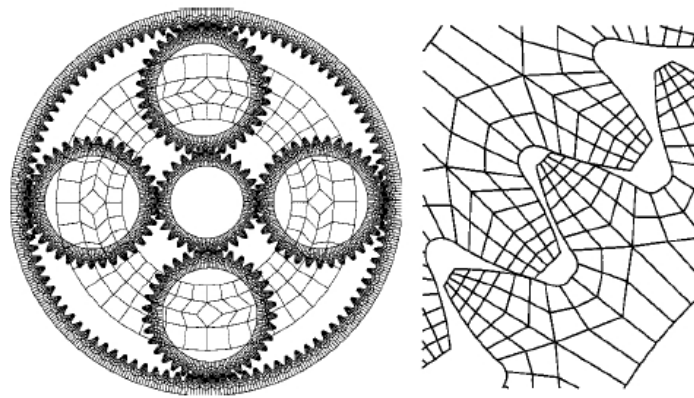


Figure 6.3 Planetary gear system – Finite element mesh (Parker et al., 2000)

Kahraman and Vijayakar (2001) investigated the influence of the flexibility of an internal gear on the quasi-static behaviour of a planetary gear set of a typical automotive transmission using a state-of-the-art nonlinear contact mechanics formulation. The model included all of the gears of a planetary gear set in their deformable form and was used to quantify the impact of the internal gear flexibility on the gear stresses and deflections. It was reported that a flexible internal gear helps improve the load sharing amongst the planets, especially in the presence of manufacturing and assembly related gear and carrier errors, although not as effectively as the method of floating the sun gear. The model was further analysed by introducing an additional generalised rim thickness parameter that takes into account the size of the gears and was used to quantify the impact of the gear rim flexibilities in dynamic gear tooth stresses (Kahraman et al., 2003) which were found to be significantly higher for all of the gears for a flexible internal gear as compared to the rigid internal gear. The study also emphasised the use of deformable body analysis, especially when the gear rims are rather flexible so as to properly represent the rim bending modes and to accurately predict the overall planetary gear set modes.

Wu and Parker (2008) studied modal properties of equally spaced planetary gears with elastic ring gears, also referred as the elastic-discrete model (Figure 6.4) and analytically determined the properties of the vibration modes which were classified into rotational, translational, planet and purely ring modes. The model, when applied for the case of diametrically opposed planets, showed only two types of modes, namely, the translational and the rotational (Parker and Wu, 2010). The elastic-discrete model was

also used to examine planetary gear parametric instabilities in case of equally spaced planets with in-phase and sequentially spaced mesh conditions (Parker and Wu, 2012a).

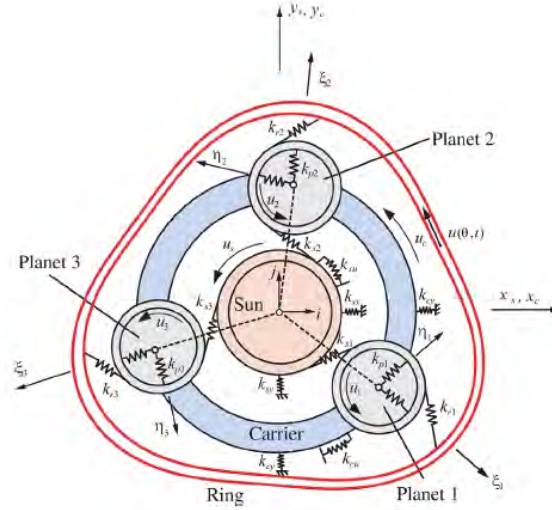


Figure 6.4 Elastic-discrete model of a planetary gear (Parker and Wu, 2012a)
(The distributed springs around the ring circumference are not shown.)

A discrete lumped parameter model of a planetary system was developed by Zhang et al. (2011) that includes the flexibility of the ring gear by dividing it into finite rigid segments connected through springs. The ring gear flexibility was found to decrease lower natural frequencies of planetary gears and the vibration modes were classified into rotational, translational, planet and ring modes.

Ambarisha and Parker (2007) used both the lumped parameter and finite element models to examine the complex, nonlinear dynamic behaviour of spur planetary gears. The comparison of dynamic responses validated the effectiveness of the lumped parameter model to simulate the dynamics of the planetary gears.

Depending on the number of planets, planet positions and the numbers of teeth on the gears, the multiple tooth meshes in planetary gears have varying numbers of teeth in contact, all of which fluctuate at the same mesh frequency. All sun-planet and ring-planet meshes have the same shape and periodicity which may differ in phase. In-phase configuration (identical mesh conditions i.e. number of teeth in contact) result in the load being shared equally between the sun-planet and ring-planet tooth meshes. However, differing mesh phasing can be used to suppress planetary gear vibration in certain harmonics of the mesh frequency and can have a dramatic impact on the

dynamic response with significant benefits in reducing noise and vibration (Parker, 2000). The required relationships to incorporate mesh phasing in analytical models were provided by Parker and Lin (2004).

Most of the analytical models developed earlier were not validated by controlled experiments to demonstrate the independent motion of planetary gear components. Ericson and Parker (2011) carried out experimental modal testing and spinning tests to characterise the dynamic behaviour of a spur planetary gear under operating conditions. The experimentally observed natural frequencies, modes, and forced response correlated well with those predicted by the lumped parameter model (Lin and Parker, 1999a). The presence of analytically observed vibration modes - rotational, translational and planet modes were confirmed by the experiments. In a further study (Ericson and Parker, 2013) the experimental results were correlated against a 2D finite element model developed using a commercial software 'Planetary 2D' (Vijayakar, 2006).

6.3 Modelling faults in planetary gear sets

The lumped parameter models described earlier in Section 6.2 were used to analyse the dynamic characteristics of the planetary gears such as natural frequencies, mode shapes, dynamic response etc. The review of the literature also emphasises the popularity of planetary LPMs to generate simulated vibration signals in the presence of gear and bearing faults, mainly due to the inherent benefits offered by the simulations such as reduced number of experiments to failure and automation of the fault diagnostic and prognostic processes.

The vibration signals from the UNSW planetary gear test rig were collected in the presence of both planet gear faults and planet bearing faults, the results of which were presented in two conference papers (Smith et al., 2013a, Smith et al., 2013b). However, the planetary simulation model developed as part of this research includes only the faults on the planet gear and comparison of the simulated vibration signals with the measured signals. Hence the existing literature pertaining to the simulation of *planetary gear faults*, and the corresponding signal processing techniques, is assessed in this thesis.

Orbital motion of the planets and multiple gearmeshes with higher dynamic loads (large torque to weight ratio) make planetary transmissions more complex and susceptible to fatigue failure due to tooth defects such as spalls and tooth root cracks. Gear tooth damage can adversely affect the dynamic behaviour of the planetary system with unacceptable noise and vibration characteristics.

Wang and Howard (2010) described a coupled transverse-torsional lumped-parameter dynamic model of a planetary gearbox; with a fluid coupling as an extra degree of freedom to assist with smooth start-up. The model takes into account variable tooth mesh stiffness, pitch and profile excitation and sun gear tooth faults (cracks and spalls of varying lengths and depths). The results were processed using frequency analysis and signal averaging techniques which were effective in indicating the tooth cracks but not sensitive enough to detect small spalls.

Chaari et al. (2011) investigated the dynamic behaviour of a planetary gear transmission with local damage on the sun gear with time varying load conditions. Three increasing sizes of damage were modelled as a reduction in the gearmesh stiffness between the sun and the planets. Spectral kurtosis was used to extract the impulsive part of the signal and to examine the influence of load, damage size and time varying transmission path on the impulse amplitudes.

Chen and Shao (2013) developed a dynamic model of a single stage planetary gear set with 21 degrees of freedom to investigate the effect of an internal gear tooth root crack. The mesh stiffness model of the internal gear pair with a tooth root crack in the ring gear was based on the potential energy principle which was incorporated into the dynamic model. The effect of the tooth root crack was seen as impulsive vibrations and sidebands in the dynamic response in the time and frequency domains, respectively.

Bahk and Parker (2011) studied the impact of tooth profile modification (TPM) on planetary gear dynamic response, which directly affects the gear noise and vibration and contact stresses. TPM was included in the LPM model (Lin and Parker, 1999a) which takes into account time-varying mesh stiffness and nonlinearity due to tooth contact loss. The results were correlated with those of a finite element model (Ambarisha and Parker, 2007).

A 2D pure torsional lumped parameter model was used to simulate sun gear tooth pitting (Cheng et al., 2011) and tooth breakage (Cheng and Niaoqing, 2011). The gear mesh stiffness of the sun-planet gear pair was calculated using a finite element contact model, taking into account geometric changes due to tooth pitting or tooth breakage (Figure 6.5 and 6.6). A feature extraction and selection approach was used to detect the severity of damage quantitatively.

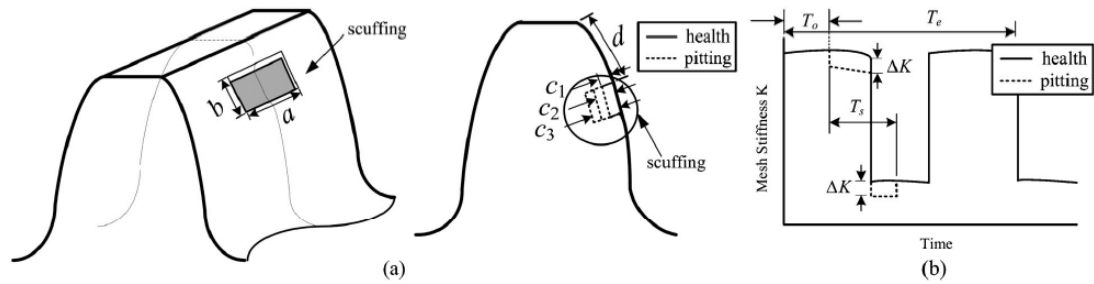


Figure 6.5 Gear mesh stiffness evolution with tooth pitting damage (Cheng et al., 2011)

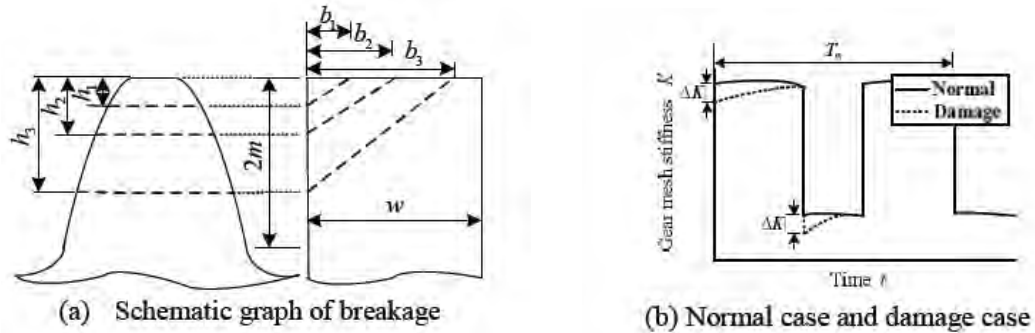


Figure 6.6 Gear mesh stiffness evolution with tooth breakage (Cheng and Niaoqing, 2011)

Chaari et al. (2006) examined the dynamic behaviour of a planetary gear train using a planar transverse-torsional model in the presence of sun gear tooth pitting and cracking. The two defects were modelled by a phase shift and a reduction in the gear mesh stiffness. The dynamic responses of the healthy planetary gear and with the tooth defect were compared using a time-frequency Wigner-Ville distribution, which enabled the determination of the defect location. However, damping at the gearmesh and at the bearing supports was not included in the model.

The above simulation models use the reduction in the gear mesh stiffness to model both types of gear faults (tooth crack and spall). However, Endo et al. confirmed that the

presence of spalls primarily results in additional geometric variations in the transmission error and is independent of load, whereas the effect of cracks is load dependent and can be modelled as a change in the gearmesh stiffness (Endo et al., 2004, Endo et al., 2009).

Yuksel and Kahraman (2004) used a deformable-body dynamic model (Kahraman et al., 2003) combined with a gear wear prediction model to investigate the influence of tooth surface wear on the dynamic behaviour of planetary gear sets.

6.3.1 Analytical models to predict sideband mechanisms

Fault diagnoses of planetary gear sets require a thorough understanding of the spectral structure to identify the presence of characteristic fault frequencies and associated modulating sidebands. Analytical models based on mathematical formulations have been developed to generate vibration signal models with and without gear/bearing faults.

Inalpolat and Kahraman (2009) investigated analytically and experimentally the mechanism of sidebands in planetary gear sets. Based on the number of planets, planet position angles and number of teeth on the stationary gear they classified the planetary gear sets into five categories each with distinct sideband behaviour in terms of spectral amplitudes and frequencies. The model included the amplitude modulation (AM) effects caused by the carrier rotation but neglected the frequency modulation (FM) effects caused by time-varying mesh stiffness and gear damage, which limited its application to undamaged planetary gear sets. In a further study, both the AM and FM effects were incorporated into a non-linear time varying dynamic model (Kahraman, 1994a) to predict the modulation sidebands due to manufacturing errors (Inalpolat and Kahraman, 2010).

Feng and Zuo (2012) considered AM/FM effects due to gear faults and periodically varying running speed (or load), and in the signal transmission path to develop mathematical models of faulty planetary vibration signals and derive their Fourier transforms. The characteristic frequency of each faulty gear was explicitly defined and used to explain the appearance of modulating sidebands and to detect and locate various gear faults.

6.3.2 Effect of transfer path on the vibration signal

Behaviour of sidebands in planetary gear vibration signals is influenced by the effect of the transfer path. The damage induced vibration signal at the meshing location has three possible paths from its origin to the sensor location as shown in Figure 6.7. For a damaged planet gear (which is also the subject of investigation using the UNSW planetary gear rig) these can be summarised as:

1. Vibration signal propagates from its origin to the ring gear and then to the gearbox casing and to the sensor.
2. From the origin (garmesh location) to the sun gear and then through the supporting shaft and bearings to the casing and finally to the sensor.
3. From the signal origin to the planet carrier and then through carrier supporting shaft and bearings to the casing and finally to the sensor.

Feng and Zuo (2012) argued that the second and the third paths only have a scaling effect rather than an AM effect during the propagation of the signal, and the vibration signal perceived by the sensor is likely to have negligible amplitude as a result of the longer transfer path and increased damping. In the case of the first path, the sensor receives a stronger signal due to the shorter path avoiding the bearings, which may cause attenuation of the signal. The transfer path through the first path is time-varying (except in the case where the ring gear is held stationary and the damage is on a ring gear tooth.).

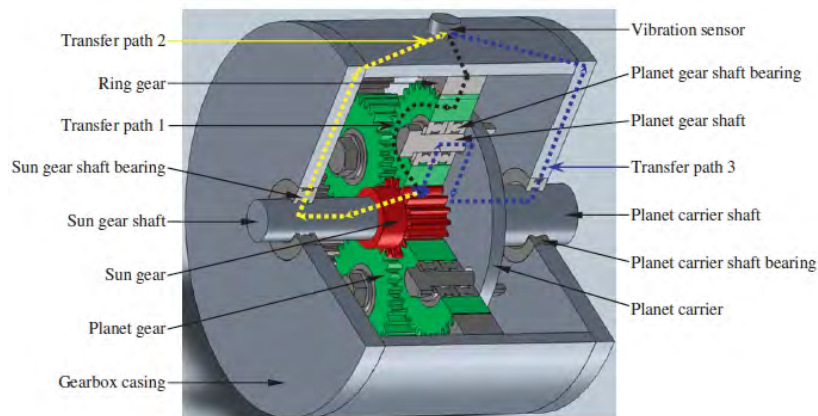


Figure 6.7 Transfer path with fault on the planet gear (Feng and Zuo, 2012)

6.4 Signal processing techniques

A detailed explanation of the source of gear vibrations and the interpretation of the vibration signals in both the time and the frequency domains was given by Randall (2011). The presence of sidebands around the gearmesh frequency (and its harmonics) caused by the gear tooth fault was discussed using graphical representations of the amplitude and phase modulation effects. The causes of the vibration induced by the gears and the conventional methods of gear fault diagnosis are discussed in detail in Chapter 2. These methods, although valid in case of planetary gears, cannot be directly applied without additional signal processing as explained below.

Condition monitoring of planetary systems, which are widely deployed in the automotive, aerospace and wind turbine industries, is extremely important to ensure the safe operation throughout the product life cycle and to enable design optimisation by reducing the noise and vibration. The traditional method of signal averaging in the time domain is quite effective in detecting gear faults, which facilitates the separation of the vibration signatures of individual fixed axis gears from the total vibration in the gearbox. However, the method cannot be applied as effectively to planetary gearboxes, mainly due to the rotating axes of the planet gears and the multiple tooth contacts where each planet gear simultaneously meshes with the sun and the ring gear. The conventional signal averaging method can only generate a single composite time domain average of all the planet gears and will not show clearly the vibration signature of individual planet gears with embedded fault characteristics (McFadden, 1991).

Vibration signals from the planetary gearboxes are normally collected by mounting an accelerometer exterior to the casing and located at the ring gear. As each planet approaches the location of the transducer, maximum amplitude of the vibration will be reached when the planet is closest to the transducer and the amplitude will gradually reduce as the planet moves away from the transducer, giving Amplitude Modulation (AM) and this is the main mechanism causing planetary gear sidebands. This relative motion of the planet gears with respect to the transducer location gives rise to planet pass modulation which is given by $N \cdot f_c$ where N is the number of planets and f_c is the planet carrier frequency (Forrester, 1998). In addition to the sidebands caused by the rotating carrier, gear manufacturing errors such as eccentricities and run-out errors of

the gears and the carrier, and tooth-to-tooth spacing, tooth thickness and indexing errors can cause three types of modulations namely, AM, Frequency Modulation (FM) and Phase Modulation (PM). The sidebands can also result due to the relative motion of the central members (such as a floating sun gear), deformation of components and planet load sharing characteristics (Inalpolat and Kahraman, 2009).

The total vibration measured by an external accelerometer is the sum of the vibrations of all the planet gears with different relative phases. McFadden (1991) proposed a windowing technique to store the vibration signals of the individual planets (generated by the planet-ring and planet-sun meshing) as the planet passes the transducer mounted on the annulus gear. The windows can be mapped to capture the complete time domain average of the tooth meshing vibration as shown in Figure 6.8.

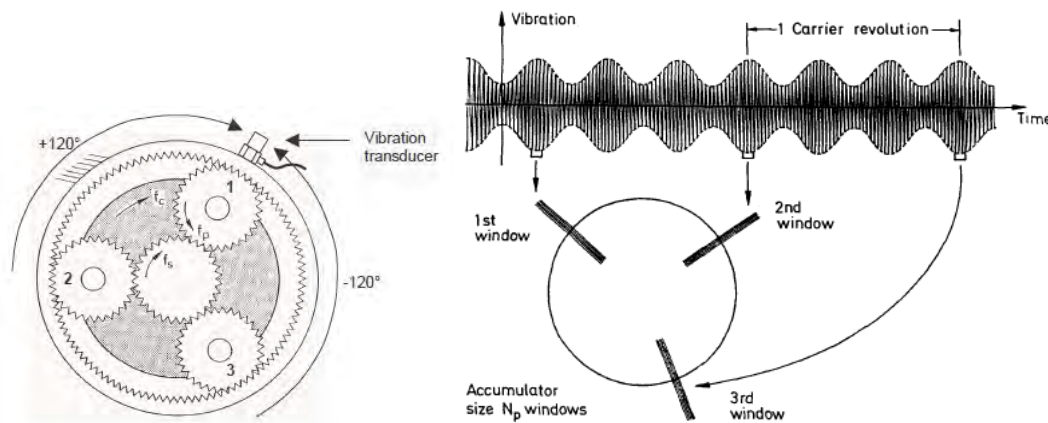


Figure 6.8 Signal modulation as seen by an externally mounted accelerometer (Forrester and Blunt, 2003, McFadden and Howard, 1990)

The signal enhancement achieved through the windowing technique (also referred to as snap-shot) was able to detect the seeded planet and sun gear tooth faults in a test rig (Howard, 1991, McFadden and Howard, 1990). However, the excessive time required to generate useable signal averages and discontinuities at the window boundaries leading to error terms in the time domain averages, were the main limitations of this method. Note that McFadden revised his earlier time domain averaging technique (which was based on a rectangular window of one toothmesh period) by using a Hanning window of total length twice the toothmesh period to eliminate these discontinuities (McFadden, 1994).

Also the technique is primarily applicable only to planetary gearboxes with hunting tooth design. Hunting ratios, where each pinion tooth contacts every gear tooth tend to equalize tooth wear and are generally preferred in industrial applications.

McFadden and Smith (1985) investigated the asymmetry of modulation sidebands and complete suppression of some of the principal meshing components observed in the vibration spectra of planetary gearboxes. It was shown that the vibration modulation is caused by the motion of the planets relative to the transducer and the different planet phases cause the asymmetry of the sidebands. Their model was able to predict the frequency content of the dominant vibration peaks of a planetary gear set, but not the relative amplitude content.

MaFadden's planet separation and signal averaging method shown in Figure 6.9 was used by Lewicki et al. (2011) to detect planetary gear and bearing faults in helicopter main rotor transmissions. The health of the gears was assessed based on the condition indicators which measure statistically the energy content of the vibration signal (Samuel and Pines, 2005).

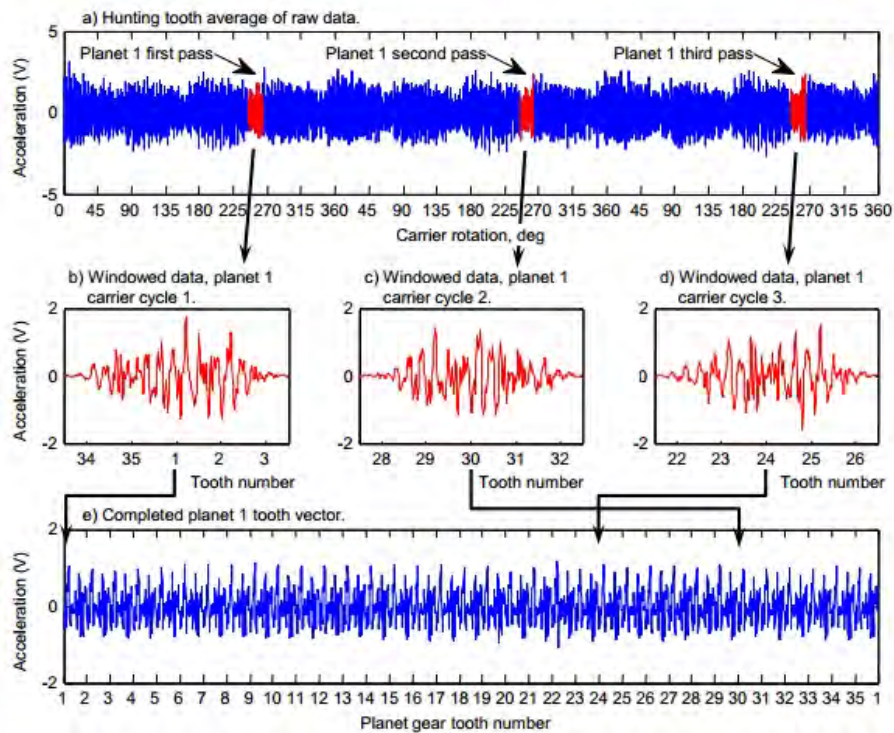


Figure 6.9 Planet gear vibration separation based on McFadden's method (Lewicki et al., 2011)

Forrester (1998) patented a specialised planet-separation algorithm to separate the individual planet vibration signatures based on selective time filtered signal averaging that takes into account each planet's contribution to the total vibration signal. The method overcomes the limitations of the snap-shot method described earlier. The significant reduction in the time required to perform separation of planet signatures enables its implementation in an operational aircraft. The method was shown to be effective in identifying planet gear and sun gear tooth spalls, where the kurtosis of the vibration signal obtained by the planet separation technique clearly indicated the presence of a fault (Forrester and Blunt, 2003).

Blunt and Keller (2006) used the planet separation method to detect a fatigue crack in a planet carrier of US army Black Hawk helicopter main transmissions. However, the method was found to be reliable mainly under test-cell conditions and ineffective under low-torque on-aircraft conditions, where less stable load environments may exist.

Planetary gearboxes used in wind turbine applications are subjected to frequent changes of wind speed leading to massive and rapid changes in the load and the output power. The conventional gear diagnostic techniques based on synchronous averaging require vibration measurements at constant speed and hence cannot be used in these situations. Barszcz and Randall (2009) applied the Spectral Kurtosis (SK) technique to detect a tooth crack in the planetary ring gear of a wind turbine. The catastrophic gear failure could not be detected by conventional methods including synchronous averaging, whereas the proposed method based on the SK was able to detect the existence of tooth crack several weeks before the gear failure.

6.5 Planetary simulation model developed in this study

One of the objectives of this research is the simulation of vibration caused by faults in a planet gear. The main differences between the fault simulation model of the planetary gearbox developed in the current research and the majority of published works are:

- The dynamic lumped parameter model of the planetary system is set up using a Simulink® block diagram by extending Endo's parallel shaft single stage gearbox simulation model (Endo, 2005). The planetary model includes multiple gear meshes (six in the current configuration with three equally spaced planets) to represent sun-

planet and ring-planet contacts. The position dependent (time-varying) gearmesh stiffness curve and transmission error (TE) curve were generated externally and incorporated in the Simulink® model with proper phase relationships. These were defined such that the timing of the gearmesh was synchronised with the time step defined in the simulation model. The time varying mesh stiffness along with the displacements, rotational speed of the planet carrier and the time increments were incorporated in the Simulink® model by defining a special Matlab® S-function.

- The effect of the two simultaneous meshes of the planet gear with the ring and sun gears was investigated since the contact with the two gears is on opposite flanks of the planet gear tooth. The fault induced vibration signals were analysed based on a combination of the conventional diagnostic techniques (dictated by the extreme non-hunting tooth design of the UNSW planetary gearbox) with the aim of obtaining clear differentiation between the two types of faults since the reduction in the stiffness due to a tooth crack will be visible in both contacts whereas a spall on one flank will be seen in only one contact.

The details of the planet gear fault simulation model and the comparison of the measured and the simulated vibration signals are presented in Chapter 7.

6.6 References

- Al-shyyab, A & Kahraman, A 2007. A non-linear dynamic model for planetary gear sets. *Proc. IMechE Part K: J. Multi-body Dynamics*, 221.
- Ambarisha, VK & Parker, RG 2006 Suppression of planet mode response in planetary gear dynamics through mesh phasing. *Journal of Vibration and Acoustics*, 128 133-142.
- Ambarisha, VK & Parker, RG 2007. Nonlinear dynamics of planetary gears using analytical and finite element models. *Journal of Sound and Vibration*, 302, 577-595.
- Bahk, C-J & Parker, RG 2011. A study on planetary gear dynamics with tooth profile modification. *Proceedings of the ASME 2011 International Design Engineering*

Technical Conferences & Computers and Information in Engineering Conference. Washington, DC, USA.

- Barszcz, T & Randall, RB 2009. Application of spectral kurtosis for detection of a tooth crack in the planetary gear of a wind turbine. *Mechanical Systems and Signal Processing*, 23, 1352-1365.
- Blunt, DM & Keller, JA 2006. Detection of a fatigue crack in a UH-60A planet gear carrier using vibration analysis. *Mechanical Systems and Signal Processing*, 20, 2095-2111.
- Chaari, F, Fakhfakh, T & Haddar, M 2006. Dynamic analysis of a planetary gear failure caused by tooth pitting and cracking. *Journal of Failure Analysis and Prevention*, 6, 73-78.
- Chaari, F, Zimroz, R, Bartelmus, W, Fakhfakh, T & Haddar, M 2011. Modelling of planetary gearbox for fault detection. Investigation on local damage size and time-varying load conditions influence to vibration response. *The Eighth International Conference on Condition Monitoring and Machinery Failure Prevention Technologies*. Cardiff, UK.
- Chen, Z & Shao, Y 2013. Dynamic simulation of planetary gear with tooth root crack in ring gear. *Engineering Failure Analysis*, 31, 8-18.
- Cheng, Z, Hu, N, Gu, F & Qin, G 2011. Pitting damage levels estimation for planetary gear sets based on model simulation and grey relational analysis. *Transactions of the Canadian Society for Mechanical Engineering*, 35, 403-417.
- Cheng, Z & Niaoqing, H 2011. Quantitative damage detection for planetary gear sets based on physical models. *Chinese journal of mechanical engineering*, 24.
- Cooley, CG & Parker, RG 2012. Vibration Properties of High-Speed Planetary Gears With Gyroscopic Effects. *Journal of Vibration and Acoustics*, 134, 061014-1-11.
- Cunliffe, F, Smith, JD & Welbourn, DB 1974. Dynamic Tooth Loads in Epicyclic Gears. *J. Manuf. Sci. Eng.*, 96(2), 578-584.

- Endo, H. 2005. *Simulation of gear faults and its application to the development of differential diagnostic technique* Ph. D. Dissertation, University of New South Wales, Sydney, Australia.
- Endo, H, Randall, RB & Gosselin, C 2004. Differential diagnosis of spall versus cracks in the gear tooth fillet region. *Journal of Failure Analysis and Prevention*, Volume 4(5), 63-71.
- Endo, H, Randall, RB & Gosselin, C 2009. Differential diagnosis of spall vs. cracks in the gear tooth fillet region: Experimental validation. *Mechanical Systems and Signal Processing*, 23, 636-651.
- Ericson, TM & Parker, RG 2011. Planetary Gear Modal Properties and Dynamic Response: Experiments and Analytical Simulation. *ASME 2011 International Design Engineering Technical Conferences and Computers and Information in Engineering Conference*. Washington, DC, USA.
- Ericson, TM & Parker, RG 2013. Planetary gear modal vibration experiments and correlation against lumped-parameter and finite element models. *Journal of Sound and Vibration*, 332, 2350-2375.
- Feng, Z & Zuo, MJ 2012. Vibration signal models for fault diagnosis of planetary gearboxes. *Journal of Sound and Vibration*, 331, 4919-4939.
- Forrester, BD 1998. A method for the separation of epicyclic planet gear vibration signatures. *Third International Conference on Acoustical and Vibratory Surveillance Methods and Diagnostic Techniques*. Senlis, France.
- Forrester, D & Blunt, D 2003. Analysis of epicyclic gearbox vibration. *HUMS 2003 Conference*.
- Howard, IM 1991. An investigation of vibration signal averaging of individual components in an epicyclic gearbox. *Propulsion Report 185*, Department of Defence, Aeronautical Research Laboratory.

- Inalpolat, M & Kahraman, A 2009. A theoretical and experimental investigation of modulation sidebands of planetary gear sets. *Journal of Sound and Vibration*, 323, 677-696.
- Inalpolat, M & Kahraman, A 2010. A dynamic model to predict modulation sidebands of a planetary gear set having manufacturing errors. *Journal of Sound and Vibration*, 329, 371-393.
- Kahraman, A 1994a. Load sharing characteristics of planetary transmissions. *Mechanism and Machine Theory*, 29, 1151-1165.
- Kahraman, A 1994b. Natural Modes of Planetary Gear Trains. *Journal of Sound and Vibration*, 173, 125-130.
- Kahraman, A 1994c. Planetary gear train dynamics. *Journal of Mechanical Design* 116, 713-720.
- Kahraman, A, Kharazi, AA & Umrani, M 2003. A deformable body dynamic analysis of planetary gears with thin rims. *Journal of Sound and Vibration*, 262, 752-768.
- Kahraman, A & Vijayakar, S 2001. Effect of internal gear flexibility on the quasi-static behavior of a planetary gear set. *Journal of Mechanical Design*, 123, 408-415.
- Kim, W, Lee, JY & Chung, J 2012. Dynamic analysis for a planetary gear with time-varying pressure angles and contact ratios. *Journal of Sound and Vibration*, 331, 883-901.
- Lewicki, DG, LaBerge, KE, Ehinger, RH & Fetty, J 2011. Planetary Gearbox Fault Detection Using Vibration Separation Techniques, NASA Report NASA/TM-2011-217127. *American Helicopter Society 67th Annual Forum and Technology Display*, . Virginia Beach, Virginia, USA.
- Lin, J & Parker, RG 1999a. Analytical Characterization of the Unique Properties of Planetary Gear Free Vibration. *Journal of Vibration and Acoustics*, 121, 316-321.

- Lin, J & Parker, RG 1999b. Sensitivity of planetary gear natural frequencies and vibration modes to model parameters. *Journal of Sound and Vibration*, 228, 109-128.
- Lin, J & Parker, RG 2000. Structured vibration characteristics of planetary gears with unequally spaced planets. *Journal of Sound and Vibration*, 233, 921-928.
- Lin, J & Parker, RG 2002. Planetary gear parametric instability caused by mesh stiffness variation. *Journal of Sound and Vibration*, 249, 129-145.
- Ma, P & Botman, M 1985. Load Sharing in a Planetary Gear Stage in the Presence of Gear Errors and Misalignment. *Journal of Mechanical Design*, 107, 4-10.
- McFadden, PD 1991. A technique for calculating the time domain averages of the vibration of the individual planet gears and the sun gear in an epicyclic gearbox. *Journal of Sound and Vibration*, 144, 163-172.
- McFadden, PD 1994. Window functions for the calculation of the time domain averages of the vibration of the individual planet gears and sun gear in an epicyclic gearbox. *Journal of Vibration and Acoustics*, 116, 179-187.
- McFadden, PD & Howard, IM 1990. The detection of seeded faults in an epicyclic gearbox by signal averaging of the vibration. *Propulsion Report 183*, Department of Defence, Aeronautical Research Laboratory.
- McFadden, PD & Smith, JD 1985. An explanation for the asymmetry of the modulation sidebands about the tooth meshing frequency in epicyclic gear vibration. *Proceedings of the Institution of Mechanical Engineers, Part C: Journal of Mechanical Engineering Science*, vol. 199, 65-70.
- Palmer, WE & Fuehler, RR 1977. Noise control in planetary transmissions. *SAE paper 770561*.
- Parker, RG 2000. A physical explanation for the effectiveness of planet phasing to suppress planetary gear vibration. *Journal of Sound and Vibration*, 236, 561-573.

- Parker, RG, Agashe, V & Vijayakar, SM 2000. Dynamic response of a planetary gear system using a finite element/contact mechanics model. *Journal of Mechanical Design*, 122, 304-310.
- Parker, RG & Lin, J 2004. Mesh Phasing Relationships in Planetary and Epicyclic Gears. *Journal of Mechanical Design*, 126, 365-370.
- Parker, RG & Wu, X 2010. Vibration modes of planetary gears with unequally spaced planets and an elastic ring gear. *Journal of Sound and Vibration*, 329, 2265-2275.
- Parker, RG & Wu, X 2012a. Parametric instability of planetary gears having elastic continuum ring gears. *Journal of Vibration and Acoustics*, 134(4), 041011
- Parker, RG & Wu, X 2012b. Unique symmetry phenomena in the vibration of planetary gears. *ISMA2012 International Conference on Noise and Vibration Engineering*. Leuven, Belgium.
- Randall, RB 2011. *Vibration-based Condition Monitoring: Industrial, Aerospace and Automotive Applications* [John Wiley & Sons].
- Saada, A & Velex, P 1995. An extended model for the analysis of the dynamic behavior of planetary trains. *ASME Journal of Mechanical Design*, 117, 241-247
- Samuel, PD & Pines, DJ 2005. A review of vibration-based techniques for helicopter transmission diagnostics. *Journal of Sound and Vibration*, 282, 475-508.
- Seager, DL 1975. Conditions for the neutralization of excitation by the teeth in epicyclic gearing. *Journal of Mechanical Engineering Science*, 17, 293-299.
- Smith, W, Deshpande, L, Randall, RB & Li, H 2013a. Bearing diagnostics in a planetary gearbox: a study using internal and external vibration signals. *26th International Congress of Condition Monitoring and Diagnostic Engineering Management (COMADEM 2013)*. Helsinki, Finland.
- Smith, W, Deshpande, L, Randall, RB & Li, H 2013b. Gear diagnostics in a planetary gearbox: a study using internal and external vibration signals. *The Tenth*

International Conference on Condition Monitoring and Machinery Failure Prevention Technologies (CM 2013 and MFPT 2013). Kraków, Poland.

Toda, A & Botman, M 1979. Planet indexing in planetary gears for minimum vibration. *ASME paper 79-DET-73*.

Velex, P & Flament, L 1996. Dynamic Response of Planetary Trains to Mesh Parametric Excitations. *Journal of Mechanical Design*, 118, 7-14.

Vijayakar, S 1991. A combined surface integral and finite element solution for a three-dimensional contact problem. *International Journal for Numerical Methods in Engineering*, 31, 525-545.

Vijayakar, SM Calyx user's Manual (<http://ansol.com>).

Vijayakar, SM 2006. Planetary 2D User's Manual, Advanced Numerical Solutions LLC, Hilliard, OH43026 USA.

Wang, ZW & Howard, I 2010. The Development of Lumped Mass Dynamic Modeling Methods of Planetary Gearbox for Fault Detection and Diagnosis. *Proceedings of the 6th Australasian Congress on Applied Mechanics*. Perth, W.A.

Wu, X & Parker, RG 2008. Modal properties of planetary gears with an elastic continuum ring gear. *Journal of Applied Mechanics*, 75.

Yuksel, C & Kahraman, A 2004. Dynamic tooth loads of planetary gear sets having tooth profile wear. *Mechanism and Machine Theory*, 39, 695-715.

Zhang, J, Song, Y & Xu, J 2011. A discrete lumped-parameter dynamic model for a planetary gear set with flexible ring gear. *Applied Mechanics and Materials*, 86, 756-761.

CHAPTER 7

SIMULATION OF UNSW PLANETARY GEARBOX

7.1 Introduction

An extensive overview of the dynamic modelling of planetary gearboxes was provided in Chapter 6, with particular emphasis on the gear fault simulation techniques and the complexities encountered in the vibration signal processing.

This chapter describes the development of an 18 DOF transverse-torsional dynamic model of the UNSW planetary gearbox using a Lumped Parameter Model (LPM) to simulate the vibration signals in the presence of planet gear faults such as tooth fillet cracks and spalls. A fault on the planet gear which simultaneously meshes with the ring and sun gears presents a unique challenge, since the contact with the two gears is on opposite flanks of the planet gear tooth. The aim of this study is to investigate the effect of these two simultaneous meshes of the faulty planet gear on the vibration signal.

Prior to describing the dynamic modelling techniques, the general arrangement of the UNSW planetary gear test rig along with the experimental set-up, details of the planet gear faults, and gear fault simulation methodology are illustrated. Finally, the details of the implemented vibration signal processing methodology (dictated mainly by the non-hunting design of the planetary gears) is described and the validation of the simulation model is presented by comparing the simulated results with the experimental measurements.

The UNSW planetary test rig was used to collect the vibration signals in the presence of both planet bearing and planet gear faults. The results of the experimentally measured vibration signals in the presence of planet gear faults were presented at the CM-MFPT

2013 conference (Smith et al., 2013b) whereas those in the presence of planet bearing faults were presented at the COMADEM 2013 conference (Smith et al., 2013a). However, in accordance with the aims of this study explained above, this chapter mainly focuses on the development of the planetary simulation model with only the planet gear faults. The extracted vibration signal was analysed to differentiate between the planet tooth crack and tooth spall.

7.2 UNSW Planetary gearbox: General arrangement

Figure 7.1 shows the basic layout of a planetary gearbox, for which there are many possible gearing arrangements. In the UNSW planetary gearbox used in this study, the ring gear was fixed, the planet carrier, connected to three equi-spaced planet gears, provided the input, and the sun gear the output, with all gears of the conventional spur type.

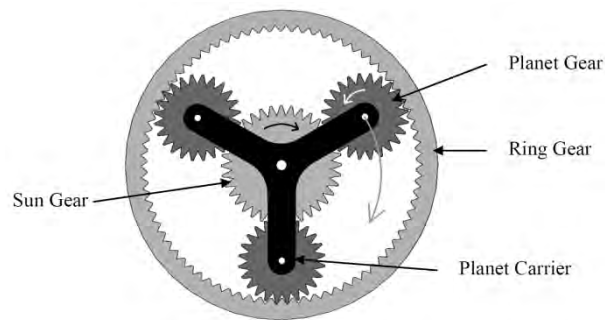


Figure 7.1 Basic layout of planetary gearbox (Bligh, 2012)

The gearbox was installed on the UNSW gear rig, which also included an initial parallel gear reduction stage. The arrangement of both gear stages is as shown in Figure 7.2, where it can be seen that the numbers of teeth on the fixed ring gear, sun gear and planet gears, respectively, were 80, 40 and 20. The input to the planetary insert was through the planet carrier which was bolted to the spur gear driven by the pinion on the drive shaft. This planetary insert arrangement – far from best-practice ‘hunting tooth’ design – was initially thought necessary due to space limitations, commercial gear availability, and the need to maintain close to a 1:1 overall ratio on the rig. The chosen arrangement provides a 1:3 increase through the planetary stage and an overall ratio of 15:16.

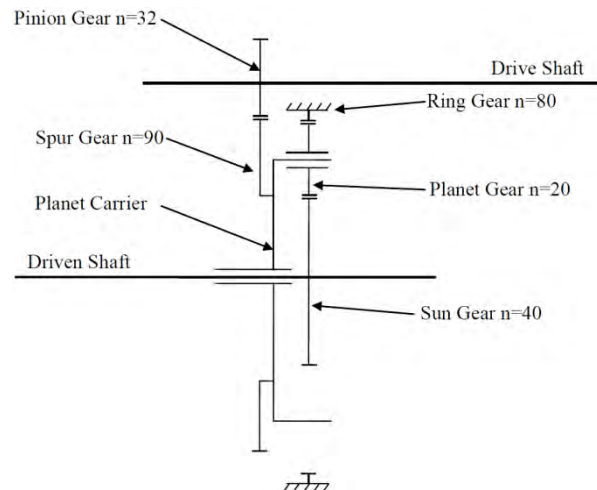


Figure 7.2 Gear details for the UNSW planetary gearbox test rig (Bligh, 2012)

Initial vibration measurements on the planetary gearbox indicated strong periodic impulsive effect at planet carrier speed possibly due to the gears “bottoming out” and was attributed to misalignment in the planetary system, especially the way in which the ring gear was assembled and fixed to the gearbox casing. This required more elaborate design modification to precisely locate the ring gear (concentric with respect to the output shaft) and fixing it to the gearbox casing. Hence an additional circular sleeve was mounted on the output shaft (on two roller bearings) to locate the ring gear concentrically with respect to the output shaft. The circular sleeve was attached to the top of the casing to prevent rotation of the ring gear [attachment not shown in Figure 7.3 for clarity]. Four cut-outs were made in the sleeve plate to facilitate the replacement of planet gears and bearings with various faults.

The planetary gearbox was capable of transmitting the vibration signals from both an internal accelerometer mounted on the rotating planet carrier and an external accelerometer mounted on the fixed ring gear. After testing it was noticed that the acceleration signals from the internal accelerometer were contaminated by electrical interference and by dropouts. The interference was identified as coming from the variable speed motor controller and also from a ground loop effect, while the dropouts served to give an artificially high kurtosis. This prevented making a conclusive assessment of the relative performance of the two measurement points and hence only the comparison of the simulated signals with the ‘externally’ measured signals (accelerometer mounted on top of the ring gear) is included in this study. The

measurements from both the internal and the external accelerometer were discussed in detail in (Smith et al., 2013b).

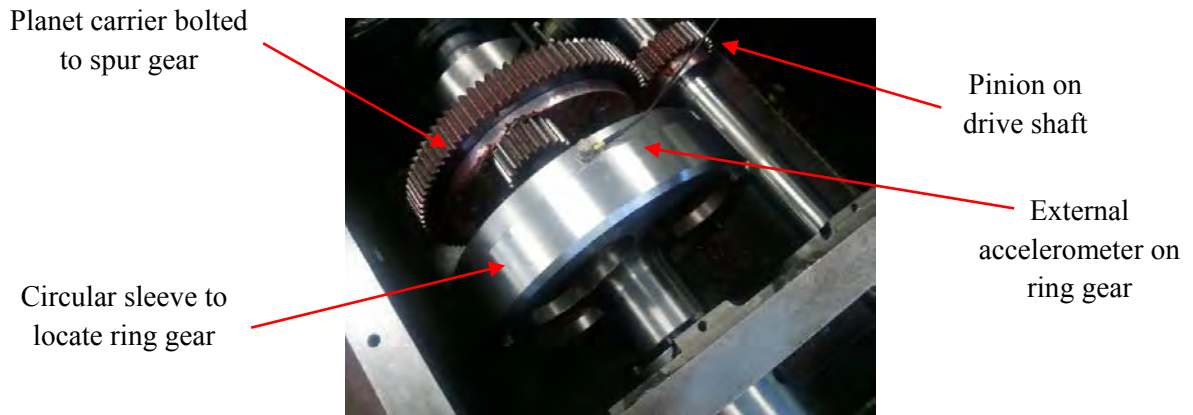


Figure 7.3 Modified design – Circular sleeve used to locate the ring gear (ring gear is moved axially and the bracket connecting ring gear to casing is not shown for clarity)

7.3 Planetary gearbox – Experimental measurements

7.3.1 Test rig

In addition to the gearbox, the UNSW gear rig (Figure 7.4) consists of an AC induction motor with variable speed controller, a recirculating hydraulic system that provides a resistance torque, and two large flywheels to reduce speed fluctuations, all connected through shafts with a number of flexible couplings to mitigate shaft misalignment. The gearbox test rig was described in detail in Chapter 5 (Section 5.2.1).

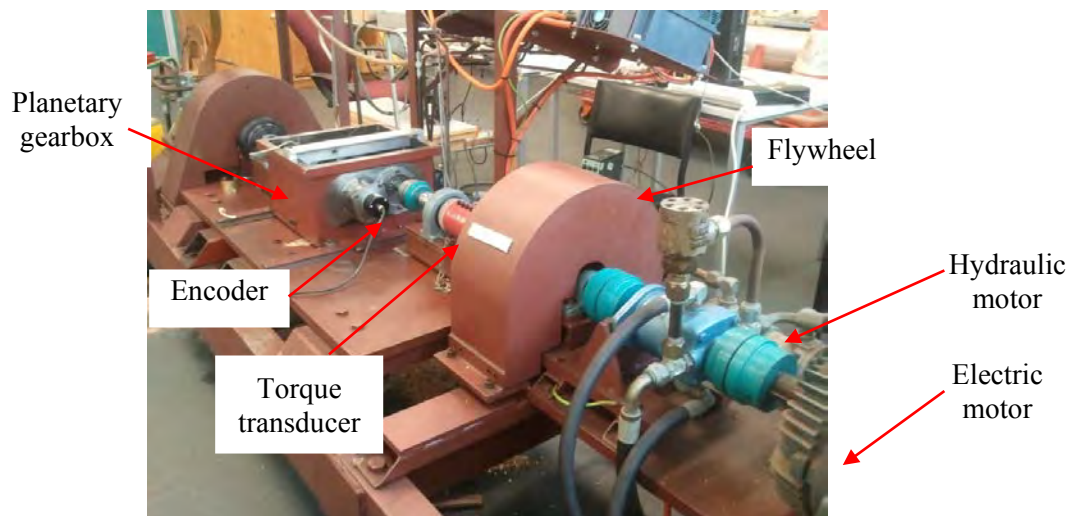
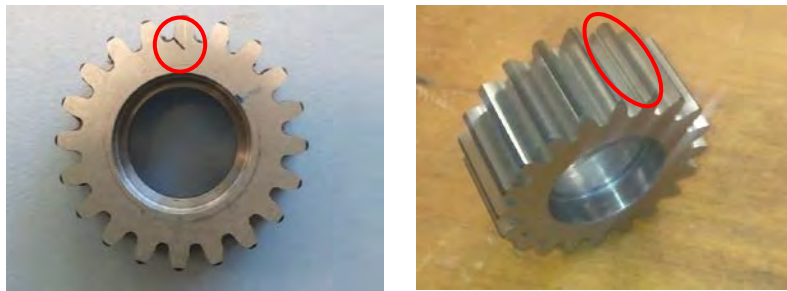


Figure 7.4 UNSW gearbox test rig with planetary gearbox

7.3.2 Seeded gear faults

To simulate various types of gear damage, two types of seeded planet gear faults were investigated in this study. The first was a tooth root crack, achieved by machining a 45° angle slot of approximately 0.5 mm width across the whole tooth at the tooth root. The slot was extended such that it met the radius drawn through the tooth centre. The second investigated fault was a tooth spall, seeded by machining a channel of 1 mm width and 0.1 mm depth across the tooth at the pitch line. The two types of gear faults are shown in Figure 7.5.



(a) Planet gear – Tooth fillet crack (b) Planet gear – Tooth spall

Figure 7.5 Seeded planet gear faults.

7.3.3 Instrumentation and data acquisition

The internal and external vibration was measured on the gearbox using, respectively, Brüel & Kjær 4394 I EPE-type and 4393 c charge-type accelerometers. The internal accelerometer was stud-mounted in the axial direction on the planet carrier, and the signal was transmitted via a Michigan Scientific B6-2 slip ring. The external accelerometer was mounted radially on the top of the outside of the ring gear, the idea being to replicate the closest measurement point that might be feasible in a more conventional diagnostic environment.

The two accelerometers, along with a once-per-revolution tachometer mounted on the output shaft, were connected to a Brüel & Kjær PULSE analyser. For each test, a record length of 20 seconds and a sample rate of 65,536 Hz were used.

Figure 7.6 shows the placement of the transducers from a top view of the gearbox (internal accelerometer not shown).

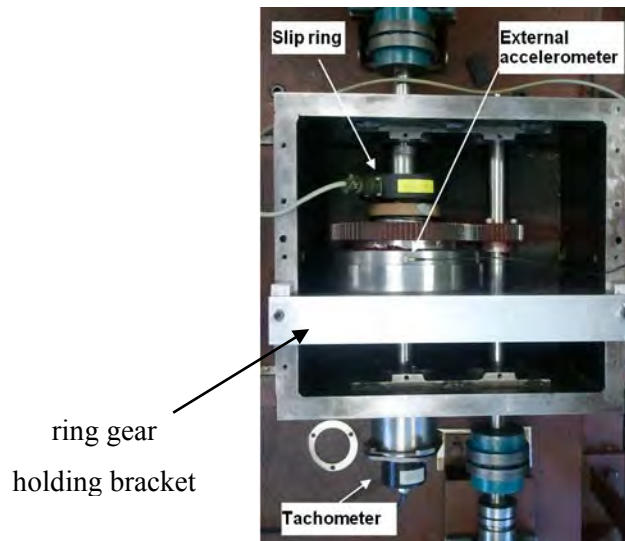


Figure 7.6 Top view of UNSW planetary gearbox showing transducer placement

7.3.4 Test program and conditions

Each test was conducted with one of the faulty planet gears installed in the gearbox, and one fault-free test was conducted as a baseline case. For the root crack and tooth spall, two tests were carried out, since the effect of these faults – stiffness-based for the former and geometric for the latter – depends on which side of the planet gear tooth meshes with the ring or the sun. Thus tests were carried out with the faulty planet gear flipped to reverse the planet-ring/planet-sun meshing relationship. All the tests are summarised in Table 7.1.

Table 7.1 Test program

Test name	Gear fault description
No fault	Baseline case with no gear fault
Tooth crack A	Tooth root crack opening when meshing with the sun
Tooth crack B	Tooth root crack opening when meshing with the ring
Tooth spall A	Tooth spall meshing with the sun – geometric fault with negligible change in mesh stiffness
Tooth spall B	Tooth spall meshing with the ring – geometric fault with negligible change in mesh stiffness

The tests were conducted at a nominal input shaft speed of 6 Hz (planet carrier speed of $f_c = 2.13$ Hz) and a constant torque load of 50 Nm. This meant the planet gears were driven at only about 20% of their rated torque load (in bending). It was not possible to test at higher load due to the allowable torque limit of the drive pinion in the parallel gear stage. The ring gear was located by a sleeve mounted via bearings on the output shaft, thus ensuring the sun, planet carrier and ring were all concentric. The ring gear was constrained from rotating by a holding bracket attached to the gearbox casing, as can be seen in Figure 7.6. Although a tachometer was used on the output shaft, no tooth numbering or angular referencing was used to relate the gear faults to the tachometer pulses. This situation reflects more closely what would be experienced in practice.

The measured vibration signals are reported under ‘Results and Discussion’ and are compared with those obtained from the simulation (Section 7.9).

7.4 Gear ratios, Expected frequencies and Torque calculations

The vibration signal from the healthy planetary gearbox (without any gear or bearing faults) will contain several gearmesh frequencies and their harmonics and sidebands. The estimation of these frequencies is essential to analyse the vibration spectra and to identify the fault frequencies. Table 7.2 shows details of the number of teeth on each gear (Figure 7.2). Note that the design is far from hunting tooth, but was initially thought to be the only possible design with respect to space and available gears. A hunting tooth design has now been worked out and will be built in the future. Table 7.3 shows the gear ratio calculations for the planetary motion based on the following procedure.

Table 7.2 No of teeth on gears in planetary gearbox

1 st Stage		2 nd Stage [Planetary insert]		
Pinion (Z_{pin})	Spur Gear (Z_{spr})	Planet (Z_p)	Ring (Z_r)	Sun (Z_s)
32	90	20	80	40

The first step consists of locking the planetary train and rotating the entire assembly by one revolution. In the second stage, the planet carrier is locked and the ring rotated such

that it is back to its original position. The summation of the two actions gives the total motion (rotations) of all the planetary insert components.

Table 7.3 Calculation of planetary motion

Step	Action	Carrier (input)	Planet ($Z_p=20$)	Ring ($Z_r=80$)	Sun (output) ($Z_s=40$)
1	Lock train and rotate entire assembly by 1 rev	1	1	1	1
2	Lock carrier and rotate ring gear by -1 rev	0	$-\frac{Z_r}{Z_p}$	-1	$\frac{Z_r}{Z_s}$
3	Add the motions	1	$1 - \frac{Z_r}{Z_p}$	0	$1 + \frac{Z_r}{Z_s}$
4	Planetary motion (based on number of teeth)	1	-3	0	3

Gear ratios

1st stage: 32:90 (reduction)

2nd stage (planetary): 1:3

Overall gear ratio:

$$\frac{32}{90} * \frac{3}{1} = \frac{16}{15} = 1.0667 \quad (7.1)$$

Nominal input shaft speed = 6 Hz

Carrier spin frequency: ω_c

$$\omega_c = -input\ speed \times \frac{Z_{pin}}{Z_{spr}} = -6 \times \frac{32}{90} = -2.13\ Hz \quad (7.2)$$

Planet Rotation Frequency (absolute): ω_{pc}

$$\omega_{pc} = \omega_c \times \left(1 - \frac{Z_r}{Z_p}\right) = -2.13 \times \left(1 - \frac{80}{20}\right) = 6.39\ Hz \quad (7.3)$$

Output shaft (sun gear) speed, ω_{os}

$$\omega_{os} = \text{input shaft speed} \times \text{overall gear ratio} = 6.39 \text{ Hz} \quad (7.4)$$

Since the planet gears and the carrier rotate in opposite directions, the net speed of the planets is the sum of the absolute speeds of the planet gear and the carrier which is known as the spin frequency of the planetary gears.

Planet Gear Spin Frequency: ω_p

$$\omega_p = -\omega_c \times \frac{Z_r}{Z_p} = 2.13 \times \frac{80}{20} = -8.52 \text{ Hz} \quad (7.5)$$

The negative sign in the above equation indicates that the planets spin in the opposite direction to the sun gear and the carrier.

Sun Gear Rotation Frequency: ω_s

$$\omega_s = \omega_c \times \left(\frac{Z_r}{Z_s} + 1 \right) = 2.13 \times \left(\frac{80}{40} + 1 \right) = 6.39 \text{ Hz} \quad (7.6)$$

Gear mesh frequencies

(Based on the input shaft speed of 6 Hz)

Spur Gear Mesh Frequency: SGMF

$$SGMF = \text{Drive shaft speed} \times Z_{pin} = 6 \times 32 = 192 \text{ Hz} \quad (7.7)$$

Planetary Gear Mesh Frequency: PGMF

(also known as epicyclic mesh frequency)

$$PGMF = \omega_c \times Z_r = 2.13 \times 80 = 170.4 \text{ Hz} \quad (7.8)$$

Planet Pass Frequency:

$$\text{Planet Pass Frequency} = \omega_c \times \text{no. of planets} = 2.13 \times 3 = 6.39 \text{ Hz} \quad (7.9)$$

The various component frequencies of the planetary gearbox are shown in Table 7.4.

Table 7.4 Gear mesh frequencies of the planetary gearbox

Gearbox Stage	Frequency	Hz
1 st Stage	Input shaft frequency	6
	Spur gear mesh frequency	192
	Carrier (input to planetary insert)	2.13
2 nd Stage	Epicyclic Mesh Frequency	170.4
	Sun gear rotation frequency	6.39
	Planet Pass Frequency	6.39

Torque calculations

Gearbox input torque: 50 Nm

Planetary insert input torque (planet carrier) T_i :

$$T_i = 50 * \frac{90}{32} = 140.625 \text{ Nm} \quad (7.10)$$

$$T_i \cdot \omega_i + T_s \cdot \omega_s + T_r \cdot \omega_r = 0 \quad (\omega_r = 0, \text{fixed ring gear}) \quad (7.11)$$

$$\text{Sun gear, } T_s = -T_i \cdot \frac{\omega_i}{\omega_s} = -140.625 * \frac{1}{3} = -46.875 \text{ Nm} \quad (7.12)$$

$$T_i + T_s + T_r = 0 \quad (7.13)$$

$$\text{Ring gear, } T_r = -93.75 \text{ Nm (holding torque)}$$

7.5 Contact ratios and mesh stiffness curves

The mesh stiffness curve for a pair of gears is influenced by the tooth contact ratio. The contact ratio between the pair of gears is defined as the ratio of the length of the line of action to that of the base pitch (Kim et al., 2012). The contact ratio specifies the average number of pairs of teeth in contact in a spur mesh. The point of contact between the mating gears travels along the line of pressure while the load is transferred from one pair of teeth to the next. The greater the ‘handover time’ from one pair of teeth to the next, the lower will be the noise and vibration levels from the gears (Smith, 1983). In typical spur gears there are two pairs of teeth in contact for about half the time and one

pair is in contact for the remainder of the time, corresponding to contact ratio 1.5. Table 7.5 shows the planetary insert gear data used to calculate the contact ratios.

Table 7.5 Planetary insert gear data

Parameter	Sun	Ring	Planet
Pressure angle, deg (α)	20	20	20
No. of teeth (Z_s, Z_r, Z_p)	40	80	20
Module, mm (m)	2	2	2
Pitch circle radius, mm (P_{cr})	40	80	20
Base circle radius, mm (R_s, R_r, R_p), $[P_{cr} \cos \alpha]$	37.59	75.18	18.79
Base pitch, mm (P_b), $[m \pi \cos \alpha]$	5.9043	5.9043	5.9043
Addendum circle radius (A_s, A_r, A_p)	42	78	22

[Note: the subscripts s, r, p denote sun, ring and planet gear respectively.]

In the case of a planetary gearbox there are multiple gearmeshes (two times the number of planet gears) as the planet gears mesh with both the sun and the ring gear simultaneously. Hence for a planetary system two contact ratios need to be defined: one for the sun-planet and other for the ring-planet gears. The two ratios need to be defined separately since the ring and the planet gear pairs have internal gear mesh, while the sun and planet gear pairs have external gear mesh.

Contact ratio: Sun/ ith Planet gear (Kim et al., 2012)

$$CR_{sp} = \frac{\sqrt{A_s^2 - R_s^2} + \sqrt{A_p^2 - R_p^2} - R_c \sin \alpha_i^s}{P_b} = 1.64 \quad (7.14)$$

Where, R_c is the distance from the carrier centre to the planet gear centre (60 mm).

Contact ratio: Ring/ ith Planet gear (Kim et al., 2012)

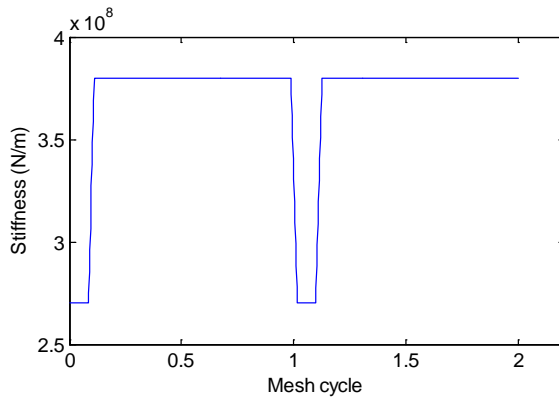
$$CR_{rp} = \frac{\sqrt{A_p^2 - R_p^2} - \sqrt{A_r^2 - R_r^2} - R_c \sin \alpha_i^r}{P_b} = 1.89 \quad (7.15)$$

The two contact ratios defined above are used to establish time-varying gearmesh stiffness curves for the sun-planet and the ring-planet respectively which are then included in the lumped parameter model of the planetary insert.

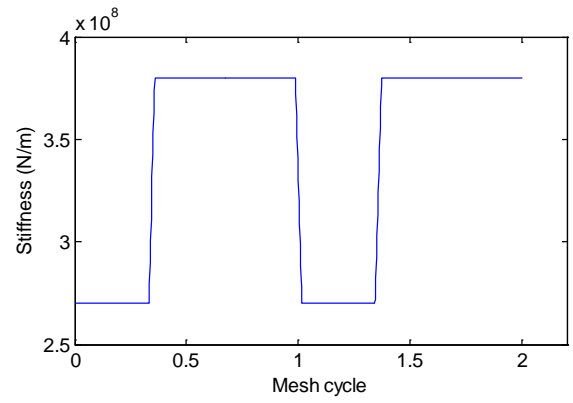
7.5.1 Gear tooth stiffness

The elastic deflection of a pair of teeth in contact is caused by the local Hertzian contact deflections as well as bending and shear deflections. The Hertzian deflections are small compared with the tooth bending and shear deflections and are neglected here. Measurements (as well as finite element analysis) have shown that the meshing stiffness of a pair of teeth remains reasonably constant as the bending stiffness of the tooth (per mm of face width) is independent of its size and varies only with shape and position of force on the tooth flank. Also, the opposing effects of contact position on the two teeth in mesh roughly cancel over the meshing cycle. In case of steel gears of standard 20° pressure angle and shape, the meshing stiffness was found to be $1.4\text{E}10$ N/m/m face width (Smith, 1983), which gives a stiffness of $2.8\text{E}8$ N/m for the planetary gears with 20 mm face width used in the gearbox under study.

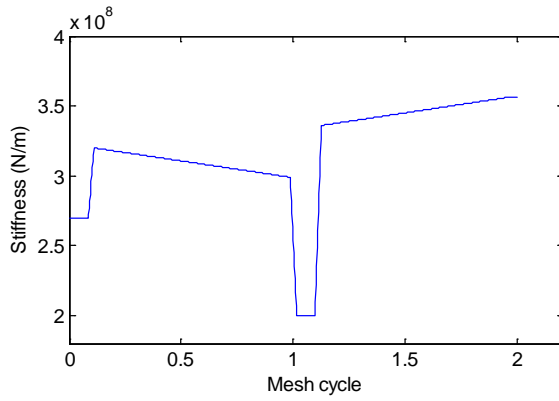
The gearmesh stiffness curves were established analytically using FEA (MSC.MARC) by H. Endo (Endo, 2005) for the undamaged and damaged spur gears. The results were also verified using commercial gear analysis software HyGears (HyGears) which showed good correlation. These mesh stiffness curves were used as a basis to define the sun-planet and the ring-planet mesh curves in the simulation of the planetary insert. However, the curves were modified to represent the actual contact ratios at these two types of meshes. In the current configuration with three equally spaced planets, there are total six gearmeshes – three sun-planet and three ring-planet gearmeshes. Figure 7.7 shows the sun-planet and the ring-planet mesh stiffness curves for the undamaged and damaged (tooth root crack) planet gear. The mesh phasing between these stiffness curves is explained in Section 7.6.



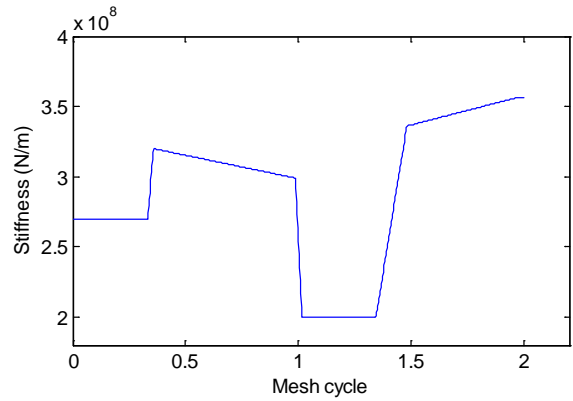
(a) Ring-Planet mesh stiffness curve
(Undamaged planet gear, contact ratio: 1.89)



(c) Sun-Planet mesh stiffness curve
(Undamaged planet gear, contact ratio: 1.64)



(b) Ring-Planet mesh stiffness curve
(planet tooth crack, contact ratio: 1.89)



(d) Sun-Planet mesh stiffness curve
(planet tooth crack, contact ratio: 1.64)

Figure 7.7 Mesh stiffness curves

7.6 Kinematic configuration and Mesh phasing

In the current configuration of the UNSW planetary gearbox, planet carrier c and the sun gear s act as the input and output members with the ring gear r held stationary. The fundamental gear mesh (tooth passing) frequency is defined as

$$\omega_m = Z_r \omega_c \quad (7.16)$$

Where ω_c is the absolute angular velocity of the planet carrier and Z_r the number of teeth on the ring gear.

A planetary gear set with equally spaced planet position angles $\psi_i = 2\pi (i - 1) / N$ is possible only if $(Z_s + Z_r) / N = \text{integer}$. The following equations determine the planetary

configuration based on the spacing of the planets and the resulting mesh phasing (Inalpolat and Kahraman, 2009).

$$\psi_i = \frac{2\pi(i-1)}{N}, \quad \frac{Z_r\psi_i}{2\pi} \neq n \quad \text{and} \quad \sum_{i=1}^N Z_r\psi_i = m\pi \quad (m, n = \text{integer}) \quad (7.17)$$

The first condition indicates that the planets are equally spaced while the second condition implies that the planets are not in phase ($Z_r/N \neq \text{integer}$). The third condition states that the dynamic gearmesh forces are sequentially phased i.e. the sum of the phase angles is an integer multiple of π . The design of the UNSW planetary gearbox satisfies the above condition which can be categorized as ‘equally spaced planets with sequentially phased gearmeshes’.

The mesh stiffness curve phasing is illustrated in Figures 7.8 and 7.9 for all six gearmeshes with and without the gear fault (tooth crack).

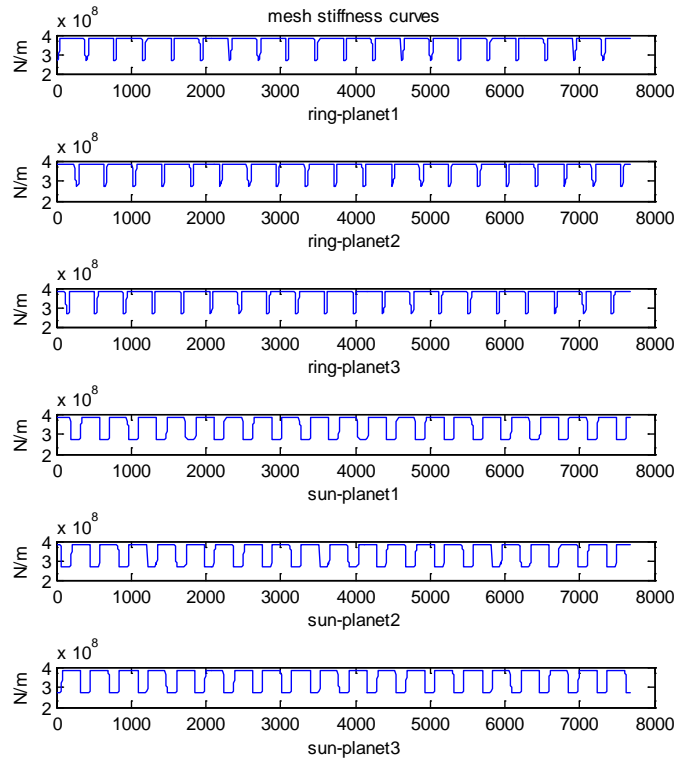


Figure 7.8 Mesh stiffness curve phasing - undamaged gear

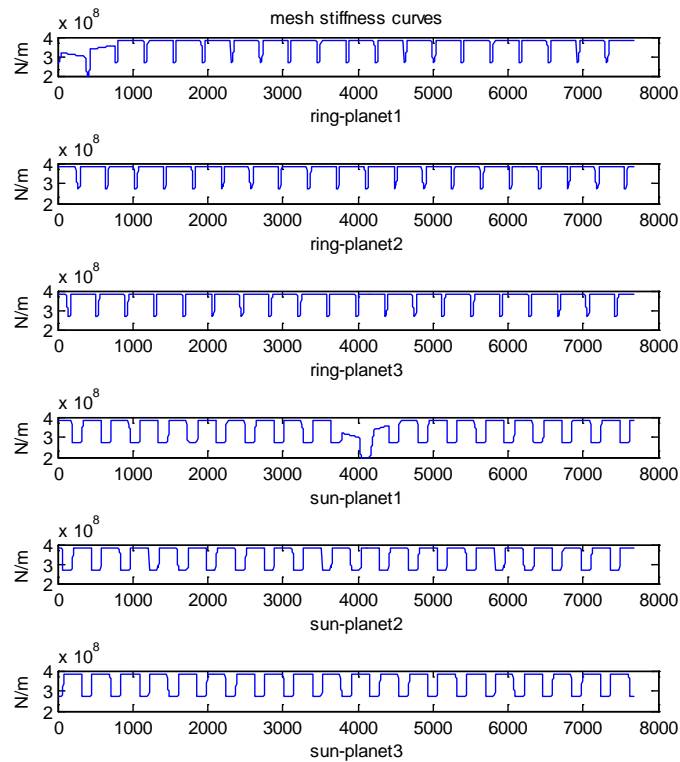


Figure 7.9 Mesh stiffness curve phasing - damaged gear (Tooth crack)

The effect of a tooth spall on the planet gear was modelled as a rectangular function as shown in Figure 7.10. The spall curve over five carrier cycles is shown in Figure 7.11 and indicates four impulses per carrier cycle since the spalled planet tooth ($Z_p=20$) meshes four times with the ring gear teeth ($Z_r=80$) per carrier cycle.

In the case of a spalled planet gear, the transmission error (TE) due to the spalled geometry was superimposed on the tooth profile error and the combined TE was inserted into the simulation model as a 'look up table'. Six TE curves were defined with similar phasing to that of the gearmesh (stiffness) curves. The TE formulation is further discussed in section 7.7.2.3.

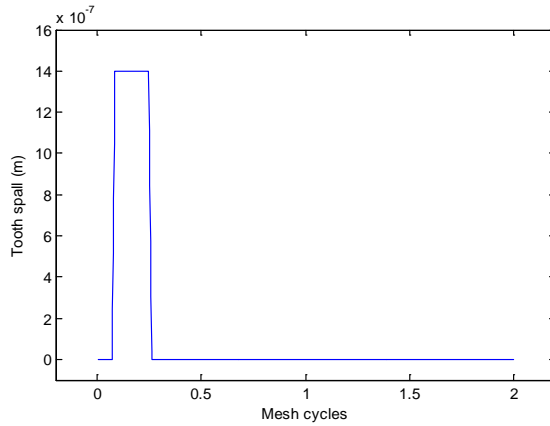


Figure 7.10 Spall geometry (1 mesh cycle)

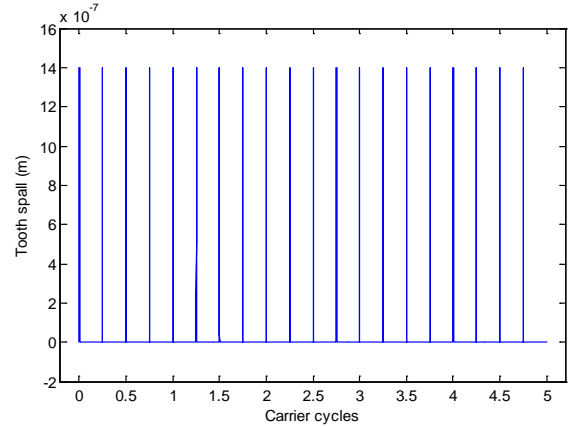


Figure 7.11 Spall curve (5 carrier cycles)

In the dynamic model created using Matlab/Simulink®, position dependent (time-varying) gearmesh stiffness and TE were defined such that the timing of the gearmesh was synchronised with the time step defined in the simulation model.

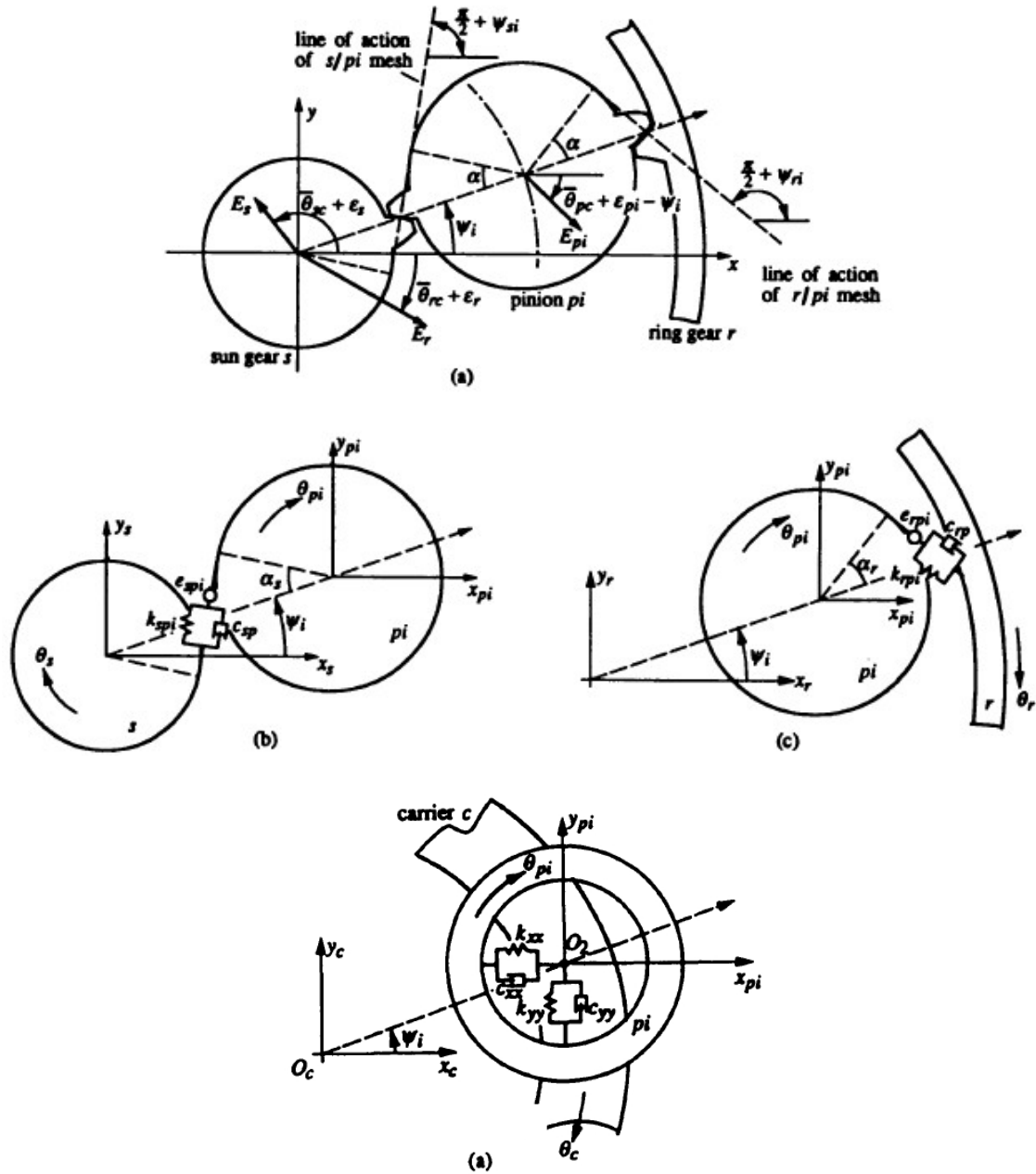
7.7 Planetary gearbox – Lumped Parameter Model

A 2D transverse-torsional lumped parameter model (LPM) of the UNSW spur planetary insert was developed based on Kahraman's model (1994). The planet carrier rotates on the bearings mounted on the output shaft to which the sun gear is also rigidly attached. This was modelled by incorporating a stiff spring (in x and y DOFs) between the planet carrier and the sun gear and a soft spring representing the sun gear support (shaft) stiffness. The model was further enhanced to include the capability of simulating gear faults such as tooth cracks and spalls. The 1st stage of the gearbox reduction through a pair of spur gears was not included in the model and hence the resulting model comprised the sun, ring and the three equi-spaced planet gears mounted on the planet carrier. The input torque was applied to the planet carrier whereas the sun gear provided the output while the ring gear was held stationary.

The schematic of the planetary insert was illustrated earlier in Figure 7.2. The system was modelled as three sub-systems (Figure 7.12) with independent sets of equations of motion namely,

- ring-planet subsystem
- sun-planet subsystem

- carrier-planet subsystem



(a) Sun-planet-ring sub-system (b) sun-planet pair (c) ring-planet pair (d) carrier-planet pair

Figure 7.12 Planetary gear sub-systems (Kahraman, 1994)

The equations of motion of the overall system were obtained by assembling the subsystems together with the support structure (boundary conditions).

In the current transverse-torsional LPM model, each component of the planetary system has three degrees of freedom (DOFs) - two translations (in x and y direction) and one

rotation (θ). The resulting LPM model has 18 DOFs based on the 3-planet configuration. The 18 DOFs are:

$[x_c, y_c, \theta_c, x_r, y_r, \theta_r, x_s, y_s, \theta_s, x_{p1}, y_{p1}, \theta_{p1}, x_{p2}, y_{p2}, \theta_{p2}, x_{p3}, y_{p3}, \theta_{p3}]$ where c, r, s and p_i correspond to the carrier, ring, sun and planet gears.

7.7.1 Assumptions

The components of the planetary gearbox – sun, ring, carrier and the three planets were considered to be rigid bodies assuming negligible elastic deformations of the gears and the carrier.

All the three planets were assumed to be identical with respect to mass, inertia, gear profile errors and this assumption leads to two identical sets of mesh stiffnesses at the sun-planet and the ring-planet contacts.

Tooth separation and backlash between the mating gear teeth leading to nonlinear behaviour were not included in the model.

Time (periodically) varying mesh stiffness due to the varying number of teeth in contact was used to model the gearmesh interactions which were represented by linear springs acting along the line of action.

Linear springs were also used to model the component bearings and supports.

Proportional damping was used to model the frictional forces at the gear mesh and at the component supports.

The gear manufacturing and assembly variations such as misalignments and gear tooth spacing errors were excluded from this study so as to limit the number of system parameters.

7.7.2 Equations of Motion

The equations of motion for the three subsystems were based on Kahraman's model (1994), however the equations were re-written in the generalised right hand co-ordinate system x, y and θ instead of x, y and u (where $u = r\theta$).

7.7.2.1 Gear pair (sun-planet, ring-planet)

Figures 7.12(a) and 7.12(b) show the two gear pairs of the planetary set with the planet i positioned at an angle ψ about gear j ($j=s, r$). Each gear has two translations (x, y) and one rotation (θ) about its centre in the plane of the gear. The gears and the planets are rigidly connected along the line of action through a gear mesh stiffness $k_{jpi}(t)$ and gear mesh damping c_{jp} . The equations of motion are defined taking into account the fact that the sun-planet is an external gear pair whereas the ring planet is an internal pair.

$$m_j \ddot{x}_j - c_{jp} \dot{p}_{jpi}(t) \sin \psi_{ji} - k_{jpi}(t) p_{jpi}(t) \sin \psi_{ji} = 0 \quad (7.18)$$

$$m_j \ddot{y}_j + c_{jp} \dot{p}_{jpi}(t) \cos \psi_{ji} + k_{jpi}(t) p_{jpi}(t) \cos \psi_{ji} = 0 \quad (7.19)$$

$$J_j \ddot{\theta}_j + R_j c_{jp} \dot{p}_{jpi}(t) \cos \psi_{ji} + R_j k_{jpi}(t) p_{jpi}(t) = T_i / n \quad (7.20)$$

$$m_p \ddot{x}_{pi} + c_{jp} \dot{p}_{jpi}(t) \sin \psi_{ji} + k_{jpi}(t) p_{jpi}(t) \sin \psi_{ji} = 0 \quad (7.21)$$

$$m_p \ddot{y}_{pi} - c_{jp} \dot{p}_{jpi}(t) \cos \psi_{ji} - k_{jpi}(t) p_{jpi}(t) \cos \psi_{ji} = 0 \quad (7.22)$$

$$J_p \ddot{\theta}_{pi} + R_{pi} c_{jp} \dot{p}_{jpi}(t) + \delta_j R_{pi} k_{jpi}(t) p_{jpi}(t) = 0 \quad (7.23)$$

Where

$j=s$ or r ; $i=1, n$ where n is number of planets

m_j, m_p are mass of gear j and planet p

J_j, J_p are the mass moment of inertia of gear j and planet p

$p_{jpi}(t)$ is the relative gear mesh displacement given by

$$p_{jpi}(t) = (y_i - y_{pi}) \cos \psi_{ji} - (x_i - x_{pi}) \sin \psi_{ji} + R_j \theta_j + \delta_j R_{pi} \theta_{pi} - e_{jpi}(t) \quad (7.24)$$

R_j, R_p base circle radii of gear and planet p

T_j mean torque applied to gear j

$\psi_{ji} = \psi_i - \delta_j \alpha_j$ where α_j is the pressure angle, $\delta_j = 1$ (external s/p_i pair), and $\delta_j = -1$ (internal r/p_i pair).

ψ_i is the planet gear position angle

$e_{jpi}(t)$ is kinematic gear profile error applied at the gearmesh as displacement excitation.

7.7.2.2 Carrier-planet pair

Figure 7.12(d) shows the carrier-planet pair with planets positioned at angle ψ_i . The rotation of the planet is completely uncoupled from the carrier motion and hence was not included in the equations of motion. The planet pin and bearing assembly was modelled using springs and dampers in the x and y directions.

$$m_c \ddot{x}_c + c_{xx}(\dot{x}_c - \dot{x}_{pi} - \dot{R}_c \dot{\theta}_c \sin \psi_i) + k_{xx}(x_c - x_{pi} - R_c \theta_c \sin \psi_i) = 0 \quad (7.25)$$

$$m_c \ddot{y}_c + c_{yy}(\dot{y}_c - \dot{y}_{pi} + \dot{R}_c \dot{\theta}_c \cos \psi_i) + k_{yy}(y_c - y_{pi} + R_c \theta_c \cos \psi_i) = 0 \quad (7.26)$$

$$J_c \ddot{\theta}_c - R_c c_{xx}(\dot{x}_c - \dot{x}_{pi} - \dot{R}_c \dot{\theta}_c \sin \psi_i) \sin \psi_i + R_c c_{yy}(\dot{y}_c - \dot{y}_{pi} + \dot{R}_c \dot{\theta}_c \cos \psi_i) \cos \psi_i - R_c k_{xx}(x_c - x_{pi} - R_c \theta_c \sin \psi_i) \sin \psi_i + R_c k_{yy}(y_c - y_{pi} + R_c \theta_c \cos \psi_i) \cos \psi_i = T_c/n \quad (7.27)$$

$$m_p \ddot{x}_{pi} - c_{xx}(\dot{x}_c - \dot{x}_{pi} - \dot{R}_c \dot{\theta}_c \sin \psi_i) - k_{xx}(x_c - x_{pi} - R_c \theta_c \sin \psi_i) = 0 \quad (7.28)$$

$$m_p \ddot{y}_{pi} - c_{yy}(\dot{y}_c - \dot{y}_{pi} + \dot{R}_c \dot{\theta}_c \cos \psi_i) - k_{yy}(y_c - y_{pi} + R_c \theta_c \cos \psi_i) = 0 \quad (7.29)$$

where,

m_c and J_c are the carrier mass and inertia.

T_c is the torque applied to the carrier

k_{xx} , k_{yy} are planet bearing spring stiffnesses in the x and y directions.

7.7.2.3 The overall assembly

The individual equations of the subsystem were combined with the support or bearing flexibilities to generate the equations of motion of the entire planetary insert.

The equation of motion in matrix form is

$$M \ddot{X} + [C + C_b] \dot{X} + [K + K_b] X = F_m + F_a(t) \quad (7.30)$$

where the displacement vector X and the diagonal mass matrix M are defined as

$$X = \begin{Bmatrix} q_c \\ q_r \\ q_s \\ q_{p1} \\ q_{p2} \\ q_{p3} \end{Bmatrix}, \quad q_j = \begin{Bmatrix} x_j \\ y_j \\ \theta_j \end{Bmatrix} \quad j = c, r, s, p1, p2, p3 \quad (7.31)$$

$$M = \text{Diag}[M_c \ M_r \ M_s \ M_{p1} \ M_{p2} \ M_{p3}], \quad M_j = \begin{bmatrix} m_j & 0 & 0 \\ 0 & m_j & 0 \\ 0 & 0 & J_j \end{bmatrix} \quad (7.32)$$

Diagonal matrices are assumed for the support (bearing) structure stiffness K_b and damping C_b .

$$K_b = \text{Diag}[K_{bc} \ K_{br} \ K_{bs} \ 0 \ 0 \ 0], \quad K_{bj} = \text{Diag}[K_{jx} \ K_{jy} \ K_{j\theta}] \quad j = s, r, c \quad (7.33)$$

$$C_b = \text{Diag}[C_{bc} \ C_{br} \ C_{bs} \ 0 \ 0 \ 0], \quad C_{bj} = \text{Diag}[C_{jx} \ C_{jy} \ C_{j\theta}] \quad j = s, r, c \quad (7.34)$$

The forcing function is the sum of mean force vector F_m and an alternating force vector $F_a(t)$. F_m is given by

$$F_m = \begin{Bmatrix} f_{cm} \\ f_{rm} \\ f_{sm} \\ 0 \\ 0 \\ 0 \end{Bmatrix} \quad f_{jm} = \begin{Bmatrix} 0 \\ 0 \\ T_j \end{Bmatrix} \quad (7.35)$$

The alternating force vector $F_a(t)$ consists of mesh frequency forces due to gear profile errors $[e_{spi}(t), e_{rpi}(t)]$ and is given by

$$F_a(t) = \begin{Bmatrix} 0 \\ \sum f_{ri} \\ \sum f_{si} \\ f_{sp1}-f_{r1} \\ f_{sp2}-f_{r2} \\ f_{sp3}-f_{r3} \end{Bmatrix} \quad (7.36)$$

The mesh frequency force vector is defined as

$$f_{ji} = [C_{jp}\dot{e}_{jpi}(t) + K_{jpi}(t)e_{jpi}(t)] \begin{Bmatrix} -\sin\psi_{ji} \\ \cos\psi_{ji} \\ R_j \end{Bmatrix}, \quad j = s, r \quad (7.37)$$

$$f_{spi} = [C_{sp}\dot{e}_{spi}(t) + K_{spi}(t)e_{spi}(t)] \begin{Bmatrix} \sin\psi_{si} \\ -\cos\psi_{si} \\ R_s \end{Bmatrix}, \quad e_{jpi}(t) =$$

(7.38)

kinematic gear profile error

In the current simulation, shaft frequency components due to gear run-out errors are taken into account in the TE formulation as described below.

The excitation of the simulation model is caused by varying transmission error (TE), mesh stiffness and gearmesh damping denoted by $e_t(\theta)$, $K_m(\theta)$ and C_m respectively. The excitation force is assumed to act in a direction along the plane of action (PoA). The position dependent variables $e_t(\theta)$, and $K_m(\theta)$ were estimated using static simulation in this case taking into account the load dependent non-linearity of gearmesh stiffness due to the effect of Hertzian contact between the meshing gear teeth. The obtained $e_t(\theta)$, and $K_m(\theta)$ values were included in the dynamic model as a ‘look-up table’. Friction forces at the gearmesh were neglected. The gears were assumed to operate under sufficient load (as generally experienced in practice) with no contact loss (Endo, 2005).

$$e_t = e_{Runout} + e_{ToothProfile} + e_{HighFreq} \quad (7.39)$$

Run-out error

$$e_{Runout} = \sum_{k=1}^N \left(\frac{20 \times 10^{-6}}{k^2} \right) \sin \left(\frac{2\pi kt}{T} + \phi_k + rand \right) \quad (7.40)$$

Tooth profile error

$$e_{ToothProfile} = \sum_{k=1}^2 \left(\frac{1 \times 10^{-6}}{k} \right) \sin \left(\frac{2\pi kt N_t}{T} + \phi_k + rand \right) \quad (7.41)$$

$$e_{ToothProfile} = \sum_{k=1}^2 \left(\frac{4 \times 10^{-6}}{4^{(k-1)}} \right) \sin \left(\frac{2\pi kt N_t}{T} + \phi_k + rand \right) \quad (7.42)$$

TE due to higher order components

$$e_{HighFreq} = \sum_{k=3}^{N_t} \left(\frac{1 \times 10^{-6}}{k} \right) \sin \left(\frac{2\pi k t N_t}{T} + rand \right) \quad (7.43)$$

Where:

N_t Number of teeth on a gear

k Order of harmonics

T shaft rotational period

ϕ_k Phase difference

$rand$ Random value generator

The schematic of the Matlab/Simulink® model is described in Appendix C (Section C.1). The matrices [K], [M] and [C] for the three sub-systems and for the overall assembly along with the force vector are given in Section C.2, whereas Section C.3 includes the input data to the Simulink® model.

7.7.3 Planetary LPM - Rigid body mode

The simulation model (LPM) of the planetary insert was verified for the rigid body mode (zero Hz frequency) by static simulation by applying the input torque to the carrier and fixing the sun gear (output). The rigid body mode displacements are listed in Table 7.6 and graphically shown in Figure 7.13.

Table 7.6 Rigid body mode

DOF No.	DOF	Amplitude
1	x_c	-1.04E-14
2	y_c	-1.49E-14
3	θ_c	-5.542051
4	x_r	1.19E-15
5	y_r	-8.94E-16
6	θ_r	1.32E-15
7	x_s	-1.11E-14
8	y_s	-1.55E-14
9	θ_s	-16.62615
10	x_{p1}	-1.06E-14
11	y_{p1}	-0.332523
12	θ_{p1}	16.626152
13	x_{p2}	0.2879734
14	y_{p2}	0.1662615
15	θ_{p2}	16.626152
16	x_{p3}	-0.287973
17	y_{p3}	0.1662615
18	θ_{p3}	16.626152

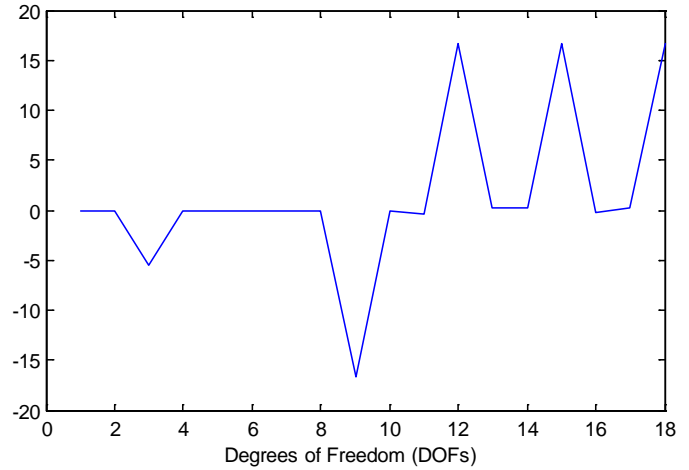


Figure 7.13 Rigid body mode (Mode 1, Frequency 0 Hz)

It is seen that the sun gear rotational displacement is three times that of the carrier (due to 1:3 ratio of the planetary insert) in the same direction since both the carrier and the sun gear rotate in the same direction. All three planets show identical rotational displacements which are in the opposite direction to the sun and the carrier.

7.8 Signal processing methodology

The measured vibration signals from the UNSW planetary gearbox were analysed using two different methods as described in (Smith et al., 2013b). Both methods commenced with order tracking to remove the effect of speed fluctuations and permit synchronous averaging, even though maximum speed variation was less than 0.1%. The regular gear meshing components were then removed from the signal with two different approaches, and the kurtosis of the residual signal was calculated, this being a measure of signal impulsivity and hence an indicator of possible damage. Finally, envelope analysis of the residual signal was conducted to determine the repetition frequencies of any impulsive events.

7.8.1 Procedure 1: Time synchronous averaging

The complete process for the first analysis procedure is shown in Figure 7.14. It is based on Stewart's FM4 parameter, which is defined as the kurtosis of the time synchronous average (TSA) signal after removal of the regular gear meshing components (Stewart, 1977), which in this case was achieved by removing the toothmesh harmonics and first-order sidebands. The components synchronous with the input shaft (i.e., the parallel gear stage) were removed with an initial stage of averaging.

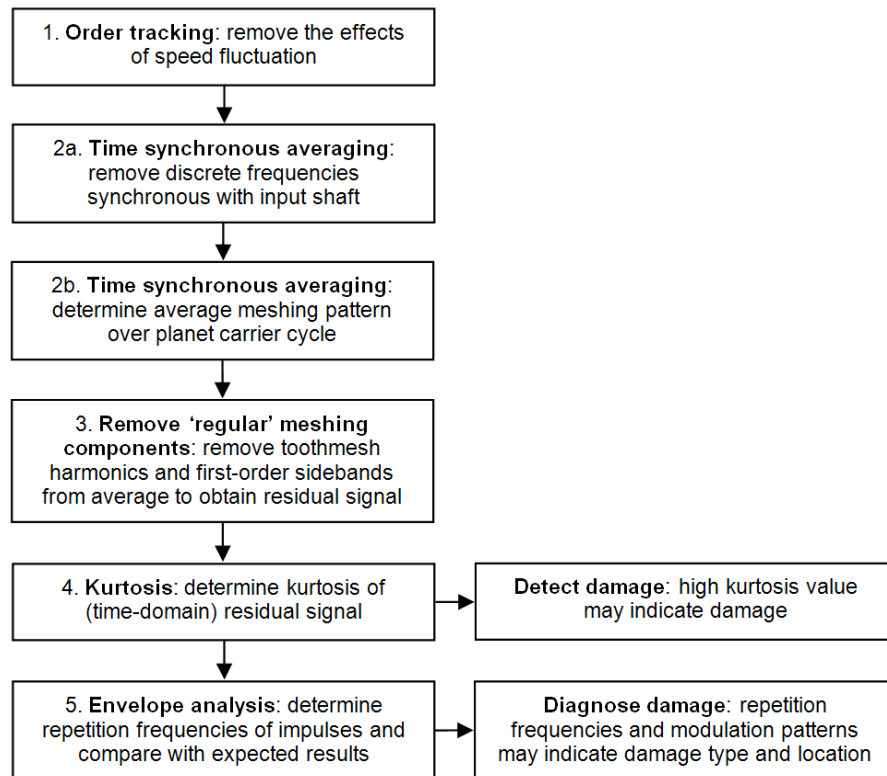


Figure 7.14 Procedure 1: Time synchronous averaging (Smith et al., 2013b)

In the planetary stage of TSA, the signal was averaged over one planet carrier cycle, and thus represents a composite of the vibration from all planet gears. The non hunting tooth design of this gearbox means that all gear pair meshes occur at the same spatial point in each planet carrier cycle, which involves exactly one planet-ring meshing cycle and two planet-sun meshing cycles. This makes techniques focused on the averaging of single meshing pairs – such as McFadden's windowing method (McFadden, 1991) and Forrester's signal weighting approach (Forrester, 1998) – difficult to apply. These difficulties prompted the use of a second signal processing approach, as outlined in the next section.

7.8.2 Procedure 2: Autoregressive linear prediction filtering and spectral kurtosis

The second procedure (Figure 7.15) used to remove regular gear meshing components was autoregressive (AR) linear prediction filtering, similar to that proposed by Wang and Wong (2002). This approach predicts the value of the signal at a given time by using a linear combination of prior values. Wang and Wong (2002) applied the technique to gear diagnostics and determined the filter coefficients based on baseline (undamaged) data, but in this study the filter was applied directly to each signal. This approach was applied to bearing diagnostics by Sawalhi et al. (2007) and is used here with the idea that – assuming the right filter length – the model will be able to predict regular meshing patterns but will be unable to predict the impulses arising from gear faults. Thus the impulses are left in the error, or residual, signal, which is then studied further. The only parameter the user need specify with this approach is the filter length. Here, the same criterion as that proposed by Sawalhi et al. (2007) is used: the best filter length is assumed to be that which maximises the kurtosis of the residual signal. The only other stipulation on filter length was that it did not exceed the period between expected fault impulses, so, to satisfy that requirement and to reduce computation time, a maximum length of one quarter of a fault separation period was imposed.

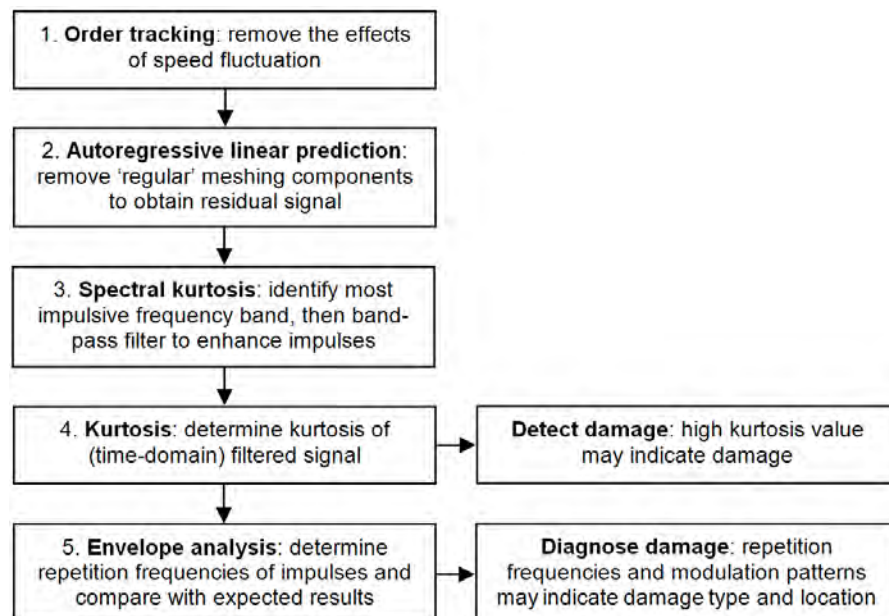


Figure 7.15 Procedure 2: AR linear prediction filtering and spectral kurtosis
(Smith et al., 2013b)

Spectral kurtosis (SK) was then applied to the residual signal to identify the band of maximum impulsivity (Antoni and Randall, 2006). The SK was determined using the computationally-efficient ‘fast kurtogram’, as developed by Antoni (2007).

7.8.3 Other signal processing approaches

Overall, the second signal processing approach (section 7.8.2) was found to be better suited than the first (section 7.8.1) to this application. Given the difficulty in forming a TSA signal for the individual planet gears (rather than a composite average, as used here), techniques based directly on the TSA signal were less likely to prove successful. For example, amplitude and phase demodulation of the toothmesh harmonics (McFadden, 1986) were tried but did not yield any useful results. This was not surprising given the large number of meshes (six) occurring in the planetary stage, and was probably further compounded by the gearbox having ‘sequential mesh phasing’ (Parker and Lin, 2004), meaning that each planet gear has a mesh cycle that is 120° out of phase with those of the other two.

Hence it was decided to use a flexible approach to remove the regular gear meshing components and to place a greater emphasis on kurtosis enhancement. Indeed, the recent application of spectral kurtosis to one planetary gearbox failure was found to provide a much more advanced warning than established techniques (Barszcz and Randall, 2009).

The signal analysis approach used to process the experimentally measured and simulated vibration signals and the discussion of results is described in the next section.

7.9 Results and Discussion

Due to the non-hunting tooth design of the UNSW planetary gearbox, the seeded gear faults are expected to produce the following impulses for each planet carrier cycle:

- Tooth root crack (actually a slot): eight impulses, with two groups of four having similar characteristics owing to the difference in planet-ring and planet-sun mesh stiffnesses and different contact ratios.
- Tooth spall: four similar sized impulses, since the fault only meshes with the ring or the sun.

In each case, the impulses are expected to be (approximately) equi-spaced in the angle-domain record. The signal measured at the external accelerometer (mounted vertically on the ring gear) would also be subject to modulation by the planet carrier frequency, f_c , due to the varying transmission path between the fault and the transducer, which would not be evident in the case of the internal accelerometer mounted on the planet carrier.

The simulated and the measured vibration signals are presented for the following four cases:

- undamaged planet gear
- planet tooth root crack
- planet tooth spall meshing with ring gear
- planet tooth spall meshing with sun gear

7.9.1 Comparison of acceleration spectra

Figures 7.16 to 7.24 show the acceleration spectra for the four cases mentioned above. TSA (time synchronous averaging) was applied to the measured vibration signals to remove the discrete frequencies synchronous with the input shaft. The residual signals were compared with the simulation results since the LPM model does not include the 1st stage reduction. The horizontal axis shows the frequency in terms of carrier orders. The spectra of the measured signals correlate well with the simulations and the plots clearly indicate the harmonics of gearmesh (80 orders or 170.4 Hz). Note that the simulations all show half mesh order components which are not prevalent in the measurements. This would normally be attributable to periodically varying stiffness, and may be emphasized in the simulations by a bsolutely constant speed, identical meshing error for the planet gears, and lower noise levels.

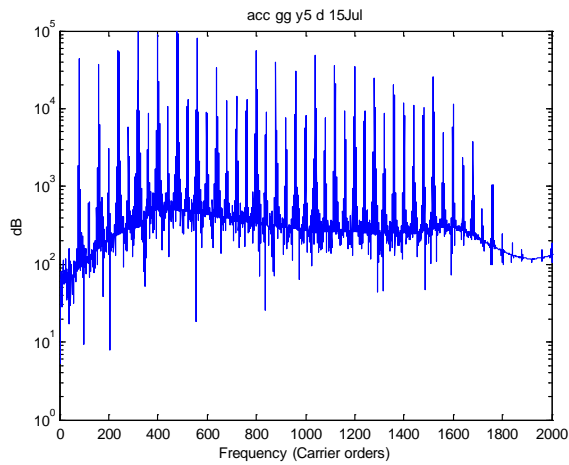


Figure 7.16 Simulation: ring gear
(Undamaged gear)

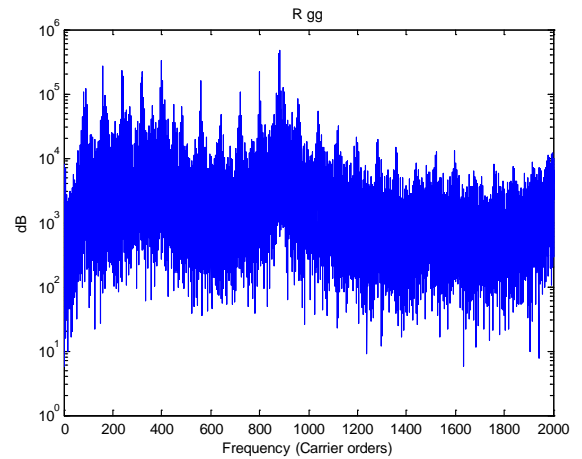


Figure 7.17 Test: ring gear
(Undamaged gear)

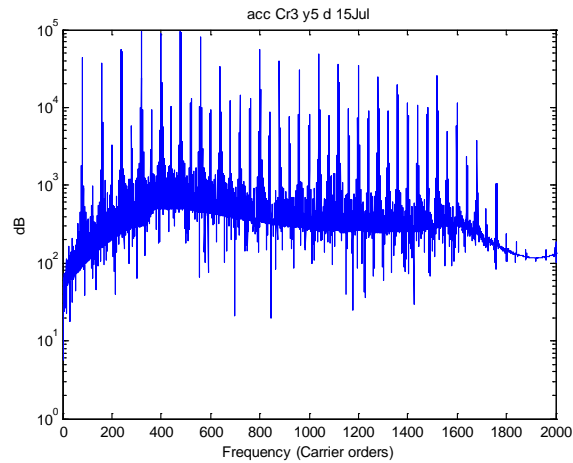


Figure 7.18 Simulation: ring gear (Tooth crack)

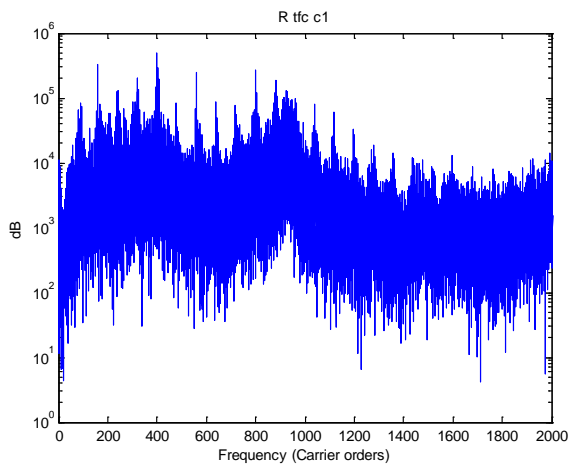


Figure 7.19 Test: ring gear
Tooth crack opening when meshing with sun

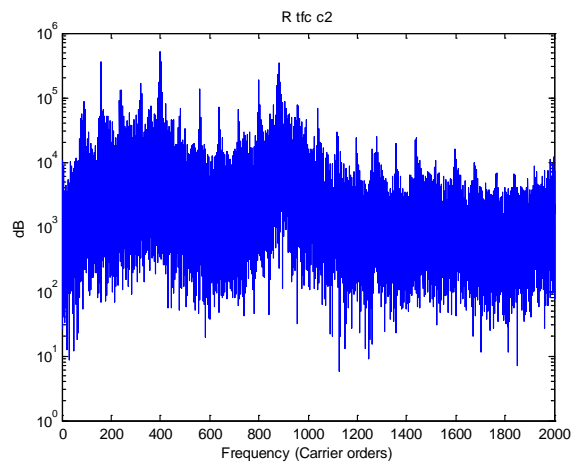


Figure 7.20 Test: ring gear
Tooth crack opening when meshing with ring

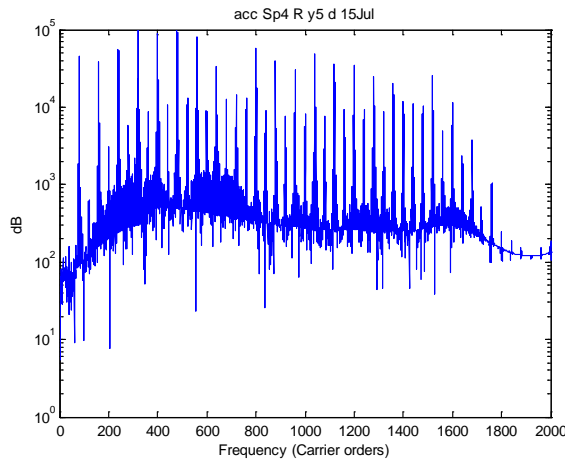


Figure 7.21 Simulation: ring gear
Tooth spall meshing with ring gear

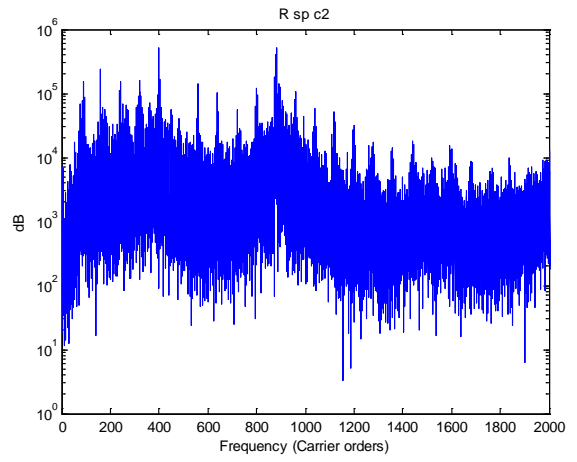


Figure 7.22 Test: ring gear
Tooth spall meshing with ring gear

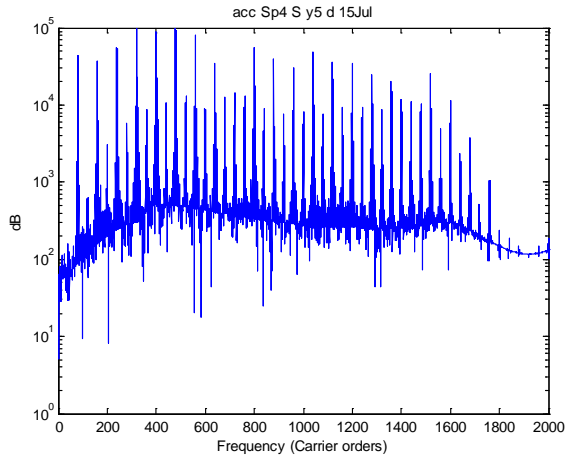


Figure 7.23 Simulation: ring gear
Tooth spall meshing with sun gear

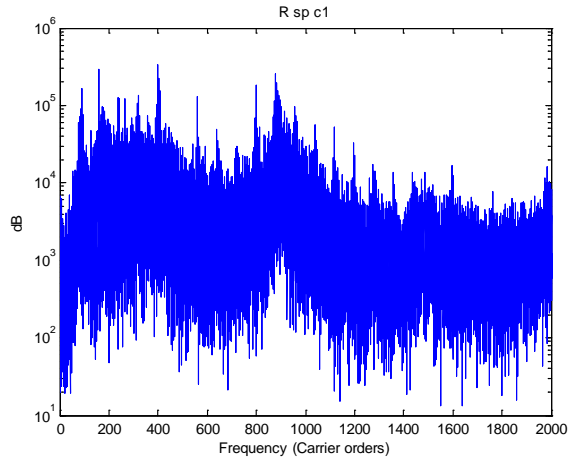


Figure 7.24 Test: ring gear
Tooth spall meshing with sun gear

7.9.2 Kurtosis with AR linear prediction filtering

In this method AR linear prediction filtering was used to remove the regular gear meshing components in the raw signal and the kurtosis of the residual signal was evaluated as an indication of the impulsiveness of the signal with gear faults (Figures 7.25 to 7.33). The length of the residual signal equivalent to four rotations of the planet carrier is displayed in all the plots. The results are summarised in Table 7.7.

Table 7.7 Kurtosis using AR method

Planet gear fault	Test		Simulation	
	Kurtosis	Impulses in AR residual signal per 4 carrier rotations	Kurtosis	Impulses in AR residual signal per 4 carrier rotations
Undamaged	5.1	---	5.8	---
Tooth crack opening with sun	10.6	32*	22.2	32
Tooth crack opening with ring	48.4	32*		
Tooth spall meshing with sun	64.8	16	8.0	16
Tooth spall meshing with ring	9.4	16	19.5	16

* Not all impulses are clear in the test results.

The characteristics of the simulated residual signals are found to match the experimentally measured signals with and without gear faults. The simulated results clearly differentiate between the two types of faults with reduction in the stiffness due to a tooth crack visible in both contacts whereas a spall on one flank is seen only in one contact. This is evident from the expected number of impulses in the AR residual signal in each case. The impulses in the simulated signal are clearer than in the test signals, especially in case of planet tooth crack, and also exhibit modulation of the impulses as expected.

The measured signal wherein the tooth spall meshes with the sun gear showed significantly higher kurtosis than when it meshes with the ring gear. This was found to contradict the findings of the simulation and may be due to a dominant transmission path through the sun gear in the gearbox which was not represented in the simulation model because the sun gear and its shaft were not connected via the casing to the ring gear.

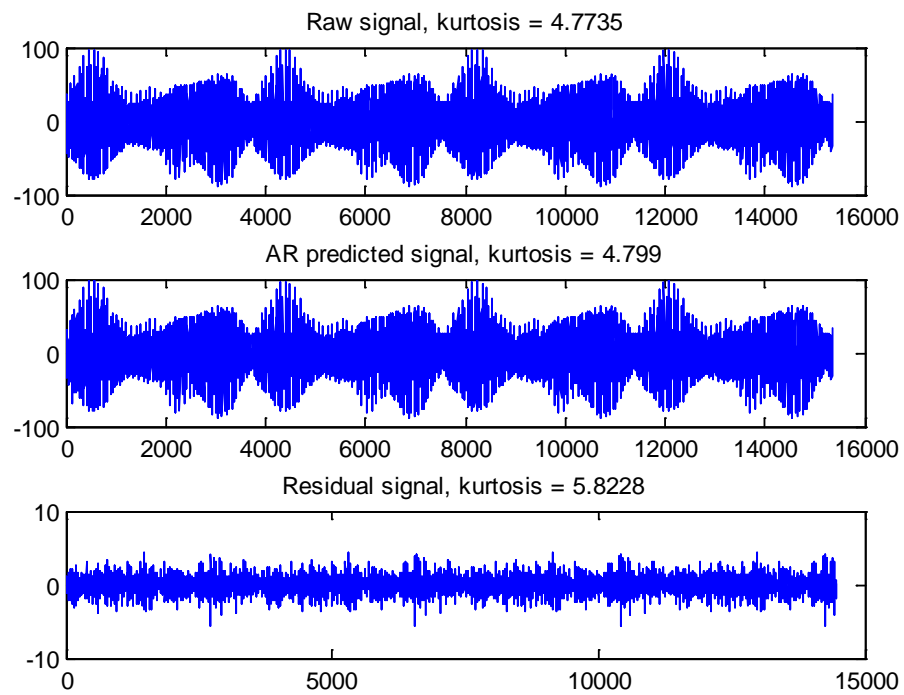


Figure 7.25 Simulation: undamaged gear (4 carrier cycles)

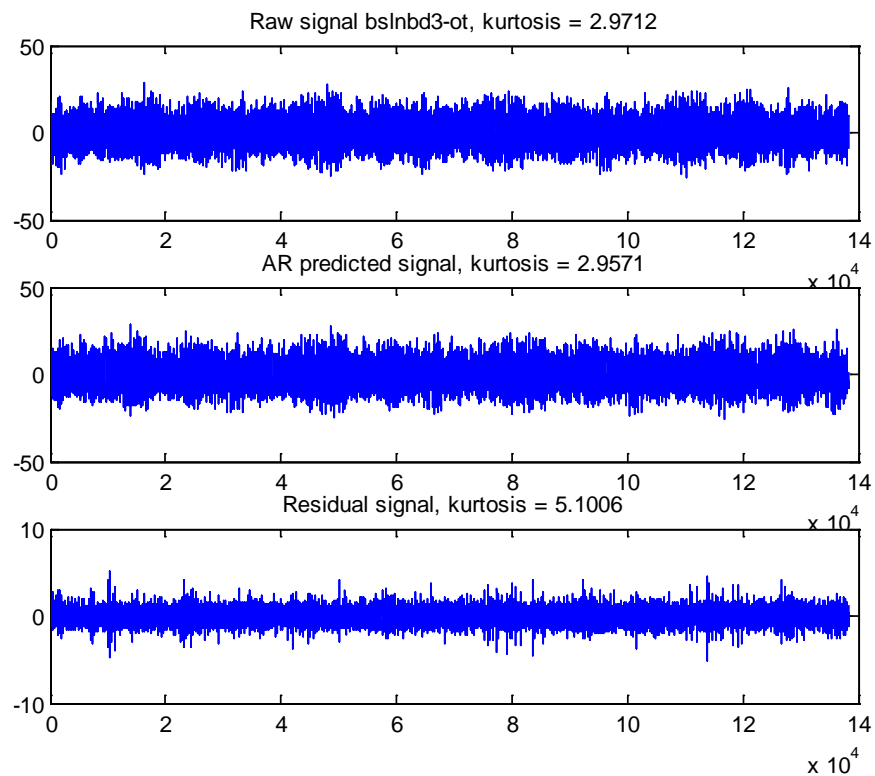


Figure 7.26 Test: undamaged gear (4 carrier cycles)

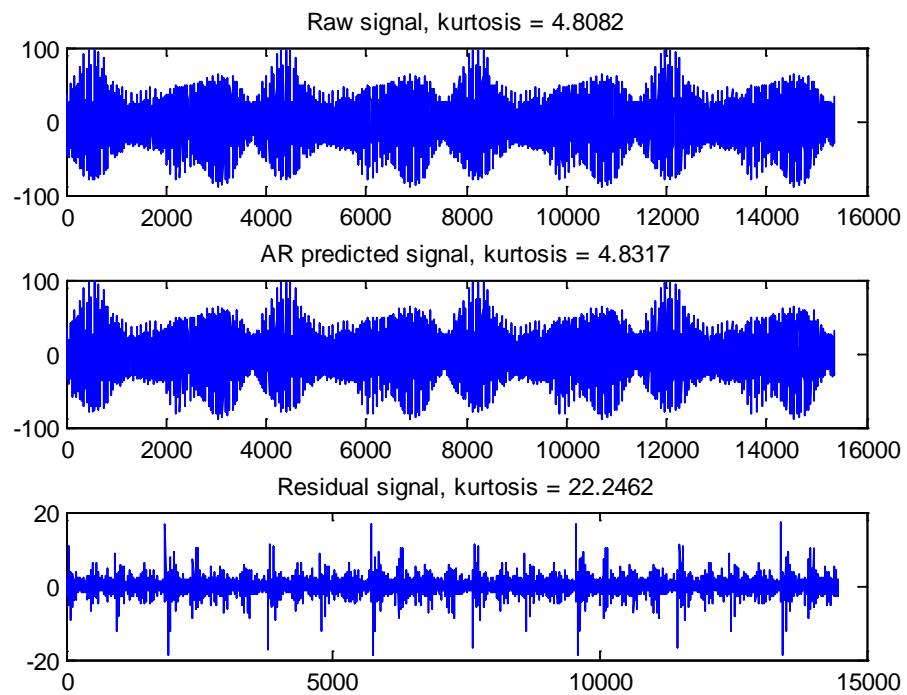


Figure 7.27 Simulation: Planet tooth crack (4 carrier cycles)

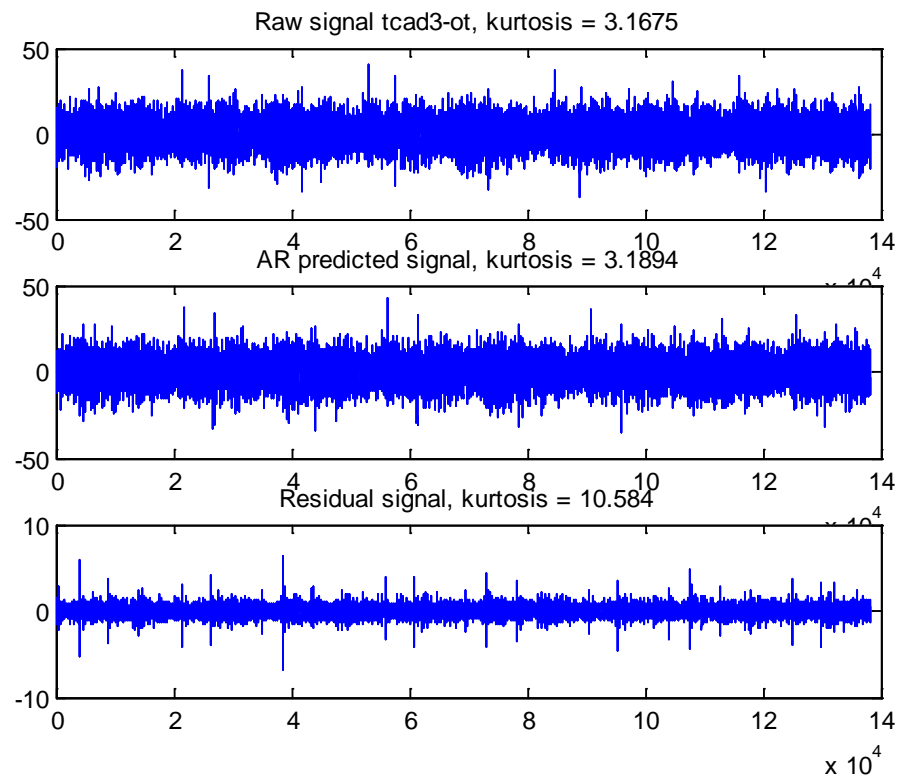


Figure 7.28 Test: Planet tooth crack opening when meshing with Sun gear (4 carrier cycles)

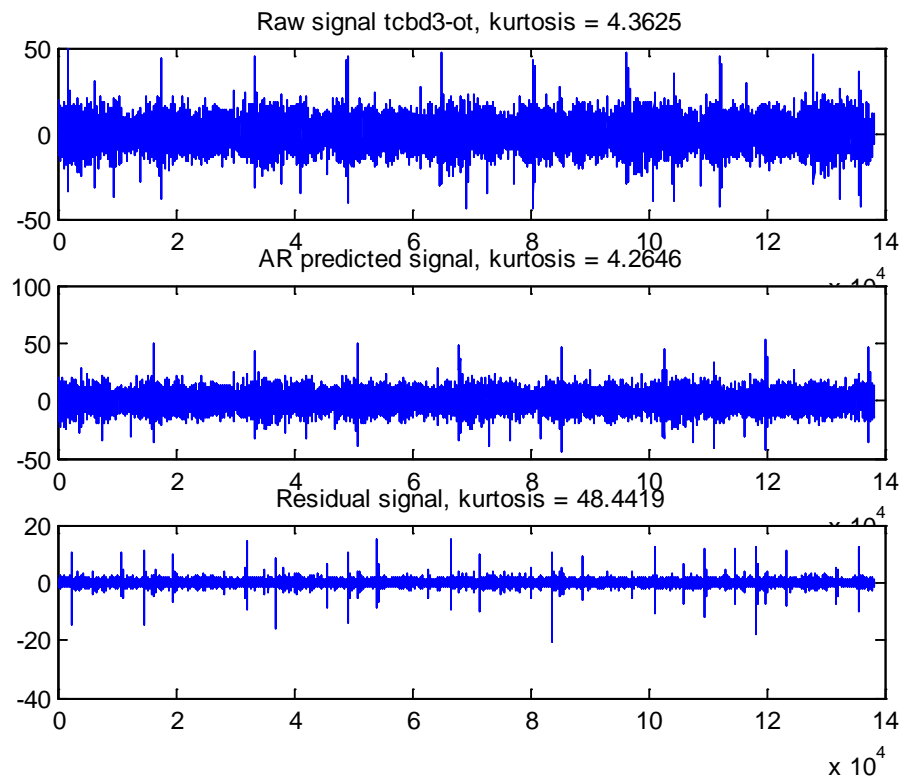


Figure 7.29 Test: Planet tooth crack opening when meshing with Ring gear (4 carrier cycles)

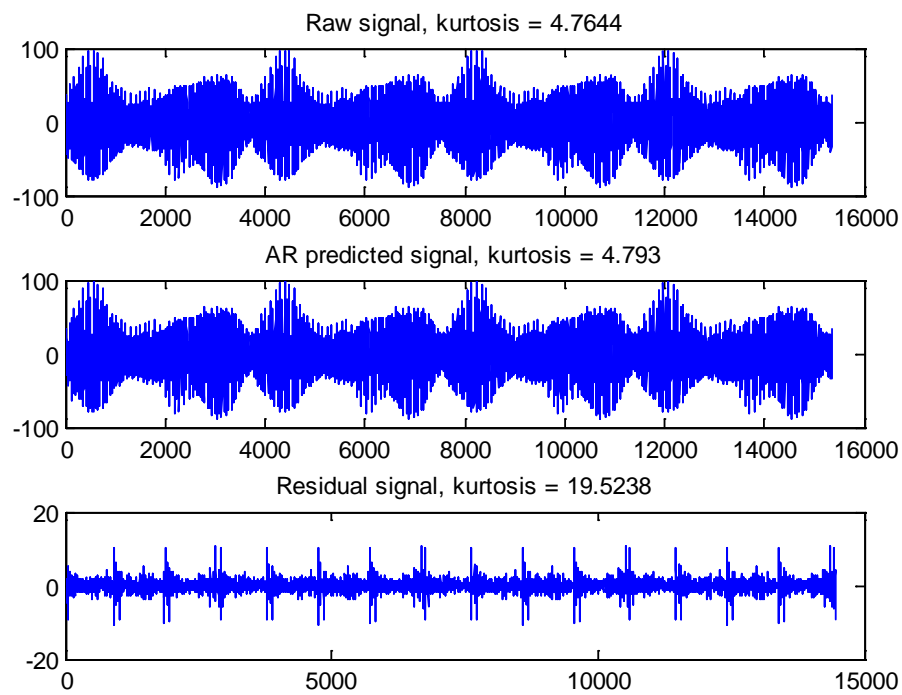


Figure 7.30 Simulation: Planet tooth spall meshing with ring gear
(4 carrier cycles)

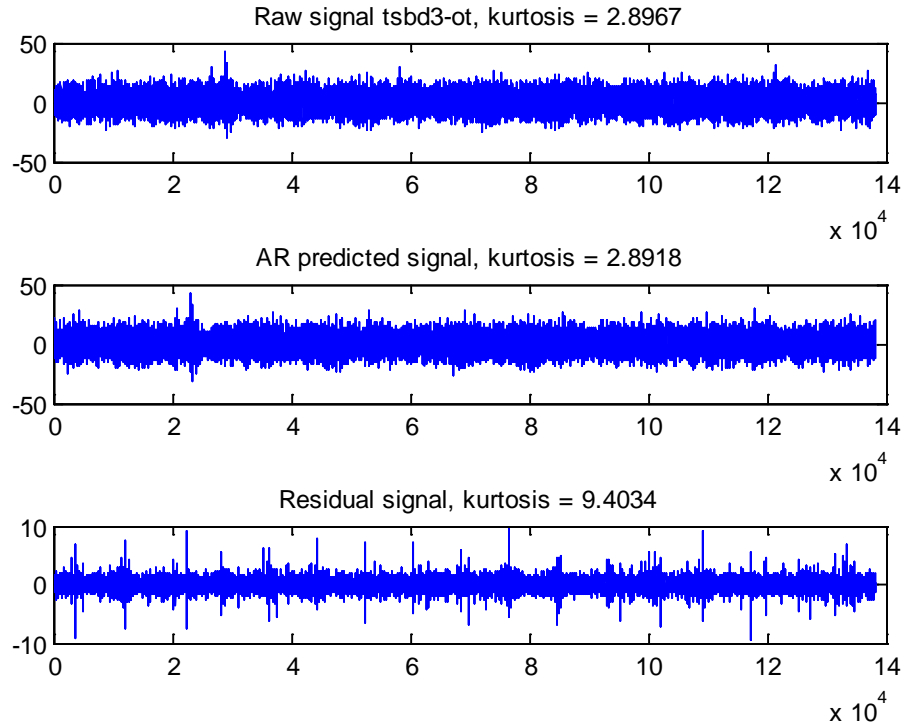


Figure 7.31 Test: Planet tooth spall meshing with ring gear
(4 carrier cycles)

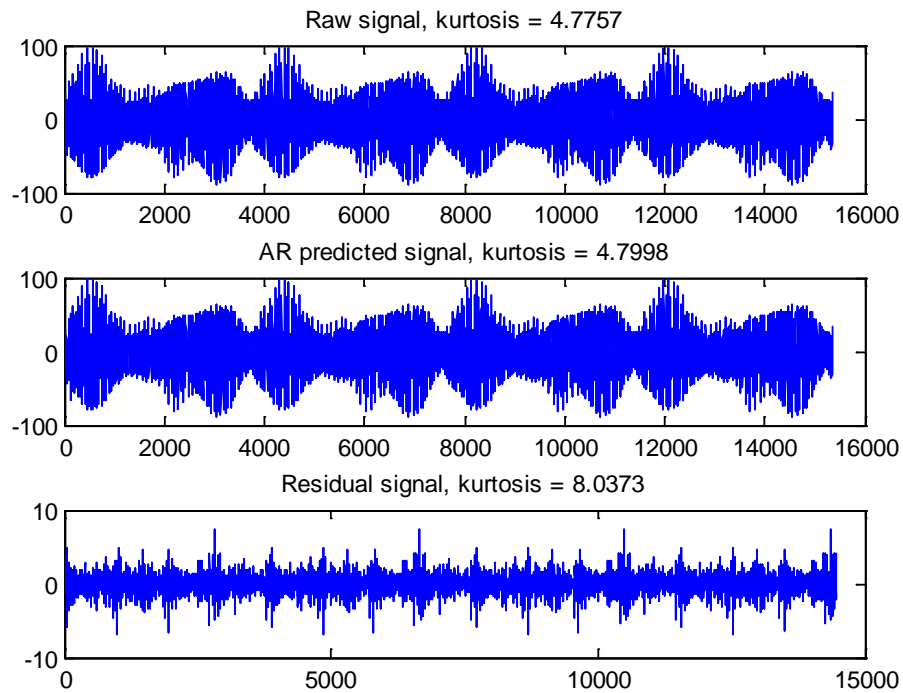


Figure 7.32 Simulation: Planet tooth spall meshing with sun gear (4 carrier cycles)

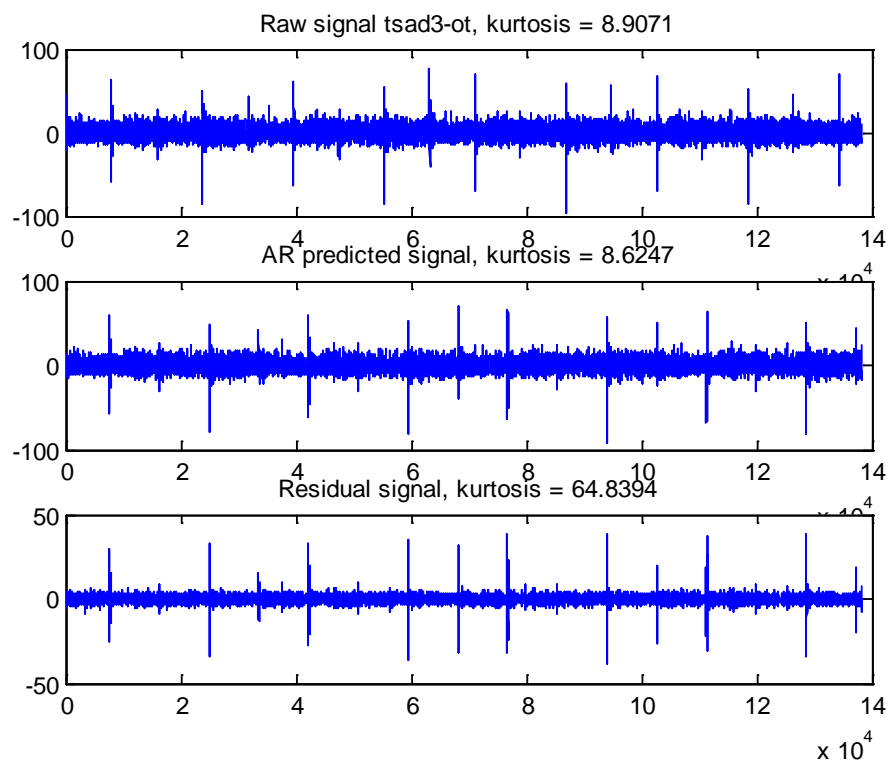


Figure 7.33 Test: Planet tooth spall meshing with sun gear (4 carrier cycles)

7.10 Conclusion

A simplified 18 DOF transverse-torsional LPM was developed to simulate gear faults such as tooth cracks and spalls in a planet gear of the UNSW planetary gearbox. The effect of the two simultaneous meshes of the planet gear with the ring and sun gears was investigated since the contact with the two gears is on opposite flanks of the planet gear tooth. Time-varying mesh stiffness curves with proper mesh phasing were defined using different contact ratios at the sun-planet and ring-planet contacts. The simulated results clearly differentiated the two types of faults with reduction in the stiffness due to a tooth crack visible in both contacts whereas a spall on one flank showed up only in one contact.

The effectiveness of the simulation models was assessed against experimentally measured vibration signals with and without gear faults using the UNSW planetary gearbox test rig. The gearbox under investigation comprised an extreme non hunting tooth design, which limited the effective use of conventional time synchronous averaging. Thus an alternative signal processing approach was employed, based on kurtosis enhancement using autoregressive linear prediction filtering. This method was found to greatly increase detection capability, with all faults easily detectable using the external acceleration signal. The simulated vibration signals showed good correlation with the measured signals.

It is proposed as part of the future work to modify the planetary gear ratios so as to achieve a hunting tooth design as encountered in most applications and implement signal averaging and windowing techniques in the diagnostics of the vibration signals.

7.11 References

- Antoni, J 2007. Fast computation of the kurtogram for the detection of transient faults. *Mechanical Systems and Signal Processing*, 21, 108-124.
- Antoni, J & Randall, RB 2006. The spectral kurtosis: application to the vibratory surveillance and diagnostics of rotating machines. *Mechanical Systems and Signal Processing*, 20, 308-331.

- Barszcz, T & Randall, RB 2009. Application of spectral kurtosis for detection of a tooth crack in the planetary gear of a wind turbine. *Mechanical Systems and Signal Processing*, 23, 1352-1365.
- Bligh, A. 2012. 'Design, Manufacture and Testing of a Planetary Gearbox For the Purpose of Internal Vibration Based Condition Monitoring'. BE Thesis, UNSW.
- Endo, H. 2005. *Simulation of gear faults and its application to the development of differential diagnostic technique* Ph. D. Dissertation, University of New South Wales, Sydney, Australia.
- Forrester, BD 1998. A method for the separation of epicyclic planet gear vibration signatures. *Third International Conference on Acoustical and Vibratory Surveillance Methods and Diagnostic Techniques*. Senlis, France.
- HyGears Gear design and analysis software V2.0. Involute Simulation Software Inc.
- Inalpolat, M & Kahraman, A 2009. A theoretical and experimental investigation of modulation sidebands of planetary gear sets. *Journal of Sound and Vibration*, 323, 677-696.
- Kahraman, A 1994. Load sharing characteristics of planetary transmissions. *Mechanism and Machine Theory*, 29, 1151-1165.
- Kim, W, Lee, JY & Chung, J 2012. Dynamic analysis for a planetary gear with time-varying pressure angles and contact ratios. *Journal of Sound and Vibration*, 331, 883-901.
- McFadden, PD 1986. Detecting Fatigue Cracks in Gears by Amplitude and Phase Demodulation of the Meshing Vibration. *Journal of Vibration Acoustics Stress and Reliability in Design*, 108, 165-170.
- McFadden, PD 1991. A technique for calculating the time domain averages of the vibration of the individual planet gears and the sun gear in an epicyclic gearbox. *Journal of Sound and Vibration*, 144, 163-172.

- Parker, RG & Lin, J 2004. Mesh Phasing Relationships in Planetary and Epicyclic Gears. *Journal of Mechanical Design*, 126, 365-370.
- Sawalhi, N, Randall, RB & Endo, H 2007. The enhancement of fault detection and diagnosis in rolling element bearings using minimum entropy deconvolution combined with spectral kurtosis. *Mechanical Systems and Signal Processing*, 21, 2616-2633.
- Smith, JD 1983. *Gears and their vibration - A basic approach to understanding gear noise*, Marcel Dekker/ Macmillan Press, Ltd.
- Smith, W, Deshpande, L, Randall, RB & Li, H 2013a. Bearing diagnostics in a planetary gearbox: a study using internal and external vibration signals. *26th International Congress of Condition Monitoring and Diagnostic Engineering Management (COMADEM 2013)*. Helsinki, Finland.
- Smith, W, Deshpande, L, Randall, RB & Li, H 2013b. Gear diagnostics in a planetary gearbox: a study using internal and external vibration signals. *The Tenth International Conference on Condition Monitoring and Machinery Failure Prevention Technologies (CM 2013 and MFPT 2013)*. Kraków, Poland.
- Stewart, RM 1977. Some Useful Data Analysis Techniques for Gearbox Diagnostics. *Proceedings of the Meeting on the Applications of Time Series Analysis, ISVR*. University of Southampton, Southampton, UK.
- Wang, W & Wong, AK 2002. Autoregressive Model-Based Gear Fault Diagnosis. *Journal of Vibration and Acoustics*, 124, 172-179.

CHAPTER 8

SUMMARY AND FUTURE WORK

8.1 Summary and conclusions

The research presented in this thesis focuses on the development of improved dynamic models to simulate gearbox vibrations due to faults in gears and bearings.

The objectives and the overall scope of the research were established in Chapter 1 along with a brief introduction to the proposed methodology.

The conclusions from the thesis can be summarised into two main categories as follows.

8.1.1 Simulation of bearing faults (Part I Chapters 2-5)

A comprehensive summary of machine condition monitoring techniques with specific reference to gears and bearings was provided in Chapter 2. A critical assessment of the suitability of the existing signal processing and diagnostic tools to analyse gear/bearing vibration signals (with and without bearing faults) was provided. The limitations of the contemporary gear/bearing simulation models were highlighted and the justification to include gearbox component flexibility through model reduction techniques was presented.

Chapter 3 summarises the Experimental Modal Analysis (EMA) and model updating of the FE model of the gearbox casing. The details of the test set-up and the finite element modelling are described. The Test-FEA correlation and Modal-based updating was carried out using the plate thickness of the casing as an updating parameter. The mode shape pairing was defined based on the MAC values which estimate the degree of correlation between the mode shape vectors of the analytical (FE) and the test model. A good correlation between the test and FE model was achieved. The validated FE model

of the casing was used in the subsequent development of improved bearing simulation models.

The importance of incorporating the dynamic characteristics of the gearbox casing was emphasized in Chapter 2. The existing LPM models lacked the component flexibility of dominant components (notably the casing) and failed to properly represent the gear/bearing interaction, which resulted in poor spectral matching over a wide frequency range. The finite element based modelling of the entire gear test rig can be an alternative but not always a feasible option as the model size and the computing resource requirements would become prohibitive. This dilemma of maintaining the model size to a reasonable limit without sacrificing the accuracy of the simulations was overcome by the application of model reduction techniques.

Chapter 4 describes a novel approach to simulate the bearing faults in the UNSW gearbox test rig (operating in the parallel shaft spur gear mode) using model reduction techniques. The Craig-Bampton (CB) method of Component Mode Synthesis (CMS) was implemented to significantly reduce the updated FE model of the casing (which had large number of DOFs).

The LPM had 22 DOFs corresponding to the gearbox internals (such as shafts, gears and bearings) and flywheels and encoders which were attached to the input and output shafts. The greatly reduced mass and stiffness matrices of the casing were combined with the LPM model in the Matlab/Simulink® environment to develop a combined (LPM + reduced FE model of casing) simulation model. The resulting combined model had a total of 146 DOFs.

Although the combined 146 DOF model included the flexibility of the casing, the gearbox internals were still represented by a significantly lower number of DOFs due to the use of the LPM approach. Hence a fully reduced dynamic simulation model of the gear test rig was developed by extracting the reduced mass and stiffness matrices of both the gearbox casing and the internal components. The resulting model had a total of 182 DOFs.

The equations of motion were redefined at the bearing/casing connection points in both the 146 and 182 DOF models. The chapter also illustrates the bearing model and gear

dynamic model (adapted from the previous work by S awalhi and Endo) and the modelling of bearing faults.

Chapter 5 describes the experimental validation of the bearing fault simulation models (146 and 182 DOF). A brief description of the test set-up, instrumentation and bearing fault details are provided. The simulation models were solved in the Matlab/Simulink environment and vibration signals were extracted in the presence of localised and extended faults in the inner and outer race of the bearing. The localised fault geometry was represented with a smooth curvature (with a radius approximately equal to that of the rolling element) at the fault entry and exit, instead of a rectangular notch as used in the earlier models, which exhibited the double impulses that were incorrectly linked to the fault width.

The vibration signals were extracted using two different approaches namely the force convolution method and the response at a slave DOF (at the accelerometer mounting position) using the Craig-Bampton method. The results of both the simulation models were compared with the initial LPM model and the measurements.

The vibration characteristics of the 146 and 182 DOF simulation models correlated well with measurements especially in the low frequency region of 2-4 kHz where the LPM model was found to be deficient. The technique of cepstrum prewhitening followed by envelope analysis was found to be effective to identify the localised (BPFI and BPFO) fault frequencies.

Due to the multiplicative interaction of the bearing and gear signals, an approach based on spectral correlation was used to identify the extended (rough) faults in the inner and outer race of the bearing.

Cepstrum prewhitening was also used to enhance the step and impulse responses at the localised fault entry and exit. The simulated results showed better agreement with the measurements in the case of the localised inner race fault than the localised outer race fault. The results confirm that the average time to impact corresponds to half the spall width and the methodology can be used to estimate the spall size which is an important monitoring parameter in bearing prognostics.

Both the simulation models were found to be effective in generating the characteristic vibrations similar to those produced by the gearbox test rig with and without bearing fault. However, the use of the full reduced model (182 DOF) substantially reduces the modelling time by eliminating the need to manually create the system matrices (of the gearbox internals) and also increases the ease of incorporating additional DOFs or modal coordinates for the internals. The full potential of the improved models can be further exploited to develop more efficient diagnostic and prognostic algorithms by simulating the faults of different sizes and locations.

8.1.2 Simulation of planet gear faults (Part II Chapters 6-7)

The condition monitoring of planetary gear trains is quite challenging due to the rotating axes of the planet gears, multiple pairs of gearmeshes and the time varying transmission path of the vibration signal (depending on the location of the fault). Unlike fixed axis gearboxes, a more elaborate (and often tailor made) signal processing approach is required to analyse the vibrations from the planetary gear train.

Chapter 6 provides a comprehensive summary of the state of the research pertaining to the simulation of planetary gear systems. A review of analytical models of the planetary transmissions, effect of mesh phasing, simulation of gear faults, and vibration signal processing techniques is presented.

Chapter 7 describes the development of a simplified 18 DOF transverse-torsional LPM model of the UNSW gearbox planetary insert. The model included the sun gear, the ring gear and the three equi-spaced planet gears mounted on the planet carrier. The input torque was applied to the planet carrier whereas the sun gear provided the output while the ring gear was held stationary. Time-varying mesh stiffness curves with proper mesh phasing were defined using different contact ratios at the sun-planet and ring-planet contacts. The model was used to simulate two types of planet gear faults, namely, a tooth crack and a spall with the former modelled as a change in the mesh stiffness (acting in both directions) and the latter as a geometric fault (on one tooth flank only) based on the transmission error due to the spalled geometry with negligible change in the mesh stiffness.

The effect of the two simultaneous meshes of the planet gear with the ring and sun gears was investigated since the contact with the two gears is on opposite flanks of the planet gear tooth. The validity of the simulation model was established by comparing vibration signals with those obtained using the UNSW gear test rig running in the planetary mode. The conventional signal processing techniques such as time synchronous averaging and windowing could not be used due to an extreme non hunting tooth design of the planetary gearbox. Hence, an alternative signal processing approach, based on kurtosis enhancement using autoregressive linear prediction filtering, was employed and was found to be quite effective in the fault detection. The simulated vibration signals showed good correlation with the measured signals and clearly differentiated the two types of faults with reduction in the stiffness due to a tooth crack visible in both contacts whereas a spall on one flank showed up only in one contact.

8.2 Recommendations for future work

The research presented in this thesis demonstrates the effectiveness of dynamic models to simulate gear and bearing faults. Even though the simulation results are encouraging, several avenues can still be explored to further improve the methodologies in order to obtain a better match with the physical responses. The following recommendations are made as a direct extension of some of the concepts used in this research.

8.2.1 Simulation of bearing faults (Part I)

- Although the 146 and 182 DOF models clearly identified the bearing faults, the spectra indicated the presence of aliasing. Several measures were tried to eliminate this, and were partially though not completely successful. The gearmesh frequencies were not as clearly observed in the spectra of the 182 DOF model. These issues need to be further investigated.
- The geometry of the extended outer race fault appears still to be impulsive and needs to be modified to ensure the smooth passage of the rolling element at entry and exit of the fault.
- The bearing model ignores the elasto-hydrodynamic effect of the oil film which has little influence on the localised faults. However, this can lead to a more impulsive vibration signal in the case of extended faults and needs to be incorporated in the bearing model.

- The force convolution method (Approach B) was found to be less effective with the SCF approach in the case of the extended bearing faults and needs to be further looked into.
- The study of fault entry/exit phenomena indicated a better match with the measurements in the case of the localised inner race fault than in the case of the localised outer race fault, but there was a tendency for higher noise in the measurements for that case also. This problem needs further investigation.
- The bearing signals are not strictly periodic and are best described as pseudo-cyclostationary as they contain some randomness due to the slippage and random spacing of the rolling elements. Hence, the modelling of this slippage of the rolling elements needs improvement before inclusion in the simulation models.
- The gathered data from the simulation models could be further utilised to train artificial neural networks (ANNs) to recognise the onset of incipient faults and fault development and thus develop more efficient prognostic algorithms.

8.2.2 Simulation of planet gear faults (Part II)

- The 18 DOF LPM of the planetary insert includes only the sun gear, ring gear and the three equi-spaced planet gears and ignores the pinion/spur gear pair (1st stage reduction) in the actual test rig. For a more realistic simulation, the entire gear test rig could be modelled similar to the model of the fixed axis spur gearbox described in Part I. The Craig-Bampton method of model reduction could be applied to take into account the dynamic characteristics of the casing.
- The experimental measurements were carried out on the UNSW planetary test rig with the faults in both the planet gears and the bearings. The current model of the planetary insert is capable of simulating only the gear faults. The model could be further updated and used to simulate the bearing faults and verified against the measured data.
- The UNSW planetary gearbox represents an extreme case of non hunting tooth design which is rarely encountered in real life applications. Hence it is suggested to modify the planetary gear ratios to achieve a hunting tooth design which will enable the implementation of signal averaging and windowing techniques in the diagnostics of the vibration signals. Such a design, which can be accommodated within the geometry, has already been devised.

8.3 Contribution to Research

- Implementation of a novel approach of bearing fault simulation using model reduction techniques which addresses the limitations of both traditional lumped parameter and finite element models
- Application of model updating techniques based on Experimental Modal Analysis to validate and update the FE model of the gearbox casing
- Inclusion of gearbox casing dynamic characteristics using the Craig-Bampton method of Component Mode Synthesis to formulate a combined model comprising an LPM of the internals and reduced FE model of the casing
- Extension of the model reduction technique to the gearbox internal components to develop a full reduced model of the internals and the casing
- Updated localised fault geometry with a smooth curvature at the fault entry and exit, instead of a rectangular notch used in the earlier models, which exhibited double impulses that were incorrectly associated with the fault width
- Validation of the simulated vibration signals with the measurements in the presence of localised and extended faults in the inner and outer race of the bearing
- Development of a transverse-torsional simulation model of the UNSW planetary insert to simulate planet gear faults such as tooth cracks and spalls
- Vibration signal processing to differentiate between the planet gear tooth crack and the spall taking into account the simultaneous meshes with the ring and the sun gear

The list of publications originating from this research is included on the following pages.

List of Publications

- [1] L. Deshpande, N. Sawalhi, and R. Randall, "Improved gearbox simulations for diagnostic and prognostics purposes using finite element model reduction techniques " *Australian Journal of Mechanical Engineering* vol. 8 pp. 91-101 2011
- [2] L. Deshpande, N. Sawalhi, and R. B. Randall, "Fault Simulation in a Gearbox Using Finite Element Model Reduction Techniques," in *IMAC-XXIX Conference and Exposition on Structural Dynamics*, Jacksonville, Florida USA, 2011.
- [3] L. Deshpande, N. Sawalhi, and R. B. Randall, "Dynamic simulation of a gearbox system in the presence of bearing faults using finite element model reduction techniques," in *The Eighth International Conference on Condition Monitoring and Machinery Failure Prevention Technologies*, Cardiff, UK, 2011.
- [4] L. Deshpande, N. Sawalhi, and R. B. Randall, "Gearbox fault simulation using finite element model reduction technique," presented at the ACOUSTICS 2011, Gold Coast, Australia, 2011.
- [5] L. Deshpande, N. Sawalhi, and R. B. Randall, "Improved simulation of bearing faults using a finite element model reduction technique," presented at the The Ninth International Conference on Condition Monitoring and Machinery Failure Prevention Technologies, London, UK, 2012.
- [6] L. Deshpande, N. Sawalhi, and R. B. Randall, "Gearbox bearing fault simulation using a finite element model reduction technique," presented at the 25th International Congress on Condition Monitoring and Diagnostic Engineering Management, Huddersfield, UK, 2012.
- [7] L. Deshpande, N. Sawalhi, and R. B. Randall, "Bearing fault simulation using finite element model updating and reduction techniques," in *7th Australasian Congress on Applied Mechanics, ACAM 7* Adelaide, Australia, 2012.
- [8] L. G. Deshpande, N. M. Sawalhi, and R. B. Randall, "Application of finite element model updating and reduction techniques to simulate gearbox bearing

faults," *Australian Journal of Multi-Disciplinary Engineering*, vol. Vol 10 No 2, pp. 1-12, 2013.

- [9] N. Sawalhi, L. Deshpande, and R. B. Randall, "Improved simulations of faults in gearboxes for diagnostic and prognostic purposes using a reduced finite element model of the casing," in *7th DSTO International Conference on Health & Usage Monitoring* Melbourne, 2011.
- [10] W. Smith, L. Deshpande, R. B. Randall, and H. Li, "Bearing diagnostics in a planetary gearbox: a study using internal and external vibration signals," in *26th International Congress of Condition Monitoring and Diagnostic Engineering Management (COMADEM 2013)*, Helsinki, Finland, 2013.
- [11] W. Smith, L. Deshpande, R. B. Randall, and H. Li, "Gear diagnostics in a planetary gearbox: a study using internal and external vibration signals," in *The Tenth International Conference on Condition Monitoring and Machinery Failure Prevention Technologies (CM 2013 and MFPT 2013)*, Kraków, Poland, 2013.

APPENDIX A

COMBINED LPM-REDUCED FE MODEL (146 DOF)

A.1 Introduction

The methodology to generate the 146 DOF combined model (LPM-reduced FE model of casing) was illustrated in Chapter 4 (Section 4.3.2). This appendix provides further details of this combined model.

Out of the 146 DOFs in the combined model, the LPM of the internals consisted of 22 DOFs. These were extracted from the original 34 DOF LPM model by removing the 12 DOFs associated with the four bearing pedestals - related to the DOFs in the x and y direction and a mass/spring system in the y direction at each pedestal (Section 4.2.5). The 22 DOFs correspond to 10 rotational and 12 translational degrees of freedom as shown below (Figure A.1):

θ_{f1}, θ_{f2} rotational degrees of freedom of flywheels 1 and 2 (rad)

$\theta_{s1}, \theta_{s2}, \theta_{s3}, \theta_{s4}$ rotational degrees of freedom of shafts at respective bearings (rad)

$\theta_{pin}, \theta_{ge}$ rotational degrees of freedom of pinion and gear (rad)

$\theta_{ec1}, \theta_{ec2}$ rotational degrees of freedom of encoders 1 and 2 (rad)

x_{pin}, y_{pin} translational degrees of freedom of pinion in x and y directions (m)

x_{ge}, y_{ge} translational degrees of freedom of gear in x and y directions (m)

x_{si}, y_{si} translational degrees of freedom of bearings in x and y directions, $i=1,2,3,4$ (m)

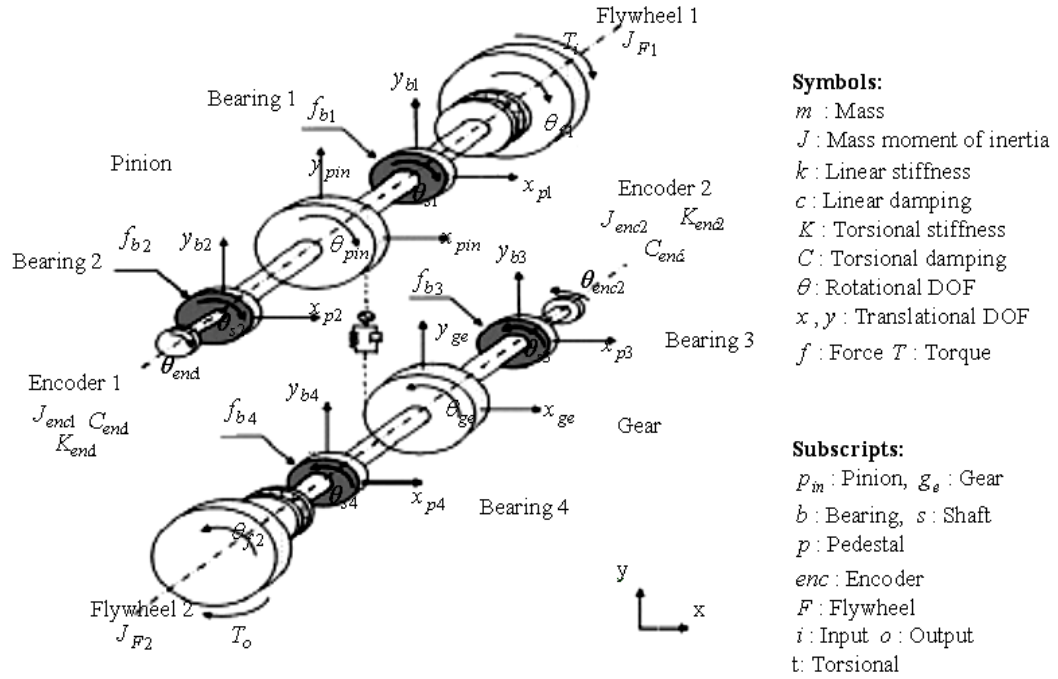


Figure A.1 22 DOF LPM - extracted from 34 DOF Model (Sawalhi, 2007)

The detailed equations of motion can be found in (Sawalhi, 2007, Sawalhi and Randall, 2008) and are not repeated in this Appendix for the sake of brevity. However, the physical parameters of the model and the resulting system matrices (mass, stiffness and damping) have been modified slightly and are provided in the next section.

A.2 Physical parameters and system matrices - LPM (22 DOF)

The physical properties of the model were based on the geometric dimensions of gearbox components and were extracted from (Gao and Randall, 2000). Table A.1 lists the various parameters of the 22 DOF model of the gearbox internals.

Table A.2 lists the physical parameters of the bearing system. The code for generating the system matrices in the Matlab format is shown in Section A.2.1.

Table A.1 Physical parameters of gear dynamic model (Gao and Randall, 2000)

	Mass		Stiffness		Damping	
Flywheel 1	J_{F1} (kg m ²)	0.3647	K_{F1} (Nm/rad)	580	C_{F1} (Nm s/rad)	10.20
Flywheel 2	J_{F2} (kg m ²)	0.5881	K_{F2} (Nm/rad)	580	C_{F2} (Nm s/rad)	12.96
Shafts	J_{S1} (kg m ²)	9.998×10^{-4}	K_{ts} (Nm/rad)	4.241×10^4		
	J_{S2} (kg m ²)	6.36×10^{-5}	K_{ts} (Nm/rad)	4.241×10^4		
	J_{S3} (kg m ²)	6.36×10^{-5}	K_{ts} (Nm/rad)	4.241×10^4		
	J_{S4} (kg m ²)	9.998×10^{-4}	K_{ts} (Nm/rad)	4.241×10^4		
Pinion	J_{pin} (kg m ²)	1.766×10^{-3}				
	m_{pin} (kg)	2.1208	$k_s = k_{\text{Sge}} = k_{\text{Spin}}$ (N/m)	7.42×10^7	C_m (N s/m)	2594
Gear	J_{ge} (kg m ²)	1.766×10^{-3}	K_m (mean) (N/m)	3.178×10^8		
	m_{ge} (kg)	2.1208				
Encoder 1	J_{ec1} (kg m ²)	2.525×10^{-5}	K_{ec1} (N m/rad)	300	C_{ec1} (Nm s/rad)	0.001
Encoder 2	J_{ec2} (kg m ²)	2.525×10^{-5}	K_{ec2} (N m/rad)	300	C_{ec2} (Nm s/rad)	0.001

Table A.2 Physical parameters of bearing model (Sawalhi, 2007)

	Mass (kg)		Stiffness		Damping	
Bearings	m_{S1}	1.2638	$K_{b1x} = K_{b1y}$ (N/m ^{1.5})	1.5×10^8	$C_{b1x} = C_{b1y}$ (Ns/m)	1376.8
	m_{S2}	0.5134	$K_{b2x} = K_{b2y}$ (N/m ^{1.5})	1.5×10^8	$C_{b2x} = C_{b2y}$ (Ns/m)	877.6
	m_{S3}	0.5134	$K_{b3x} = K_{b3y}$ (N/m ^{1.5})	1.5×10^8	$C_{b3x} = C_{b3y}$ (Ns/m)	877.6
	m_{S4}	1.2638	$K_{b4x} = K_{b4y}$ (N/m ^{1.5})	1.5×10^8	$C_{b4x} = C_{b4y}$ (Ns/m)	1376.8

Note: Radius of pinion/ gear $r_p = r_g = 0.0463$ m

Some parameters have been modified to obtain better match with measurements.

A.2.1 System matrices

Mass Matrix

```
M(1:22,1:22)=diag([j1 j1 jp jb2 jec1 jg jb3 jb4 jec2 j2 mb1 mb1 mp
mp mb2 mb2 mg mg mb3 mb3 mb4 mb4]);
```

Mass moment of inertia of flywheel 1 and 2 (j1, j2)

Mass moment of inertia of encoder 1 and 2 (jec1, jec2)

Mass moment of inertia of pinion and gear (jp, jg)

Mass moment of inertia of bearing 1 to 4 (jb1, jb2, jb3, jb4)

Mass of pinion and gear (mp, mg)

Mass of bearing 1 to 4 (mb1, mb2, mb3, mb4)

Stiffness Matrix

```
Ki(1, 1:2)=[kt1,-kt1];
```

```
Ki(2, 1:3)=[-kt1,kt1+kts,-kts];
```

```
Ki(3,[2,3,4,6,14,18])=[-kts,2*kts+km*rp^2,-kts,-km*rp*rg,-
km*rp,km*rp];
```

```
Ki(4,3:5)=[-kts, kts+kec1, -kec1];
```

```
Ki(5, [4,5])=[-kec1, kec1];
```

```
Ki(6,[3,6,7,8,14,18])=[-km*rp*rg,2*kts+km*rg^2,-kts,-kts,km*rg,-
km*rg];
```

```
Ki(7,[6,7,9])=[-kts, kec2+kts, -kec2];
```

```
Ki(8,[6,8,10])=[-kts, kt2+kts, -kt2];
```

```
Ki(9, [7,9])=[-kec2, kec2];
```

```
Ki(10,[8,10])=[-kt2, kt2];
```

```
Ki(13,[13,11,15])=[2*ks,-ks,-ks];
```

```
Ki(14,[3,6,12,14,16,18])=[-km*rp,km*rg,-ks,km+2*ks,-ks,-km];
```

```
Ki(17,[17,19,21])=[2*ks,-ks,-ks];
```

```
Ki(18,[3,6,14,18,20,22])=[km*rp,-km*rg,-km,km+2*ks,-ks,-ks];
```

```
Ki(11,[11,13])=[ks+kb1x,-ks];
```

```
Ki(12,[12,14])=[ks+kb1y,-ks];
```

```
Ki(15,[15,13])=[ks+kb2x,-ks];
```

$Ki(16, [16, 14]) = [ks + kb2y, -ks];$

$Ki(19, [19, 17]) = [ks + kb3x, -ks];$

$Ki(20, [20, 18]) = [ks + kb3y, -ks];$

$Ki(21, [21, 17]) = [ks + kb4x, -ks];$

$Ki(22, [22, 18]) = [ks + kb4y, -ks];$

Damping Matrix

$dampC(1, 1:2) = [ct1, -ct1];$

$dampC(2, 1:2) = [-ct1, ct1];$

$dampC(3, [3, 6, 14, 18]) = [cm*rp^2, -cm*rp*rg, -cm*rp, cm*rp];$

$dampC(4, 4:5) = [cec1, -cec1];$

$dampC(5, 4:5) = [-cec1, cec1];$

$dampC(6, [3, 6, 14, 18]) = [-cm*rp*rg, cm*rg^2, cm*rg, -cm*rg];$

$dampC(7, [7, 9]) = [cec2, -cec2];$

$dampC(8, [8, 10]) = [ct2, -ct2];$

$dampC(9, [7, 9]) = [-cec2, cec2];$

$dampC(10, [8, 10]) = [-ct2, ct2];$

$dampC(13, 13) = 0;$

$dampC(14, [3, 6, 14, 18]) = [-cm*rp, cm*rg, cm, -cm];$

$dampC(17, 17) = 0;$

$dampC(18, [3, 6, 14, 18]) = [cm*rp, -cm*rg, -cm, cm];$

$dampC(11, [11]) = [cb1x];$

$dampC(12, [12]) = [cb1y];$

$dampC(15, [15]) = [cb2x];$

$dampC(16, [16]) = [cb2y];$

$dampC(19, [19]) = [cb4x];$

$dampC(20, [20]) = [cb4y];$

$dampC(21, [21]) = [cb3x];$

$dampC(22, [22]) = [cb3y];$

A.3 Simulink model - 146 DOF

The schematic of the 146 DOF Simulink model is shown in Figure A.2. The inputs to the model are input and output torques, system matrices (mass, stiffness and damping) and the time varying gearmesh stiffness. The outputs are acceleration, velocity and displacement. Figure A.3 shows the Simulink module to calculate the excitation forces and the accelerations and also illustrates the procedure to combine the 22 DOF LPM with the 124 DOF reduced casing model. The bearing model (Figure A.4) is represented by a special Matlab S-function (Sawalhi, 2007) and evaluates the bearing forces from the displacements and rotational speed at each time step. The gear dynamic model (gear S-function) incorporated into the Simulink model is based on the model developed by Endo to simulate the gear faults (Endo, 2005). The set of equations of motion with time varying mesh stiffness were solved using ordinary differential equation solver (ode45) with variable time step in the Matlab/Simulink environment.

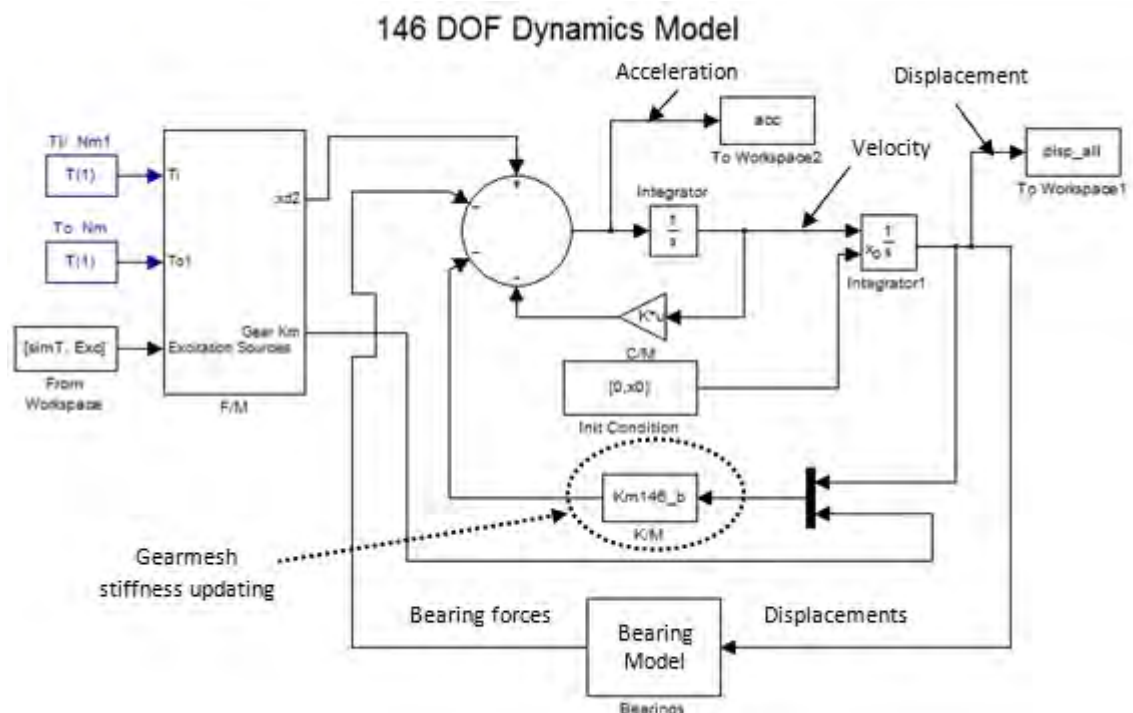


Figure A.2 146 DOF Simulink model

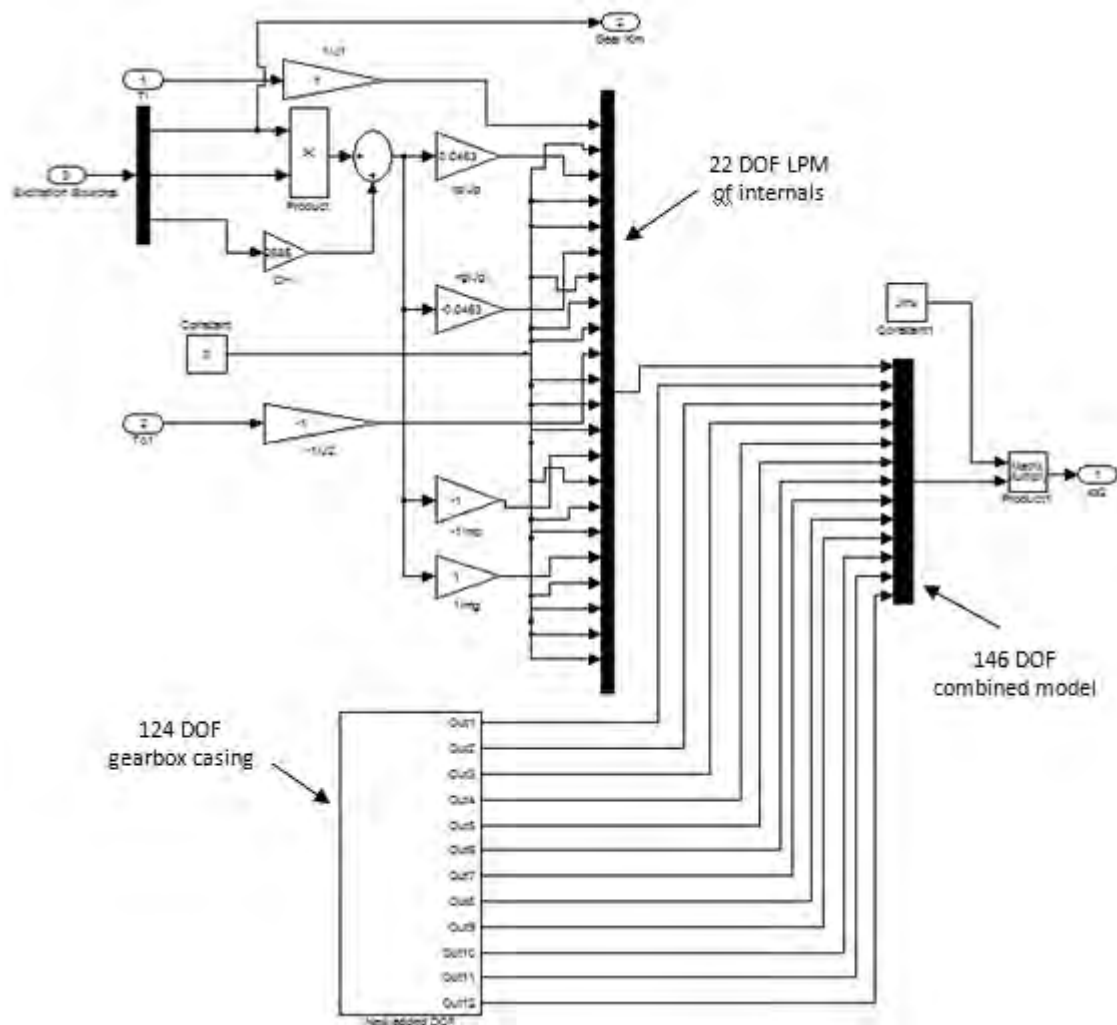


Figure A.3 Combining LPM and reduced FE model of casing

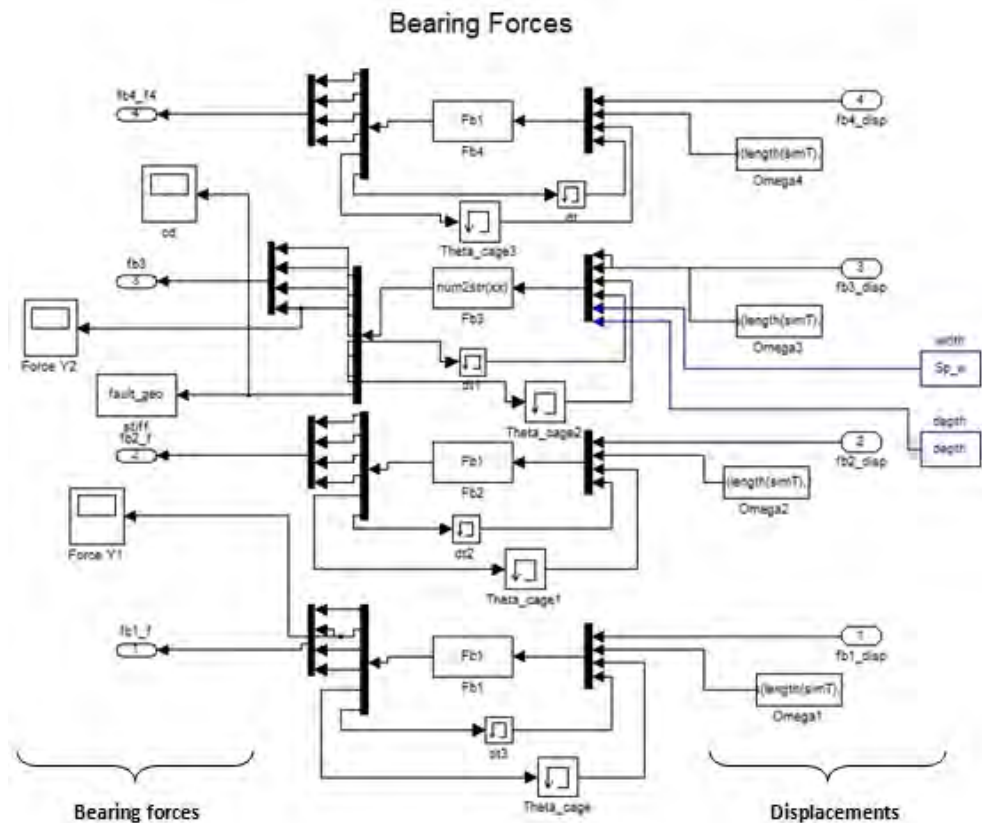


Figure A.4 Bearing S-function [similar to 34 DOF LPM (Sawalhi, 2007)]

A.4 References

- Endo, H. 2005. *Simulation of gear faults and its application to the development of differential diagnostic technique* Ph. D. Dissertation, University of New South Wales, Sydney, Australia.
- Gao, Y & Randall, RB 2000. Simulation of geometric, static and dynamic gear transmission errors, (Report CEVA-2000-01). Centre of Expertise in Vibration Analysis, UNSW, Sydney, .
- Sawalhi, N. 2007. *Diagnostics, prognostics and fault simulation for rolling element bearings*. Ph. D. Dissertation, University of New South Wales, Sydney, Australia.
- Sawalhi, N & Randall, RB 2008. Simulating gear and bearing interactions in the presence of faults: Part I. The combined gear bearing dynamic model and the simulation of localised bearing faults. *Mechanical Systems and Signal Processing*, 22, 1924-1951.

APPENDIX B

FULL REDUCED MODEL (182 DOF)

B.1 Introduction

The methodology to generate the full reduced model (182 DOF) was presented in Chapter 4 (Section 4.4.1). This appendix provides further details of the full reduced model (182 DOF) which is developed by combining the reduced models of both the gearbox casing and the internals. The reduced model of the casing is essentially the same as that used in the 146 DOF combined (LPM-FEM) model described in Chapter 4 and Appendix A. Hence, the additional details of the reduced FE model of the gearbox internals - input and output shaft subsystems excluding the casing are provided in this Appendix.

B.2 Gearbox internals

B.2.1 Physical parameters

The material properties of steel were assigned to the finite elements representing the input and output shaft (nominal diameter 0.024 m) and the pinion and the gear. The flywheels and the encoders mounted on the two shafts were modelled as inertial elements (Figure 4.11). Table B.1 shows the inertia and stiffness properties of the flywheels and the encoders.

Table B.1 FE model properties of gearbox internals

Flywheel rotational inertia (Input shaft)	0.3647 kgm ²
Flywheel rotational inertia (Output shaft)	0.5881 kgm ²
Flywheel rotational spring stiffness	740 Nm/rad
Encoder rotational inertia	2.525 x10 ⁻⁵ kgm ²
Encoder rotational spring stiffness	3000 Nm/rad

B.2.2 Master Degrees of Freedom (MDOFs)

The MDOFs were selected so as to enable connection of the reduced model of the internals with the reduced model of the casing and to capture the dynamic characteristics of both the internal components and the casing. The MDOF set mainly included the DOFs associated with the nodes corresponding to the bearing centre points, shaft-gear connection points, flywheels, and gearmesh locations (Figure 4.11).

Eight MDOFs (physical coordinates) were selected for each shaft along with a total of 42 modal coordinates resulting in a 58 DOF reduced model of the gearbox internals. The summary of the selected MDOFs is shown in Table B.2.

Table B.2 FE model of gearbox internals – Summary of MDOFs

Input shaft	Master Degrees of Freedom (MDOFs)	Output shaft	Master Degrees of Freedom (MDOFs)
Flywheel 1	Rz	Flywheel 2	Rz
Pinion	Rz	Gear	Rz
Gearmesh 1	Ux, Uy	Gearmesh 2	Ux, Uy
Bearing 1	Ux, Uy	Bearing 3	Ux, Uy
Bearing 2	Ux, Uy	Bearing 4	Ux, Uy

Ux, Uy are translations in the x (longitudinal) and y (vertical) direction. Rz is rotation in the z (axial) direction.

The Craig-Bampton model reduction was applied to the FE model of the internals based on the selected MDOFs. The reduced models of both the internals (58 DOFs) and the

casing (124 DOFs) were assembled in the Matlab/Simulink environment to create the reduced dynamic model of the entire UNSW gear test rig with a total of 182 DOFs.

B.3 Simulink model - 182 DOF

The methodology to set up the 182 DOF Simulink model is similar to the 146 DOF model described in Appendix A. The main difference is that the 22 DOF LPM model is now replaced with 58 DOFs of the internals which are combined with the 124 DOF reduced model of the casing.

The schematic of the 182 DOF Simulink model is shown in Figure B.1. The inputs to the model are input and output torques, system matrices (mass, stiffness and damping) and the time varying gearmesh stiffness. The outputs are acceleration, velocity and displacement. Figure B.2 shows the Simulink module to calculate the excitation forces and the accelerations and also illustrates the procedure to combine the 58 DOFs of the internals with the 124 DOFs of the reduced casing model. The bearing model (Figure B.3) is represented by a special Matlab S-function (Sawalhi, 2007) and evaluates the bearing forces from the displacements and rotational speed at each time step. The gear dynamic model (gear S-function) incorporated into the Simulink model is based on the model developed by Endo to simulate the gear faults (Endo, 2005). The simulations were carried out under 50 N m load at 10 Hz constant shaft frequency. The set of equations of motion with time varying mesh stiffness were solved using ordinary differential equation solver (ode45) in the Matlab/Simulink environment.

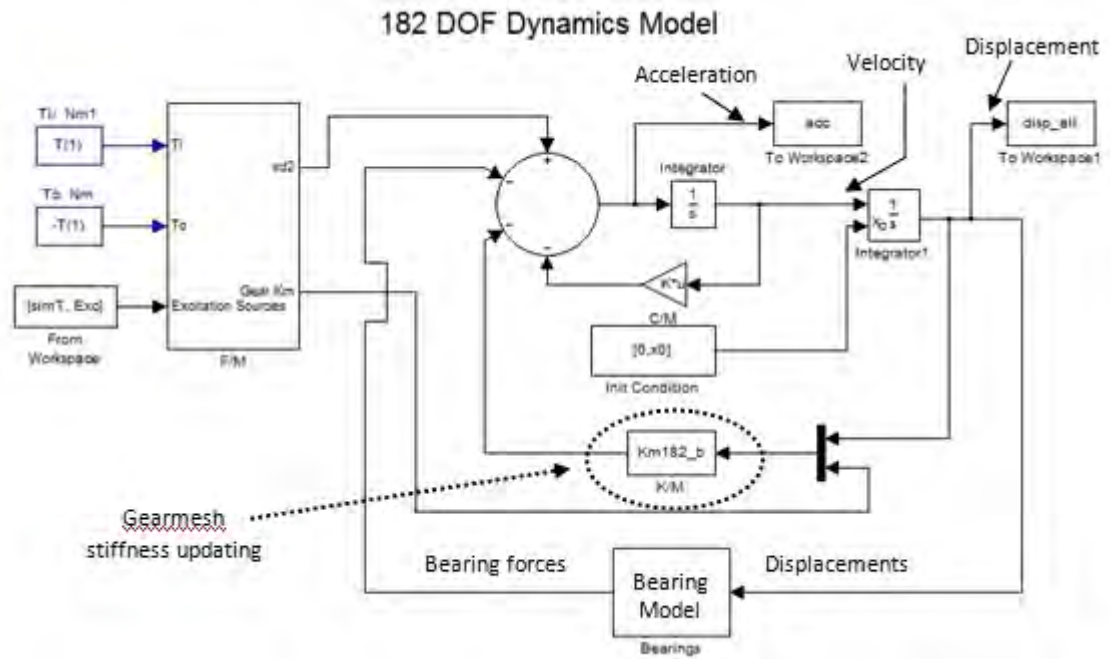


Figure B.1 182 DOF Simulink model

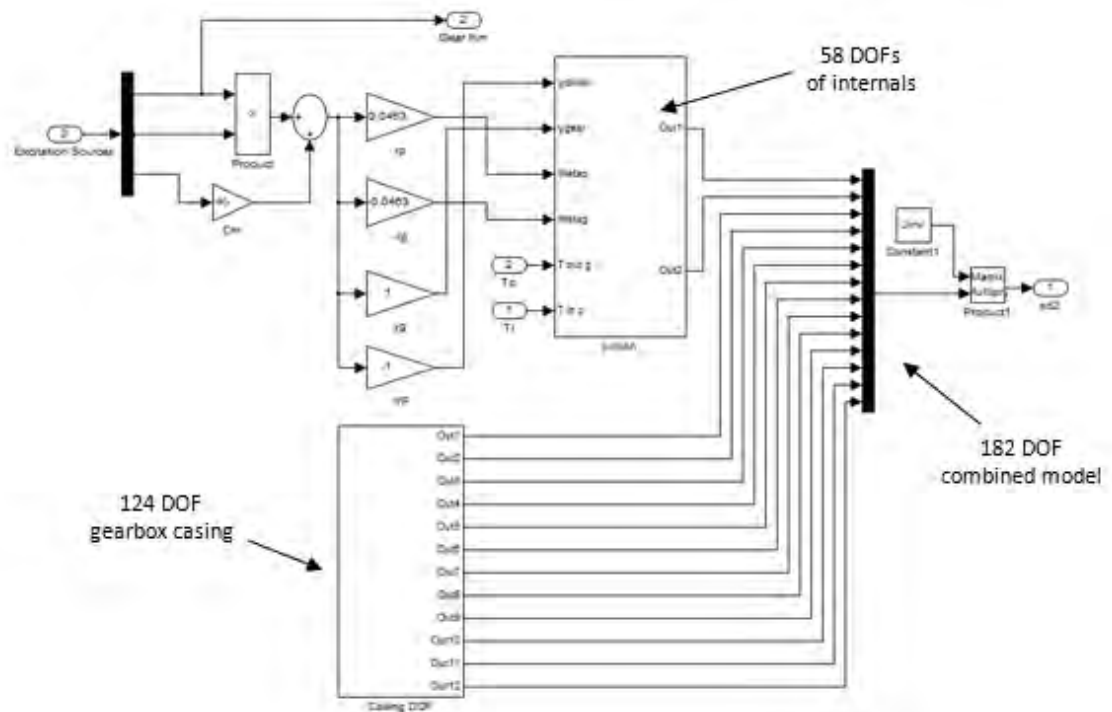


Figure B.2 Combining reduced FE models of casing and internals

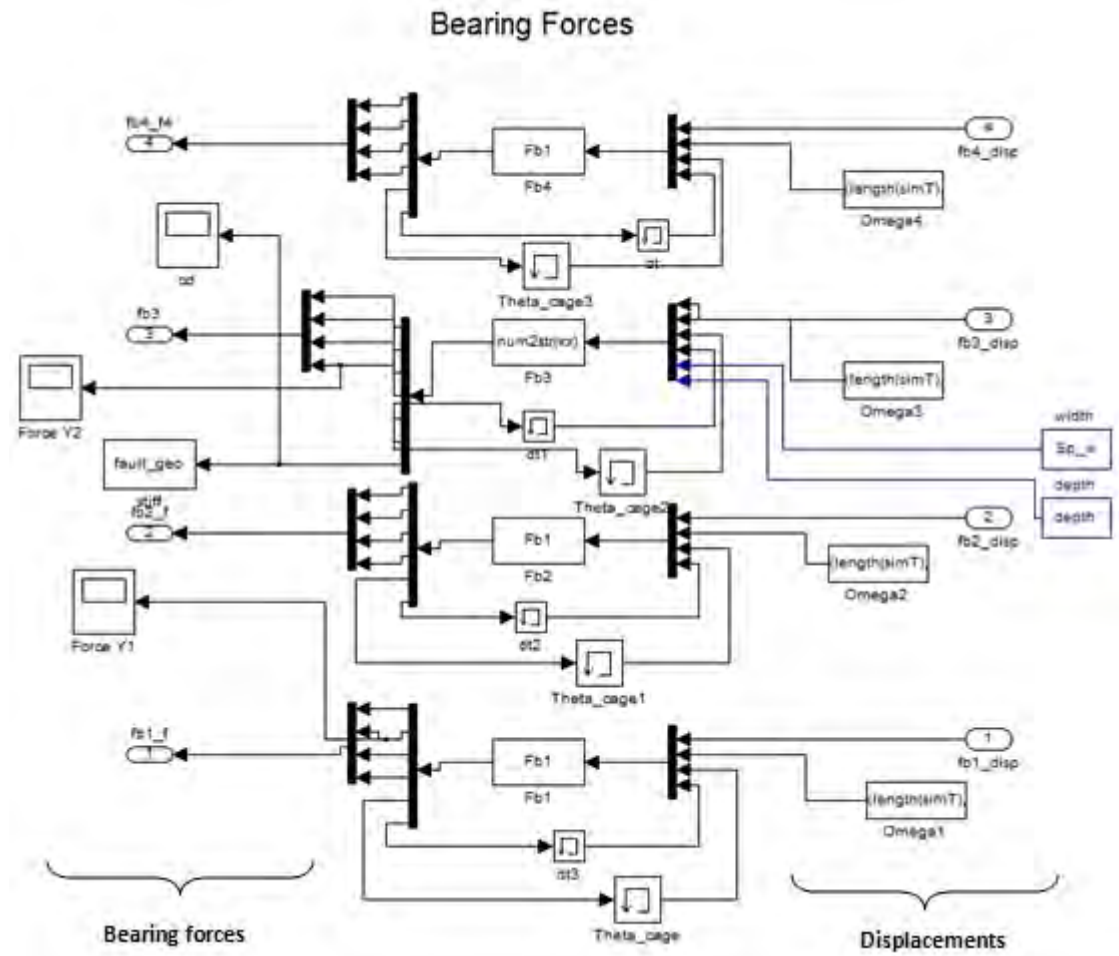


Figure B.3 Bearing S-function [same form as 146 DOF bearing model, Figure A.4]

B.4 References

- Endo, H. 2005. *Simulation of gear faults and its application to the development of differential diagnostic technique* Ph. D. Dissertation, University of New South Wales, Sydney, Australia.
- Sawalhi, N. 2007. *Diagnostics, prognostics and fault simulation for rolling element bearings*. Ph. D. Dissertation, University of New South Wales, Sydney, Australia.

APPENDIX C

PLANETARY SIMULATION MODEL

The methodology of the planet gear fault simulation and the discussion of results were presented in Chapter 7. This appendix provides further details of the 18 DOF lumped parameter model. Section C.1 illustrates the schematic of the Matlab/Simulink model. The detailed equations of motion for each planetary sub-system and for the overall assembly are included in Section C.2. The physical parameters or the input data used in implementing the model is shown in Section C.3.

C.1 Simulink model: Planetary gear

The block diagram in Figure C.1 shows the overall Matlab/Simulink® model of the 18 DOF LPM of the planetary insert. Figure C.2 shows the module (F/M) to calculate the excitation forces and the accelerations. The second order differential equations of motion (Chapter 7, Section 7.7) with time varying mesh stiffness were solved using ordinary differential equation solver (ode45) with variable time step.

In contrast to the parallel shaft gear, the Simulink model of the planetary gear includes multiple gear meshes (six in the current configuration with three equally spaced planets) to represent sun-planet and ring-planet contacts. The time varying mesh stiffness along with the displacements, rotational speed of the planet carrier and the time increments are incorporated in the Simulink model by *adapting* a special Matlab® S-function (Endo, 2005).

The inputs to the model are input, output and the holding torque applied to the planet carrier, sun and the ring gear (which is held stationary) and mass and damping matrices and time varying gearmesh stiffnesses. The outputs are accelerations, velocities and displacements at the 18 DOFs defined in the LPM.

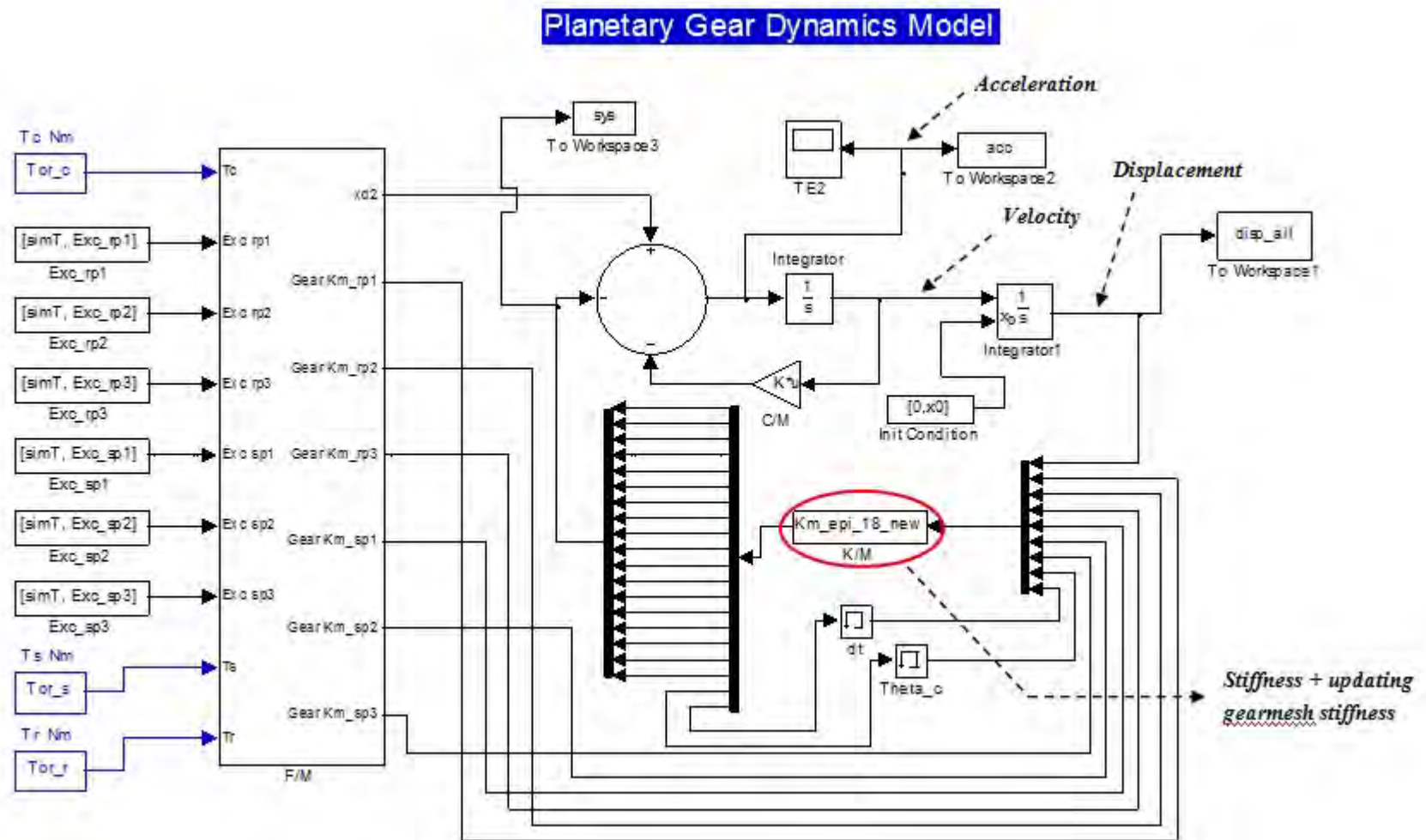
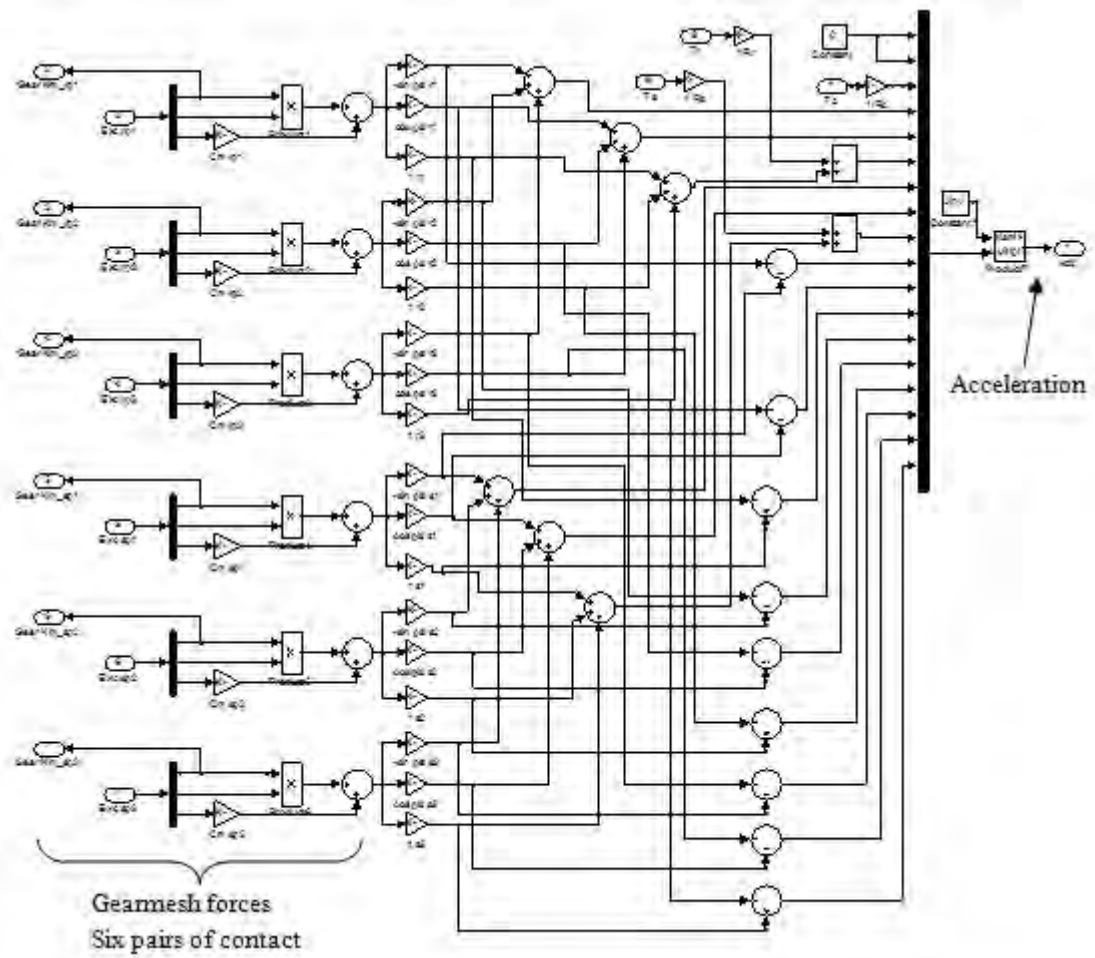


Figure C.1 Planetary gear Simulink model



C.2 Planetary gear LPM – Equations of motion

The general equations of motion of the planetary gear set are described in Chapter 7 Section 7.7. This section illustrates the detailed equations of motion for each sub-system and derives the individual mass, stiffness and damping matrices and the overall assembly matrices of the system. For simplicity only the equations with the stiffness terms are shown. Refer to Section 7.7 for the nomenclature of the various parameters used in the equations. The equations of motion for the three subsystems were based on Kahraman's model (1994), however the equations were re-written in the generalised right hand co-ordinate system x, y and θ instead of x, y and u (where $u = r\theta$).

Sun gear - Planet i pair

The relative gearmesh displacement $P_{spi}(t)$ is given by

$$P_{spi}(t) = (y_s - y_{pi}) \cos \psi_{si} - (x_s - x_{pi}) \sin \psi_{si} + R_s \theta_s + R_p \theta_p - e_{jpi}(t)$$

$$m_s \ddot{x}_s - h_{spi} k_{spi}(t) [y_s \cos \psi_{si} - y_p \cos \psi_{si} - x_s \sin \psi_{si} + x_{pi} \sin \psi_{si} + R_s \theta_s + R_p \theta_p] \sin \psi_{si} = 0$$

$$m_s \ddot{y}_s - h_{spi} k_{spi}(t) [y_s \cos \psi_{si} - y_{pi} \cos \psi_{si} - x_s \sin \psi_{si} + x_{pi} \sin \psi_{si} + R_s \theta_s + R_p \theta_p] \cos \psi_{si} = 0$$

$$J_s \ddot{\theta}_s - h_{spi} k_{spi}(t) R_s [y_s \cos \psi_{si} - y_{pi} \cos \psi_{si} - x_s \sin \psi_{si} + x_{pi} \sin \psi_{si} + R_s \theta_s + R_p \theta_p] = T_s/n$$

$$m_s = \begin{bmatrix} m_s & 0 & 0 \\ 0 & m_s & 0 \\ 0 & 0 & m_s \end{bmatrix}$$

$$k_{s11}^{(i)}/k_{spi}(t) = c_{s11}^{(i)}/c_{sp} = \begin{bmatrix} \sin^2 \psi_{si} & -\cos \psi_{si} \sin \psi_{si} & -R_s \sin \psi_{si} \\ -\sin \psi_{si} \cos \psi_{si} & \cos^2 \psi_{si} & R_s \cos \psi_{si} \\ -R_s \sin \psi_{si} & R_s \cos \psi_{si} & R_s^2 \end{bmatrix}$$

$$k_{s12}^{(i)}/k_{spi}(t) = c_{s12}^{(i)}/c_{sp} = \begin{bmatrix} -\sin^2 \psi_{si} & \cos \psi_{si} \sin \psi_{si} & -R_p \sin \psi_{si} \\ \sin \psi_{si} \cos \psi_{si} & -\cos^2 \psi_{si} & R_p \cos \psi_{si} \\ R_s \sin \psi_{si} & -R_s \cos \psi_{si} & R_s R_p \end{bmatrix}$$

$$m_p \ddot{x}_{pi} + h_{spi} k_{spi}(t) [y_s \cos \psi_{si} - y_p \cos \psi_{si} - x_s \sin \psi_{si} + x_{pi} \sin \psi_{si} + R_s \theta_s + R_p \theta_p] \sin \psi_{si} = 0$$

$$m_p \ddot{y}_{pi} + h_{spi} k_{spi}(t) [y_s \cos \psi_{si} - y_{pi} \cos \psi_{si} - x_s \sin \psi_{si} + x_{pi} \sin \psi_{si} + R_s \theta_s + R_p \theta_p] \cos \psi_{si} = 0$$

$$J_p \ddot{\theta}_p + h_{spi} k_{spi}(t) R_p [y_s \cos \psi_{si} - y_{pi} \cos \psi_{si} - x_s \sin \psi_{si} + x_{pi} \sin \psi_{si} + R_s \theta_s + R_p \theta_p] = 0$$

$$m_p = \begin{bmatrix} m_p & 0 & 0 \\ 0 & m_p & 0 \\ 0 & 0 & J_p \end{bmatrix}$$

$$k_{s12}^{(i)T}/k_{spi}(t) = c_{s12}^{(i)T}/c_{sp} = \begin{bmatrix} -\sin^2 \psi_{si} & \cos \psi_{si} \sin \psi_{si} & R_s \sin \psi_{si} \\ \cos \psi_{si} \sin \psi_{si} & -\cos^2 \psi_{si} & -R_s \cos \psi_{si} \\ -R_p \sin \psi_{si} & R_p \cos \psi_{si} & R_s R_p \end{bmatrix}$$

$$k_{s22}^{(i)}/k_{spi}(t) = c_{s22}^{(i)}/c_{sp} = \begin{bmatrix} \sin^2 \psi_{si} & -\cos \psi_{si} \sin \psi_{si} & R_p \sin \psi_{si} \\ -\sin \psi_{si} \cos \psi_{si} & \cos^2 \psi_{si} & -R_p \cos \psi_{si} \\ R_p \sin \psi_{si} & -R_p \cos \psi_{si} & R_p^2 \end{bmatrix}$$

Ring gear - Planet i pair

The relative gearmesh displacement $P_{rpi}(t)$ is given by

$$P_{rpi}(t) = (y_r - y_{pi}) \cos \psi_{ri} - (x_r - x_{pi}) \sin \psi_{ri} + R_r \theta_r - R_p \theta_p - e_{jpi}(t)$$

$$m_r \ddot{x}_r - h_{rpi} k_{rpi}(t) [y_r \cos \psi_{ri} - y_{pi} \cos \psi_{ri} - x_r \sin \psi_{ri} + x_{pi} \sin \psi_{ri} + R_r \theta_r - R_p \theta_p] \sin \psi_{ri} = 0$$

$$m_r \ddot{y}_r - h_{rpi} k_{rpi}(t) [y_r \cos \psi_{ri} - y_{pi} \cos \psi_{ri} - x_r \sin \psi_{ri} + x_{pi} \sin \psi_{ri} + R_r \theta_r - R_p \theta_p] \cos \psi_{ri} = 0$$

$$J_r \ddot{\theta}_r - h_{rpi} k_{rpi}(t) R_r [y_r \cos \psi_{ri} - y_{pi} \cos \psi_{ri} - x_r \sin \psi_{ri} + x_{pi} \sin \psi_{ri} + R_r \theta_r - R_p \theta_p] = T_r/n$$

$$m_r = \begin{bmatrix} m_r & 0 & 0 \\ 0 & m_r & 0 \\ 0 & 0 & J_r \end{bmatrix}$$

$$k_r^{(i)}/k_{rpi}(t) = c_r^{(i)}/c_{rp} = \begin{bmatrix} \sin^2 \psi_{ri} & -\cos \psi_{ri} \sin \psi_{ri} & -R_r \sin \psi_{ri} \\ -\sin \psi_{ri} \cos \psi_{ri} & \cos^2 \psi_{ri} & R_r \cos \psi_{ri} \\ -R_r \sin \psi_{ri} & R_r \cos \psi_{ri} & R_r^2 \end{bmatrix}$$

$$k_{r12}^{(i)}/k_{rpi}(t) = c_{r12}^{(i)}/c_{rp} = \begin{bmatrix} -\sin^2 \psi_{ri} & \cos \psi_{ri} \sin \psi_{ri} & R_p \sin \psi_{ri} \\ \cos \psi_{ri} \sin \psi_{ri} & -\cos^2 \psi_{ri} & -R_p \cos \psi_{ri} \\ R_r \sin \psi_{ri} & -R_r \cos \psi_{ri} & -R_p R_r \end{bmatrix}$$

$$m_p \ddot{x}_{pi} + h_{rpi} k_{rpi}(t) [y_r \cos \psi_{ri} - y_{pi} \cos \psi_{ri} - x_r \sin \psi_{ri} + x_{pi} \sin \psi_{ri} + R_r \theta_r - R_p \theta_p] \sin \psi_{ri} = 0$$

$$m_p \ddot{y}_{pi} + h_{rpi} k_{rpi}(t) [y_r \cos \psi_{ri} - y_{pi} \cos \psi_{ri} - x_r \sin \psi_{ri} + x_{pi} \sin \psi_{ri} + R_r \theta_r - R_p \theta_p] \cos \psi_{ri} = 0$$

$$J_p \ddot{\theta}_p - h_{rpi} k_{rpi}(t) R_p [y_r \cos \psi_{ri} - y_{pi} \cos \psi_{ri} - x_r \sin \psi_{ri} + x_{pi} \sin \psi_{ri} + R_r \theta_r - R_p \theta_p] = 0$$

$$M_p = \begin{bmatrix} M_p & 0 & 0 \\ 0 & M_p & 0 \\ 0 & 0 & J_p \end{bmatrix}$$

$$k_{r12}^{(i)T}/k_{rpi}(t) = c_{r12}^{(i)T}/c_{rp} = \begin{bmatrix} -\sin^2 \psi_{ri} & -\cos \psi_{ri} \sin \psi_{ri} & -R_p \sin \psi_{ri} \\ -\sin \psi_{ri} \cos \psi_{ri} & \cos^2 \psi_{ri} & R_p \cos \psi_{ri} \\ -R_p \sin \psi_{ri} & R_p \cos \psi_{ri} & R_p^2 \end{bmatrix}$$

$$k_{r22}^{(i)}/k_{rpi}(t) = c_{r22}^{(i)}/c_{rp} = \begin{bmatrix} \sin^2 \psi_{ri} & -\cos \psi_{ri} \sin \psi_{ri} & -R_p \sin \psi_{ri} \\ -\sin \psi_{ri} \cos \psi_{ri} & \cos^2 \psi_{ri} & R_p \cos \psi_{ri} \\ -R_p \sin \psi_{ri} & R_p \cos \psi_{ri} & R_p^2 \end{bmatrix}$$

Carrier -Planet Pair

$$m_c \ddot{x}_c - K_{xx} (x_c - x_{pi} - R_c \theta_c \sin \psi_i) = 0$$

$$m_c \ddot{y}_c - K_{yy} (y_c - y_{pi} + R_c \theta_c \cos \psi_i) = 0$$

$$J_c \ddot{\theta}_c - R_c K_{xx} (x_c - x_{pi} - R_c \theta_c \sin \psi_i) \sin \psi_i + R_c K_{yy} (y_c - y_{pi} + R_c \theta_c \cos \psi_i) \cos \psi_i = T_c/n$$

$$m_p \ddot{x}_{pi} - K_{xx} (x_c - x_{pi} - R_c \theta_c \sin \psi_i) = 0$$

$$m_p \ddot{y}_{pi} - K_{yy} (y_c - y_{pi} + R_c \theta_c \cos \psi_i) = 0$$

$$m_c = \begin{bmatrix} m_c & 0 & 0 \\ 0 & m_c & 0 \\ 0 & 0 & J_c \end{bmatrix} \quad k_{c11}^{(i)} = \begin{bmatrix} K_{xx} & 0 & -R_c K_{xx} \sin \psi_i \\ 0 & K_{yy} & R_c K_{yy} \cos \psi_i \\ -R_c K_{xx} \sin \psi_i & R_c K_{yy} \cos \psi_i & R_c^2 (K_{xx} \sin^2 \psi_i + K_{yy} \cos^2 \psi_i) \end{bmatrix}$$

$$k_{c12}^{(i)} = \begin{bmatrix} -K_{xx} & 0 & 0 \\ 0 & -K_{yy} & 0 \\ R_c K_{xx} \sin \psi_i & -R_c K_{yy} \cos \psi_i & 0 \end{bmatrix} \quad k_{c22} = \begin{bmatrix} K_{xx} & 0 & 0 \\ 0 & K_{yy} & 0 \\ 0 & 0 & 0 \end{bmatrix}$$

$$k_{c12}^{(i)T} = \begin{bmatrix} -K_{xx} & 0 & R_c K_{xx} \sin \psi_i \\ 0 & -K_{yy} & -R_c K_{yy} \cos \psi_i \\ 0 & 0 & 0 \end{bmatrix}$$

$$c_{c11}^{(i)} = \begin{bmatrix} C_{xx} & 0 & -R_c K_{xx} \sin \psi_i \\ 0 & C_{yy} & R_c K_{yy} \cos \psi_i \\ -R_c C_{xx} \sin \psi_i & R_c C_{yy} \cos \psi_i & R_c^2 (C_{xx} \sin^2 \psi_i + C_{yy} \cos^2 \psi_i) \end{bmatrix}$$

$$c_{c12}^{(i)} = \begin{bmatrix} -C_{xx} & 0 & 0 \\ 0 & -C_{yy} & 0 \\ R_c C_{xx} \sin \psi_i & -R_c C_{yy} \cos \psi_i & 0 \end{bmatrix}$$

$$c_{c22} = \begin{bmatrix} C_{xx} & 0 & 0 \\ 0 & C_{yy} & 0 \\ 0 & 0 & 0 \end{bmatrix}$$

Overall [K] and [C] matrices

$K =$

$$K = \begin{bmatrix} \sum k_{c11}^{(i)} + ks & 0 & ksc & k_{c12}^{(1)} & k_{c12}^{(2)} & k_{c12}^{(3)} \\ & \sum k_r^{(i)} & 0 & k_{r12}^{(1)} & k_{r12}^{(2)} & k_{r12}^{(3)} \\ ksc' & & \sum k_{s11}^{(i)} + ks & k_{s12}^{(1)} & k_{s12}^{(2)} & k_{s12}^{(3)} \\ & & & k_{s22}^{(1)} + k_{r22}^{(1)} + k_{c22}^{(1)} & 0 & 0 \\ & \text{symmetric} & & & k_{s22}^{(2)} + k_{r22}^{(2)} + k_{c22}^{(2)} & 0 \\ & & & & & k_{s22}^{(3)} + k_{r22}^{(3)} + k_{c22}^{(3)} \end{bmatrix}$$

$$C = \begin{bmatrix} \sum c_{c11}^{(i)} & 0 & 0 & c_{c12}^{(1)} & c_{c12}^{(2)} & c_{c12}^{(3)} \\ & \sum c_r^{(i)} & 0 & c_{r12}^{(1)} & c_{r12}^{(2)} & c_{r12}^{(3)} \\ & & \sum c_{s11}^{(i)} & c_{s12}^{(1)} & c_{s12}^{(2)} & c_{s12}^{(3)} \\ & & & c_{s22}^{(1)} + c_{r22}^{(1)} + c_{c22}^{(1)} & 0 & 0 \\ & & & & c_{s22}^{(2)} + c_{r22}^{(2)} + c_{c22}^{(2)} & 0 \\ & & \text{symmetric} & & & c_{s22}^{(3)} + c_{r22}^{(3)} + c_{c22}^{(3)} \end{bmatrix}$$

Stiff spring between carrier & sun (ks)

$$ks = \begin{bmatrix} 1E9 & 0 & 0 \\ 0 & 1E9 & 0 \\ 0 & 0 & 0 \end{bmatrix}$$

$$ksc = \begin{bmatrix} -1E9 & 0 & 0 \\ 0 & -1E9 & 0 \\ 0 & 0 & 0 \end{bmatrix}$$

Table C.1 shows the mesh frequency force vector which is incorporated in the Simulink model of the planetary gear insert.

Table C.1 Mesh frequency force vector

$$F = F_m + F_a(t) \quad F_m : \text{mean force} \quad F_a(t) : \text{alternating force}$$

No	DOF	F_m	F_a
1	x_c	0	0
2	y_c	0	0
3	θ_c	T_c	0
4	x_r	0	$[c_{rp}\dot{e}_{rp1}(t) + k_{rp1}(t)e_{rp1}(t)](-\sin\psi_{r1}) +$ $[c_{rp}\dot{e}_{rp2}(t) + k_{rp2}(t)e_{rp2}(t)](-\sin\psi_{r2}) +$ $[c_{rp}\dot{e}_{rp3}(t) + k_{rp3}(t)e_{rp3}(t)](-\sin\psi_{r3})$
5	y_r	0	$[c_{rp}\dot{e}_{rp1}(t) + k_{rp1}(t)e_{rp1}(t)](\cos\psi_{r1}) +$ $[c_{rp}\dot{e}_{rp2}(t) + k_{rp2}(t)e_{rp2}(t)](\cos\psi_{r2}) +$ $[c_{rp}\dot{e}_{rp3}(t) + k_{rp3}(t)e_{rp3}(t)](\cos\psi_{r3})$
6	θ_r	T_r	$[c_{rp}\dot{e}_{rp1}(t) + k_{rp1}(t)e_{rp1}(t)](R_r) +$ $[c_{rp}\dot{e}_{rp2}(t) + k_{rp2}(t)e_{rp2}(t)](R_r) +$ $[c_{rp}\dot{e}_{rp3}(t) + k_{rp3}(t)e_{rp3}(t)](R_r)$
7	x_s	0	$[c_{sp}\dot{e}_{sp1}(t) + k_{sp1}(t)e_{sp1}(t)](-\sin\psi_{s1}) +$ $[c_{sp}\dot{e}_{sp2}(t) + k_{sp2}(t)e_{sp2}(t)](-\sin\psi_{s2}) +$ $[c_{sp}\dot{e}_{sp3}(t) + k_{sp3}(t)e_{sp3}(t)](-\sin\psi_{s3})$
8	y_s	0	$[c_{sp}\dot{e}_{sp1}(t) + k_{sp1}(t)e_{sp1}(t)](\cos\psi_{s1}) +$ $[c_{sp}\dot{e}_{sp2}(t) + k_{sp2}(t)e_{sp2}(t)](\cos\psi_{s2}) +$ $[c_{sp}\dot{e}_{sp3}(t) + k_{sp3}(t)e_{sp3}(t)](\cos\psi_{s3})$
9	θ_s	T_s	$[c_{sp}\dot{e}_{sp1}(t) + k_{sp1}(t)e_{sp1}(t)](R_s) +$ $[c_{sp}\dot{e}_{sp2}(t) + k_{sp2}(t)e_{sp2}(t)](R_s) +$ $[c_{sp}\dot{e}_{sp3}(t) + k_{sp3}(t)e_{sp3}(t)](R_s)$
10	x_{pl}	0	$[c_{sp}\dot{e}_{sp1}(t) + k_{sp1}(t)e_{sp1}(t)](\sin\psi_{s1}) -$ $[c_{rp}\dot{e}_{rp1}(t) + k_{rp1}(t)e_{rp1}(t)](-\sin\psi_{r1})$
11	y_{pl}	0	$[c_{sp}\dot{e}_{sp1}(t) + k_{sp1}(t)e_{sp1}(t)](-\cos\psi_{s1}) -$ $[c_{rp}\dot{e}_{rp1}(t) + k_{rp1}(t)e_{rp1}(t)](\cos\psi_{r1})$
12	θ_{pl}	0	$[c_{sp}\dot{e}_{sp1}(t) + k_{sp1}(t)e_{sp1}(t)](R_s) -$ $[c_{rp}\dot{e}_{rp1}(t) + k_{rp1}(t)e_{rp1}(t)](R_r)$

13	x_{p2}	0	$[c_{sp}\dot{e}_{sp2}(t) + k_{sp2}(t)e_{sp2}(t)](\sin\psi_{s2}) - [c_{rp}\dot{e}_{rp2}(t) + k_{rp2}(t)e_{rp2}(t)](-\sin\psi_{r2})$
14	y_{p2}	0	$[c_{sp}\dot{e}_{sp2}(t) + k_{sp2}(t)e_{sp2}(t)](-\cos\psi_{s2}) - [c_{rp}\dot{e}_{rp2}(t) + k_{rp2}(t)e_{rp2}(t)](\cos\psi_{r2})$
15	θ_{p2}	0	$[c_{sp}\dot{e}_{sp2}(t) + k_{sp2}(t)e_{sp2}(t)](R_s) - [c_{rp}\dot{e}_{rp2}(t) + k_{rp2}(t)e_{rp2}(t)](R_r)$
16	x_{p3}	0	$[c_{sp}\dot{e}_{sp3}(t) + k_{sp3}(t)e_{sp3}(t)](\sin\psi_{s3}) - [c_{rp}\dot{e}_{rp3}(t) + k_{rp3}(t)e_{rp3}(t)](-\sin\psi_{r3})$
17	y_{p3}	0	$[c_{sp}\dot{e}_{sp3}(t) + k_{sp3}(t)e_{sp3}(t)](-\cos\psi_{s3}) - [c_{rp}\dot{e}_{rp3}(t) + k_{rp3}(t)e_{rp3}(t)](\cos\psi_{r3})$
18	θ_{p3}	0	$[c_{sp}\dot{e}_{sp3}(t) + k_{sp3}(t)e_{sp3}(t)](R_s) - [c_{rp}\dot{e}_{rp3}(t) + k_{rp3}(t)e_{rp3}(t)](R_r)$

C.3 Planetary LPM simulation – Input data

Table C.2 Planetary insert gear data

Parameter	Sun	Ring	Planet
Pressure angle, deg (α)	20	20	20
No. of teeth (Z_s, Z_r, Z_p)	40	80	20
Module, mm (m)	2	2	2
Pitch circle radius, mm (P_{cr})	40	80	20
Base circle radius, mm (R_s, R_r, R_p), $[P_{cr} \cos \alpha]$	37.59	75.18	18.79
Base pitch, mm (P_b), $[m \pi \cos \alpha]$	5.9043	5.9043	5.9043
Addendum circle radius (A_s, A_r, A_p)	42	78	22

Table C.3 Mass and Moment of inertia

		Mass (kg)	Mass moment of inertia (kg m ²)
planet carrier	m_c	1.978001	J_c 0.004544
sun gear	m_s	0.638885	J_s 0.000592
ring gear	m_r	2.239868	J_r 0.57
planet gear	m_p	0.128018	J_p 0.000034
pinion	m_{pin}	0.390503	J_{pin} 0.000241
spur gear	m_g	2.779465	J_g 0.014309

Table C.4 Bearing support stiffness and damping

	Stiffness		Damping	
planet gear	$K_{xx} = K_{yy}$ (N/m)	1.2×10^8	$C_{xx} = C_{yy}$ (N s/m)	425
ring gear	$k_{brx} = k_{bry}$ (N/m)	1×10^9	$c_{brx} = c_{bry}$ (N s/m)	1.695×10^5
	k_{br_th} (N m/rad)	5.65×10^6		
sun gear	$k_{bsx} = k_{bsy}$	1×10^7	$c_{bsx} = c_{bsy}$ (N s/m)	5.235×10^3
garmesh	$k_{sp} = k_{rp}$	3×10^8	c_m	620

C.4 References

- Endo, H. 2005. *Simulation of gear faults and its application to the development of differential diagnostic technique* Ph. D. Dissertation, University of New South Wales, Sydney, Australia.
- Kahraman, A 1994. Load sharing characteristics of planetary transmissions. *Mechanism and Machine Theory*, 29, 1151-1165.